The Arxan-Chaihe Volcanic Field of Monogenetic Volcanism in intracontinental settings in NE China

A thesis presented in partial fulfilment of the requirements for the degree of **Doctor of Philosophy in Earth Science**

At Massey University, Palmerston North, New Zealand

Bo'xin Li

2023

Abstract

Pliocene to Recent Arxan-Chaihe Volcanic Field (ACVF) is composed of at least 47 vents, representing various types of volcanism, such as Strombolian style, phreatomagmatic explosive, effusive, and lava-fountaining eruptions. These eruptions produced scoria cones, fissure-aligned spatter cones, and tuff rings with a few surrounding maar craters. Field observations imply that the lava-fountaining eruptions are more common on the western side of ACVF, represented by Yanshan (YS)-the Triple Vent, and Daheigou (DHG). In the southwest part of ACVF, lava flows and loose pyroclastic ejecta, such as scoria, mark the eruption events that took place during the Holocene era about 2000 years ago. Dichi (Earth Pond) Lake, with fissures on its eastern side, formed by lava-effusive eruption styles with spatter rows occurring along a fissure, while the low-lying western side of the vent chain is a maar volcano cut into the pre-eruptive lava sheets. Tianchi (Heaven Lake) Lake and Tuofengling (Camel Hump) Lake on the western side of ACVF preserves a range of well-exposed pyroclastic deposits consistent with edifice-building successions. These are composed of scoriaceous pyroclastic materials, yielding construction histories of complex cones (with both "wet" and "dry" explosive eruptive phases). The most significant and largest vent is in the eastern corner of ACVF, Tongxin Lake, a complex phreatomagmatic eruption-style volcano with a maar crater and thick rim deposits. Tongxin Lake is interpreted to be a maar lake that erupted into an intra-montane basin. Intact pyroclastic deposits are preserved within a km from the crater rim and at least 5 meters thick. Stratigraphic and granulometric analyses from five sites around Tongxin Lake indicate the tuff ring of Tongxin was built by processes associated with magma-water interactions that fueled violent explosive eruptions during distinct syn-eruptive stages. Geochemistry is consistent with at least three magma sources contributing to the formation of the complex eruptive products that build the large tuff ring of the maar edifice. Geomorphology terrain analyses performed through GIS-based applications (QGIS) imply that the diverse range of local geology, especially the pre-eruptive topography, was confined and reshaped by the subsequent Pliocene to Recent volcanism in ACVF. Lava flows within ACVF were emplaced over large areas around the two major fluvial systems: Halaha River in the west and Chaoer River in the east of ACVF. The lava flows

in the west of ACVF are generally young and can be modelled using the Q-LavHA plug-in of QGIS. The model has been utilized to simulate lava flow inundation and indicates diverse flow along the flow axis as well as lateral and temporal variations during the evolution of the edifice. Other studies of ACVF, e.g., hazard management, concluded that violent phreatomagmatic explosive events had impacted the fluvial valleys that are commonly associated with structural weakness zones in ACVF. In addition, lava-effusive and lava-fountaining eruptions in urban areas and along major utilities (e.g., roads, geopark facilities or powerlines) also could be heavily impacted by fissure-fed lava flows and potential phreatomagmatic explosions controlled by the local hydrology conditions.

Acknowledgements

The author gratefully would like to thank all people in relation to this research. All the contributions are very valuable under the helps from all angles. First of all, the author must show his huge appreciation to his three supervisors; they are Prof. Károly Németh, Mrs Julie Palmer, and Prof. Alan Palmer. Their kindness, patience, and spirits of integrity always inspire the author to fight through the barriers of the research. For the author's chief supervisor, Prof. Károly Németh, your suggestions and support are very far-sighted; they always gave the author a glimpse of a new way of thinking. Also, the contributions of all published works from Prof. Károly Németh are critical to finalising the procedures of the thesis. In the meantime, all suggestions from the author's co-supervisor, Prof. Alan Palmer, have fully filled the integrality of the thesis logic and publications. My great appreciation to the author's other two co-supervisors – Prof. Alan Palmer and Mrs Julie Palmer, is to demonstrate their huge support and help the way of the research, thesis finalization, and language correction on a high academic level. Besides, the three supervisors provided support for the author's daily life in New Zealand and a huge appreciation for their friendship with the author.

During the field trip seasons, two of the author's supervisors contributed greatly. In 2018, the first documented logs of Tongxin Lake deposits were performed under the supervision of Prof. Alan Palmer, who contributed the whole logic of observations on deposits and subsequent general observations around Tongxin Lake. In the meantime, Prof. Alan Palmer provided a range of unique and valuable information for understanding the behaviours of volcanic deposits and foresight of the distributions of the volcanic materials around Tongxin Lake. In 2019, under the lead of Prof. Károly Németh, detailed observations on both Arxan and Zalantun areas in relation to the volcanism were successfully achieved. During this period of time, Prof. Károly Németh provided very detailed and insightful opinions on the volcanism of the Arxan-Chaihe areas based on his unique previous experiences. There were many others whose contributions were valuable to the success of the trips; they are Dr Jing Wu, Dr Chunqing Sun, and mostly, much appreciated to Prof. Jiaqi Liu from The Institute of Geology and Geophysics, Chinese Academy of Sciences (IGGCAS); their efforts had

become a part of the success of the two-seasoned field trips in ACVF; also, thanks to the cooperations supported by the Zalantun local governments.

The author would like to give big thanks to the managers back in the labs at Massey University; they are Ian Furkert and Anja Moebis. Especially huge thanks to Ian Furkert for his patience and academic support for the lab works, utilisations of types of equipment and friendly advice on the management of daily works. Also, huge thanks to the staff of Waikato University, who provided parts of geochemistry analyses on the samples.

A specific appreciation to the author's best friend, Dr Callum Rees; I am so grateful for your friendship, sense of humour, and, especially, your valuable academic opinions and suggestions on this project.

Last but not least, my heart goes to my parents, Mrs Zhan Hou and Mr Keqiang Li, who have unconditionally been supporting every single day of my life. Your personalities always encourage me to step on every high level. Lastly, the author would like to show his great appreciation and love to his wife, Bi'zhu Li, who has been accompanying me every moment of my daily life, including providing valuable suggestions on thesis writing strategies, passing exams for my driving license, and especially patience to me. Without all support from your love and encouragement, I could not achieve this.

Table of content

List of Figures

List of Tables

List of abbreviations

Arxan-Chaihe Volcanic Field (ACVF)

Longgang Volcanic Field (LVF)

Auckland Volcanic Field (AVF)

Tongxin Lake/Volcano (TX)

Yanshan-Triple Vent (YS)

Da Heigou/Dahei Gou/Daheigou (DHG)

Dichi Lake (DC)

Newer Volcanics Province (NVP)

Red Rock Volcanic Complex (RRVC)

Chapter1: Introduction

1. *Context of the research*

1) Monogenetic volcanism

Small-volume volcanoes with a single eruption period are common in basaltic composition with broad eruption style ranges. Fragmented magma can produce pyroclasts in a wide range of grain sizes and shapes, as well as chemical properties within a single eruptive unit reflect on a complex magmatic system and its interaction with the eruptive environment, even in such small-volume eruptions. Monogenetic volcanism is typically represented as "small volcanoes", but how small? In comparison to large stratovolcanoes, monogenetic volcanoes have small eruption volumes in a relatively short eruptive duration (commonly in weeks) Németh and Kereszturi (2015). Even for the largest extensions of one (El Negrillar Volcanic Field, Chile), the total volume is still considered to be about 1-3 times less than a common polygenetic stratovolcano (Németh, 2010b; Smith & Németh, 2017). The majority of monogenetic volcanoes are basaltic, with rarer andesitic or even rhyolitic compositions (Bacon, 1990; Straub et al., 2008; Valentine & Gregg, 2008). Usually, monogenetic volcanoes form clusters which form a volcanic field within a larger volcanic field (de Silva & Lindsay, 2015). An individual volcano may have a short-lived eruption duration, but the entire volcanic field may have very long-lived activity, even longer than a single stratovolcano, e.g., the volcanic activity length of the Arxan-Chaihe Volcanic Field (ACVF) vs Mt. Changbai in the frontier between China and the Korea DPR (Kereszturi & Németh, 2012a; Németh, 2010b, 2012; Németh & Kereszturi, 2015; Smith & Németh, 2017). The distribution trends of these "small" (typically less than 1 km^3 dense rock equivalent volume) (Kereszturi et al., 2013) volcanoes commonly reveal the regional tectonic settings and contribute to the understanding of the evolution of tectonic basins (Cañón-Tapia, 2016; Cañón-Tapia & Walker, 2004; Mazzarini & Isola, 2010; Mazzarini et al., 2016; Uslular et al., 2021). Based on the erosional features of a monogenetic volcano, geologists can even reconstruct the post-eruptive environment, such as the surface erosion in relation to impacting the volcanic clasts, regional prevailing wind directions in relation to the distal ash distributions, and topographic

evolution (Bemis & Ferencz, 2017; Fornaciai et al., 2010; Kereszturi & Németh, 2012b; Nemeth, 2001; Németh & Martin, 1999; Németh et al., 2003a; Zarazúa-Carbajal & De la Cruz-Reyna, 2021). Monogenetic volcanism generally can be found in intra-plate continental settings, far away from tectonic plate boundaries (Smith & Németh, 2017). Thus, the origin of such volcanism is related to regional structural features such as fault zones or graben subsidence processes. Monogenetic volcanism commonly involves explosive eruptions and phreatomagmatic activity with explosive interactions between magma and water. The typical pyroclastic density current deposits that are commonly associated with volcanoes erupted through explosive phreatomagmatism with the deposit texture and trend evident by their typical sedimentary patterns in the field (Martí et al., 2018; Németh, 2012; Valentine & Gregg, 2008; White, 1990). In comparison to stratovolcanoes, monogenetic volcanoes can erupt dominantly primitive compositions directly connected to deep mantle sources, e.g., mafic materials (Nemeth et al., 2003b; Smith et al., 2008). The magma evolution of monogenetic volcanism consists of highly contained crystal fractionation and fewer interactions between magma batches and bedrocks (assimilation) (Kereszturi & Németh, 2016a). In recent years, however, growing evidence shows that the compositional variations recorded within monogenetic volcanic successions are dominantly linked to variations of deep source regions (Brenna et al., 2012; Brenna et al., 2018; Brenna et al., 2015; Jankovics et al., 2015; Jankovics et al., 2019; Smith et al., 2021). The temporal and spatial distributions of monogenetic volcanism have been studied in various volcanic regions on Earth in different geotectonic settings, such as Western Pannonian Basin in Hungary (Martin & Németh, 2004), Auckland Volcanic Field in NZ (McGee et al., 2013), and Arxan-Chaihe Volcanic Field (ACVF) in NE China (Li et al., 2020; Németh et al., 2017a; Sun et al., 2016; Tang et al., 2005; Wang et al., 2014). Different types of structural settings can cause different patterns of vent distribution, e.g., fissure-triggered volcanic fields in Hawaii (Nakamura, 1977; Takada, 1994) and the western Pannonian Basin in Hungary (Kereszturi et al., 2011; Nemeth et al., 2003b). ACVF has a linear distribution pattern of its volcanic edifices, which follow deep regional tectonic fault zones and the basement structure (Li et al., 2020; Wang et al., 2014; Zhao et al., 2008).

In general, monogenetic volcanoes can be separated and recognised by five geoform types: maar, scoria (cinder) cone, tuff ring, tuff cone, and effusive lava flows ('a'ā and pahoehoe). These types of volcanoes form typical landscapes and topography.

- Maar

A maar is formed by a range of explosive eruptions in relation to phreatomagmatism, powered by a dyke in which magma under encounters underground water and triggers increasing interaction surface area to have maximum energy transfer (Rittmann, 1962; Wohletz, 1986; Wohletz & McQueen, 1984a; Wohletz & Sheridan, 1983). Based on this definition, a maar may have crater-formed topography with a low rim rising from a deep floor excavated through to bedrock up to 2 km deep (Wood, 1979). The different magnitudes of the eruptions can generate different volumes of ejected materials that control the depth of the maar crater floor. Some of them this is a few hundred metres; others are a few kilometres deep (DeHon, 2015). The surrounding deposits are generally mixtures of bedrock fragments and very large quantities of juvenile clasts in typical stratified patterns (DeHon, 2015; Lorenz, 1975; Lorenz, 1985; Lorenz, 2003a, 2003b; Valentine & van Wyk de Vries, 2014; Valentine & White, 2012; White & Ross, 2011). Also, large volumes of lava flow are recognisable at the proximal and intermediate locations away from the vent centre. A maar volcano always has an unstratified diatreme structure that usually contains blocks of bedrock with massive tuff materials in the intermediate depth of the diatreme. In the lower part of the diatreme, a feeder dike with shattered bedrock breccias can be found (White, 1991). Diatreme deposits are formed by the post-eruptive collapse due to the unstable mechanism of the conduit wall (Lorenz, 2003a).

- Scoria/cinder cone

A scoria/cinder cone forms a topographic cone-like structure built up of ejected materials (Macdonald, 1972). The ejected materials are commonly loose, vesicular and mafic scorias which form the entire topography of the cone. Mixtures of other pyroclastic materials can spread around the cone in a circular shape. Some of them may follow an elongated fissure trend; thus, the distributions of the scoria cones are depicted as a linear trend (Fodor & Broz, 2015). Basically, a scoria cone is formed by a

series of eruptions of lava fountains or strombolian-type magma fragmentation. Such eruption style commonly involves a high degassing rate while magma batches ascend. In the deposits of cinder cones, usually, ballistic trajectory objects can be found among the scoria clasts; this indicates the volcanic bombs erupted from the vent commonly due to the viscous and elastic nature of the eruptive materials (Wood, 1980). As eruptions progress from a scoria cone, the decreasing gas content results in the magma becoming thicker and more vicious; thus, a scoria cone may change into a spatter cone with welded cinders spreading around the cone body (Fodor & Németh, 2014; Wood, 1980). Also, a scoria cone can produce large volumes of lava flows, such as recorded in extensive intracontinental volcanic fields that evolved a long time over thick continental crusts like those in the Arabian Peninsula (Camp et al., 1991; Németh & Moufti, 2023).

- Tuff cone

The definition of a tuff cone is a steep-sided structure with a rim up to a hundred metres high. These are formed by phreatomagmatically explosive eruptions that produce stratified ash, with accidental lithics present in the lapilli as bedrock fragments dislodged from the edifice surrounding the vent (Wohletz & Sheridan, 1983). In comparison to maar volcanoes, a tuff cone is a constructional geoform commonly built on top of a pyroclastic mound and formed under situations of large volumes of external water contents. Tuff cones may be the only section of volcanoes due to water collecting within the crater (Brand & Broz, 2015). The base of the tuff cones is mound-like (Murtagh & White, 2013; White, 1996a). The deposits around the tuff cone show a range of stratified structures with well-recognised bedding, in which the thickness of each layer is usually centimetres to millimetres. Typically, the bedding consists of "turbidite-like" grain size variation, i.e., alternating sandy and silty pyroclastic materials (Brand & Broz, 2015; White, 1996a). The pyroclastic succession of a tuff cone can be extensively palagonitised. This clay mineral assemblage forms due to the alteration of mafic volcanic glass, the result of secondary water-magma interactions of water vapour and heat present in the wet conditions the metastable glassy pyroclast layers accumulate in (a) as (Brand & White, 2007; Farrand & Singer, 1992).

- Tuff ring

In comparison to tuff cones, tuff rings are low dip angle geoforms consisting of pyroclastic beds surrounding a very shallow crater with a relatively large crater floor area; the rim is low, usually less than 50 m high, and only depicts an outline of the boundary of the volcano (Broz & Nemeth, 2015). From this definition, the slope angle of a tuff ring is low, about 2-15 degrees (Wohletz & Sheridan, 1983), formed by the pyroclastic deposits due to the small eruptive volume. The juvenile deposits will gradually grade into reworked fan deposits in the distal areas (Kereszturi & Németh, 2012a; Németh, 2010b). Compared to maar volcanoes, the deposits of a tuff ring display abundant dune structures, which grade laterally into coarse lapilli and pyroclastic breccias beds in the proximal areas (Heiken, 1971; Kereszturi & Németh, 2012a). Wohletz and Sheridan (1983) revealed that a tuff ring could generate the initial explosive breccia, then a range of thinly bedded units triggered by energetic surges. Subsequently, research by Broz and Nemeth (2015) and Németh et al. (2012) indicated that deposits of a tuff ring contain dune-bedded and tuffaceous laminations. Those beds are intercalated with coarse lapilli and breccias in proximal areas. Due to the shallow crater floor, a tuff ring experiences only shallow depth water-magma interactions with limited excavations of the country rocks, and therefore it is inferred that beneath their crater floor, they have no diatreme formation like maar volcanoes have. Instead, remnants of lava ponds and some collapsed domes are reported to be found under the tuff ring crater floors (Affleck et al., 2001; Lorenz, 1986). The extension of a tuff ring is commonly no more than a kilometre away from the rim of a cone. Tuff rings are produced under short eruptive events. Sometimes they were formed by a single event or several short-lived events; thus, the deposits of a tuff ring contain a range of laminated bedding Separated by erosional surfaces (Heiken, 1971; Németh et al., 2012; Nemeth & Kereszturi, 2013; Wohletz & Sheridan, 1983).

- Effusive lava flows

Lava flows in volcanic fields can extend thousands of square kilometres in areas. Two major geoforms of lava flows ('a'ā and pāhoehoe) present the different morphologies on volcanic fields. Pāhoehoe type contains smooth surfaces with ropy structures that are looked like twisted ropes piling with each other (Macdonald, 1953). Whaleback

shapes or hummocks are commonly observed on surfaces of such a type of lava flow. The typical internal structure of the pāhoehoe type is lava tubes. When the earlier flows crusted and chilled, the latter flows were still in advance under the thin crust, and then the tube formed. 'A'ā type refers to the lava flows with very rough and spinose surface structures. Usually, the surfaces of 'a'ā flows contain large fragments due to the cracking of the spinose structures, while the front of flows was rolling toward the moving direction (Macdonald, 1953).

- Petit-spot volcanism

Petit-spot volcanism is a relatively new addition to the spectrum of monogenetic volcanism. It was first described in the northwest of the Pacific Plate, near the Japan Subduction Zone. Petit-spot volcanoes are revealed by a range of volcanic regimes existing for more than 8 million years; also the activity is commonly about 600 km along with the direction of the plate movement. Such volcanoes are found on the subducting oceanic plate due to tectonic plates sinking deeper into the Earth's upper mantle, fissures occur where the plate begins to bend causing small volcanoes to erupt (Hirano, 2011). Petit-spot volcanoes are characterised by basalt with high alkali compositions. The ages of such volcanoes are generally ranging from 0.05-8.5 million years (mostly discovered in Japan Trench). The evidence of petit-spot volcanism indicates the flexure of the plate, with respect to the ascending melts from the asthenosphere (Hirano, 2011; Hirano & Machida, 2022; Machida et al., 2017).

2) Roles of phreatomagmatism

The phreatomagmatic explosive eruption is seemingly one of the major volcanic types in every monogenetic volcanic field. During the volcanic evolution processes, with magma ascent to the surface, countless interactions between external and internal processes occur in the pre-eruptive phase (Kereszturi & Németh, 2012a). For example, degassing will occur during the magma ascent from its source to the surface. While the magma erupts through the vent, explosive or effusive eruption behaviours are determined by the eruptive conditions, as represented by internal factors such as the chemical composition of the magma and external parameters such as the availability of water (Kereszturi & Németh, 2012a). The identification of a monogenetic volcano

is very important information by utilising field observation and data collection. Commonly, volcanic deposits are generated by a range of discontinued eruptions and associated pyroclastic sedimentation (Kereszturi & Németh, 2012a).

The following section describes the external interaction between water and magma. Magma fragmentation usually happens when the melt comes into contact with an external water supply, triggering phreatomagmatic or Surtseyan-style explosive eruptions (Lorenz, 1985; Németh et al., 2008; White, 1996a; Zimanowski & Buttner, 2002; Zimanowski et al., 1997). The water can present as surface water or groundwater aquifers preserved in porous country rocks and/or fractures (Buttner et al., 1999; Kokelaar, 1986; Lorenz, 1986; Lorenz & Kurszlaukis, 2007; Sottili et al., 2012; White, 1996a, 1996b; White & Ross, 2011; Wohletz, 1986; Zimanowski & Wohletz, 2000). The phreatomagmatic explosion takes place at a shallow depth in the subterranean water system. However, if the magma ascent meets the bottom of a lake or the sea, even in the water-saturated sediments, a littoral cone or rootless cone can form (Fagents & Thordarson, 2007; Hamilton et al., 2010b; Hamilton et al., 2010a; Jurado-Chichay et al., 1996a; Jurado-Chichay et al., 1996b; Mattox & Mangan, 1997; Thorarinsson, 1953). A volcanic crater, ranging in size from 0.1 km to 2.5 km in diameter, is produced by phreatomagmatic eruptions (Lorenz et al., 1970). Around the world, examples such as the Coragulac Maar, Mount Gambier (Newer Volcanics Province), SE Australia and Devil Mountain Maar, Seward Peninsula, Alaska, have undergone a series of multiple vent eruptions and represented more than one eruption phase which has generated complex craters in a small volume, with an amalgamated diameter of over 3 km (Begét et al., 1996; Van Otterloo et al., 2014). Single eruptions or multi-eruptions take place over a short period, and the phreatomagmatic processes occur by Molten Fuel-Coolant Interaction (MFCI). Similar to the metal smelting processes, the MFCI requires three parameters:

- Premixing between magma and external water with steam vapour;
- Steam vapour leading to magma fragmentation and explosive shockwaves;
- Magma fragmentation of pre- and syn-eruptive processes (Büttner & Zimanowski, 1998; Wohletz, 1986).

In the initial eruptive processes, magma fragmentation can trigger other eruptive processes, depending on the surrounding conditions (e.g., the depth of the fragmentation taking place). In some cases, magma fragmentation does not trigger other eruptive processes, such as when the temperature of the mixture is not much higher than the boiling temperature of the injected coolants (in this case, meaning water) (Kokelaar, 1983; Kokelaar, 1986; Sheridan & Wohletz, 1981; White, 1996b; Wohletz & McQueen, 1984a; Wohletz & McQueen, 1984b). In contrast, the excavation of an eruptive crater may play an important role in the topography of the pre-eruptive landforms and form a pit at the surface, forming a maar crater (Lorenz, 1985). A maar volcano should be located in geological areas with groundwater. Tuff rings are formed by the shallow explosive interaction between magma and external water or water-saturated sediments, and their crater floor is nearly on the pre-eruptive surface (Wohletz & Sheridan, 1983). Both maar volcanoes and tuff rings form as a result of phreatomagmatic eruptions. Tephra accumulations, fallout and pyroclastic density currents, as well as base surge deposits, form the ejecta rings around craters (Carrasco-Núñez et al., 2007; Funiciello et al., 2003; Gençalioğlu-Kuşcu et al., 2007; Németh & Cronin, 2011; Németh et al., 2008; Sottili et al., 2012; Sulpizio et al., 2008; Sulpizio & Dellino, 2008; Vazquez & Ort, 2006; White & Ross, 2011). Commonly, phreatomagmatic eruptions can produce a range of pyroclastic materials, including a diverse range of accidental lithics (e.g., shape, grain size, vesicles and microlite compositions) in maar systems. The accidental lithics often come from the collapse of the wall rock (Auer et al., 2007; Kereszturi & Nemeth, 2011; Németh, 2010b; Pardo et al., 2009; Raue, 2004).

In the phreatomagmatic eruption processes, vent migration and wall-rock collapse can form pyroclastic units that consist of coarse-grained breccias, well-bedded lapilli and ash-dominant deposits with different degrees of sorting of particles, ballistic bomb sags, as well as including angular to sub-rounded accidental lithic blocks (Aranda-Gómez & Luhr, 1996; Chough & Sohn, 1990; Kereszturi et al., 2010; Lorenz, 1974; Lorenz, 2007; Martin & Nemeth, 2005; Németh et al., 2011; Sohn, 1996; White & Schmincke, 1999; Wohletz & Sheridan, 1983). Dune bedding and cross-bedding form in response to transportation by pyroclastic density currents (Alvarado et al., 2011;

Auer et al., 2007; Dellino et al., 2004b; Dellino et al., 2004a; Lorenz, 2007; Ngwa et al., 2010; Pardo et al., 2009). In monogenetic volcanoes that undergo a range of styles of phreatomagmatic eruptions over time, the availability of external water may diminish, and fragmentation can gradually or abruptly shift towards more magmatic volatile-driven eruptions that can eventually form columnar jointed lavas, as well as the scoria or spatter cones in the final stage of the eruptions. Either way, these volcanic craters will be filled with post-eruptive products, including effusive lava and their erosional fans, as well as sediments forming in the crater lakes (Aranda-Gómez et al., 1992; Hetényi et al., 2012; Lorenz, 2007; Martí et al., 2011; K. Németh & J. D. L. White, 2009).

Low-lying landforms (especially valleys) are often associated with phreatomagmatic volcanism (Lorenz, 1973, 1986; Lorenz & Büchel, 1980). Phreatomagmatism can provide evidence for the presence of extensive surface and groundwater in a territory where the syn-eruptive phases occur (Németh, 2010a). For instance, studies of Miocene to Pliocene fields in the western Pannonian Basin (Martin & Németh, 2004) and the Western Snake River Plain in Idaho (Godchaux et al., 1992; Wood & Clemens, 2004) have provided an understanding between the volcanology and paleogeomorphology. In fluvial and lacustrine conditions, e.g., Western Snake River Plain (Godchaux & Bonnichsen, 2002; Godchaux et al., 1992), the fields provide opportunities to assess and identify the mechanisms of volcanism under magma-water interactive patterns and also for the reconstruction of paleoenvironments, paleohydrology, as well as pre-eruptive landforms (Németh, 2010a).

3) Intraplate volcanism

Intraplate volcanism displays a range of volcanic styles that are generated from the interior of continents. These volcanoes are distant from and do not involve lithospheric plate boundary processes. Intraplate volcanism is responsible for 5% of volcanoes around the world (Decker & Decker, 1999; Siebert, 2008). There are two major intraplate volcanism models. The first one is in regard to the consistent mantle plumes that are formed by the convection of deep mantle materials with high viscosity (Decker & Decker, 1999). When the hot and solid materials ascend from the deep mantle source, partial melting will occur during their ascent due to the pressure-dependent melting point (Decker & Decker, 1999). When the mantle plumes reach the

lithospheric plate, a range of volcanic islands will form. Commonly, intraplate volcanism can generate volcano swarms with large numbers of vents. Such large numbers of small volcanoes within small areas are inferred to be an indicator of magma uprise, such as "hot spots" on Earth and often represent volcanism in a very narrow time slice, e.g., 2000 years of Yanshan in ACVF (Bai et al., 2005). Previous research shows that those hot spots move very slowly by mantle convection, with respect to each other; this behaviour has created several volcanic chains with linear patterns. For instance, some chains of Pacific islands (Hawai'i) indicate that the mantle plumes move in about a few centimetres per year (Clague & Jarrard, 1973; Jackson, 1976; Molnar & Atwater, 1973; Winterer, 1973); the motion velocity of Atlantic hot spots is approximately several centimetres annually (Burke et al., 1973; Molnar & Francheteau, 1975).

The second model for intraplate volcanism occurs when magma leaks through lithospheric extension (Foulger, 2007; Foulger, 2011; Homrighausen et al., 2021; Turcotte et al., 1978). This model suggests that the local intraplate volcanism is a reflection of the distribution of the contemporaneous lithospheric stress field (Foulger, 2011; Johnson, 1989; Turcotte et al., 1978). Lithosphere-extension-driven models involve shallow and near-surface volcanic processes. The volcanism is triggered by the ascent of pre-existing melts both in the mantle and lithosphere, ejecting to the surface through tectonic deformations. Decompression of the mantle during upwelling results in lithosphere thinning processes (delamination), eventually forming rift systems, e.g. the East African Rift (Foulger, 2021; Foulger & Natland, 2003). Such intraplate volcanism can create large numbers of volcano swarms and build large igneous provinces, e.g. lava flows extending hundreds to thousands of kilometres from the source amounting to total magmatic output over 1000's km^3 in a relatively short period of time, typically less than a million of years (Anderson, 2005; Foulger, 2007; Foulger, 2021).

2. *Geological background*

The Arxan (Aershan) -Chaihe Volcanic Field (ACVF) lies in the Northeast of China (Fig 1). The total area is approximately 2000 km^2, in which different types of monogenetic volcanoes are located. They are recognised as scoria cones and tuff rings commonly

surrounding maar craters. The field has several medium-length (5-7 km) lava flows that follow stream valleys. A gravity gradient extending along the western side of the Songliao Graben (Liu, 1993; Liu et al., 2001) was formed by continental rifting during the middle Cretaceous (Liu et al., 2001; Yang et al., 1985), suggesting the existence of an extensive NE-SW elongated Mesozoic basin within a basement. There are at least 46 vents within ACVF, and most of them are recognised as monogenetic volcanoes. During the early part of the Late Pleistocene, eruption patterns of ACVF volcanism were dominated by phreatomagmatic and magmatic styles, which formed the volcanoes such as Tongxin (also known as Woniupaozi/**WNPZ**) and Wusulangzi Lake (Fig 2). Magmatic and effusive style eruptions were the major eruptive pattern slater in the Late Pleistocene; in particular, Strombolian eruptions were the most common eruption type (Bai et al., 2012). Most of the craters developed crater lakes, e.g., Tianchi Lake, Tuo Fengling Lake, Wusulangzi Lake and Tongxin Lake. Water-filled craters are not obviously maar volcanoes, and the origin of most of the crater lakes is poorly established. Two major fluvial systems flowing through the ACVF are the Halaha River and Chaoer River. Exposed aa type and pahoehoe lava flow morphologies are well-developed. Along the Chaoer River, vertical columnar jointing with evolved hexagonal shape can be seen, indicating the large volume of the basaltic lava flow was emitted from the nearby vents and later incised by existing fluvial networks. On the western side of ACVF, two large vents, Yanshan (**YS**) -the Triple Vent, and Daheigou (Dahei Gou/**DHG**), preserve hundreds of miles of lava flows and overlying scoria deposits (Fig 15A & 16D).

ACVF is located on the eastern side of Inner Mongolia, near the Great Xing'an Mountain Range (Fig 1) (the Greater Khingan Range written by some sources (Liu et al., 2017)). This range is part of the Central Asian Orogenic Belt (CAOB), which formed approximately a billion years ago during the Phanerozoic tectonism of the Asian continent (Xiao et al., 2009). During this period, the Solonker Suture was generated by massive tectonic movements accreting the North China craton to the Siberian craton along a length of almost 2000 km (Zhang et al., 2014). This suture has been interpreted as the closure of the Palaeo-Asian Ocean (Eizenhöfer, 2020; Li, 2006; Xiao et al., 2003). The Great Xing'an Mountain is an extension of the collision of the two above-

mentioned cratons alongside Solonker Suture. Today the southwestern side of the Great Xing'an Range is bounded by well-developed fault lines (Fig 1), and the ACVF lies in an intra-continental setting. The eastern side of ACVF lies about 2000 km from the subduction zone on the eastern side of Japan. Due to the pushing from the western margin of the Pacific Plate onto the East Asian Plate, the eastern side of NE China was formed by two microplates: Jia Musi Microplate and Middle Craton Microplate (Liu, 1993; Liu et al., 2004; Liu et al., 2020). Another fault system has been generated by this mechanism, and between the two fault systems, there is huge subsidence forming the Songliao Graben (Fig 1) (Liu, 1993, 1999). NE China is basically a continental rift zone, and ACVF is the west margin of the Songliao Graben tectonic basin (Liu et al., 2021; Liu et al., 2001).

The Great Xing'an Range is composed of plutonic rocks emplaced during the Cretaceous in response to mantle upwelling (Wang et al., 2006). Late Mesozoic volcanism occurred when the lithosphere in NE China, and adjacent regions, became thinner than usual, resulting in clusters of magmatic activity (Fan et al., 2003; Kinoshita, 1995, 2002; Wu et al., 2005; Zhou & Armstrong, 1982; Zhou & Li, 2000). The total area covered by Late Mesozoic igneous rocks is approximately 100,000 km^2 in the Great Xing'an Range/Mountain (source from https://www.orrbodies.com/resource/geology-nei-mongol-inner-mongolia-north-eastern-china/). Volcanic rock also occurs around the regions of the Songliao Basin and the southeastern side of the boundary between Mongolia and China (Yarmolyuk & Kovalenko, 2004). This igneous activity was in response to tectonism in the Mongol-Okhotsk suture and the Japan subduction zone (Wang et al., 2006). It is believed that the Late Mesozoic magmatism in the Great Xing'an Mountain began at about 160 Ma and spanned the entire time interval from Late Jurassic to Early Cretaceous, which is about 160- 90 Ma, based on the Rb-Sr and Sm-Nd geochronology (Lin et al., 1998; Shao et al., 1998). In general, there were four intervals in which large amounts of magma were shifting and migrating by lithospheric delamination from the west to east on the northeastern side of Aisa, about 163-106 Ma, 147-140 Ma, 125-120 Ma, and 116-113 Ma (Kinoshita, 1995; Wang et al., 2006; Wang et al., 2002; Wu et al., 2005; Yarmolyuk

& Kovalenko, 2004). In these periods, the apex of magmatic movements happened around 160-140 Ma to 120-130 Ma (Table 1).

Tectonic events (Ma)	description
163-106	Mantle delamination, the start of the Mesozoic volcanism, the closure of the Mongol–Okhotsk Ocean
147-140	A long duration of volcanism, volcanism migration from west to east in the whole of northeast Asia
125-120	
116-113	

Table 1: the tectonic events of the Great Xing'an Range in the Mesozoic eras (Wang et al., 2006)

Magmatic activity during the Cenozoic was triggered by rifting in the Japan Sea. After about 15 Ma, the entire area of NE China was undergoing rifting, particularly forming the Changbai Mountain lying on the east flank of the Songlian Graben (Liu et al., 2001). Around 14-13 Ma and 11-7 Ma, two major fault zones formed (Yitong-Yilan Fault and Fushan-Mishan Fault). This happened just after the opening of the Japan Sea. These two fault zones resulted in subsequent volcanism moving to the southeast margin of NE China (Fan et al., 2004; Liu et al., 2001).

In general, the chronology of this era can be divided by:

- 86-61 Ma

The earliest stage of basaltic volcanism was from the Late Cretaceous to the Early Paleogene. In this period, three volcanic clusters formed and shaped the southeastern part of Songliao Plain (Liu et al., 2004).

- 49-39 Ma

Large volumes of basaltic lavas, including basanites, olivine-basanites as well as alkaline basalts, erupted and shaped the topography of the southern parts of the Songliao Plain (Liu et al., 2004).

- 39-29 Ma

This was a relatively quiet period of volcanism in the south of Songliao Graben. No specific dating, but a thin layer of tholeiitic basaltic materials intercalated with fluvial and lacustrine sediments are present from this time period. (Wang & Sun, 1980).

- 29-16 Ma

On the east and southeast margins of Songliao Graben, several basaltic layers and volcanic rocks were found, and two small volcanoes were formed around 21 Ma on the southeastern side of Songliao Graben. Farther east, near the Changbai region, the oldest basaltic regime was formed at approximately 28.4 Ma (Wang & Sun, 1980).

- 16-13 Ma

During a period of intensive volcanism in NE China, the volcanism spread near the central part of Songliao Graben, which is the tectonic basement of Songliao Plain. About 16.7-15 Ma, a new eruptive centre formed in the ancient fluvial areas of the Halaha River. This event may be the earliest Cenozoic volcanism in relation to the Great Xing'an Range (Liu, 1993).

- 11-7 Ma

Volcanism resurged on both sides of Songliao Graben after a short period of quiescence around 13-11 Ma. The 10-9 Ma, Wuchagou basalts mark a mafic eruption in the Halaha River region. The composition of this event is generally tholeiitic basalts in comparison to the east side of Songliao Plain, which is alkaline basalts (Liu et al., 2001).

- 4.5-2.1 Ma

Volcanism occurred on the eastern flank of Songliao Graben, with several fluvial terraces composed of basaltic clasts, to the east of the Wuchagou region recognised (Liu, 1988). The volcanic evolution of the western side of Songliao Graben is unknown.

- 1.5-0.8 Ma

There are no records of volcanism on the Great Xing'an Range (west flank of Songliao Graben) at this time. Nevertheless, on the east side of Songliao Graben, the fault systems were active, and the Longgang volcanic field formed (Liu et al., 2004).

- 0.58 Ma-now

Most of the volcanism in NE China was formed during the Pleistocene (Kuritani et al., 2013; McGee et al., 2015; Sun et al., 2018; Wang, 1979; Wang & Chen, 2005). The world-famous Wudalianchi-Nuomin Volcanic Field (a UNESCO Global Geopark) formed a range of scoria cones on the northern and northeastern boundaries of the Songliao Graben (Feng et al., 1979; Gao et al., 2013; Gong, 1997; Li & Guo, 1986; Shao & Zhang, 2008).

Research on volcanism in NE China began in the late 20th century. Liu (1987) published K-Ar dates from samples from ACVF of 0.34±0.203 Ma. Then, Liu (1989) recognised that different volcanic episodes occurred in the pre-Cenozoic and Cenozoic eras; the volcanism is recorded in western Inner Mongolia and along the far western side, near Xinjiang and Gansu Provinces. The nine volcanic episodes span a wide age range as mentioned above, and the last 10,000 years. The geochronological data of basaltic volcanic material is restricted to west Inner Mongolia in northern China (Luo and Chen (1990) and not NE China, which includes eastern Inner Mongolia and the other three provinces. Liu et al. (1999) reviewed the distributions of volcanism in China. In the late 90s, Wang et al. (1999) suggested that the tectonic background triggering the volcanism in NE China is upwelling of the asthenosphere and rifting processes in intra-continental settings. Liu et al. (2001) went on to propose that Cenozoic volcanism was likely created by the intra-continental rifting system, perhaps in response to the development of the Japan Sea subduction zone. After the initial studies of general volcanism in NE China, pieces of research on ACVF emerged in the early 21st century. Tang et al. (2005) utilised the magnetotelluric measurement revealing that the vents in ACVF might be fueled by the same magma conduit plumbing system. Another piece of research (Wang et al., 2006) proposed that the volcanism occurring in the Late Jurassic until the Early Cretaceous migrated from the west of the Great Xing'an Range to the eastern side of the range. This interpretation was based on the widespread presence of volcanic rocks in NE China and the Ar-Ar dating method. This research correlated the Mesozoic volcanism in NE China to the closure of the Mongol-Okhotsk Ocean. In recent research, Zhou et al. (2014) analysed zircons from the basement

(country rock) of the Zhalantun side (eastern half of ACVF) and yielded a date of 481 Ma, suggesting a basement formed in the early in the Late Paleozoic.

The first detailed research on ACVF was by Bai et al. (2005), who documented two distinctive, active volcanoes, Yanshan (YS) and Gaoshan (GS). C^{14} dating on charcoal samples associated with the eruptive from these two volcanic edifices yield a 2000 cal yr BPdate. The Yanshan and Da Heigou volcanoes produced scoria deposits and lava flows recognized over large areas (Fig 1, 12C and 15A). Zhao and Fan (2010) subsequently showed that YS and GS were created by a range of violent Strombolian-type eruptions. Wang et al. (2013) reviewed the general eruption types and geomorphology of Cenozoic volcanism in ACVF and recognized its geoconservation value. On the basis of their research, Wang et al. (2014) proposed that ACVF be officially designated a global UNESCO geopark based on the Cenozoic volcanism and volcanic landscapes, which included volcanic cones, craters, calderas, lava plateaus, lava tubes, columnar jointing, lava hornito, lava domes, sub-rhyolite peak forest landforms, crater lakes, lava-dammed lakes, and hot springs. Yu and Cong (2006) analysed the mantle xenoliths that implied the lava flows around YS and GS came from different sources with different depths due to xenoliths crystallising from the fluid of the mantle. Zhao et al. (2008) provided the first comprehensive summary following the modern volcanology approach to understand eruption styles in ACVF, in which the Cenozoic volcanism contains varieties of eruptive types, ejecta and two major episodes of volcanism-Pleistocene and Holocene.

3. Questions arising from the literature review for the study areas

There are large areas of basaltic materials in ACVF set within a range of geomorphological settings covering thousands of square kilometres. These first drew interest in the search for ore belts and mineral deposits. Later the geoconservation and geoheritage values of the region were recognized, and that led to the establishment of the global UNESCO geopark. Research has focused on the recognition and morphologies of volcanic edifices, their distribution and classification of volcanic materials. Work on the origin of the magma and the ascension processes that created the small volumes of volcanoes in ACVF is warranted.

Intraplate volcanism commonly preserves the pre-existing geomorphology of basaltic provinces involving continental flood basalts. These events can produce hundreds of thousands of cubic kilometres in less than one million years to form large igneous provinces that commonly feature plateau landforms. Lava plateaus and their related geoforms appear to cover vast areas of ACVF. However, their true extent and volume have never been quantified. In this research, the selection of vents in ACVF is studied.

Tongxin Lake represents the largest crater of the vents in the northeastern corner of ACVF. Lava flows surround the large crater. Also, this lake is on one side of the Chaoer River, which is one of the two major fluvial systems in ACVF. The satellite images show that the river was greatly reformed by the local topography. Thus, Tongxin Lake has drawn interest in not only its genesis but also the local hazard predictions.

There are several questions arising, they are:

- What is the mechanism that triggered the volcanism in ACVF? (Chapters 1 & 6)
- How could these small-volume volcanoes produce such large quantities of lava flows and ejecta? (Chapter 5)
- Do the lava flows, and their resultant geomorphology provide insight into the pre-eruptive topography? (Chapters 5 & 6)
- For the two big and youngest vents, YS and DHG, how did lava flows inundate the pre-existing topography, and how did the lava flows interact with the fluvial network? (Chapter 5)
- Is this really such a large volume that it can be called an intracontinental basaltic flood field? (Chapter 5)
- Are 46 volcanoes sufficient to produce a total volume of lava calculated from the field? (Chapter 5)
- How does that compare to other basaltic volcanic fields such as Auckland or South Auckland, those in Saudi Arabia or in Victoria near Melbourne? (Chapter 7)
- What is the volcanic type of Tongxin Lake? (Chapter 3)
- Do the thick volcaniclastic deposits preserved around the Tongxin crater indicate the construction of the volcanic edifice of Tongxin itself? (Chapter 3)

- How has the Chaoer River, the secondary large fluvial system in ACVF, been impacted by the Tongxin volcanism? (Chapter 3)
- Did volcanic activity shape the course of the river, how did it impact the depositional system, and did the activity pose a potential damming hazard? (Chapter 3)
- What eruptive scenarios can be modelled from the textural studies of the preserved volcaniclastic deposits, with special reference to their deposition, bedding formation and distribution? (Chapter 3)
- Can bulk geochemistry be used to develop a realistic petrogenesis model to explain the trigger mechanism of the volcanism that created the Tongxin Lake? (Chapter 3)
- How did the ascending magma control the eruption style ultimately responsible for the formation of Tongxin Lake? (Chapter 3)
- How can the diverse ranges of geology enhance the geotourism, geoconservation and geoheritage and help understand the geodiversity of the region? (Chapter 4)

4. Outlines of aims and objectives

The overall aims of this research are:

1) To provide preliminary observations on the range and style of volcanism in the previously understudied ACVF, including tectonic settings
2) To provide specific detail on one of the major features of ACVF, Tongxin Lake, including detailed descriptions of key localities, granulometry of pyroclastic deposits, SEM analysis and a preliminary assessment of the geochemistry of the eruptives
3) To provide an overview of geodiversity methods on ACVF to show the overall distribution of geological elements in this area
4) To provide details of lava emplacements by accessing through remote-sensing methods, to support local hazard assessments.

Note that aims 3 and 4 were introduced because the COVID-19 pandemic meant that further fieldwork was not possible, and the scope of the research had to change from field-based activities to remote sensing.

Based on the aims above, there are four objectives that need to be performed in this research:

- The main objective of this research is to describe the Cenozoic volcanism in the Tongxin Lake region of ACVF, including the eruption styles, distributions of volcanic materials, as well as geomorphology of the vents, and lava flows in ACVF.
- Specifically, Tongxin Lake, the largest vent in ACVF, will be provided with an intact and detailed observation from both fieldwork and lab work.
- The lesser objective is to utilise the GIS-based tool with technologies of remote sensing in order to analyse the young volcanic surface morphologies with respect to revealing the evolutionary histories of Cenozoic volcanism in ACVF; this part is for the future assessments of volcanic risks to locally populated areas.
- The final objective is to establish the diverse ranges of geology that may interest the local tourism and heritage purposes for the ACVF geopark.

Please note that due to the COVID situation and lockdown in China, the planned third field trip was unable to be performed and carried out. The third field season would have resulted in more detailed descriptions of other volcanoes/features in the field. Thus, this research project was turned immediately to GIS-based analyses, which are about geodiversity, geomorphology, and young lava flows, in order to discuss geoheritage and hazard aspects of the area.

5. Thesis structure

1) Chapter 1: General introduction

A general outline of the basics of the thesis and fundamental background required to link the following key chapters

2) Chapter 2: Basic elements of the Arxan-Chaihe Volcanic Field, Inner Mongolia, NE China

This chapter is a published paper and provides correct bibliometric information about the published works (Li, B., Németh, K., Palmer, J., Palmer, A., Wu, J., Proctor, J., & Liu, J. (2020). Basic Volcanic Elements of the Arxan-Chaihe Volcanic Field, Inner Mongolia, NE China. In N. Károly (Ed.), Updates in Volcanology (pp. Ch. 10). IntechOpen. https://doi.org/10.5772/intechopen.94134).

Chapter 2 is about the overall recognition of the Cenozoic volcanism in ACVF with utilisations of field works. This chapter is based on the two seasons of fieldwork in Arxan UNESCO Geopark and Tongxin Lake near Chaihe Town. The general geomorphology of volcanoes in ACVF is described, including their types of cone structures, i.e., scoria cones, tuff rings, tuff cones and complex cones, and the morphologies of the lava flows around YS, DHG and Dichi Lake are described. Ages of Cenozoic volcanism have been collated and compared to previous research. The chapter provides detailed field observations in large remote uninhabited undeveloped and previously poorly described areas.

3) Chapter 3: Violent phreatomagmatic explosive eruptions in the Pleistocene Tongxin Volcano and its implication for volcanic hazards of the Arxan-Chaihe Volcanic Field, Inner Mongolia, NE China

This is a manuscript to be submitted to the Journal of Volcanology and Geothermal Research (JVGR).

In order to model the syn-eruptive behaviours of the key vents in ACVF, I chose the largest vent in this area, Tongxin Lake. Thus, Chapter 3 concentrates on the quantitative analyses of Tongxin Lake with fundamental geological methods. This chapter presents field data on Tongxin Lake, stratigraphic logs of surrounding pyroclastic deposits, labwork-driven datasets (sedimentology and bulk rock geochemistry), and the first detailed geological map of Tongxin Lake.

4) Chapter 4: Geodiversity estimate of the Arxan-Chaihe Volcanic Field extends across two geoparks in Inner Mongolia, NE China

This chapter is based on a published paper (Li, B. x., Németh, K., Zakharovskyi, V., Palmer, J., Palmer, A., & Proctor, J. (2023b). Geodiversity estimate of the Arxan-Chaihe Volcanic Field extending across two geoparks in Inner Mongolia, NE China. Geological Society, London, Special Publications, 530(1), SP530-2022-2130. https://doi.org/doi:10.1144/SP530-2022-130).

Due to the COVID situation that happened at the end of 2019, the research turned to remote-sensing-based analyses. Thus the overall geodiversity of ACVF was placed after Chapter 3 in order to categorise the geological features and ranges in the area. In Chapter 4, the geodiversity shows that the young lava flows play an important role in understanding Cenozoic volcanism with respect to lava emplacement. The diverse range of geology in ACVF and surrounding areas is presented using GIS-based analyses, e.g., QGIS software and its related remote sensing techniques. The analysed parameters include geology, slope, elevation, geomorphology and local hydrology. These aspects of ACVF have been interrelated to provide an overview of the geodiversity of the region. The data are presented as a series of maps.

5) Chapter 5: Eruption scenario builder based on the most recent fissure feed and lava-producing eruptions of the Arxan-Chaihe Volcanic Field (ACVF), NE China

Subsequently, Chapters 5 and 6 concentrate on the young lava flow analyses by utilisations of remote sensing techs on the major fissure-driven vents to reveal the behaviours of lava emplacement with a glimpse of future possible risks in this area.

This chapter is based on a published paper (Li, B. x., Németh, K., Palmer, J., Palmer, A., Zakharovskyi, V., & Gravis, I. (2023a). Eruption Scenario Builder Based on the most recent fissure-feed lava-producing eruptions of the Arxan-Chaihe Volcanic Field (ACVF), NE China. In N. Dr. Károly (Ed.), Updates in Volcanology - Linking Active Volcanism and the Geological Record (pp. Ch. 1). IntechOpen. https://doi.org/10.5772/intechopen.109908).

GIS-based analyses of the Yanshan and DHG vent locations and youngest lava flows in the surrounding areas utilising Sentinel Satellite Imagery with nine different optical spectrums reveal the lava flow blocks with respect to forming in different periods.

These have been further analysed to provide a chronology of volcanic activity and, in particular, lava flows.

6) Chapter 6: Geodiversity elements of a young fissure system as an immediate precursory event of the youngest fissure-fed eruption within the Arxan UNESCO Global Geopark, Inner Mongolia in NE China

This chapter has been published (Li, B.; Nemeth, K. Geodiversity elements of a young fissure system as an immediate precursory event of the youngest fissure-fed eruption within the Arxan UNESCO Global Geopark, Inner Mongolia in NE China, MDPI: Basel, Switzerland, doi:10.3390/IECG2022-13807), https://sciforum.net/paper/view/13807.

GIS-based analyses have been used to investigate the geological factors controlling the evolution of fissure-fed eruptions in ACVF. This research is performed on the areas of the smallest vent of ACVF, the Dichi Lake, which may have been formed by a single eruption. Cross sections have been from most lakes in the Arxan area, such as Wusulandzi, Dichi Lake and Tianchi Lake, to demonstrate regional morphological changes. Topographical changes are consistent with fissure-fed eruption behaviours. Using combinations of geodiversity concepts and Sentinel Satellite Imagery, it is concluded Dichi Lake and its surrounding lava flows indicate that the Cenozoic volcanism in ACVF reflects a strong structural control.

7) Chapter 7: Synthesis and Conclusion

The final thesis chapter discusses the findings of the previous five chapters and draws conclusions about the volcanic history of ACVF, its geoheritage and geoconversation values, hazard investigations and how geologically diverse and significant the region is.

MASSEY UNIVERSITY
GRADUATE RESEARCH SCHOOL

STATEMENT OF CONTRIBUTION
DOCTORATE WITH PUBLICATIONS/MANUSCRIPTS

We, the candidate and the candidate's Primary Supervisor, certify that all co-authors have consented to their work being included in the thesis and they have accepted the candidate's contribution as indicated below in the *Statement of Originality*.

Name of candidate:	Bo'xin Li
Name/title of Primary Supervisor:	Prof. Károly Németh
Name of Research Output and full reference:	
Basic elements of the Arxan-Chaihe Volcanic Field, Inner Mongolia, NE China	
In which Chapter is the Manuscript /Published work:	Chapter 2
Please indicate:	
• The percentage of the manuscript/Published Work that was contributed by the candidate:	Bo'xin Li, 80%
and	
• Describe the contribution that the candidate has made to the Manuscript/Published Work:	
Prof. Károly Németh, Mrs Julie Palmer, A/Prof. Alan Palmer, Dr. Jing Wu, Prof. Jonathan Procter, Prof. Jiaqi Liu	
For manuscripts intended for publication please indicate target journal:	
IntechOpen	
Candidate's Signature:	Bo'xin Li
Date:	
Primary Supervisor's Signature:	Prof Karoly Nemeth (Digitally signed by Prof Karoly Nemeth, DN: cn=Prof Karoly Nemeth, c=SA, o=Saudi Geological Survey, ou=National Earthquake and Volcano Program, email=nemeth.k@sgs.gov.sa, Reason: I am approving this document, Location: Jeddah, Kingdom of Saudi Arabia, Date: 2023.05.08 12:59:36 +03'00')
Date:	8 May 2023

(This form should appear at the end of each thesis chapter/section/appendix submitted as a manuscript/ publication or collected as an appendix at the end of the thesis)

Chapter 2: Basic elements of the Arxan-Chaihe Volcanic Field, Inner Mongolia, NE China

This chapter has already been published in an InTech book (https://www.intechopen.com/chapters/73823). Please note that the field campaigns were led by Professor Karoly Nemeth from Massey University, accompanied by colleagues from the Institute of Geology and Geophysics, Chinese Academy of Sciences (IGGCAS). The majority of this research was done by Bo'xin Li, the candidate of PhD, who was under the supervision of Prof. Karoly Nemeth, Prof. Alan Palmer, Mrs Julie Palmer and Prof. Jonathan Procter.

1. *Abstract*

The Arxan-Chaihe Volcanic Field, Inner Mongolia, NE China, is a Pleistocene to Recent volcanic field still considered to be active. In this chapter, we provide an update on current volcanological research conducted in the last four years to describe the volcanic architecture of the identified vents, their eruptive history and potential volcanic hazards. Here we provide an evidence-based summary of the most common volcanic eruption styles and types of the field experienced in its evolution. The volcanic field is strongly controlled by older structural elements of the region. Hence most of the volcanoes of the field are fissure-controlled, fissure-aligned and erupted in Hawaiian to Strombolian-style, creating lava spatter and scoria cone chains. One of the largest and most complex volcanoes of the field (Tongxin) experienced a violent phreatomagmatic explosive phase creating a maar in an intra-mountain basin, while the youngest known eruptions formed a triple vent set (Yanshan) that reached violent Strombolian phases and created an extensive ash and lapilli plains in the surrounding areas. This complex vent system also emitted voluminous lava flows that changed the landscape by damming fluvial networks, providing a volcanological paradise for the recently established Arxan UNESCO Global Geopark.

Keywords: scoria, spatter, fissure, maar, tuff ring, pyroclastic density current, ash, tumuli, lava flow

2. *Introduction*

The Arxan-Chaihe Volcanic Field (ACVF) is a young intracontinental volcanic field located in the northeast of China (Fig 1). The volcanic field is best defined as a monogenetic volcanic field on the basis of the presence of small-volume volcanic edifices, eruptive products and typical landforms such as tuff rings, scoria (cinder) cones, fissure-controlled vents, and complex but small volcanic cones being the key elements of the volcano types preserved. Early research in the region focused on characterising the volcanology of the area. However, in recent years research on the active volcanism in Northeast (NE) China has shed some light on magma genesis, volcanic edifice growth and volcanic hazards at some iconic locations such as the Changbaishan volcano, Longgang or Wudalianchi Volcanic Fields (Fig 1) (Liu et al., 2001). This research has defined the basic characteristics of some of these volcanic regions, outlining the geochemical characteristics of the volcanic rocks and linking magma genesis to lithospheric processes. Volcanological research about NE China is increasingly appearing in the international literature (Feng & Whitford-Stark, 1986; Pan et al., 2017; Ramos et al., 2019; Sun et al., 2018; Wei et al., 2013; Wu et al., 2019; Xiao & Wang, 2009). However, their volcanic regions are largely unstudied. Among these is the Arxan-Chaihe Volcanic Field (ACVF). Several research outputs have made basic observations of the volcanic history of the region, but a systematic study has only recently been undertaken. Here we report a summary of volcanological observations made in the last six years of research on the ACVF. The aim of the study is to understand the eruptive history, volcanic stratigraphy, eruption styles and associated volcanic hazards that may be associated with the ACVF.

In this book chapter, we summarise the field-based observations of two major field campaigns to provide some basic descriptions of the recognised volcanic products, including the most accessible and iconic volcanoes that form the core of the newly established Arxhan UNESCO Global Geopark (Németh et al., 2017a). We included Tongxin Lake on the northeast corner of ACVF, the Heaven Lake, Tuofengling Lake, Dichi Lake and Yanshan volcanic group (informally identified as the "Triple Vent") (Fig 2) to provide evidence of the important role of explosive hydro volcanism, fissure-fed eruptions, Strombolian-style eruptions and various large-volume lava outpouring to

the volcanic architecture of the field. We demonstrate that the Tongxin Lake near Chaihe township (Fig 2) is a tuff ring of explosive phreatomagmatic origin that covered an area of at least 13 km2 (Fig. 2). Eruptions from Tongxin Volcano were probably the most violent in the ACVF indicating the importance of externally-driven explosive hydro volcanism during the eruptive history of ACVF. In contrast, the youngest known eruption site at Yanshan (C14 - 2040 +/-75; 1960+/-70; 1990+/-100; 1900+/-70, BP) (Wang et al., 2014) is a nested scoria and spatter cone with three distinct vents forming a volcanic complex producing scoria-fall, agglutinated and clastogenic lavas. This location demonstrates probably the most common type of volcanic eruption in the ACVF. They are also the most voluminous and the youngest.

The region at and nearby the Dichi Lake vent produced the smallest eruptive volumes in ACVF (Fig 2). The crater wall of Dichi Lake is composed of lava flows. These were disrupted by an explosive event that left produced angular breccias as a pyroclast ring around the now water-filled crater, best defined as a maar volcano. From Dichi Lake, however, a NE-SW trending fissure exposing a chain of vents gradually builds spatter cones and small scoria cones (Fig 2).

The majority of the volcanoes on the western side of the ACVF, closer to Arxan, are clearly volcanoes that erupted through the magmatic explosion and effusive processes and formed lava spatter cones, spatter ramparts, scoria cones, and associated lava flows. Large, elongated craters in this region are filled by water, for example, Tuofengling (Fig 2). Tuofengling was first interpreted as a scoria cone, but recent field mapping has revealed it is a complex volcanic cone with a basal tuff ring capped by a scoria cone complex. The field-based data presented here provide evidence of one of the largest Pleistocene phreatomagmatic explosive eruptions in the ACVF that formed a maar within a closed intramountain basin (Fig 2).

3. Geological settings

ACVF locates about 2000 km away from the Japan subduction zone (Fig 1). Thus, the background settings are generally under control by intra-continental settings influenced by a distant convergent plate margin.

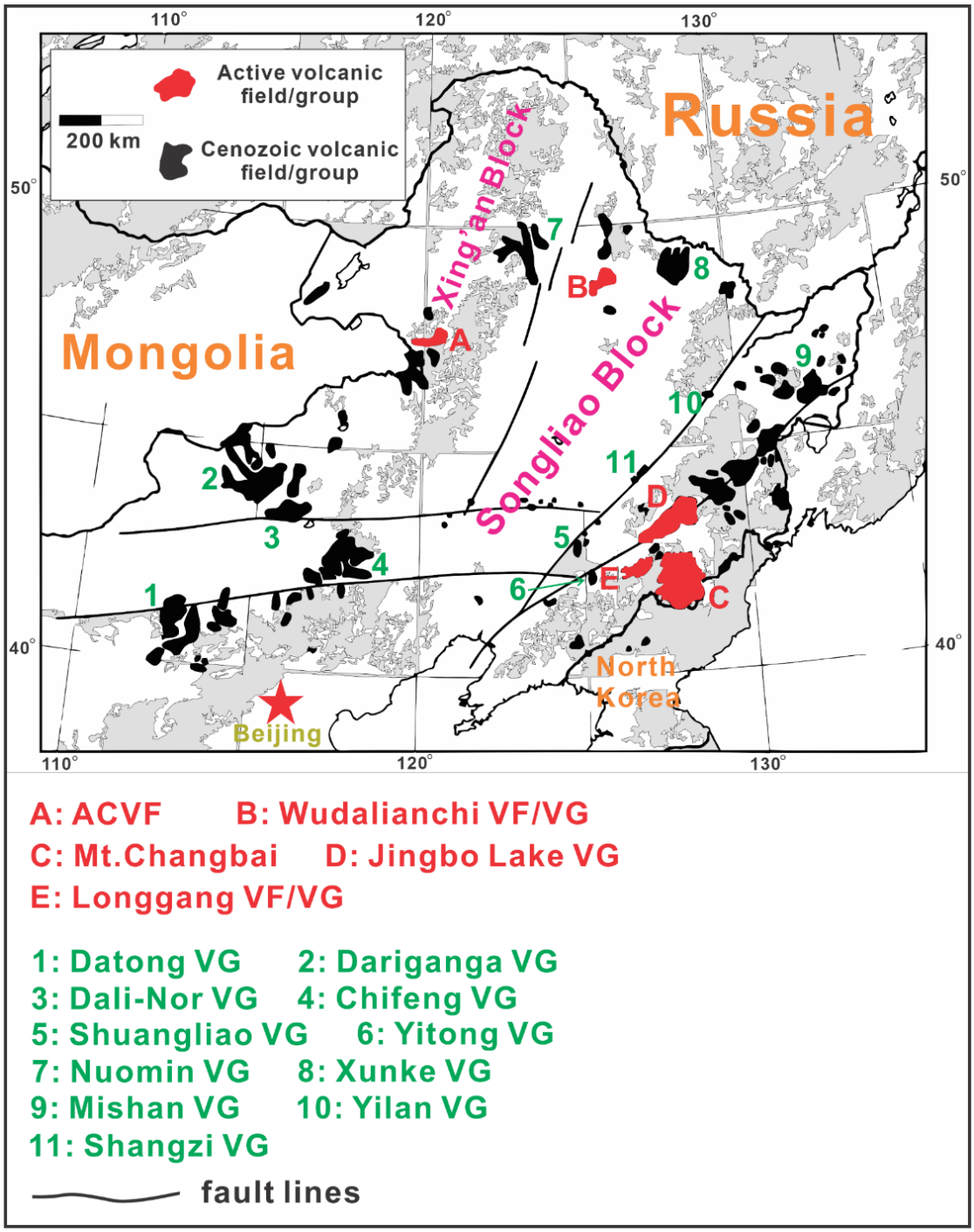

Figure 1:: The general geological map of NE China: the red areas mark the active volcanic fields; the black areas indicate the ceased Cenozoic volcanic fields; also, the solid lines in the territory of NE China are the markers of regional fault systems (Liu et al., 2001). VF- volcanic field, VG – volcanic group.

From the satellite map, ACVF is located towards the southeast end of the Great Xing'an Range (also known as Da Hinggan Mountains; both names are legitimate, but this paper utilises the name Great Xing'an Range). The highest ridges in ACVF are nearly 1500 m above sea level. The ACVF is located near the current political boundaries

between China, Russia and Mongolia (Fig 1). The regional fault systems align NE-SW with the vents of ACVF, suggesting that the volcanic field is associated with major supracrustal weakness zones or even be linked to rifting and/or reactivation of Mesozoic structural zones separating major tectonic terrains (Figs 1 & 2). The rifting history of the region occurred in two major phases (Bai et al., 2005) around the Songliao Graben (Fig 1). It is believed that Songliao Graben subsidence is related delamination of the lithosphere and thinning of the upper crust of NE. China (Bai et al., 2005; Gao & Li, 2014; Jia et al., 2016; Liu, 1989). One of the conventional concepts is that the ascending asthenosphere caused by the subduction of the down-going slab into the upper mantle initiated and sustained the delamination processes that were manifest as rifting in NE. China (Liu et al., 2001). ACVF is located on the west flank of Songliao Graben (Fig 1). Hence the regional tectonic setting, characterised by the fault-controlled features, resulted in fissures and NE-SW orientation and alignment of vents (Fig 2). These are correlated with macro scale the tectonics of NE China. Volcanoes of ACVF overlie from Mesozoic basement rocks, such as granites and metamorphosed sediments (Ji et al., 2018; Liu et al., 2019; Wan et al., 2019; Zhang et al., 2020; Zheng et al., 2011). The eruptive products are interfingered with various Quaternary sediments that accumulated in intra-mountain basins and along fault-controlled valley networks (Fig 2). The granitoid basement is strongly fractured, intruded by younger mafic to intermediate dyke swarms and usually covered by thick surface material derived from erosion and in situ weathering. Basement rocks are abundant in pyroclastic rocks as accidental lithics, especially those formed during explosive magma and water interaction. These lithics are preserved as xenoliths in individual or cored bombs in pyroclastic breccias or as accidental lithics of ash and lapilli in pyroclastic density current (PDC) deposits and within lava flows. Among the country-rock debris, there are low-grade metamorphic rocks or meta-sediments (commonly referred to informally as "mudrocks") in minor amounts within the pyroclastic beds. These rocks are also part of the Late Mesozoic basement assemblages.

The region around ACVF includes two main fluvial systems (Halaha River and Chaoer River) and several lacustrine systems (Figs 2 & 3). The lacustrine systems have likely been formed after major lava flows diverted the fluvial channels. For example, a lake

formed when lava flows from the Yanshan – Gaoshan volcanic systems blocked the Halaha River approximately 2000 years ago (Figs 2 & 3) (Wang et al., 2014). Major structural zones facilitated the storage of groundwater that was driven down to the lowlands, where springs and/or channels developed between major lava flow units (Liu et al., 2001; Wang et al., 2015b).

Annual precipitation is about 450 mm; the average temperature is around −2.7 °C in the range of −25.1 °C in January to 16.8 °C in July, with about six months of the year below 0 °C. These data indicate that ACVF lies within typical subarctic conditions with a strong monsoonal influence (Zhao et al., 2016). Data relating to paleo-monsoon conditions in NE China are rarely found. However, research based on the lacustrine sediments found in the bottom of crater lakes in ACVF shows that around the Last Glacial Maximum (LGM), about 18000 BP, there was a significant enlargement of the northern grassland areas, and warm periods are recorded during mid- Holocene (10000-6000 BP) (Wang et al., 2015b). These stages were influenced by the East Asian Monsoon. More recently, the areas in the forest are enlarging; this might indicate the influence of the warm periods of the mid-Holocene (Wang et al., 2015b). The present region is covered by typical subarctic forest (Betula), grass and shrubland. Volcanic landforms are heavily vegetated, and large and continuous exposures are rare, making geological mapping challenging. Soil formation is intense, and even seemingly young volcanic landforms are covered by thick Holocene sediments or typical sub-arctic mass-movement-generated cover beds. The sub-arctic environments and high latitude lead to the frozen ground for half the year (Oct to Apr) and only five months when the ground is not frozen (mid-Apr to Sep). A major wildfire in 1987, the Black Dragon Fire event, caused widespread destruction of the vegetation around Yanshan-Triple Vent and Gaoshan. Nowadays, that area of forest and vegetation is regenerating and nearly covers the volcanic sites. This means that during field trips, some of the areas cannot be assessed and observed.

4. *Arxan-Chaihe Volcanic Field*

The Arxan-Chaihe Volcanic Field (ACVF) is recognised as a monogenetic volcanic field covering an area of nearly 2000 km2 (Liu & Ding, 1998; Németh et al., 2017a; Zhao et al., 2008). Within this area, at least 47 vents have been identified so far; however, this

is likely a minimum number (Németh et al., 2017a). ACVF has been experiencing high erosion triggered by dramatic temperature changes and fluctuating surface water runoff. Two major fluvial systems within ACVF, the Halaha River and Chaoer River, facilitate surface erosions (Figs 2 & 3). They rework the volcanic materials and modify the general topography. Within ACVF, volcanic landforms typical of a monogenetic volcanic field, such as tuff rings, scoria/cinder cones, fissures, lava flows, as well as ponded lava flows, have been recognised (Németh et al., 2017a; Zhao et al., 2008). This great diversity of monogenetic volcanic landforms gave the region its high geoheritage value and was the basis for the protection of volcanic landforms by the establishment of a geopark network in the region through intensive work since 2004. The western side of the ACVF became a registered national geopark in the system of the UNESCO Global Geopark Network in 2017 (http://www.unesco.org/new/en/natural-sciences/environment/earth-sciences/unesco-global-geoparks/list-of-unesco-global-geoparks/china/arxan/). The recognition of the region's volcanic geoheritage in the highest level shows the importance of the ACVF as an intraplate volcanic field that is far from active plate margin processes and still recognised as an active volcanic region (Németh et al., 2017a). The ACVF is one of the lesser-known volcanic regions of the world, and its physical volcanology and implications for potential volcanic hazards have not yet been studied extensively.

5. Vent locations and volcano morphology

So far, ACVF preserves at least 47 (known) vents in a 2000 km^2 area (Fig 2). From these 47 vents, only 35 were investigated in more detail and assigned to some volcanic geoforms (Fig 3 and Table 2). The age of the volcanoes was mainly assigned by their relative stratigraphy (Table 2), as sporadic and random absolute age dates are available (Fan et al., 2011; Liu, 1987; Sun et al., 2017; Wang et al., 2014) only from a handful of identified volcanoes (Table 2). As absolute age dating using radiometric tools such as K-Ar or Ar-Ar methods is problematic in young mafic volcanoes, most of the data is derived from lava flows and coherent lava as pyroclasts from volcanic edifices. Lava flows, however, show that volcanism was spread through time in the wider ACVF region (Table 3). This means that the available age data should be viewed

with care, and many data may not include a representative for an eruption age of the volcano located in the vicinity of the sampling point but shows the ages of earlier lava flows. The volcanic landforms identified in ACVF include tuff rings, scoria/spatter cones, complex volcanic cones and tumuli structures, respectively (Fig 4). Tongxin Volcano (Fig 4A) is the largest tuff ring preserved in the ACVF, with a rim-to-rim diameter of 1.4-1.1 km. The volcanic edifice is sandwiched between cliffs of basement rock (granite and metavolcanic), forming a typical intramountain basin that has been gradually filled from the north by an alluvial fan (Fig 4A). The bedrock is exposed about 306 m above the present-day crater lake surface, which is commonly flanked with debris. The average elevation of the ring boundary is approximately 800 m above sea level. The central bottom of the lake is nearly flat, with a present-day water depth of no more than 13 m.

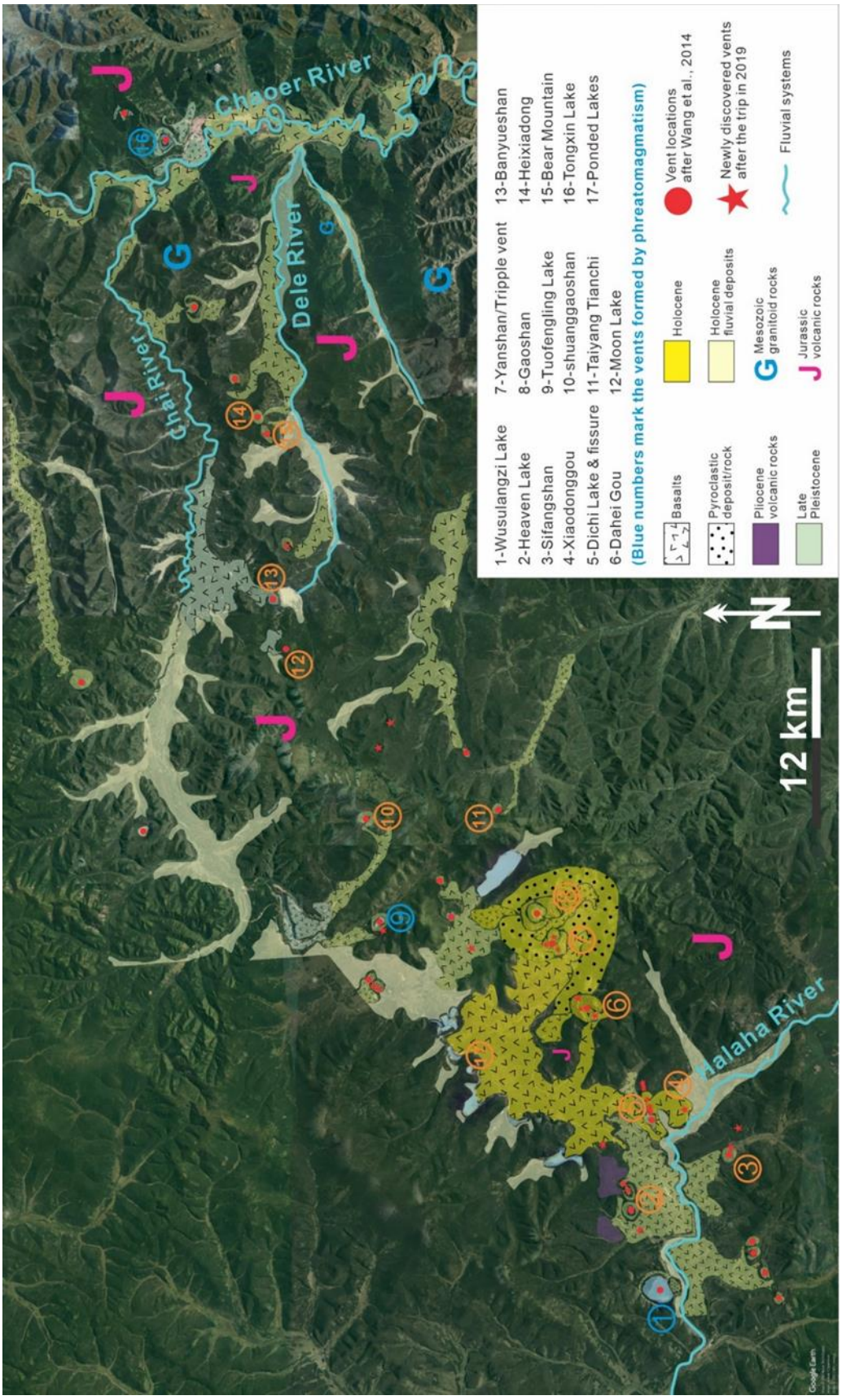

Figure 2: The map of vent distributions of ACVF (red dots) in relationship with the patterns indicating the distributions of volcanic eruptive products from previous research (Zhao et al., 2008). Numbers refer to locations mentioned in the text.

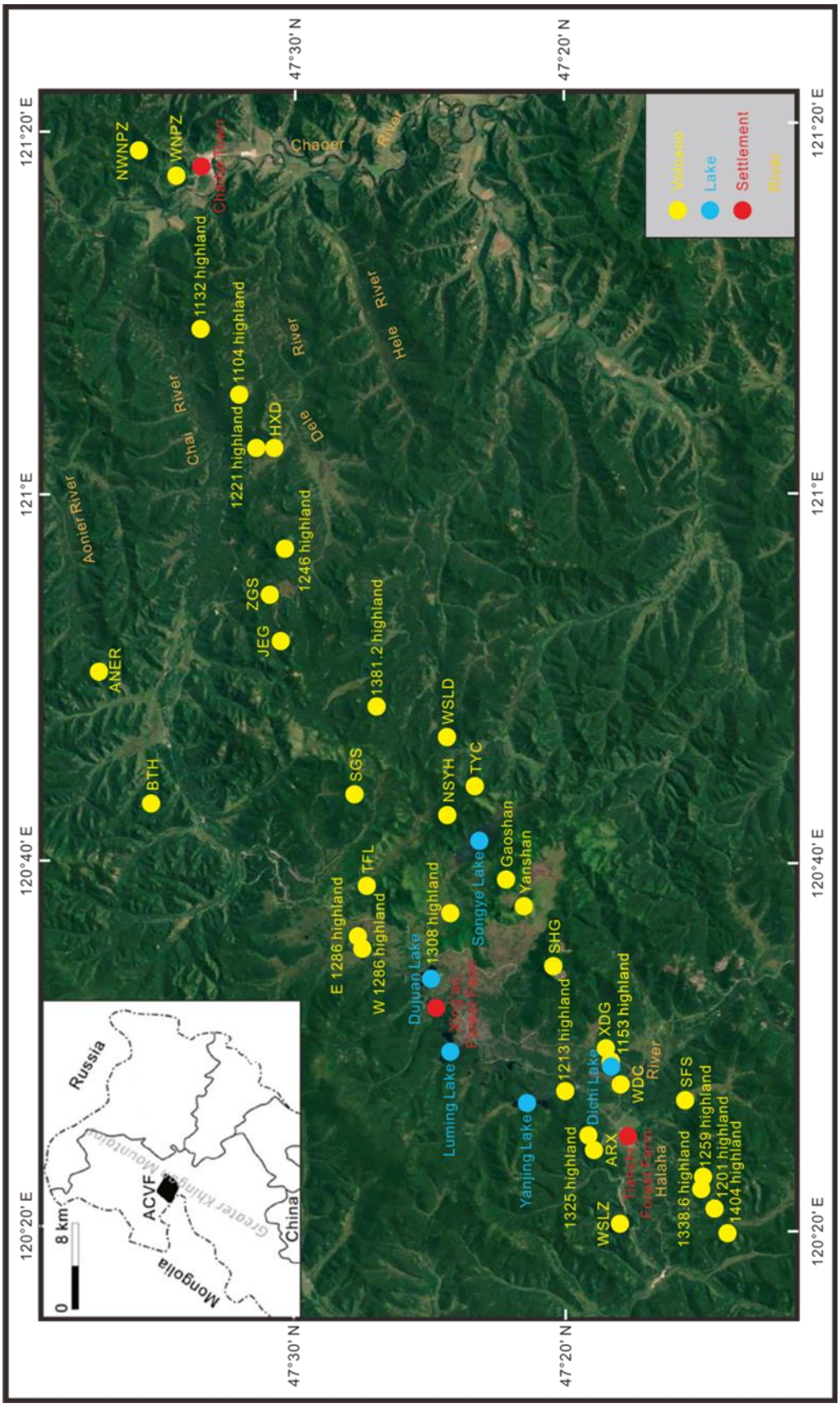

Figure 3: A Google Earth map showing the volcanic locations from where basic volcanological information is available. The names and abbreviations also correspond to the common name of the locations entered into various publications.

Name on Fig 3	Formation Age	Location	Map view shape	Type of volcano or main eruptive product	Area of the lava flow ($km^{2)}$	The main type of eruption	The relative height of the edifice (m)
1 Gaoshan	Holocene	47°22′N, 120°39′E	circular horseshoe	composite cone	5	violent Strombolian	362
2 Yanshan	Holocene	47°21′28″N, 120°37′30″E	circular horseshoe	scoria cone	50	violent Strombolian	233
3 SHG	Holocene	47°20′28″N, 120°34′14″E	circular horseshoe	scoria cone	25	Strombolian	224
4 XDG	Holocene	47°18′28″N, 120°29′40″E	circular horseshoe	spatter cone	5	Hawaiian	110
5 WNPZ	Late Pleistocene	47°34′13″N, 121°17′22″E	circular	maar with tuff ring, base-surge	7	phreatomagmatic	198
6 WSLZ	Late Pleistocene	47°17′54″N, 120°20′10″E	circular	maar with tuff ring, base-surge	2	phreatomagmatic	150
7 BTH	Late Pleistocene	47°35′18"N, 120°43′08"E	ellipse	tuff ring, base-surge	-	phreatomagmatic (?)	
8 ZGS	Late Pleistocene	47°30′52″N, 120°54′44″E	long horseshoe	collapsed or breached scoria cone	23	Strombolian	136
9 JEG	Middle Pleistocene	47°30′25″N, 120°52′00″E	circular horseshoe	composite cone	3	Strombolian	178
10 TFL	Middle Pleistocene	47°27′19″N, 120°38′36″E	long horseshoe	composite cone	12	Strombolian and phreatomagmatic	170
11 SGS	Middle Pleistocene	47°27′51″N, 120°43′34″E	long horseshoe	collapsed or breached scoria cone	12	Strombolian	168
12 TYC	Middle Pleistocene	47°23′23″N, 120°44′00″E	circular horseshoe	composite cone	11	Strombolian	122
13 1104-highland	Middle Pleistocene	47°32′2″N, 121°5′00″E	circular horseshoe	composite cone	20	Strombolian	154
14 1132-highland	Middle Pleistocene	47°33′00″N, 121°9′20″E	circular horseshoe	composite cone	10	Strombolian	182
15 ANER	Middle Pleistocene	47°37′17″N, 120°50′30″E	circular horseshoe	composite cone	25	Strombolian	172
16 NWNPZ	Middle Pleistocene	47°35′35″N, 121°19′00″E	circular horseshoe	spatter cone	1	Hawaiian	205
17 1404-highland	Middle Pleistocene	47°14′8″N, 120°19′47″E	circular horseshoe	collapsed or breached scoria cone	-	Strombolian	254
18 1201-highland	Middle Pleistocene	47°14′31″N, 120°21′3″E	long horseshoe	fissure-oriented breached scoria cone	-	Hawaiian, Strombolian	50
19 WSLD	Middle Pleistocene	47°24′25″N, 120°46′49″E	horseshoe	collapsed or breached scoria cone	-	Strombolian	50
20 SFS	Middle Pleistocene	47°15′45″N, 120°26′54″E	horseshoe	composite cone	8	Strombolian	126

21 1153-highland	Middle Pleistocene	47°18’21”N, 120°29’4”E	long horseshoe	fissure-oriented breached scoria cone	-	Hawaiian, Strombolian	35
22 WDC	Middle Pleistocene	47°18’00”N, 120°27’50”E	circular horseshoe	collapsed or breached scoria cone	-	Strombolian	20
23 1213-highland	Middle Pleistocene	47°20’2”N, 120°27’27”E	circular horseshoe	collapsed or breached scoria cone	-	Strombolian	73
24 1308-highland	Middle Pleistocene	47°24’17”N, 120°37’8”E	long horseshoe	collapsed or breached scoria cone	-	Strombolian	38
25 1381.2-highland	Middle Pleistocene	47°26’53”N, 120°48’32”E	circular horseshoe	collapsed or breached scoria cone	-	Strombolian	131
26 1246-highland	Middle Pleistocene	47°30’18”N, 120°57’06”E	circular horseshoe	collapsed or breached scoria cone	-	Strombolian	196
27 NSYH	Middle Pleistocene	47°24’23”N, 120°42’28”E	circular horseshoe	collapsed or breached scoria cone	-	Strombolian	66
28 1259-highland	Middle Pleistocene	47°14’56”N, 120°22’13”E	circular horseshoe	collapsed or breached scoria cone	-	Strombolian	60
29 1338.6-highland	Middle Pleistocene	47°14’56”N, 120°22’40”E	circular horseshoe	collapsed or breached scoria cone	-	Strombolian	138
30 W-1286-highland	Middle Pleistocene	47°27’30”N, 120°35’18”E	horseshoe	collapsed or breached scoria cone	-	Strombolian	76
31 E-1286-highland	Middle Pleistocene	47°27’39”N, 120°35’49”E	horseshoe	collapsed or breached scoria cone	-	Strombolian	45
32 1325-highland	Middle Pleistocene	47°19’09”N, 120°25’00”E	horseshoe	collapsed or breached scoria cone	-	Strombolian	175
33 ARX	Middle Pleistocene	47°19’00”N, 120°24’16”E	semi-round	scoria cone	25	Strombolian	130
34 HXD	Middle Pleistocene	47°30’44”N, 121°2’35”E	horseshoe	composite breached scoria cone	6	Strombolian	204
35 1221-highland	Middle Pleistocene	47°31’18”N, 121°3’32”E	cone	spatter cone	8	Hawaiian, Strombolian	117

Table 2: Parameters for previously studied volcanoes in the ACVF

Sample No.	Location, Code (on Table 2) or Type	Dating method	Age	Reference
08AES02	WNPZ - 5	K-Ar	0.162±0.02 Ma	Fan et al. (2011)
07AES02	TFL - 10	K-Ar	0.246±0.05 Ma	Fan et al. (2011)
07CH04	Chaoer River – lava flow	K-Ar	0.269±0.03 Ma	Fan et al. (2011)
08AES09	WSLZ - 6	K-Ar	0.45±0.03 Ma	Fan et al. (2011)
08AES12	Budong River – lava flow	K-Ar	0.587±0.06 Ma	Fan et al. (2011)
07CH11	JEG - 9	K-Ar	0.743±0.07 Ma	Fan et al. (2011)
07CH09	Dele River – lava flow	K-Ar	1.365±0.16 Ma	Fan et al. (2011)
08AES04	TFL - 10	K-Ar	2.3±0.06 Ma	Fan et al. (2011)
08AES10	Budong River – lava flow	K-Ar	6.7±0.18 Ma	Fan et al. (2011)
Nt202	Tianchi forest farm – lava flow	K-Ar	0.34±0.203 Ma	Liu (1987)
NW223	Wuchagou – lava flow	K-Ar	8.93±0.64 Ma	Liu (1987)
NW214	Wuchagou – lava flow	K-Ar	9.94±0.63 Ma	Liu (1987)
ARS002	TFL - 10	K-Ar	0.34±0.03 Ma	Meng et al. (2018)
ARS003	Dujuan Lake – lava flow	K-Ar	0.42±0.10 Ma	Meng et al. (2018)
ARS004	ARX - 33	K-Ar	0.53±0.03 Ma	Meng et al. (2018)
YL708	JEG - 9	tephra	14.2 ka	Sun et al. (2017)
	Yanshan – 2 - under scoria fall	^{14}C	1990 cal a BP	Bai et al. (2005)
	Yanshan – 2 - under scoria fall	^{14}C	1900 cal a BP	Bai et al. (2005)

Table 3: Absolute dating results for the volcanic rocks of the ACFV (Fan et al., 2011; Liu, 1987; Sun et al., 2017; Wang et al., 2014). Samples marked as "lava flow" derived from extensive flow fields without exact information from their source vent.

The volcanic edifice itself is partially stripped off due to surficial erosion, and the thickest tephra succession preserved on its western side is about 22 m thick. Due to thick soil cover (commonly over 2 meters thick and impenetrable by manual trenching) and grass cover, the pyroclastic deposits associated with the former volcano commonly form only a thin drape of ash and lapilli. In well-protected areas in the foothills, however, deposits have been identified over 10-meter thickness about 2-3 km away from the volcano. As preliminary field mapping showed, most of the deposits derived from Tongxin Volcano accumulated in a broad braided river system of the Chaoer River, and post-eruptive fluvial processes are likely responsible for the removal of the erodible ash and lapilli.

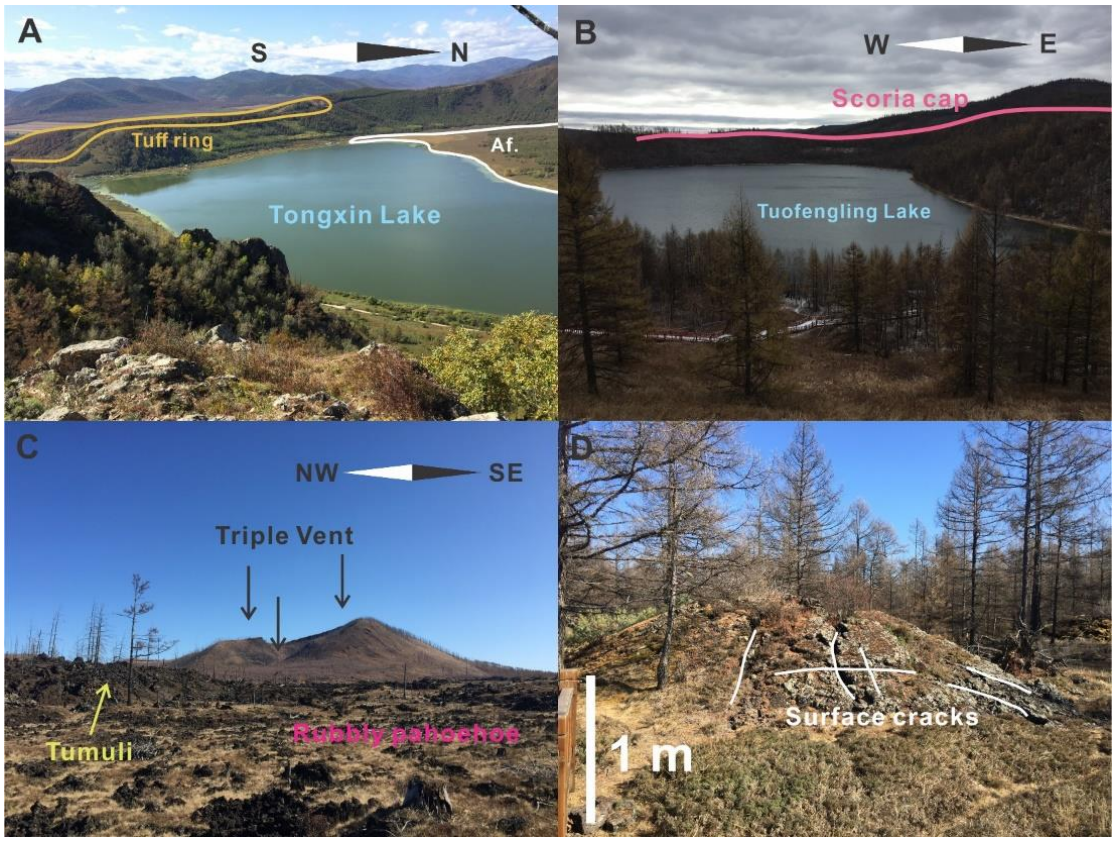

Figure 4: Four types of volcanic geoforms identified in ACVF, such as A-tuff ring; B-complex cone; C-scoria/cinder cone; D-tumuli.

There are no similar, large and preserved tuff rings known from the ACVF. However, small phreatomagmatic volcanoes are suspected or have been associated with the basal sections of large scoria cones. Tuofengling Lake (Camel Humps Lake in Chinese) is an excellent example of such volcano edifice architecture (Fig 4B). This volcano hosts an elongated lake suggesting that this volcano might be a complex volcano with multiple vents along the lake axis. This volcano appears different in its edifice architecture from Tongxin Volcano. In Tongxin Volcano, the country rocks are exposed in the inner basement hosting the crater lake, while in Tuofengling, no basement is exposed. The volcanic edifice surrounding the crater lake is entirely volcanic in origin and part of a larger volcanic edifice. The preserved and accessible sites exposing typical lava spatter, agglomerate, scoriaceous deposits, and various clastogenic lava flows suggest a largely magmatic explosive eruption style being responsible for the formation of them. However, from observations of the crater rim, at least two different volcanic deposits were found. The majority is typical of scoria and spatter cone complex, while in the basal sections, thick pyroclastic successions indicate

explosive hydro volcanism occurred as recorded by chilled pyroclast-dominated units predating the formation of the main central cones that were later disrupted, giving space to form a broad and elongated crater within them (Fig 4B).

The youngest volcanic sites of the ACVF, i.e., approximately 2000 years ago (Wang et al., 2014), demonstrate a typical volcanic landform considered to be a common form of volcano type across the ACVF. Yanshan Hill, marked as a single volcanic edifice, in fact, consists of at least three preserved volcanoes, informally named the Triple Vent forming a volcanic complex. This volcano is a nested and closely spaced scoria cone edifice (Fig 4C). The main edifice is a steep-sided scoria cone with slope angles of about 45°. The elevation of this volcano is about 1590 m above sea level. The volcanic complex was the source of extensive lava flows that reached 4 km to the west and captured the Halaha River causing major landscape modification and damming of the fluvial system. The lava flows show inflation and deflation features, development of pressure ridges, tumuli and outbreaks leading to the formation of a complex laterally changing surface flow morphologies ranging from rubble pahoehoe to aa lava morphotypes. Such large and complex volcanoes are the main volcanic landforms along with the main structurally controlled vents and with NE-SW trending structural elements. The complexity and estimated edifice volumes, as well as the large volume of associated lava flows of these volcanoes, suggest these eruptions changed the actual erupting points within km-ranges, were likely long-lasting events and were capable of sustained eruptions such as sub-Plinian or violent Strombolian style eruptions. This is supported by the extensive ash plain mapped around Yanshan.

Across the field, there is evidence of ponded lava flows, leaving behind a range of ponded lakes, clastogenic lava flows or agglomerates (Fig 4D). Based on the previous studies and evidence from 2019 fieldwork, the vents in ACVF are mostly fissure-controlled.

6. <u>Evidence of explosive hydro volcanism</u>

Explosive hydrovolcanism is the result of magma-and-water explosive interactions (Meng et al., 2018). Phreatomagmatism is a term reserved for magma and groundwater interaction commonly involving molten-coolant interaction (Meng et al.,

2018). In the ACVF, pyroclast textures and deposit characteristics indicate that in low-lying areas, along fluvial valleys, phreatomagmatic explosive eruptions took place (Fig 2). While shreds of evidence of sustained phreatomagmatic explosive eruptions that formed maar or tuff ring volcanoes alone are not common, evidence of intermittent phreatomagmatic phases during eruptions are compelling. Evidence for phreatomagmatism can be seen in the form of quenched pyroclasts, the glassy and angular texture of juvenile particles and the relative abundance of country-rock fragments as accidental lithics in the pyroclastic successions. Indirectly, volcanic landforms may also be linked to the occurrence of phreatomagmatism in the course of volcanic eruptions; however, typical "wet" phreatomagmatic landforms are rarely preserved at ACVF.

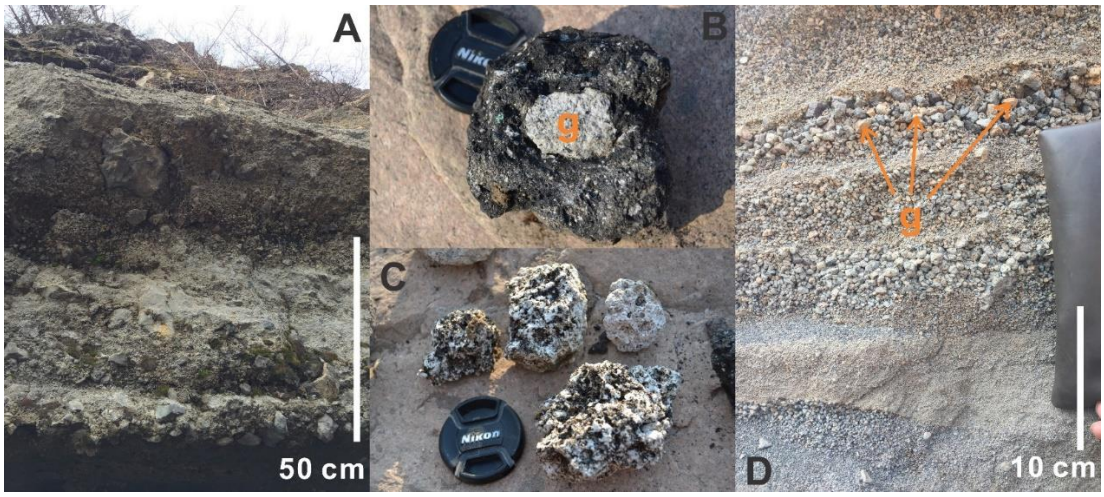

Figure 5: Typical pyroclastic deposit characteristics associated with explosive phreatomagmatic eruptions at the ACVF Are linked to accidental lithic-rich pyroclastic breccias, inferred to be phreatomagmatic shower curtain deposits (A), the abundance of cored/loaded (B) and partially melted accidental lithics in chilled lavas (C), and typical angular and low vesicularity juvenile pyroclasts forming typically graded beds in a combination of shower and pyroclastic density current-derived beds (D), captured on the south of Tongxin Lake, about 12 km away from the lake). The Brown letter "g" indicates "granite".

The most typical and complete site where evidence for explosive hydro volcanism, phreatomagmatism has been identified in the ACVF is Tongxin Lake (Figs 2 & 3). Tongxin Lake has been recognised as a large tuff ring, partially draping over the rugged mountainous region (Fig 2). Two significant outcrops on the west flank of the ring margin have revealed deposits primarily formed by sustained phreatomagmatic eruptions. Dune-bedded, cross-stratified and wavy, accidental lithic-rich pyroclastic

successions were observed and inferred to be the product of a combination of pyroclastic density currents and fallout. The succession of interbedded coarse-grained and fine-grained units suggest rapid changes in particle concentration, transportation style and interaction with microtopography. The majority of the pyroclasts are dense (i.e., low vesicularity), angular to subangular, with delicate chilled margins. Accretionary lapilli is common in fine ash beds.

Features indicative of phreatomagmatism can be found at other sites, such as Tuofengling/Camel Humps Lake, the southwestern side of Tianchi/Heaven Lake, and in sporadic outcrops south of Wusulangzi Lake (Fig 2). The deposits at Tuofengling Lake form a basal unit beneath the dominant scoria/cinder deposits. This unit is composed of a range of indurated parallel bedded, pyroclastic beds abundant in angular and dense lapilli within a fine ash matrix. The average grain sizes from the deposits of Tuofengling are greater than the majority of the deposits recorded at Tongxin Lake (Fig 5A), and they are also more indurated than those from Tongxin Volcano.

Bombs and accidental lithics in the eruptive products from Tongxin Volcano are commonly cored/loaded and/or granitoid lithics are fused or partially melted (Figs 5B & C). Cauliflower-shaped bombs with xenoliths are strong evidence for country-rock entrapment prior to the explosive disruption of the clasts during an eruption. Among the shell of the juvenile materials, large amounts of lithic debris are intercalated within. All these lithics are irregular-shaped, and the juvenile materials are pasted onto the surface, chilled and formed into cauliflower-shaped bombs or juvenile pyroclasts. The general shape of those juvenile pyroclasts is sub-angular to angular. They probably came into contact with external water and became chilled and fragmented in a brittle fashion to form angular, low-vesicular pyroclasts. Pyroclastic successions, which are rich in accidental lithics and contain large volumes of chilled, angular juvenile pyroclasts, commonly form unsorted and graded beds intercalated with fine tuff that also contains accretionary lapilli (Fig 5D). These textural features and outcrop scale sedimentological characteristics are common among phreatomagmatic pyroclastic successions. Commonly, the fine-sized grains indicate that explosive phreatomagmatic fragmentation was accompanied by blasts; on the contrary, the coarse-grained and moderately sorted beds imply fallout origin.

6. *Evidence of fissure-controlled volcanism*

ACVF preserves a range of fissure-controlled vents (Fig 2). Those vents are always aligned NE-SW with the regional tectonic trend (Fig 6). Along with those fissures, several small craters with exposed fissures can be observed, for example, Tianchi/Heaven Lake (Figs 6 & 7) and Dichi Lake (Fig 8). These two vent systems are not only the scenic spots of ACVF but also, they preserve the typical topography and landforms of fissure-fed volcanoes.

Fissure eruptions are common in monogenetic volcanic fields (Németh & Kósik, 2020). In ACVF, at least five distinct fissures can be identified from satellite images. They appear as linear ridge crests associated with closely spaced crater rows (Fig 2). In general, ACVF eruptions occur along fissures formed by regional faulting systems (Liu et al., 2001); however, the volcanoes have yet to be documented in detail. An elongated vent structure is apparent on a satellite view of Tianchi/Heaven Lake (Fig 6). The central part of the lake is bumped out through the surrounding topography, which indicates the presence of steep-sided and agglutinated scoria/cinder cone as the main volcano architecture in that area (Fig 6). A series of the lava flows with large amounts of scattered spatter deposits can be seen on the western side of the lake (Fig 6). The shape of the lake suggests an outpouring may have occurred on the southeast section of the present-day water-filled, lacustrine basin (Fig 7A). Two other locations marking fissure structures on both sides of the lake are shown by the large green arrow in Fig. 6. The orientation of the fissures implies Tianchi Lake, too, follows the orientation of the regional structures (NE-SW). The brown dots in Fig 6 indicate two rows of spatter and lava ramparts surrounding the margins of an eruptive fissure. This morphological setting and the presence of proximal spatter deposits and clastogenic lava flows are interpreted to be the result of fissure eruptions that formed the Tianchi Lake Volcano. Also, the angle of repose of the main cone of Tianchi Lake Volcano is nearly 37-41 degrees suggesting a relatively young age of the volcano as Tianchi Lake Volcano is a scoria cone similar to other scoria cones in the world, i.e., the one in AVF (Auckland Volcanic Field) (Kereszturi & Németh, 2012a). The total surface area of Tianchi Lake is approximately 0.1 km^2, with about 1.2 km in its perimeter. With the well-established forests and vegetation around the lake, field observations and sampling are difficult

(Fig 7A). However, on the outer rim of the lake and the surrounding areas, volcanic materials are well-exposed and easily sampled.

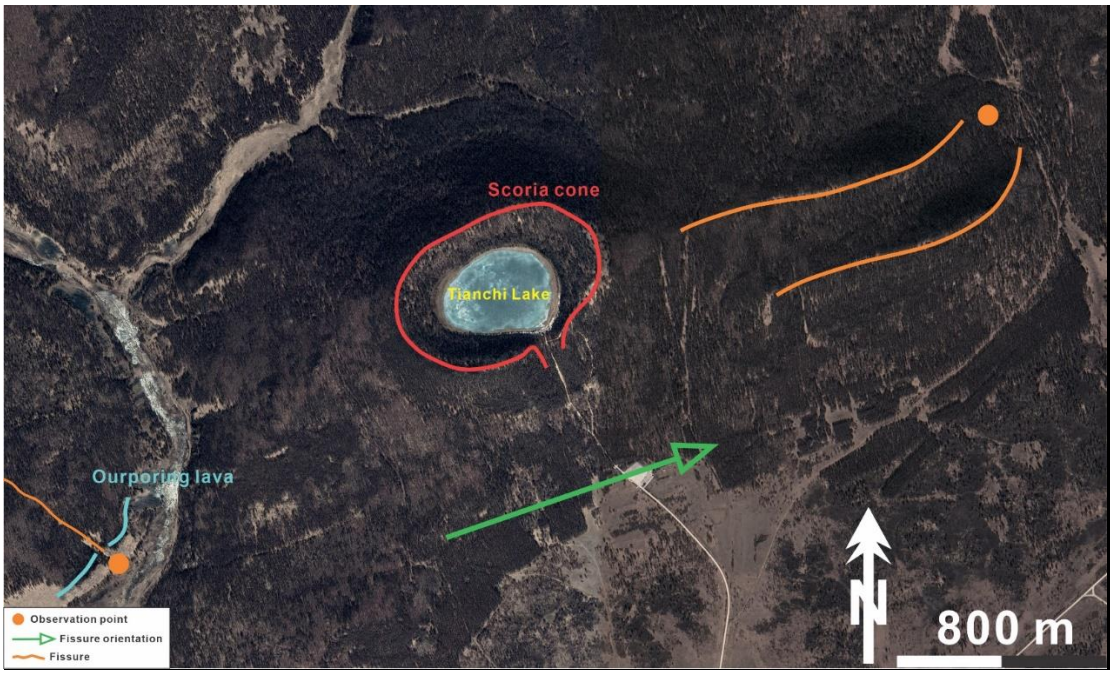

Figure 6: Within Tianchi Lake, a shallow and elongated lake sits well above the surrounding background topography suggesting the lake itself is a crater lake in a constructional volcanic landform such as a scoria cone. On both sides (E and W), the elongated water-filled crater continues into an elongated zone of depression surrounded by a spatter rampart (brown arrows). The overall orientation of the fissures is the same as the main structural setting of the ACVF (green arrow).

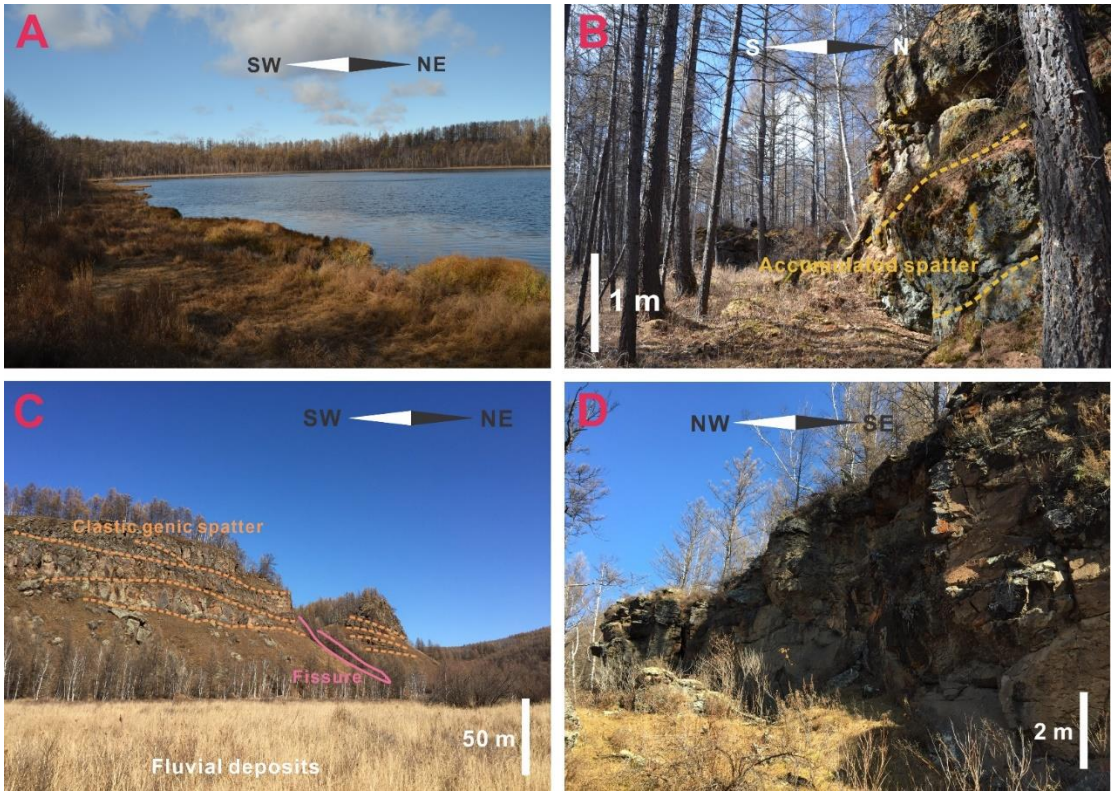

Figure 7: The field observations of Tianchi Lake (A) area showing spatter ramparts and clastogenic lava flows in the eastern (B) and western (C) regions of Tianchi Lake. Platy lava flows also crop out more or less in the same elevation as the lake floor itself (D).

Preliminary observations on the Tianchi Lake Volcano so far have been interpreted as it is a complex, elongated scoria cone. No phreatomagmatic deposits have been identified yet in the area, suggesting that the volcano, despiting it is hosting of a shallow lake, was formed purely by magmatic explosive and effusive processes. During the dry season (August to October, annually), the height of the water level of the crater lake drops a few metres (Fig 7A). Along the eastern and western sides of the preserved scoria cone, the fissure is marked by a 10 meters high wall of lava consisting of flows and spatter ramparts. Evidence of agglutinated interbeds within lava flows, as well as some clastogenic origin flows, attests to fissure lava fountaining and shifting of active vent locations occurring. The surface structures of the fissure are similar to the lava flow but are considerably harder, thereby preserving the original volcano architecture well. Occasionally, some lithic xenoliths (granite) can be observed within the spatter and lava flows. The rarity of vesicles in the lava flows, and the agglutinated texture suggest the lava was degassed during the eruption, indicating that some sort of lava pool must have occupied the main axis of vents. On the western side of the

main cone (Fig 7C), an approximately 50 m high wall of weakly stratified agglomerate and interbedded clastogenic lava flows formed due to explosive magmatic eruptions from a sustained lava fountaining stage forming a wall-like topography. In the middle part of the "wall", a small gap between them might be the fissure structures aligning with the orientation. Field observations could only be taken from one side of the branch of the Halaha River. On the other side, the bedded and agglutinated nature of the rocks is clearly visible, suggesting the proximal location of the region. The horizontally stratified structures of the "wall" might indicate various stages of the cone building as well as the longevity of the eruptive phase. The thickness of the lava flows on the western side of Tianchi/Heaven Lake is about 4-6 m (Fig 7D). The lava displays textures consistent with fluid transportation; there are also a moderate amount of bubbles. Within the bulk rock, some mafic minerals, including olivines and pyroxenes, can be seen. The top of these lava flow structures is eroded by vegetation, but in some places, the typical structures of the a'a' type are still preserved.

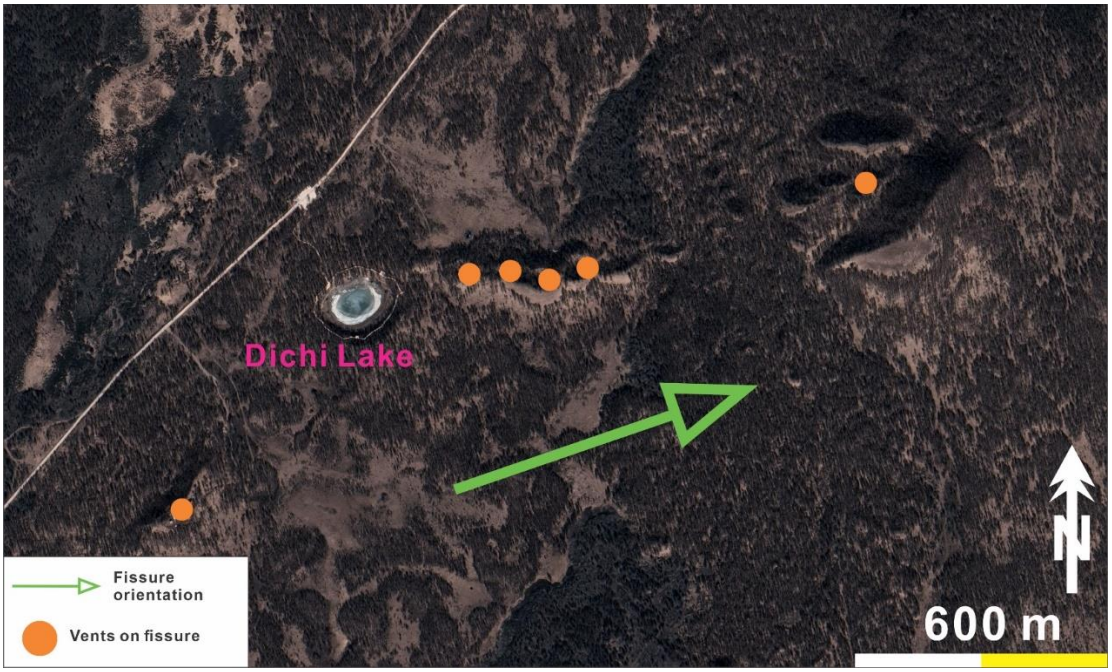

Figure 8: The GoogleEarth satellite image of the vicinity of Dichi Lake showing a chain of craters (brown dots) preserved and oriented to the main structural zones of ACVF (green arrow).

Along with Tianchi/Heaven Lake, Dichi Lake is another small vent sitting on a fissure estimated to be about 3 km long. This lake might be the smallest one in ACVF (Fig 8). The green arrow in Figure 8 marks the regional trend of the fissure orientation, which is also NE-SW, the same orientation as Tianchi Lake. In comparison to Tianchi Lake,

this fissure system is narrower but longer. The surrounding topography is flat without the tiny bumps due to local tumuli (Fig 8). Observations from the proximal areas of the Dichi Lake confirm the presence of pyroclastic breccias composed of dm-to-m sized angular blocks of lava commonly forming well-defined zones several metres across. This deposit is estimated to be a few metres thick and sitting on a lava platform exposed in the crater wall of the Dichi Lake. There is no sign of deposits that may indicate PDC-generating eruptions or accumulation of typical base surge deposits. On the basis of this observation, Dichi Lake is likely a product of a short-lived, single explosive blast triggered by magma-water interaction along a fissure when the fissure hit the lowermost point of the region (Fig 8).

In the densely vegetated area of the Dichi Lake, a volcanic cone chain (Fig 9A) with small-preserved craters is still recognisable (Fig 9B). On the top of the small volcanic cones along the fissure, large blocks of scoria can be found hosting dm-sized spindle-shaped bombs (Fig 9D). The reddish colour of most of the recovered bombs indicates high-temperature emplacement.

Figure 9: The field observations of Dichi Lake show small (tens of metres across) crater chains (A) with shallow but recognisable craters (B). In the crater wall of DIchi Lake, lava flows exposed that are covered by pyroclastic breccia deposits (C). In the flank of the crater chains, fluidly shaped lava bombs suggest proximal portions of those areas (D). Dichi Lake is best interpreted as a result of a single, short-lived phreatomagmatic blast (explosion crater) in the fissure edge.

7. *Evidence of spatter-dominated volcanism*

Spatter deposits are the typical dry eruption phase during the building of volcanic cones. In ACVF, spatter deposits are shown on the vents, which are scoria cones or fissure-related vents, such as Dichi Lake. However, one location preserves intact spatter deposits in the basal section of Tongxin Volcano (Fig 10A). The rest of the vents

in ACVF only preserve scoria deposits from non-welded (black) to welded (red) varieties.

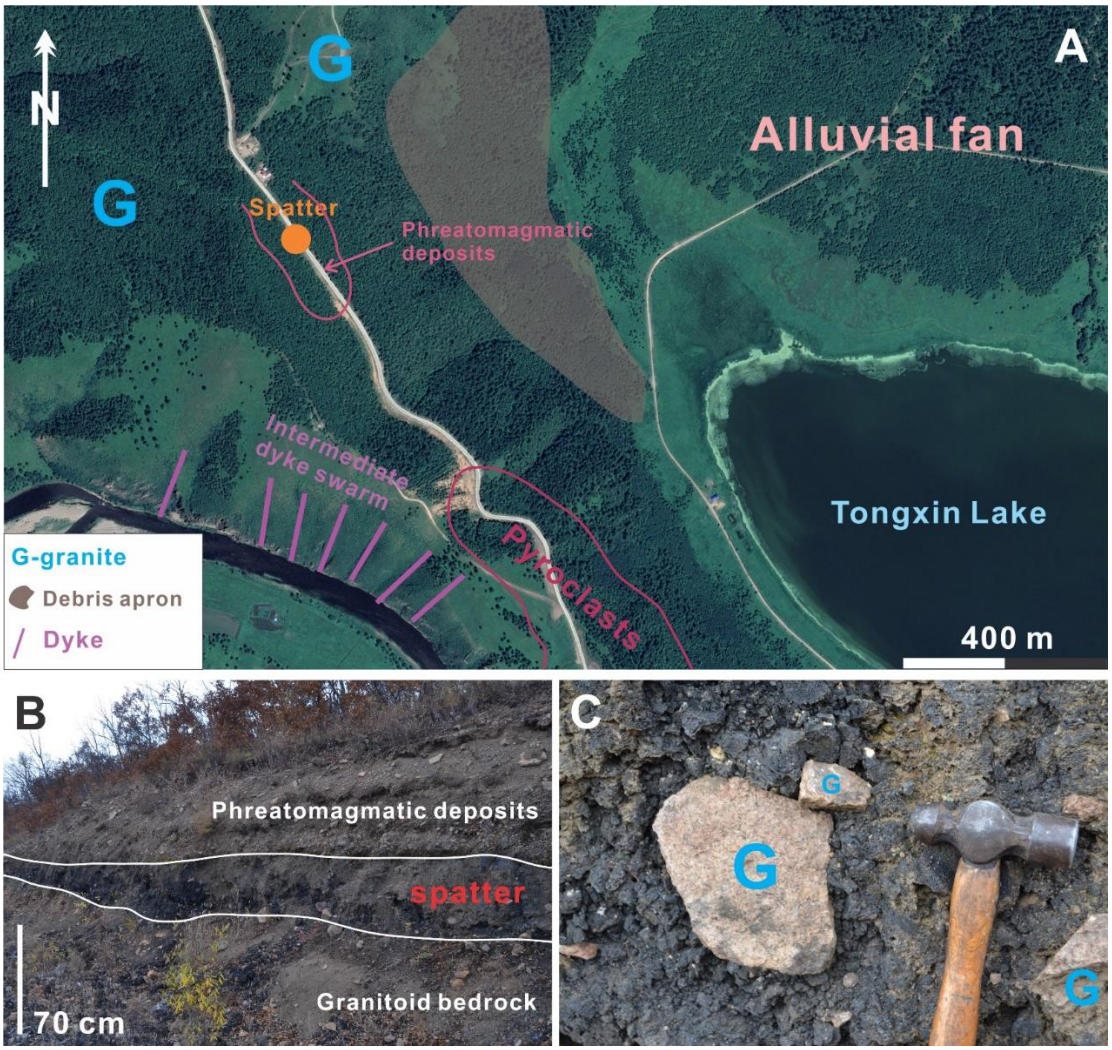

Figure 10: The spatters deposits on the northwestern side of Tongxin Lake (A). The blue letter "G" means "granite" for country rocks. Spatter deposits lay on the bedrock (B), and granitoid lithics are commonly captured within the spatter deposit (C).

At Tongxin Volcano, the basal pyroclastic deposits along the western rim of the phreatomagmatic volcano preserve an about 2 m thick undulating, laterally discontinuous spatter unit (Fig 10A). On the top of the spatter unit, 30-50 cm of unsorted and laterally continuous PDC deposits were found suggesting dramatic eruption style change from a lava fountain stage to a phreatomagmatic blast eruption prior to the eruption becoming more sustained phreatomagmatic in style. Here the spatter deposits are in contact with the country rock. Based on the contact relationships, Tongxin Volcano might have experienced an initial dry-eruptive phase

followed by explosive phreatomagmatism. The distribution of the spatter deposits on Tongxin Volcano is elongated and expanded about 30 m long. On both ends of the spatter deposit, the thickness is thinner than the thickness on the middle part, and the shape is lens-like. Large accidental lithic bombs and blocks are commonly intercalated into the spatters, suggesting some sort of excavation of the country rock through the initial magmatic explosive phase of the Tongxin eruption. The weight of debris of the spatter is low due to the high vesicularity of the spatters. The spatter deposits are hardly found in other areas surrounding Tongxin Lake. However, at least two outcrops preserving the deposits in contact with bedrock indicate the dry-eruption phases, which are correlated with this spatter deposit.

Spatter beds are common elsewhere in the ACVF, especially along the previously described fissure-aligned vents. Spatter deposits have also been recovered within exposed scoria cone sections, indicating a switching on and off nature of the cone growing phases of those eruptions between Hawaiian and Strombolian style eruptions.

8. Evidence of lava-ponding in craters and topography lows

Lava ponding in ACVF is another feature characteristic of the volcanism in the region. The topography of the lava flows indicates an overwhelming dominance of various types of aa and rubbly pahoehoe lava flow morpho-types for the ACVF.

In ACVF, not only small vents formed but also large craters formed that acted as traps for lava flows. In addition, lava is commonly ponded in local basins or valley networks. A large crater (about 1.1 km across) from where one of the youngest and most extensive lava flows initiated to form a significant volcanic landform with a typical volcanic morphology (Fig 11). The local name for this location is Dahei Gou, which means "the big melanocratic valley". Actually, there are two territories with the same name, but in consideration of the descriptions of volcanism of ACVF, the name "Dahei Gou" can only be a marker to define this unique location of ponded lava in a large crater. Dahei Gou Crater is located about 4.9 km northeastern of the three young volcanic cones of Yanshan (Fig 11). The satellite image (Figs 2 & 11) indicates that these two groups of vents (cones) have the same orientation as the Tianchi and Dichi fissures.

Thus, it is believed that there are at least two major regional structures controlling the vent distributions of ACVF.

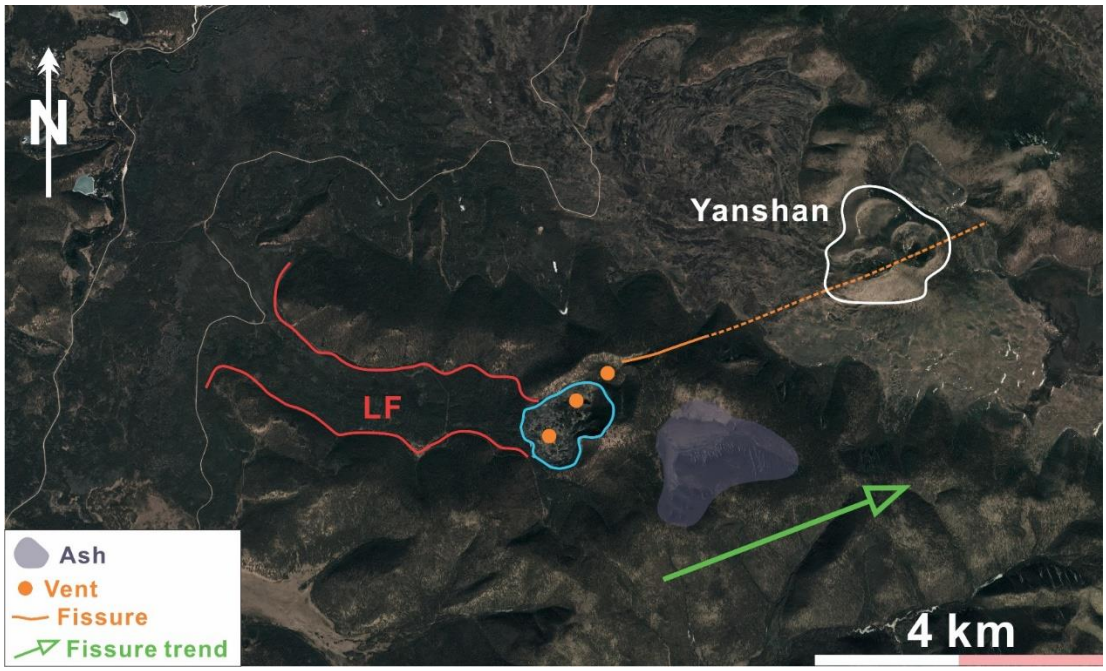

Figure 11: The satellite view of Dahei Gou (Big Black Valley), also this photo depicts the relationship with Yanshan-Triple Vent. The dashed line indicates the extrapolation of the major fissure trend. The blue curve marks the caldera rim of Dahei Gou.

The Dahei Gou crater is heavily vegetated, and only small tracks lead to the remote interior of a complex crater system. From the entrance of the valley, where the main lava flows spread along the Halaha River valley to the crater is about 4 km (Fig 11). The valley from the crater is filled with about 1 km wide lava flow along a 4 km length, exposing typical flow margin features such as small to medium-sized tumuli and pressure ridges (Figs 12A & B).

Within the crater, a breakout zone can be identified along which the lava flow outpours. In that area, rafted spatter sections and large slabs of lava in a randomly packed chaotic nature are evident. Inside the crater, individual tumuli, ramped-up lava rubbles, and large piles of aa blocks form a rugged topography. Along the crater margin, lava flows preserve several meter-long cracks parallel to the crater margin (Fig 12D). These zones are interpreted as fractures along the inflated and ponded intra-crater where ponded lava collapsed upon the partial emptying of the large crater. The major body of the intra-crater lava flow is shown in Fig 12C. Along the crater margin, on the inner crater wall, drain back features can be seen that are partially collapsed

back to the crater, suggesting a dramatic outpouring event tapped the lava toward the valley. Dahei Gou is composed of at least three major nested crater systems, indicating vent migration, crater infill and sudden lava release forming a pit-like crater system. The total area of this crater is approximately 1 km^2. The perimeter is about 4 km (Fig 11). Observations from the field indicate the presence of scoriaceous pyroclastic beds and agglomerate layers that formed due to explosive magmatic eruptions. On the eastern flank of the Dahei Gou, thick, black scoria ash drapes the landscape that has been partially down-cut by erosion (Fig 11). The textural similarities and the proximity of these ash plains to Yanshan deposits suggests that it might be part of the youngest eruptions of the Yanshan – Gaoshan volcanic system; however, this needs to be confirmed in future research.

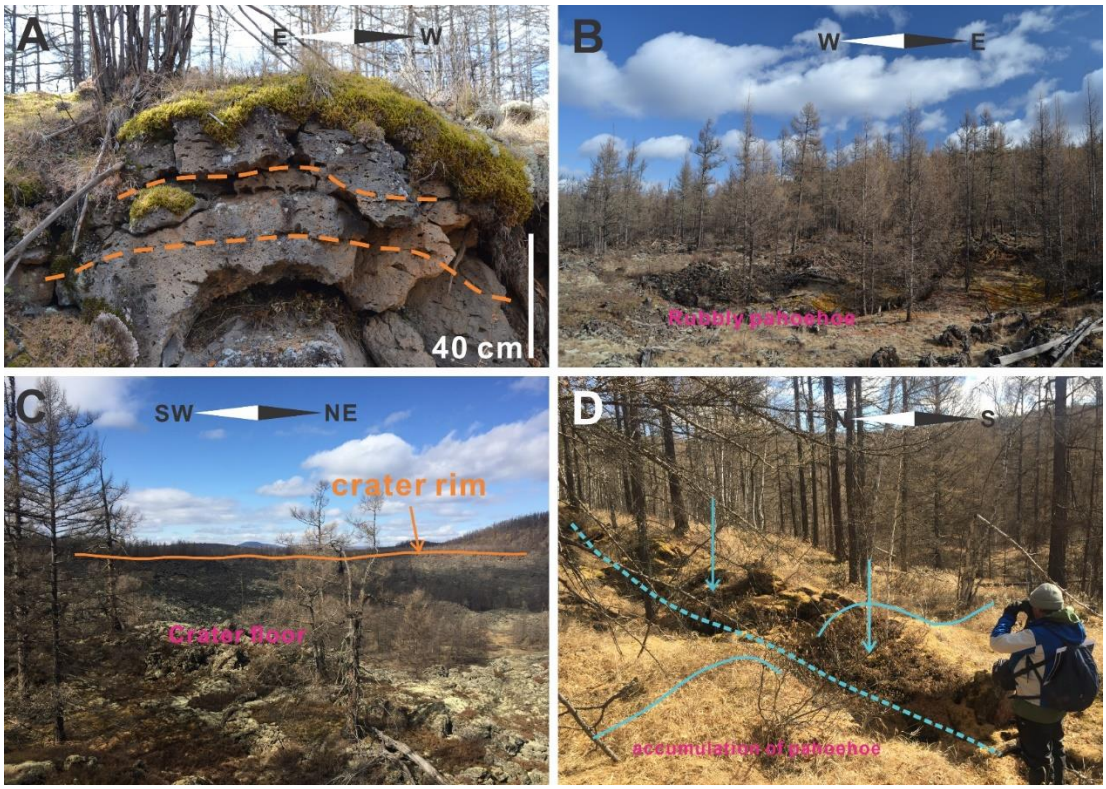

Figure 12: The major characteristics of Dahei Gou. Lava flows from the Dahei Gou show pahoehoe surface textures in the lava fan regions with vesicles aligned following inflationary features (A), while deflationary features leave behind collapsed lava tube roofs (B). The crater is filled with remaining parts of collapsed ponded lava zones, and along with the crater margins, lava drawback features are prominent (C). Along the crater margins, margin-parallel cracks indicate collapse events (D).

In the Arxan region, where lava flows are captured in the river valley, they form tumuli and lava tube networks that are partially collapsed, e.g., the fluvial areas of the Halaha

River. Such areas are prominent around Wusulangzi Lake and Tianchi Lake (Fig 13). Eventually, in these areas, the lava flows are ponded around and form a range of significant landforms; some of them have already become scenic spots for volcanological educational purposes.

Along Halaha River, large lava caves are partially open, reaching a width of about 4 metres (Fig 13A). The lava flows formed successive layers with unambiguous and parallel boundaries. This suggests that the flows ponded during several influx stages contemporaneously. The lava dripped from the ceiling (Fig 13B) but had no time on the ground consolidating while the processes were ongoing, giving them a typical shape that was well preserved. Due to the roughness of the lava flow surface, the ponded lakes developed as the Halaha River became blocked (Fig 13C). The lake is no more than 6 m deep. Some of the ponded lakes have been misinterpreted as the sites of small cones; however, they are tumuli that formed along the flow margin. Cone and star shape tumuli displaying the cone shape form group of dozens of tumuli in this region (Fig 13D). The cracks on the top of the tumuli indicate the upwelling and shape-forming processes were accompanied by tremendous volumes of steam. During the slow movement of lava flows, the gas and vaporised steam would occasionally gather and form large bubbles. Some of them were emitted through the surface of the flow. Thus, the inner parts of the tumuli are empty voids with a cone shape. In the Halaha River area, some tumuli are linear in shape (about 4 m in length and about 3 m in height) and align with each other. Most are similar in size and volume.

Figure 13: The ponded lava flow topography around fluvial areas of Halaha River exposes partially open lava tubes (A) that are draped by lava stalagmites (B). The blocked Halaha River forms a network of lakes and swamps (C). Tumuli are typically formed in the flat Halaha River valley where the cooling effect slowed down and eventually ponded the lava flows derived from the Dahei Goe volcano and Yanshan- Gaoshan volcanic system about 500 m above the valley floor (D).

9. *Evidence of violent Strombolian style eruptions*

Dry-eruption types of volcanism are the most common type of explosive volcanism in the ACVF. Large cones along the NE-SW trending ridge tops form a chain of cones that are vegetated and difficult to access. Most of these cones preserved edifice-building sections where ash, lapilli and bomb beds suggest normal Strombolian-style volcanism. In the youngest known vent complex, the Gaoshan (High Hill) and Yanshan (Hill of Fire)-Triple vent, large amounts of scoriaceous deposits form the cones and also spread across the landscape to form an extensive "ash plain" (Fig 14). The location of Gaoshan and Yanshan on the southeastern boundary of ACVF, is the location of several scoria cones representing the eruptive products of Strombolian style volcanism. In this section, Yanshan-Triple Vent forms a more closely spaced vent system than those at Gaoshan, inferred on the basis of the special distribution pattern of the volcanic

products and the presence of multiple vents within one volcanic massif. The origins of Gaoshan are still being investigated.

Yanshan - Triple Vent is located in the central part of ACVF (Fig 2). The highest peak in Yanshan is 1597 m above sea level. The total area of this "dry" hill is approximately 2 km^2, with a perimeter of nearly 5.3 km. On every side of the hill, the burnt forests cover the slopes of the hill; this was a fire hazard at the end of 1987, i.e., the Black Dragon Fire event.

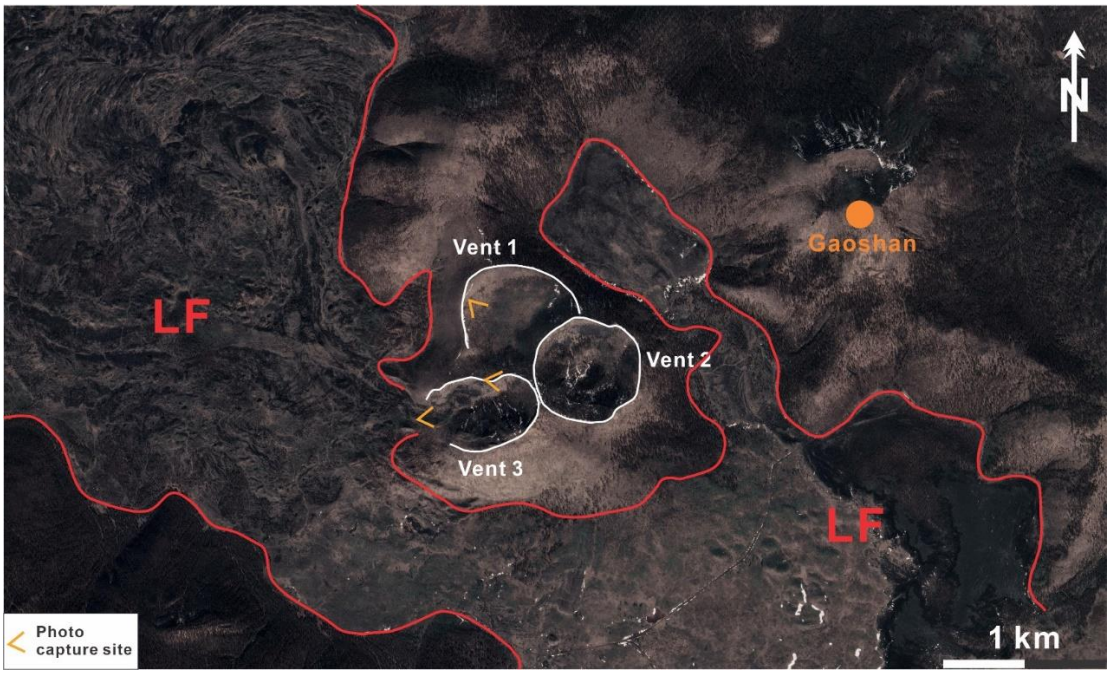

Figure 14: The satellite view of Yanshan-Triple Vent. White lines mark the outlines of the three vents; red lines mark the outlines of the lava flow (LF). Yellow arrowheads show viewpoints from where Fig. 15 A, B and C were taken.

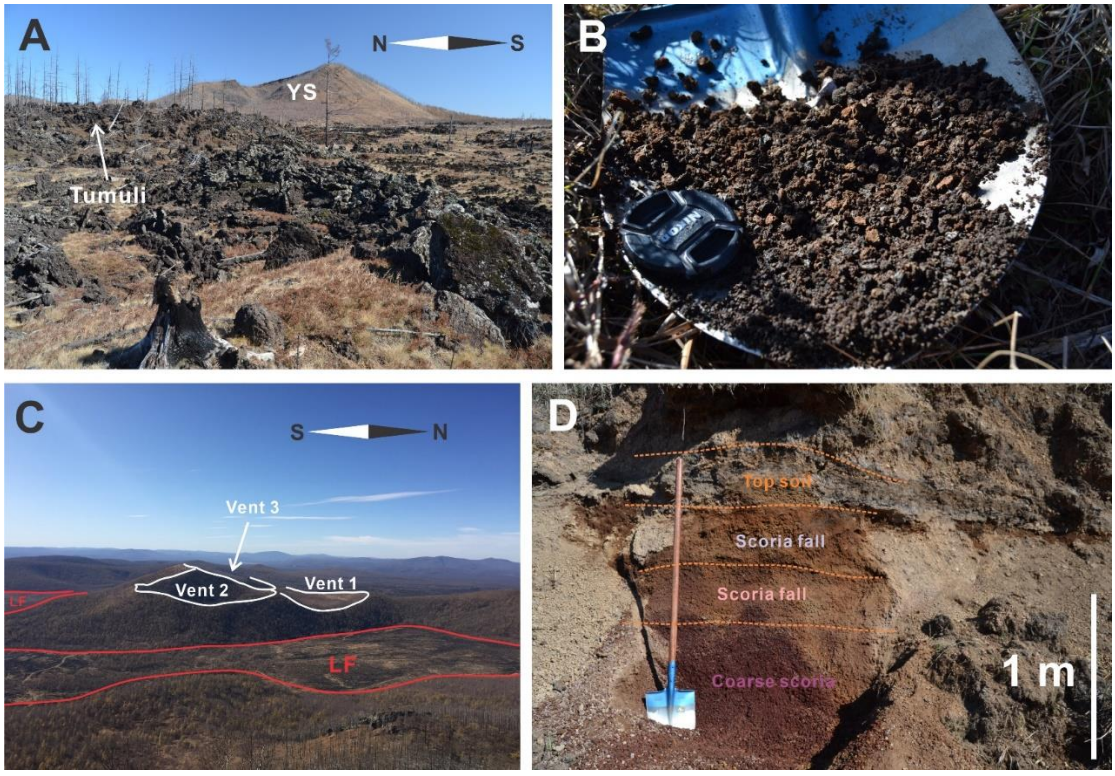

Figure 15: The detailed field observations of the Yanshan-Triple vent. A view from the south shows a complex cone and an open crater toward the west. Rubbly pahoehoe and tumuli around the cone form a rugged surface morphology (A). The surrounding area is covered by thick ash and a lapilli blanket of black and reddish scoria (B). The ash-plain trench just about 2 km east of the vents shows multiple tephra layers indicating repeated and sustained eruptions (D).

As Fig 14 shows, the lava flows cover most of the area surrounding Yanshan. The slope on the right side of the cone complex reaches 44◦ due to the welded nature of the proximal scoria beds. Slope angles are lower on the eastern side of the cone complex, where a breached section of the cone formed the lava-outpouring point from where a lava flow at least 3.77 km long flowed into the Halaha River valley. Some 5 km from the source, scoriaceous ash and lapilli formed at least 1 m thick units suggesting the youngest eruption products were dispersed widely. This dispersal pattern is suggestive of a violent Strombolian or sub-Plinian stage of eruption during the growth of the edifice complex.

Outlines of the ridge crests of the three vents can be pointed out from various observation points. Vent 1 is a flattened, shallow scoria ring structure (Figs 16A & B). In the crater rim crest, a scoria deposit can be reached beneath a c.50 cm thick soil. On vent 3, a clear crater wall collapsed, and rafting from where the main lava flow

escaped the crater is recorded (Fig 16C). The lava ponded in the crater and flowed out of the ring structures, forming an outlet. The width of the breakage is narrow (Fig 16C), not more than about 250 m, which means the flux of the lava flows may reach a threshold value triggering the collapse of the edifice sector. The crater rim of the main crater composes of agglutinate, clastogenic lava and densely welded scoria beds (Fig 16D).

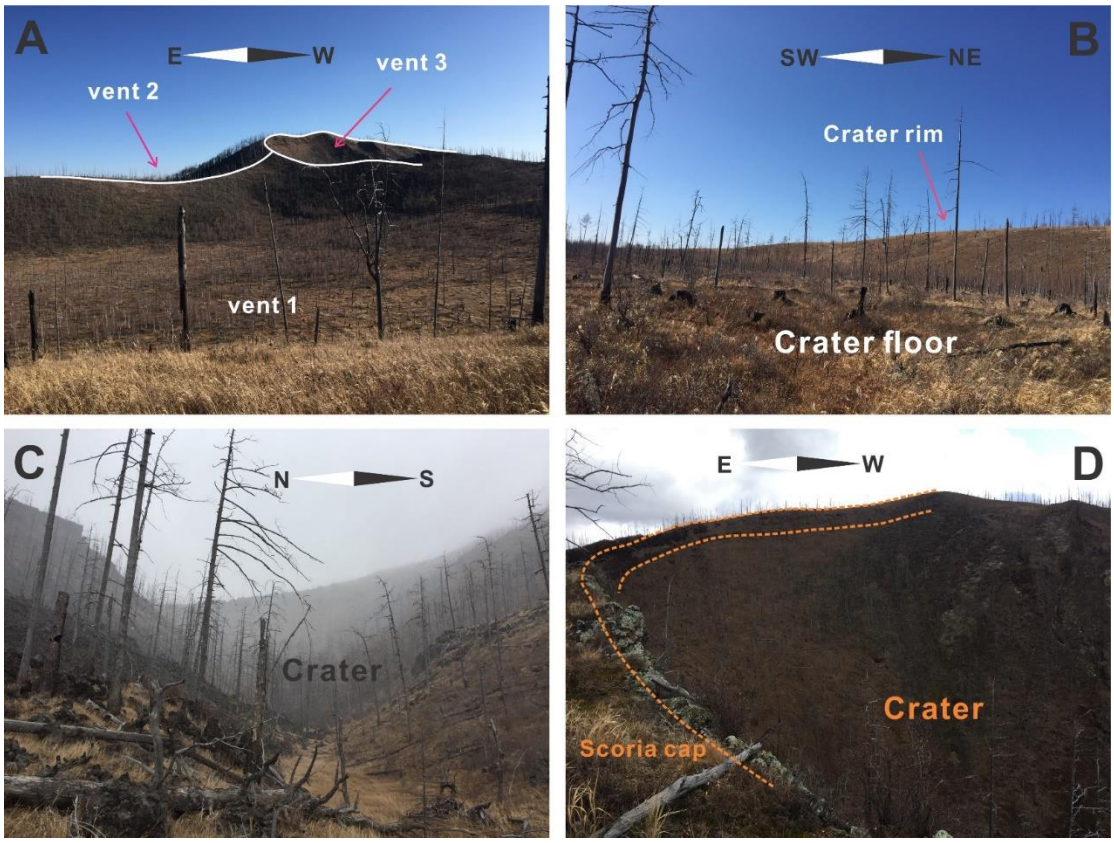

Figure 16: Yanshan - Triple Vent field details. On "A", a photo was taken from the western rim of vent 1, showing the overgrowth of vents 2 and 3. Vent 3 is the source of the main lava flows outpouring from a breached section of the elongated (fissure-aligned) crater (C). The inner crater wall of vent 3 exposes a set of agglomerates, welded scoria, spatter, and localised clastogenic lava flows, all indicative of lava fountain-dominated eruptions and intermittent more violent Strombolian phases (D).

10. Discussion and comparison of ACVF to other similar volcanic fields elsewhere

The volcanism and volcanoes of ACVF were the subjects of fieldwork in 2018 and 2019. The observations made play a critical role in understanding the genesis, evolutionary history, types of landforms, and classification of topography. The observations made at ACVF are compared to several volcanic fields elsewhere in the world in terms of type and topography (Table 4).

1) The Crater of Moon, Idaho, USA, is an extensive volcanic field alongside the eastern bank of Snake River in the NE USA. It has about 25 cinder cones and large areas covered with lava flows over an area of about 1600 km^2 (Green & Short, 1971; Kereszturi & Németh, 2016b; Leeman et al., 1976). In early research, this volcanic field was interpreted as a continental rift system, with a c. 45 km long segment of the Great Rift. The lava flow morphotypes, the dominance of explosive magmatic eruptions over phreatomagmatic volcanism, and the type of monogenetic volcanoes made this field a good analogy with ACVF; however, the volcanoes of the Crater of Moon are smaller, less complex and closer spaced than those at ACVF.
2) The Laki fissure in Iceland is a fissure-driven volcanic cluster. Within it, there are two major vents, volcano Grímsvötn and volcano Thordarhyrna, which represent the genesis of polygenetic volcanism. Significantly, the eruptions in 1783-1785 led to huge mortalities, famine, as well as a global temperature drop (Greeley & King, 1977; Thordarson et al., 2001; Thordarson & Self, 1993). The Iceland volcanic fields belong to the Mid-Atlantic Ridge and the Greenland–Iceland–Faeroe Ridge, which are triggered by mantle plumes and formed North Atlantic Igneous Province. The fissure-controlled nature of the Laki eruption can be adopted as an analogy for the fissure-controlled volcano distribution on small and large scales at ACVF. The lava flow morphotypes, however, are more pahoehoe types, e.g., low viscosity melt, and make the lava flow fields of Laki appear different from those at ACVF.
3) Harrats of Saudi Arabia are clusters of the basaltic volcanic fields on the western coastal territories and part of the Red Sea Rift between the African and Arabian continental slabs. Harrat Rahat is one of the large volcanoes among them. It is about 20000 km^2, and within it, there are approximately 500 individual vents radiating in every direction. The lava flows extend about 100 km to the west along the axis of the field (Murcia et al., 2015; Thordarson & Self, 2003). Harrat Rahat is a good analogy for ACVF in respect of the common large size of the volcanoes, complex volcano architecture, common features of ponding, inflation, deflation and occurrences of ponded lava within large craters and outside in flat-lying areas. Phreatomagmatism in Harrat Rahat has been recognised as associated with the smallest volcanoes of the field (Thordarson & Self, 2003). The size of the field and

the number of vents are also significantly larger than those recorded at ACVF (Murcia et al., 2015).

4) The Chichinautzin Monogenetic Volcanic Field is located in the central part of Mexico and belongs to Trans Mexican Volcanic Belt. There are more than 220 vents located within c. 6000 km^2 area. Most volcanoes in this field are basaltic andesite or basaltic trachyandesite (Murcia et al., 2014; Nieto-Torres & Martin Del Pozzo, 2019). Chichinautzin shares similarities to ACVF with respect to the similar individual volcano sizes, geochemistry, surface area and some aspects of forming nested vents and complex vent systems. However, Chichinautzin is a far more evolved complex, and it is likely volcanoes were longer lived compared to those in ACVF, where other than nested vent complex formation, the majority of its volcanoes are more typical of monogenetic volcanism.

11. Conclusion and volcanic eruption scenarios

Volcanism always causes a range of significant hazards to human societies. Not only the life expectancy but they can also harm the foundations of infrastructures, expose communities, disrupt the business, and put additional risks on the surrounding environments (Lorenzo-Merino et al., 2018). The hazards and threats from volcanic eruptions and their related tectonic disasters are increasing annually to vulnerable societies. This is caused by the specific natural features of a volcanic field. The volcanic products, especially the mapped PDC deposits at Tongxin Volcano, can generate a range of very fertile soils and lands, which are utilised intensively for agriculture. However, the presence of thick and extensive PDC deposits indicates that the threat of violent phreatomagmatic explosive events that can devastate large regions is ever-present. On the other hand, the lava flows common at ACVF, which constitute the bulk of the volcanic products, are very good construction materials. In general, the major effective regions under the shadows of volcanic eruptions are the proximal and intermediate areas, which can be impacted by the significant and severe threats from lava flows as well as deadly PDC flows.

Volcanic fields Ages	Rock Types	Tectonic Settings	Vent numbers	Volcano types
Arxan-Chaihe Volcanic Field (ACVF) Late-Pleistocene to Holocene	**Majority:** Basalt/Trachybasalt **Minority:** Basaltic Andesite	Intra-continental, rifting system	47+ 2000+ km^2	Tuff rings, Scoria cones, Fissures vents, Caldera, Complex cones
Craters of Moon Idaho, USA Holocene	Basalt/Picro-Basalt, Trachybasalt/Tephrite Basanite, Trachyandesite/Basaltic Trachyandesite	Rift zone, Continental crust (> 25 km)	25 1600 km^2	Cinder cones, Fissure vents, Tuff rings
Laki Fissure, Iceland Holocene	Basalt / Picro-Basalt	Rift zone, Oceanic crust (< 15 km)	130 600 km^2	Calderas, Craters, Fissure vents
Harrat Rahat Saudi Arabia Pliocene to Holocene	**Majority:** Basalt/Picro-Basalt, Trachybasalt/Tephrite Basanite, Trachyandesite/Basaltic Trachyandesite **Minority:** Trachyte/Trachydacite	Intraplate, Continental crust (> 25 km)	500 20000 km^2	Tuff cones, Tuff rings, Scoria cones, Lava domes
Chichinautzin Mexico Pleistocene to Holocene	**Majority:** Andesite/Basaltic Andesite, Trachyandesite/Basaltic Trachyandesite, Dacite, Basalt/Picro-Basalt **Minority:** Trachybasalt/Tephrite Basanite	Subduction zone, Continental crust (> 25 km)	220 6000 km^2	Tuff cones, Scoria cones, Lava shields, tuff rings
Auckland Volcanic Field (AVF) New Zealand Late-Pleistocene to Holocene	Trachybasalt/Tephrite Basanite, Basalt/Picro-Basalt, Foidite	Subduction zone, Continental crust (> 25 km)	53 360 km^2	Maars, Tuff rings, Lava shields, Scoria cones

Table 4: Comparisons of ACVF to other volcanic fields (data from https://volcano.si.ed)

In ACVF, several volcano types have been identified, but all of them show features of typical monogenetic volcanoes with small eruptive volume, small edifice size, typical deep-sourced magma systems and suspected short eruption duration. The majority of the volcanoes identified formed through dry magmatic explosive eruptions forming lava spatter cones (Fig 17A), scoria cones (Fig 17B) or complex fissure-aligned volcano chains (Fig 17C). These volcanoes pose hazards to their immediate surroundings. However, because we do not know where the next eruption will take place, they pose prediction uncertainty. The strong fissure alignments of the vents in hundreds of

metres to tens of kilometres in length, however, suggest that new vents likely will open along those main regional structure-controlled zones. The identification of fissure-fed, dominantly Hawaiian and Strombolian style eruptions suggests that once a new vent opens, the active vents likely will migrate along the fissure axis within the hundreds of metres to several kilometres length, making it difficult to mitigate the volcanic hazard. Due to the propagation of fissures through periods, volcanoes can be classified not only by type but also by eruption types. Generally, Strombolian eruptions and phreatomagmatic eruptions are the two major eruption types. Otherwise, the transition type or switching of the eruption types between two major eruptive behaviours is another major hazard event. It seems that phreatomagmatism occurred at ACVF (Fig 17D), but it is not the most significant type of volcanism. Phreatomagmatism seems to have occurred in low-lying areas and/or along major fluvial networks. This style of volcanism formed a very violent event at Tongxin (Fig 17D). Similar eruptions in the fluvial valleys, where most of the human population lives today, could be catastrophic. It is also evident that the Tongxin eruption started just like any other volcanic eruption at ACVF, as lava fountains along a migrating fissure (Fig 17D1). Once the rising magma along the fissure hit an active hydrogeological zone, violent phreatomagmatic explosions took place (Fig 17D2). Similar situations were suggested at Dichi Lake, only on a significantly smaller scale (Fig 17E). The nature of this eruption-style transition, accompanied by the fissure-fed nature of the volcanism, needs further study to develop realistic eruptions scenario-based volcanic hazard study of the region.

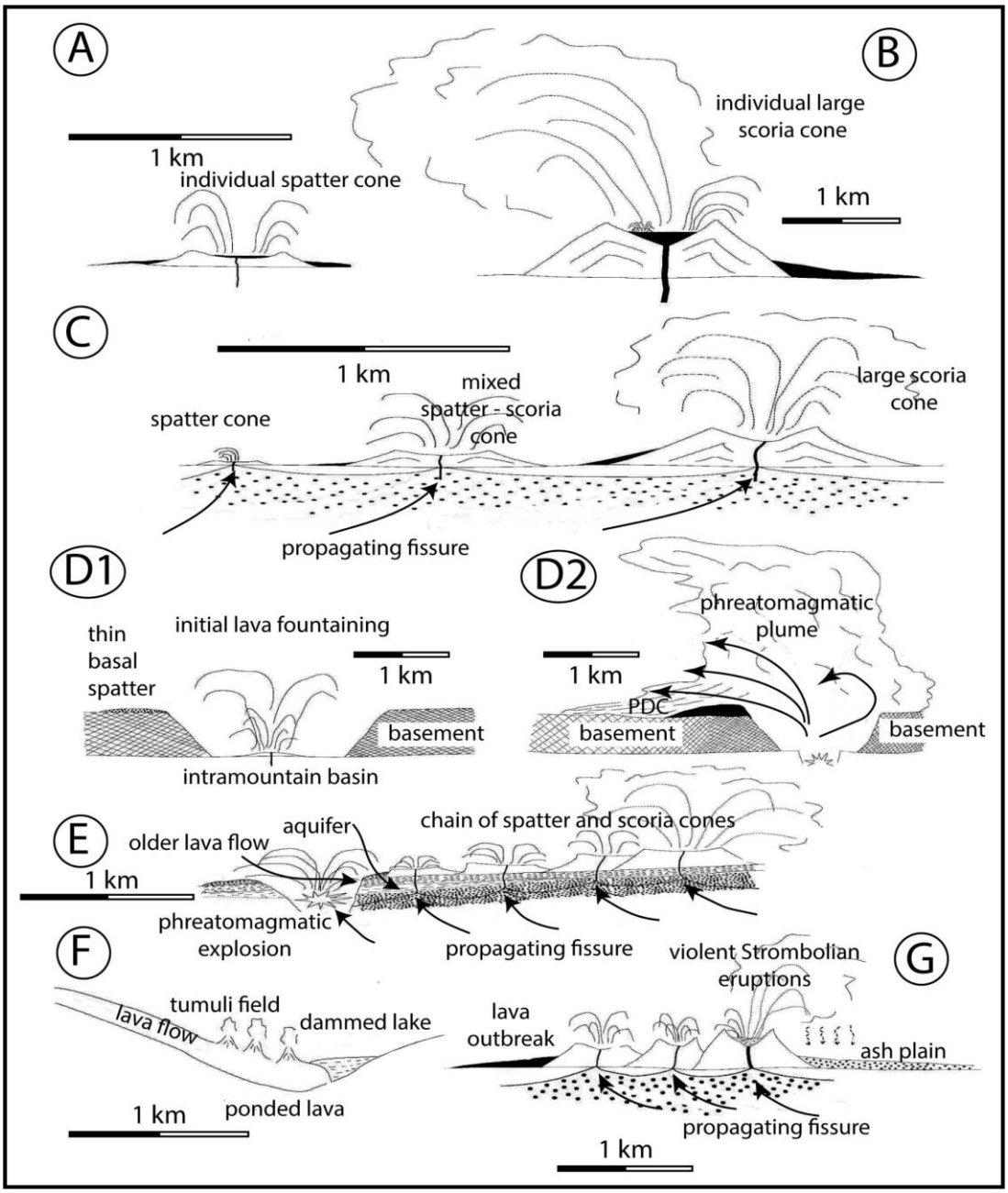

Figure 17: Typical volcano types identified at ACVF and their inferred schematic volcanic eruption scenarios. An explanation is in the main text. Horizontal scales are approximate only.

Effects on the local topography are represented as the lava pouring into the fluvial systems changes the river flow patterns (Fig 17F). By damming rivers, temporary lakes can form, changing the local hydrogeology that may promote explosive phreatomagmatism in the course of the ongoing eruption.

The lava ponding has also been recognized as an important process in the development of the lava fields. The complex high-altitude volcanoes with multiple vents, shifting active vent locations and lava ponding in large craters are features that

need to be considered in volcanic hazard eruption scenarios, as sudden collapse of scoria cone sectors and outpour of ponded lava could initiate large lava flows to areas that normally would not be considered as regions susceptible to lava flow hazards (Fig 17G).

Epilogue:

Basically, from Chapter 2, the ACVF contains a range of typical volcanic features which were created in the Cenozoic eras. Many of them were identified in the previous research. However, the genesis of each vent is still under debate. Thus, in the next chapter, this project will concentrate on the largest vent in ACVF, Tongxin Lake, as an example of detailed research in relation to its recognitions, vent type classifications, and qualified & quantified analyses. Also, the next chapter will utilise fundamental concepts of theoretical geology to examine Tongxin Lake in all aspects as much as possible.

MASSEY UNIVERSITY
GRADUATE RESEARCH SCHOOL

STATEMENT OF CONTRIBUTION
DOCTORATE WITH PUBLICATIONS/MANUSCRIPTS

We, the candidate and the candidate's Primary Supervisor, certify that all co-authors have consented to their work being included in the thesis and they have accepted the candidate's contribution as indicated below in the *Statement of Originality*.

Name of candidate:	Bo'xin Li
Name/title of Primary Supervisor:	Prof. Károly Németh
Name of Research Output and full reference:	
Violent phreatomagmatic explosive eruptions in the Pleistocene Tongxin Volcano and its implication for volcanic hazards of the Arxan-Chaihe Volcanic Field, Inner Mongolia, NE China	
In which Chapter is the Manuscript /Published work:	Chapter 3
Please indicate:	
• The percentage of the manuscript/Published Work that was contributed by the candidate:	Bo'xin Li, 80%
and	
• Describe the contribution that the candidate has made to the Manuscript/Published Work:	
Prof. Károly Németh, Prof. Alan Palmer, Mrs Julie Palmer, and Dr. Callum Rees	
For manuscripts intended for publication please indicate target journal:	
Journal of Volcanology and Geothermal Research (JVGR)	
Candidate's Signature:	Bo'xin Li
Date:	4/04/2023
Primary Supervisor's Signature:	Prof Karoly Nemeth (Digitally signed by Prof Karoly Nemeth; DN: cn=Prof Karoly Nemeth, c=SA, o=Saudi Geological Survey, ou=National Earthquake and Volcano Program, email=nemeth.k@sgs.gov.sa; Reason: I am approving this document; Location: Jeddah, Kingdom of Saudi Arabia; Date: 2023.05.08 13:00:28 +03'00')
Date:	8 May 2023

(This form should appear at the end of each thesis chapter/section/appendix submitted as a manuscript/ publication or collected as an appendix at the end of the thesis)

Chapter 3: Violent phreatomagmatic explosive eruptions in the Pleistocene Tongxin Volcano and its implication for volcanic hazards of the Arxan-Chaihe Volcanic Field, Inner Mongolia, NE China

This is a manuscript that will be submitted to the Journal of Volcanology and Geothermal Research (JVGR); it is in the stages of submission processes. The 80% contributions of this chapter were made by the author, Bo'xin Li, who is under the supervision of Prof. Karoly Nemeth, Porf. Alan Palmer and Mrs Julie Palmer.

1. *Abstract*

Arxan-Chaihe Volcanic Field (ACVF) is a monogenetic volcanic field in eastern inner Mongolia, northeast China, with at least 46 vents in an area of approximately 2000 km^2, formed in the Holocene era. The topography surrounding the field is significantly reshaped by the local volcanism, typical of the fluvial and lacustrine environments surrounding the volcanic vents. The seasonal variations are extreme; temperatures range from 35°C to -40°C during the year. ACVF is an intracontinental volcanic field located in the southern part of the Great Xing'an Range, approximately 2000 km to the west of the Japan subduction zone. Tongxin Lake, located in the northeast corner of ACVF, is believed to be the largest vent in the field and is deemed a maar. Field mapping in 2018 and 2019 found phreatomagmatic eruptions have occurred and built a range of pyroclastic density current (PDC) deposits. Three major locations have well-preserved PDC deposits, with clear evidence of violent eruption phases. Several locations preserve typical fluid-like pāhoehoe, and blocky aa lava flows. The local geological setting is strongly related to regional tectonics, which is an intra-mountain rifting zone. ACVF is essentially a blank canvas, so lab work included standard sedimentary and geochemical analyses to characterise the deposits, together with mapping and preliminary modelling of the field. The sedimentology is predominantly based on field observations supported by grain-size analysis, point-counting, shape and surface texture analyses, and construction of sedimentological/stratigraphic columns. Shape and surface textures were quantified using 2D and 3D images on the

scanning electron microscope. In the absence of high-resolution geospatial mapping, we relied on the available paper maps and field observations. A 3D model rendering was applied by the AutoCAD program with applied proper elevation database; in the graph, the morphologies of surrounding areas of Tongxin Lake, indicating the distributions of volcanic materials, can be depicted. Geochemical analyses have enabled the modelling of magma evolution and petrogenesis using TAS and binary diagrams to understand the volcanic eruptive sequence, juvenile material types, the varieties of major and trace elements and their roles during the volcanic evolutionary history. Geochronology is established from field relationships.

Keywords: Maar volcano, tuff ring, pyroclastic density current, base surge, directed blast, intramountain basin, scoria, sideromelane, volcanic glass

2. *Introduction*

Monogenetic volcanism is defined as a range of small (0.01 km^3 or less in a total volume of a single vent) and short-lived (typically no more than 102 years) volcanoes that commonly occur in clusters within a constrained area (Connor et al., 2000; Guilbaud et al., 2011; Le Corvec et al., 2013a; Le Corvec et al., 2013b; Németh & Kereszturi, 2015). Although monogenetic volcanoes have a short eruptive sequence, their volcanic architecture can be complex, sometimes involving different magma batches within a short time frame.

Studying monogenetic volcanism facilitates knowledge of global volcanism and will help the understanding of

1) The relationships between monogenetic volcanism and polygenetic volcanism,
2) Regional geological settings connected to the genesis of monogenetic volcanism,
3) Syn-eruptive processes operating and how these compare to other volcanic fields,
4) Help the understanding of how global monogenetic volcanism, regional geology setting and plate evolution are related,
5) Also, the local volcanic hazard is highly dependent on monogenetic volcanism.

Monogenetic volcanism produces a variety of ejecta, including air-fall pyroclasts, pyroclastic density currents and their reworked pyroclastic successions. The volcanic

eruptions are either explosive or effusive, creating characteristic sedimentary, emplacement or textural features recognisable within the accumulated eruptive products.

Monogenetic volcanism commonly involves the interaction of water with magma. When this occurs in a terrestrial environment, it is called phreatomagmatism. The water and ascending magma interactions can trigger explosions driven by molten fuel-coolant interaction (MFCI). MFCI can lead to highly energetic explosions and fragmentation of the magma batches (Kereszturi & Németh, 2012a; Zimanowski, 1998; Zimanowski et al., 1995). Massive explosions triggered by phreatomagmatism can blast the country rocks on the conduit wall, leaving behind a debris-filled diatreme. In this case, the resulting volcanic deposits host information on the magma fragmentation and pyroclast accumulation connected to the eruptive environment.

In the territory of ACVF (approximately 2000 km^2), at least 47 vents have been identified. These 47 vents include scoria (cinder) cones, complex cones, and volcanic fissure-aligned crater rows and tuff rings with maar craters. Scoria cones result from "dry", mild explosive eruptions induced by small-volume magma through shallow-level gas bubble outbursts occurring in a steady periodicity (Li et al., 2020; Németh & Cronin, 2011; Németh et al., 2009; Németh et al., 2017a). In general, the volcanic hills are cone-shaped, with welded scoria exposed in the preserved crater rims and proximal flanks of the cones. In ACVF, the scoria cones are the most prominent volcanic geoforms (Németh et al., 2017b; Németh & Moufti, 2017; Wang et al., 2014). Scoria cones commonly form groups within ACVF. For instance, the youngest known vent complex, Yanshan (2040±75 and 1960±70 yrs B.P), is a triple vent consisting of three distinct cones within a morphologically distinct geoform (Bai et al., 2005). The slope of the Yanshan cone is steep. On the southeast side of the cone, the slope angle is nearly 47°. At 234 m above mean sea level, Yanshan is higher than the scoria cones (probably twice as high as regular scoria cones), making it a dominant landscape feature judging by its size and areas of lava flows erupted from it (Bai et al., 2005; Zhao et al., 2021a). Some vents show succession with basal tuff ring structures overgrown by a scoria cone. This indicates that some vents have experienced multiple eruption phases and display a range of volcanic ejecta. For example, Tuofengling Lake is a

complex cone with “wet” and “dry” deposits. The tuff deposits are nearly 10 m thick, and the top scoria cone reaches about 2-3 m in height. Small scoria cone vents form linear features that follow fissures orientated with the regional tectonic trend. Generally, all fissures in ACVF strike SW-NE. For instance, Dichi Lake (Fig 9E) is one of five small scoria cones located in an SW-NE-orientated fissure. Each cone is no more than 100 m in diameter with approximately 3 m high. The fissures at ACVF are clearly visible from satellite images, and images suggest there could be up to seven cones with the same orientation, SW-NE.

At least five tuff rings are recognised at ACVF (Li et al., 2020). Tongxin Lake and Tongfegnling Lake (Fig 4A & 4B) are constructed by a range of pyroclastic deposits consistent with explosive phreatomagmatic eruptions being the main process forming these volcanoes. PDC deposits, radially distributed around the craters, dominate the tuff rings. In a preliminary study, the focus of this paper is Tongxin Lake, which has been defined as a maar with a range of “base surge” deposits on the ring-shaped lake rim (Zhao, 2010). Tongxin Volcano is unique within this tuff ring with its distinctive, broad and flat-floored crater. It represents the largest known, well-exposed phreatomagmatic volcano in ACVF. Initial explosive magmatism gradually shifted to a complex and sustained phreatomagmatic explosive phase forming a maar in an intramountain basin. Detailed study of changing eruption styles within complex monogenetic volcanoes sheds light on the internal and external processes operating, their relative role, and their spatial and temporal variations, thereby providing an understanding of the volcano’s growth. Understanding such variations helps to develop evidence-based eruption scenario models. Tongxin Volcano is an important link to understanding the delicate relationship between the controlling parameters of the evolution of sustained monogenetic volcanism and forming a large volcanic edifice with significant eruptive volume under the intramountain environment, possibly in the Last Glacial age.

Overall, Tongxin Volcano offers an excellent window to look into the Quaternary landscape evolution of a monogenetic volcanic field formed in a rapidly changing terrestrial, cold temperate climate far from active plate boundaries; hence, the results

contribute to our understanding of intracontinental volcanism in a changing environment.

3. *Geological settings*

The largest geologically and geomorphologically distinct area in NE China is the Songliao Graben (Fig 1). This regional feature was formed by tectonic subsidence in response to intra-continental rifting (began in Triassic to mid-Jurassic) that occurred in four main stages: opening of the Japan sea at approximately 15 Ma; extension associated with the Yi-Yi fault propagations around 14 to 13 Ma, and the Fu-Mi fault evolutions from 11 to 7 Ma; and final graben formation around 4.5 Ma (Liu, 1988; Liu, 1989; Liu, 1993; Liu et al., 2001). After the events of the opening of the Japan Sea, mantle upwelling predominated the tectonics (Li et al., 2021; Qiu et al., 2020; Ward et al., 2021). The Songliao Graben is flanked to the east by the Great Xing'an Range with an elevation of 145-400 m above sea level. On the western and northwestern sides of the graben, various monogenetic volcanic fields, such as the Longgang Volcanic Field and the intracontinental volcanic massif, i.e., Mt.Changbai, are distinct landforms along China and North Korean political boundary. The northern boundary of the graben is marked by the Wudalianchi volcanic field (Liu, 1988, 1993, 1999; Liu et al., 2001). These volcanic fields are the outcome of the magma that found its way to the surface, presumably along major fault systems flanking and underlying the graben. This could explain why volcanism subsides in the centre of the graben. Each volcano within the volcanic field has produced small-volume, short-lived eruptions, the basis for calling it a monogenetic volcanic field. The volcanism in the Songliao Graben is one of the most studied volcanic regions in China and has been explored intensively in the past 25 years.

There are six major fault systems in NE China (Fig 1, dark concrete lines), all with SW-NE orientation. The faults extend beneath the Great Xing'an Range, are uplifted in the SE corner of the graben and mark the eastern margin of Songliao Graben. The Great Xing'an Range is the boundary between Xing'an Block and Songliao Block (Lin & Wang, 2006; Wang et al., 2015; Wang et al., 2016). The black star in Figure 1 marks the location of the Arxan-Chaihe Volcanic Field (ACVF) near the southeast side of the Great Xing'an Range. ACVF is approximately 2000 km from the Japan subduction zone in an

intra-continental setting. The Great Xing'an Range and its related fault belt are suspected of having been torn by the Japan Subduction Zone (Liu et al., 2001; McGee et al., 2015). The subduction front tears pieces off Eastern Asia through the rollback process. The subduction front has migrated slowly toward the east dragging fragments of lithosphere off eastern Asia with it (Ren et al., 1997; Ren et al., 2002). This process resulted in the opening of the China/East Sea and the collision eastward of the Korean Peninsula (Gilder et al., 1991; Sohn, 1996; Sohn & Park, 2005). The same forces opened the Okhotsk Sea (Kravchinsky et al., 2002; Tang et al., 2014; Watson, 1985), rotating the western side of Kamchatka and tearing continental lithospheric fragments like Sakhalin off Asia (Cormier, 1975; Gorbatov et al., 1997; Lander & Shapiro, 2007; Taran, 2009). Rifting movements are widely known in NE China (Liu, 1989; Liu, 1993). Ascension of the asthenosphere during the Cenozoic facilitated back-arc rifting and associated volcanism (Liu, 1989). The Japan Subduction zone has been migrating eastwards towards the Pacific Ocean at 4.5 cm per year, and the effect of the subduction zone on NE China has gradually weakened (Gilder et al., 1991; Ren et al., 2002).

In the immediate vicinity of ACVF, Palaeozoic sediments and meta-sediments crop out at the surface, forming block-shaped horst and graben fault-bounded structures that follow the regional tectonic trend. The older rock units typically crop out in the east, where the Palaeozoic succession is exposed at the surface, especially Cambrian meta-sediments (the amphibolite facies of Xinghuadukou Group and the greenschist facies of Jiageda Group; both groups have an 1157 ± 32 Ma of Sm-Nd isochron age) in Great Xing'an Range (Feng et al., 2018; Sun et al., 2014). Closer to ACVF, Mesozoic granitoid (Xinghua and Xinganqiao units)basement are exposed (Ge et al., 2015). Earlier studies have identified four phases of granitoid intrusions in the Great Xing'an Range, U-Pb method dated at 957-786, 479-418, 265, and 209-192 Ma (Ge et al., 2015). The presence of Late Mesozoic volcanism (zircon U-Pb and whole-rock Ar-Ar ages of 174 to 122 Ma) in the southern areas of the Great Xing'an Range (Zhang et al., 2010b) is consistent with Late Mesozoic intrusions (Ouyang et al., 2015). In the southern part of the Great Xing'an Range, Cenozoic mafic to ultramafic volcanic rocks is being intruded prior to explosive and effusive basaltic volcanism. The first reliable date published is

0.340±0.203 Ma (Liu, 1987, 1999; Liu et al., 2001). More recent studies have revealed volcanic eruptions in Arxan areas around 2000 yrs BP (Bai et al., 2005).

A well-developed rift system is present in NE China, where the ascension of the asthenosphere has triggered delamination processes at the base of the lithosphere, where it is in contact with the asthenosphere (Li et al., 2018; Wei et al., 2019). The network of well-developed faults around the Great Xing'an Range has meant some magma that may have experienced high speed (approximately 37-64 m/s deeper than 7 km of depth) ascension (Gonnermann & Manga, 2013; Rutherford, 2008). Furthermore, it is highly likely that the contamination from the lithosphere occurred during magma ascension (Browne & Gardner, 2006; Russell et al., 2012; Rutherford & Hill, 1993).

Stratigraphy and hydrogeology ACVF lie within the subarctic climatic zone. Seasonal monsoons occur in summer and winter from the northwest and southeast, respectively; the average temperature is -2.6 °C, and the average precipitation is around 452 mm per annum (Cui & Zhao, 2019; Leng et al., 2021; Lu et al., 2021; Wu et al., 2019). It is typically extremely cold in winter and has high precipitation in summer. The average temperature is approximately -2.7℃, ranging from -25.1℃ in January to 16.8℃ in July, and the period of annual temperature below zero can last at least six months (Németh et al., 2017a).

Two major river systems flow through ACVF. The Chaoer River flows from the northern regions of Tongxin Lake to the south, and the Halaha River in the western part of ACVF flows initially west to east and then south from east of Tianchi Town. Halaha River flows from the western side of ACVF, going through the south of Arxan Heaven Lake (Tianchi Lake), where analyses of lake sediments have revealed a history of vegetation and climate change over the last 250,000 years since the Last Glacial Maximum (LGM). From 7.5 to 6 cal. Kya BP, the water level of Heaven Lake rose rapidly and in the interval 5-3 cal. Kya BP. After 3 cal. Kya BP, the lake water level fluctuated and eventually 2.3-1.5 cal. Kya BP (Leng et al., 2021).

Tongxin Lake is located in an intra-mountainous setting approximately 2000 km from the Japan subduction zone. It lies within the Great Xing'an Range, a hilly area with

glades covering the surfaces of the mountainous lands. The basement of the range is composed of Mesozoic meta-sediments intruded by a granitoid sill formed by early rifting activities (Liu, 1987, 1988; Liu, 1989; Liu, 1993, 1999; Németh, 2016; Németh et al., 2017a). During the Cenozoic era, the Japan subduction zone moved to the east as a subduction rollback effect by the westward subduction of the Pacific Plate beneath Asia.

4. Methodology

1) Field works on the Tongxin Volcano

Tracking back on the previous research pieces, although several papers were trying to describe the field observation on Tongxin Lake, they still lack the details on systematical analyses and its eruptive products in the adjacent areas.

Two seasons of field trips, the fall of 2018 and 2019, were spent visiting key locations exposing the pyroclastic succession within a 15km radius of Tongxin Lake. Fieldwork was concentrated in the immediate vicinity of Tongxin Lake and the region in the south of the lake. Towards the north, mapping followed the deposits until they had pinched out or we reached a municipality boundary where we had no permission to work. In the area around Tongxin Lake, a range of volcanic successions with continuous exposure are preserved. Well-exposed volcanic sequences can be traced on the western flank of the crater rim surrounding the lake. In places, the exposed section is over 10 m thick, and there are locations where the initial deposits associated with Tongxin Volcano are exposed. We have used deposits in five well-exposed outcrops to establish a composite section that represents the volcanic history of the Tongxin Volcano. The most significant stratigraphic sections are informally named Site 1 (S1) and Site 2 (S2), respectively. S1 is on the inner wall of the tuff ring; otherwise, S2 is on the outer wall. Both pyroclastic successions are composed of a range of intact parallel bedded tuff and lapilli tuff, commonly displaying dune structures and cross-bedding. Three lithofacies are identified based on grain size and textural characteristics, including parallel/planar bedding (PB), non-bedded or massive (NB), and dune and cross-bedding (DC). Nearly identical sets of lithofacies are seen in both S1 and S2. These two sites were described in detail, and stratigraphic columns were drawn

showing the lithofacies and would be a standard for comparisons and analogue to interpret the other three locations (Fig 18). Other locations with volcanic deposits share similar or identical lithofacies assemblages. Thus, S1 and S2 are the key locations documenting the pyroclastic stratigraphy of Tongxin Volcano.

Lava flows are widely distributed to the northwest, west and south of Tongxin Lake. The modern Chaoer River, one of the large fluvial systems in ACVF, cuts through the lavas (Fig 19) (Németh et al., 2017a). Typical lava flow structures and textures in cross-sectional view include columnar jointing, fluidal shapes with a specific orientation, sheared bubbles, and rotated and partially homogenised lithic xenoliths intercalated within a plagioclase-dominated groundmass. However, the actual thickness of the lava flows is unknown due to the lack of exposed sites where both upper and basal contacts can be observed. However, on the bridge site (Fig 18, LF1), an outcrop preserving a contact between flow and the baked paleosol, the thickness of the flow in this site is approximately 3 to 5 m.

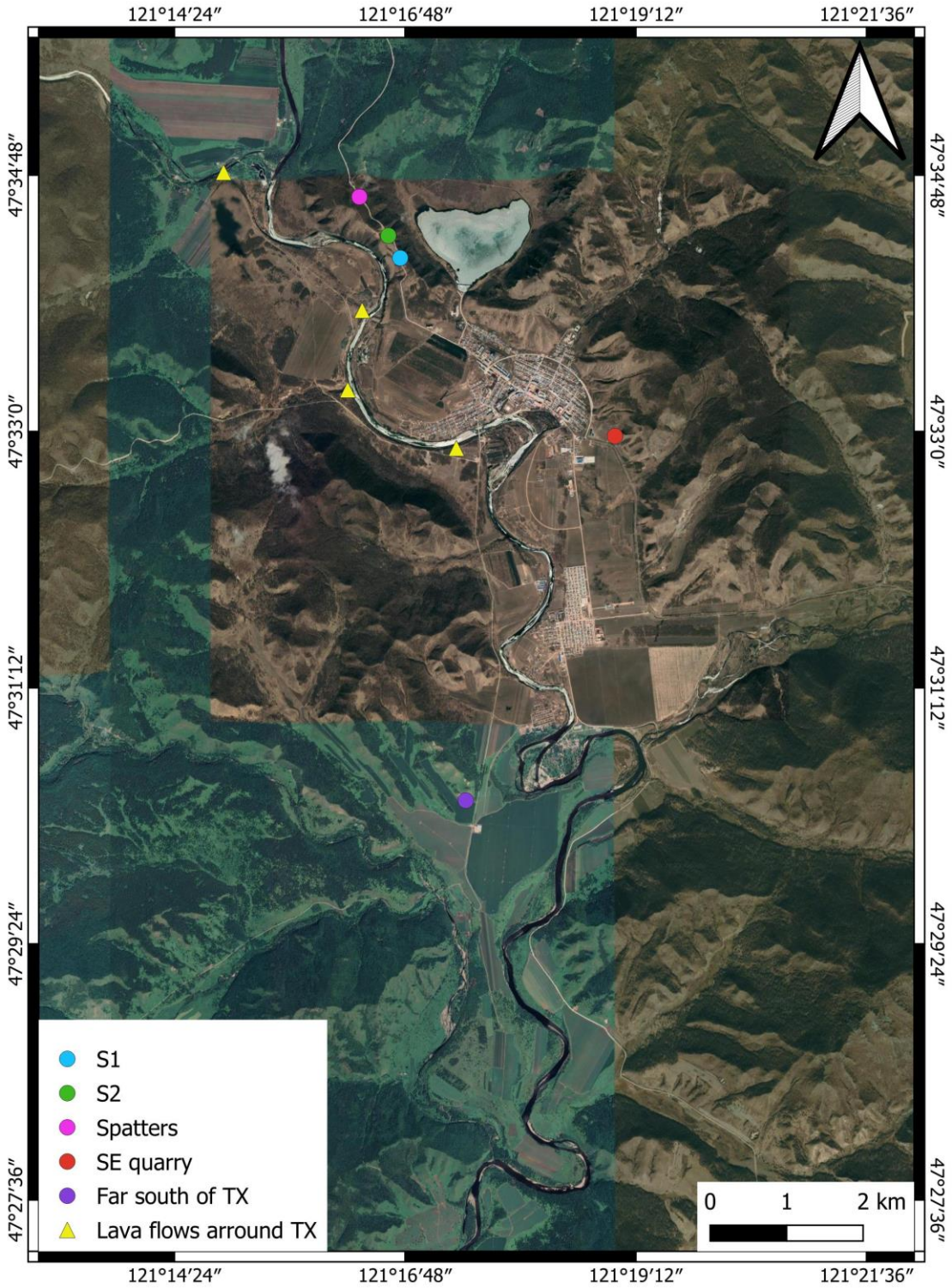

Figure 18: Major locations of sampling; those names of locations will be correlated to the ones in the following contents.

There are three locations where the volcanic deposits are in direct contact with the underlying country (granitoid) rock. One of the locations contains well-preserved lava spatter deposits deposited immediately over the underlying crystalline basement horst at 770 m above sea level on the east rim of Tongxin Lake. This is representative

of an early phase of dry explosive eruption in the early phase of the Tongxin Volcano. The other two locations, where similar well-exposed basal contact relationships are observed, preserve similar lava spatter-dominated deposits, but here, they are finer-grained and include fine, scoriaceous dark lapilli beds a few cm thick. They are about 3.2 km from the centre of Tongxin lake, which is their suspected source. The data in these columns are based on the key locations with the most complete and well-exposed pyroclastic successions. Representative samples were collected for granulometry, pyroclast morphometry, texture and geochemical analyses to identify spatial and temporal variations through the eruptive history of the volcano.

2) Construction of 3D models

3D model maps are an efficient way to interpret the regional variations of topography from a perspective 3D photo from any direction. This may require highly detailed field works, e.g.,, GPS locations and contour data, as well as the real-time renderer with a high polygon algorithm (sourced from https://qgis.org/en/site/forusers/download.html). Also, this set of 3D models must be checked through real satellite maps, especially the observation locations and their surrounding areas in relation to the topography trends. By applying this method, the dynamic geomorphology can be fit with the regional observation on a realistic scale, i.e., by utilising the data from https://srtm.csi.cgiar.org/srtmdata/, then exporting the contour data to AutoCAD 2021, then eventually creating the 3D topography map. A minimum volume of the lava flows can be estimated by multiplying the depth of the flow by the surface area of the top of the flows and projecting the slope angles of valley sides using a slope map based on the Shuttle Radar Topography Mission (SRTM) data (Fig 20).

3) Stratigraphy of the volcanic units around Tongxin Lake

Tongxin Volcano produced two types of eruptive materials, lava flows and explosive pyroclastic deposits. Systematic analyses, including the recognition and classification of their facies, structures, sorting, and average grain size variations, were undertaken following methods outlined and applied to small-volume monogenetic volcanoes (Sohn & Sohn, 2019a; Sohn & Sohn, 2019b; Sohn & Park, 2005). The observable

textures and surface characteristics of the lava flows are described, and geochemical analyses were undertaken.

4) Granulometry

Pyroclastic deposits, which included a wide range of grain sizes and lithologies (mostly country rocks), were oven-dried at 45°C for dehydration on the samples and dry sieved using sieves from 62 µm to 16 mm screens at half phi intervals. After sieving processes, componentry analysis was undertaken using a SCHOTT, KL1500 optical microscope. Manual point counting was deemed the most appropriate method for the wide range of grain sizes in a single sample. The relative abundance of country rock and mineral fragments detected in the pyroclastic deposits was noted with the aim of inferring the explosion locus and excavation processes.

Density measurements for pyroclastic deposits are critical for porosity calculations. Two different types of density are essential to calculate the final porosity: envelope density and true density (Dukhin et al., 2013; Edwards et al., 2016; Webb, 2001). Both types are measured from the coarse size fraction (5.66-16 mm grain diameter) in the samples. The envelope density was measured using a Micromeritics GeoPyc 1360 Density Analyser, and the true density was evaluated using a Quantachrome Ultrapycnometer 1000. The final porosity was calculated by the ratio between envelope and true density following the method outlined in (Horgan, 1996; Horgan, 1999; Horgan, 1998).

Electron microscopy enables 2D and 3D imagery of the surface of the pyroclasts at a microscale (for 3D images: 125 to 63 µm; for 2D images: 707 to 125 µm), enables the recognition of the degree of crystallinity and geometric forms of individual clasts. These above-mentioned measurements were performed on plugs for each sample in the grain size range of 1 mm to 88 µm.

5) Geochemical analysis

Geochemical analysis of pyroclasts and coherent lava rocks collected from stratigraphically-controlled sections was undertaken to facilitate the recognition of stratigraphic chemical trends and temporal variations across the sequence of the

Tongxin Volcano. Samples were prepared to utilise CARBOLITE AAF 1100 furnace to estimate the loss of ignition (LOI) and Xrfuse 2 with 12:22 X-ray flux to make the glass pellets for XRF analysis. Whole-rock element analyses were undertaken on 26 samples chosen from the major deposits and lava flows. The samples include two pyroclastic deposits from the west rim, deposits in contact with the underlying country rock, and lava flow in the proximal and intermediate areas of the lake.

5. Results

1) Distribution of eruptive products of Tongxin Volcano

During two seasons (2018 and 2019), some 50 locations were observed, many described in detail, with numerous locations preserving volcanic products noted on field maps (Fig 18). The major outcome of the field surveys is an outline of the volcanic stratigraphy in the vicinity of Tongxin Volcano. Areas proximal, intermediate and distal to the present-day Tongxin Lake were visited as reference locations from which to locate the vent of the volcano. The chosen sites are evenly distributed from the proximal to distal areas, offering insight into the progression of the volcanic events that formed the Tongxin Volcano. For ease of discussion and to build field correlations between the different locations, this article will use the term “site” for locations without specific names. Also, the location of a specific site will be named by its direction from Chaihe Town, the local community centre of tourism and a significant populated settlement in this remote part of China.

Two major rock groups were recognised in the field, i.e., volcanic and country rocks. At least five mappable geological boundaries are recognised between underlying country rocks and volcanic products. The distribution of the volcanic rocks (Fig 19) reflects a combination of the primary processes operating on pyroclasts and lava flows across the rugged horst and graben landscape at the time of emplacement and the erosion forces acting upon them since volcanism ceased.

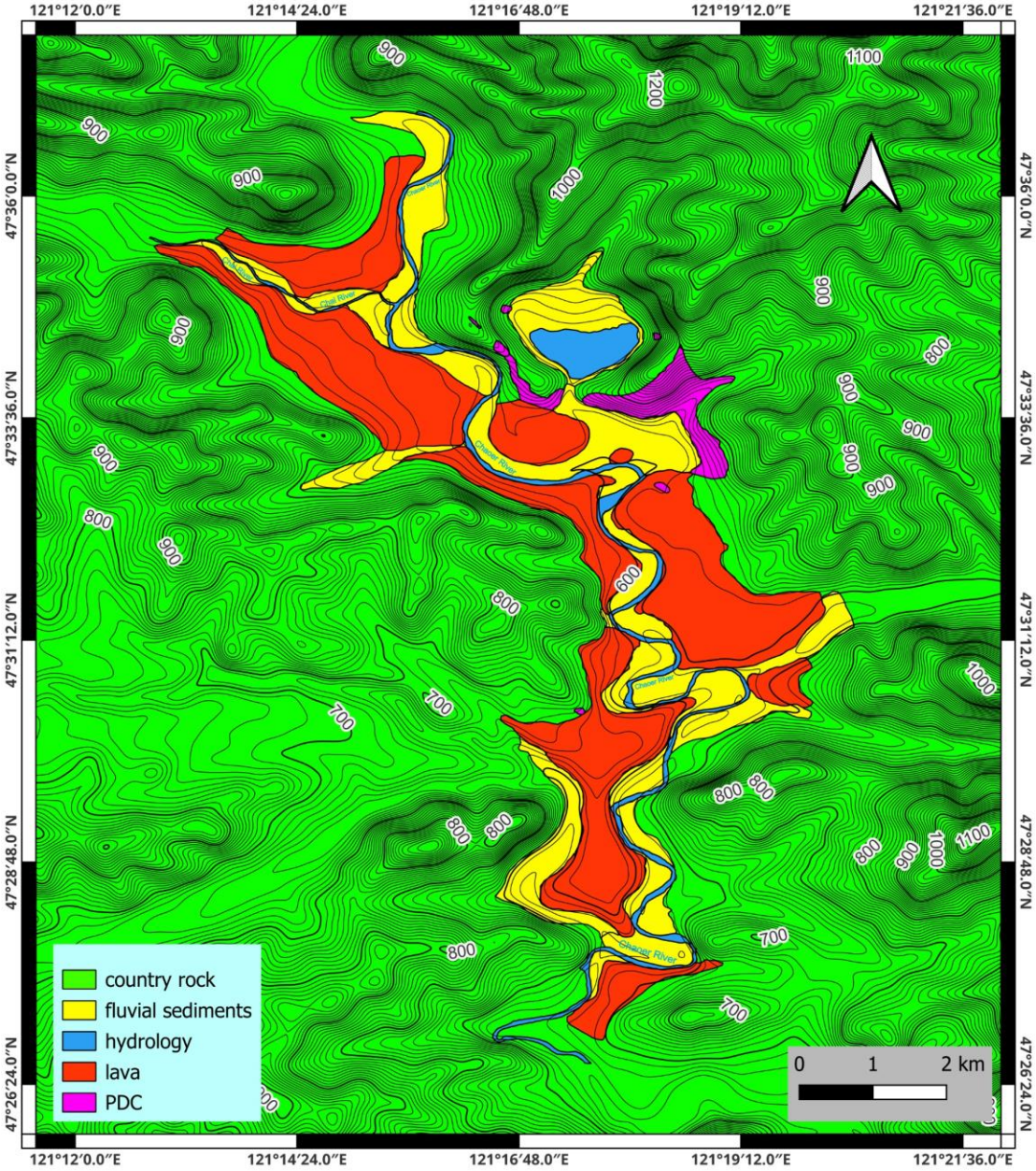

Figure 19: a geological map of Tongxin lake; please note that the coordinate system is WGS 84/Pseudo-Mercator grid system. The interval of the contour lines is 100 m in their elevations

Landscape and topography have evolved rapidly since the volcanism complicating the interpretation of the lateral distribution of the pyroclastic deposits and their correlatives in proximal to distal regions of Tongxin Volcano.

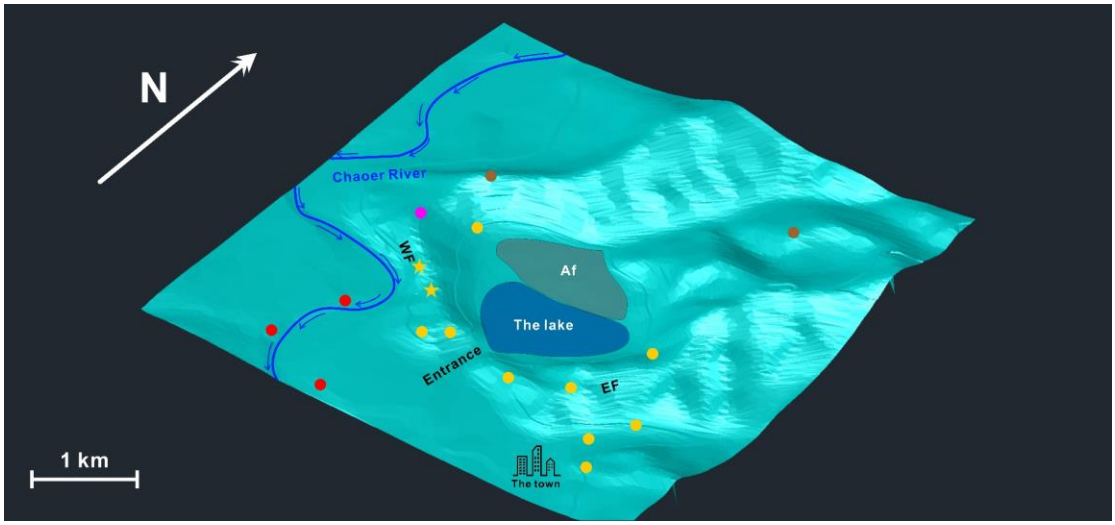

Figure 20: 3D model of the topography of Tongxin Lake. Topography data from https://srtm.csi.cgiar.org/srtmdata/, WF = west flank; EF = east flank; Af = alluvial fan.

Key locations of intact and *in situ* pyroclastic rocks are shown in Fig 19, which shows a view of the southeast region of Tongxin Lake. The pyroclastic materials include lava flows and spatter deposits (Fig 19), and in the southwest, lava flows are up to 8 m thick with well-preserved structures, including columnar jointing and flow features such as pipe vesicles. The distribution of the pyroclastic deposits follows the topography on the lake's western flank, and on the south flank, the top of the rim is totally covered by pyroclastic materials overlain by soil that is over a metre thick in places. Deposits on the eastern flank are not as well exposed as those described above.

In general, the geomorphology of the volcanic materials indicates the syn-eruptive landscape of rugged basement rocks forming a typical horst and graben architecture that is covered by pyroclastic deposits with laterally quickly changing thickness.

2) Volcanic stratigraphy

Detailed sedimentological/stratigraphic columns were measured and drawn for five key locations (Fig 18). Samples for analysis were selected from these columns. The aim of the laboratory techniques was to explore the vertical and lateral changes preserved in the pyroclastic deposits.

By combining facies, bedding features, sorting, and average grain size variations, volcanic lithofacies were identified and interpreted, including magma fragmentation,

pyroclastic transportation, and syn-eruptive deposition processes. The following bedding features observed include:

i. Massive (m) - no visible bedding, although weak imbrication may be observed.
ii. Stratified (s) - bedding visible; it can include linear features within the bedding but not sublayers.
iii. Parallel bedding (pb) - distinctive layering shows contacts between beds.
iv. Cross bedding (cb) - bedding cuts at an angle between the upper and lower bedding planes.
v. Dune structure (d) - beddings that display a bump-up shape similar to a dune, but these are bedding structures rather than real dunes.
vi. Normal grading (ng) - grain size varies from coarse-grained at the base and getting finer-grained up through the unit.
vii. Reversed grading (rg) - grain size gradually changes from fine debris at the base, becoming coarser-grained towards the top.

Thus, with those classifications of different facies based on the grain sizes and following bedding structures, the volcanic strata can be presented as every combination between each parameter shown in Table 5.

	Massive	Stratified	Parallel bedding	Cross bedding	Dune structure	Normal grading	Reverse grading
T	T-m	T-s	T-pb	T-cb	T-d	T-ng	T-rg
LT	LT-m	LT-s	LT-pb	LT-cb	LT-d	LT-ng	LT-rg
LS	LS-m	LS-s	LS-pb	LS-cb	LS-d	LS-ng	LS-rg
TB	TB-m	TB-s	TB-pb	TB-cb	TB-d	TB-ng	TB-rg
PB	PB-m	PB-s	PB-pb	PB-cb	PB-d	PB-ng	PB-rg

Table 5: Classifications of bedding structures and facies. T, LT, LS, TB and PB mean tuff, lapilli tuff, lapilli sand, tuff breccia and pebble breccia, respectively.

In Table 5, the abbreviations of each term represent typical geological features and deformations. Generally, they are:

- T means tuff, with the smallest grain size (2ϕ-4ϕ).
- LT means lapilli tuff, with grain size variations of 2ϕ to 1.5ϕ.
- LS means lapilli stone, with grain sizes ranging from 1.5ϕ to -1ϕ.
- TB means tuff breccia, with grain sizes spanning from -1ϕ to -2.5ϕ.

- PB means pebble breccia, with grain sizes of -2.5ϕ to -4ϕ, specifically including bombs with the largest grain sizes of more than -4.5ϕ but not counting in the normal distribution.

There are at least 30 locations where pyroclastic deposits are preserved around Tongxin Lake. Only five sites have intact successions that can be systematically analysed and sampled, but S1 and S2 are considered the primary sites.

At each site, field logs and descriptions of the exposed sequences provide an overview of the volcanic successions, including lithofacies, structures and visual grain size. The vertical and lateral changes of the facies were noted. Commonly, structures provide an indicator of how the pyroclastic materials behaved during the syn-eruptive or immediate post-eruptive stages. Grain size analyses were performed to reveal the syn-eruptive and depositional process patterns within these volcanic deposits that can change very rapidly. The normal distribution curves and cumulative curves revealing the percentage of grain size fractions indicate the sedimentary and depositional behaviours of the deposits. Thus, it is not possible to evaluate every single unit with specific grain sizes (some of the units are very thin, only a few millimetres thick). Based on this limitation, the MGS can previously provide average grain size variations, which have well-visible comparisons for the vertical evolutions on a set of deposits.

Site 1 (S1):

At S1, located on the west side (N 47° 34’ 219”, E 121° 16’ 749”) of the inside wall of Tongxin Lake (Fig 18, blue dot), approximately 13 m of the section is measured. The well-exposed, parallel-bedded, cliff-forming deposits are all primary pyroclastic beds without any signatures of reworking (Fig 21). At the base of the section, i.e., lower parts of unit 1 (Fig 22C), there are approximately 1.5m of massive pyroclastic deposits with no recognisable bedding features. This section is comprised of medium to large-size fractions (LS to TB with 2-45 mm in diameter) of fine to coarse lapilli in a fine-grained matrix. Volcanic bombs, ballistic projectiles up to 20 cm across, dominate the accidental lithic fragments in the non-bedded deposits. Olivine phenocrysts are occasionally visible in volcanic juvenile pyroclasts. These dark-coloured grains are juvenile volcanic clasts on the basis of their shape, vesicularity and mineral

components. The clasts are generally subangular to angular in shape. Angular to subangular xenoliths of light-pink granite is enclosed by a dark, glassy groundmass. Rare olivine xenocrysts with anhedral shapes occur as xenoliths. This part of S1 is distinguished as LS lithofacies. The upper part of unit 1 (Fig 22C), about 60-75 cm in thickness, consists of parallel bedded coarse-grained lapilli with occasional bombs and intercalated within thin lapilli beds. The thickness of each lapilli bed is approximately 3-5 cm. This is overlain by the lower part of unit 2, 35-40 cm thick and dominates the middle part of the section. The unit contains bombs, commonly 7-8 cm in diameter (Fig 21A & B). Most of them are accidental lithics rather than juvenile materials. The shapes of the clasts, including accidental lithics, are generally angular to sub-angular. Mafic materials, including individual olivine crystals, are visible to the naked eye. The upper part of unit 1 is assigned as LS lithofacies, and the lower part of unit 2 is assigned as PB lithofacies.

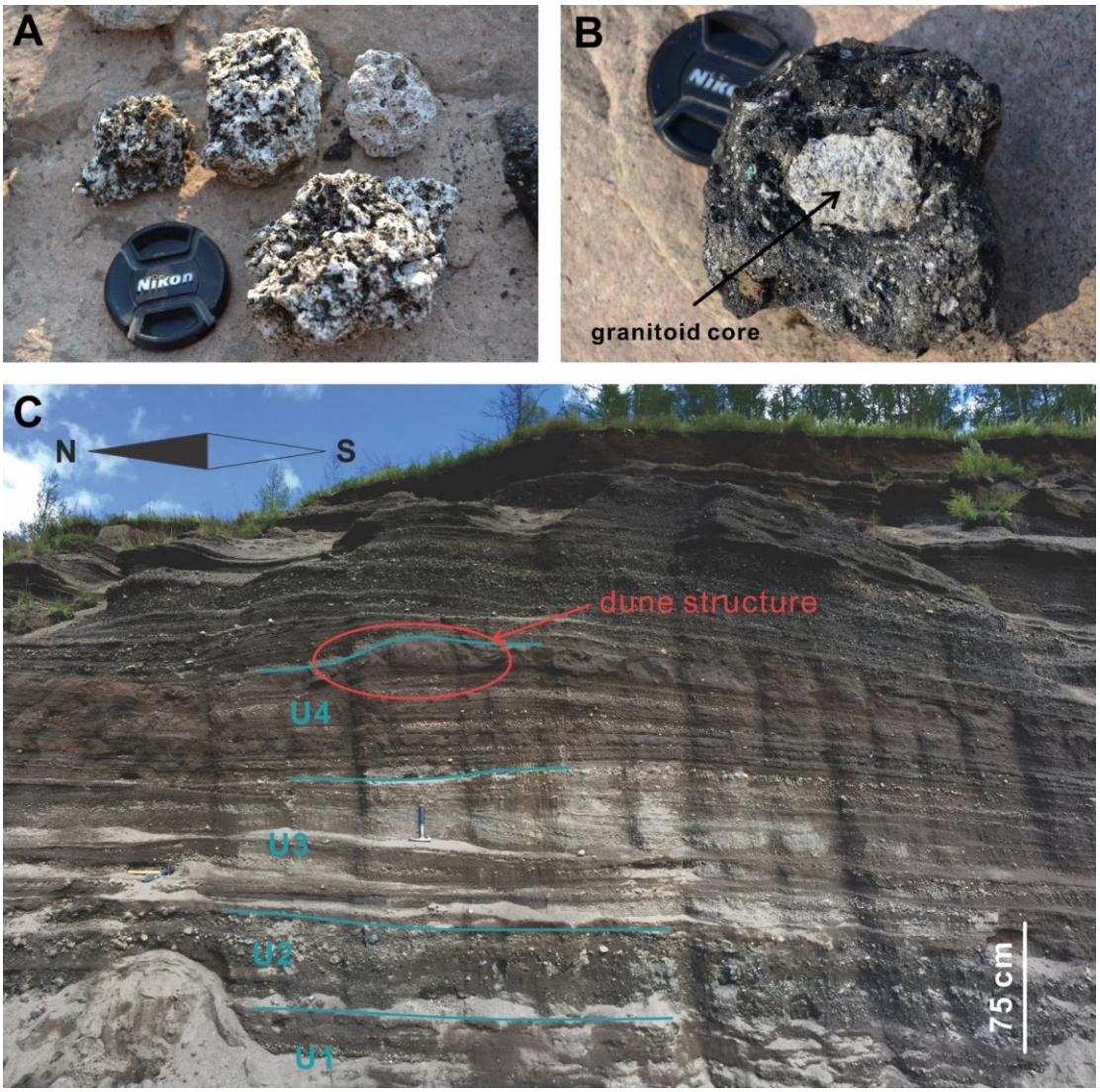

Figure 21: A general observation on S1, photo A depicts the thermally altered granitoid country rocks; photo B shows a cauliflower-shaped bomb with a core of granitoid country rock that thermally popped within the capturing melt as recorded in micro-scale mingling textures along with the contact between the country rock and the encapturing coherent magmatic rim. Photo C is the dune structure within the S1 deposit.

The upper part of unit 2, with approximately 3-4 m in thickness (Fig 22C), consists of alternating parallel bedded, coarse and fine laminae. Fine to coarse lapilli-sized accidental lithic materials are dispersed in the dark juvenile groundmass, with individual olivine crystals observed in the groundmass. LT, T and LS lithofacies are identified. There is no evidence of reworking. Clast shapes are angular to sub-angular. The thickness of each bed (no more than 15 cm) varies greatly in the lower part of S1; thus, this section is more clearly bedded than the remainder of S1. The upper part of the unit is partially covered by sets of taluses, which obscures the bedding details. Unit 2 can be placed into PB lithofacies.

Unit 4 (Fig 21C, red ellipse) preserves distinctive cross-bedding and dune structures similar to those widely documented in volcanic deposits from other locations around the world (Moufti & Németh, 2016; Németh, 2012; Smith, 1986; Sohn & Sohn, 2019b; Sohn & Park, 2005; White, 1992). The section preserving dune structures is about 1.5 m in thickness. The dune structure has a wavelength of 55-65 cm and an amplitude of 10-20 cm in the thickest part (Fig 22B). The grain sizes of the clasts within the "dune" are ash to fine lapilli.

Unit 7 to unit 10 are massive, non-bedded deposits about 1.3 m thick. It consists of sub-angular to angular clasts, about 1-3 cm in diameter. Juvenile clasts dominate with secondary amounts of accidental lithic materials present. There is no evidence of ballistic projectiles. Thus, this section is interpreted as LT and LS lithofacies. The overlying section, 20-25 cm in thickness, consists of well-developed parallel bedded fine and coarse sublayers with no evidence of cross-bedding or dune. Each bed is between 3-5 cm thick. Grain sizes are generally small to medium in diameter (0.5 to 2 cm in general). Juvenile clasts dominate with lithic materials present in secondary amounts. This section belongs to the LT to TB lithofacies. Near the top of S1 (upper part of unit 10 and unit 11), the massive unit immediately beneath the topsoil has a very thin, fine-grained drape separating unit 11 into two symmetric sub-layers. Unit 11 is about 40-55 cm thick. Each of the sub-layers is approximately 25 cm thick; the clasts comprising the units are 2-3 cm in diameter. The fine-grained drape is 2 to 4 cm thick and consists of fine to coarse sands. This unit belongs to the PB lithofacies (Fig 22A). Some 20-25 cm of topsoil overlies the section. The contact between the soils and the underlying volcanic deposits is sharp, with no significant erosion observed.

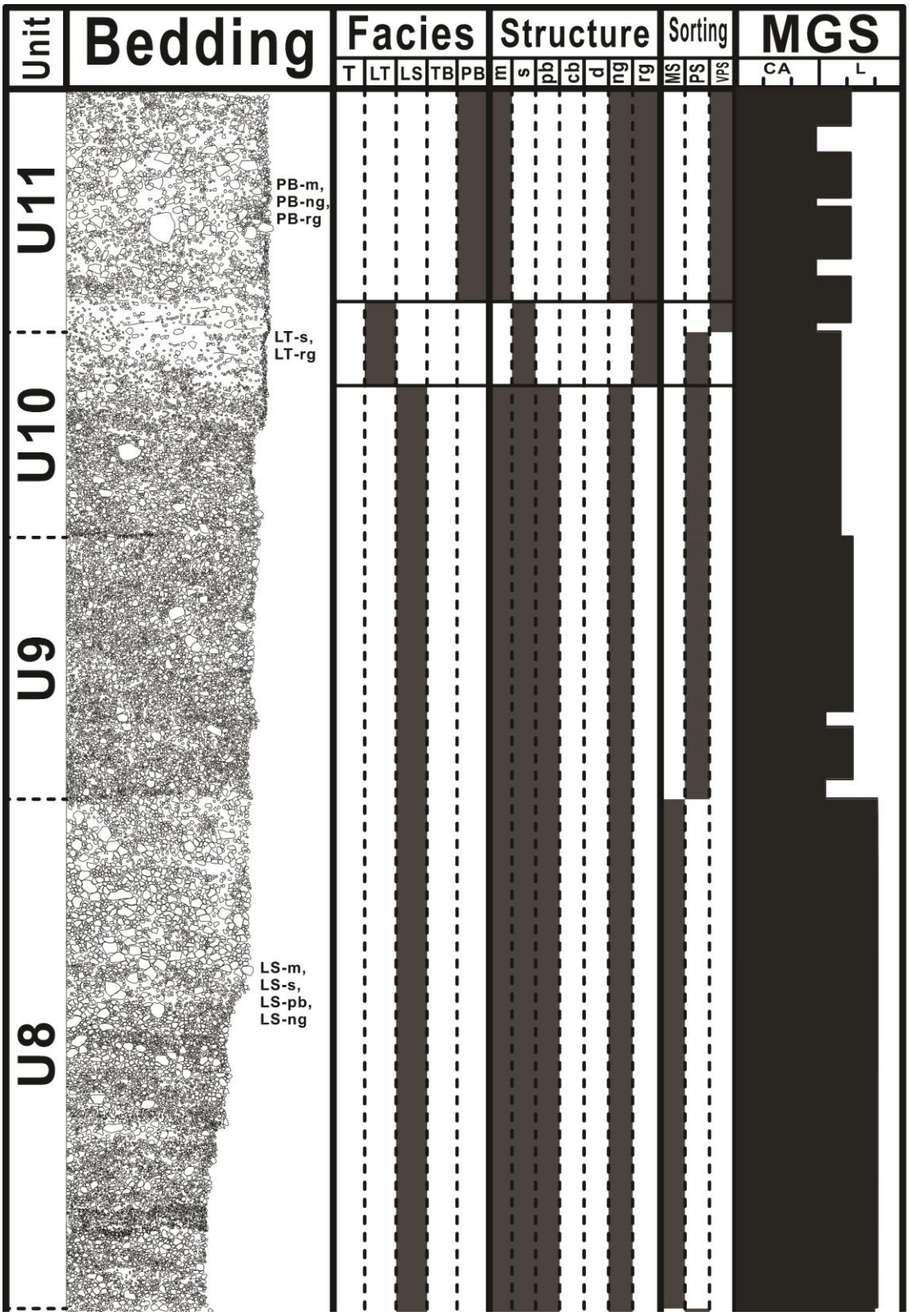

Figure 22A: Stratigraphy column of S1 deposits.

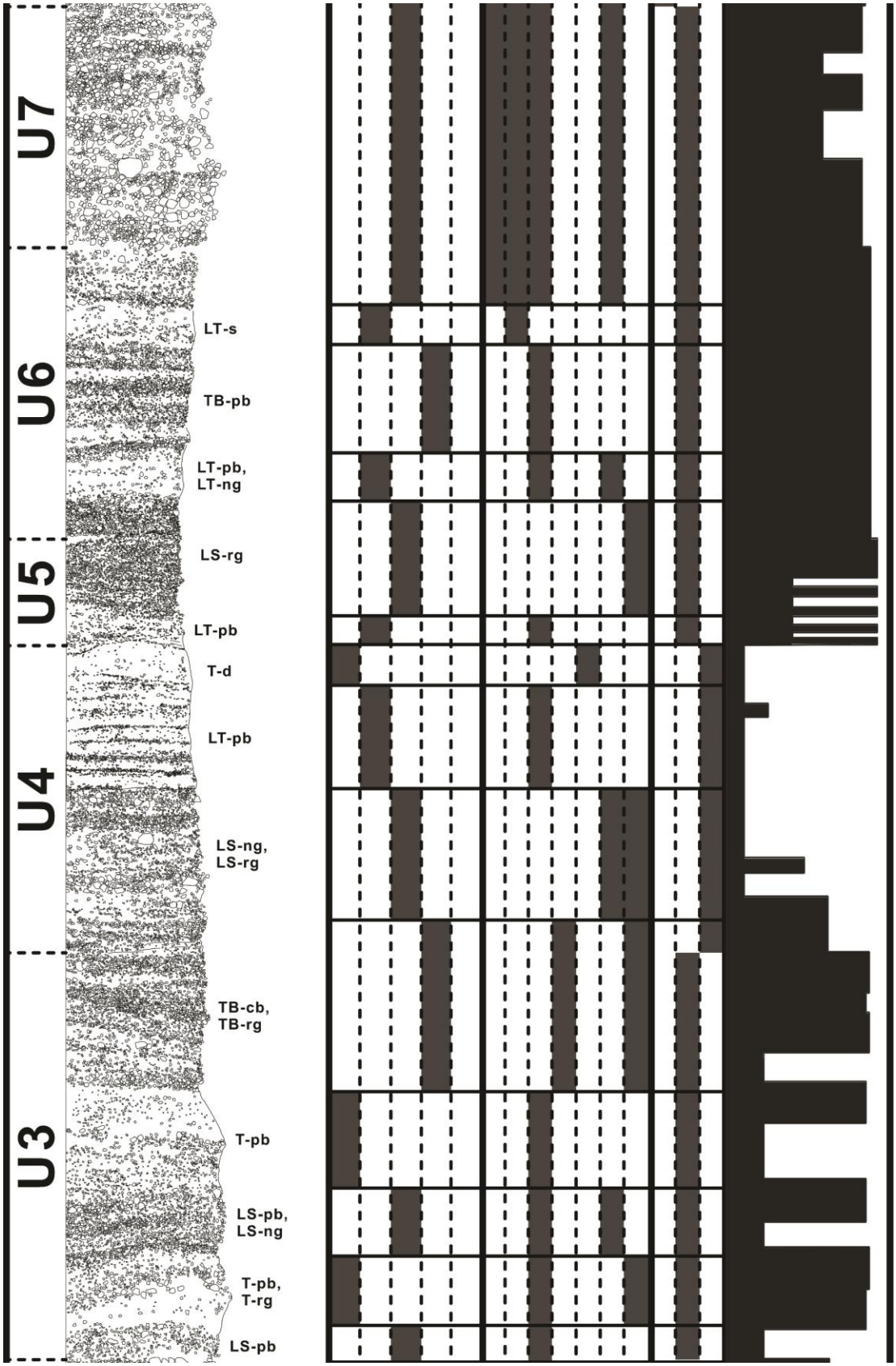
U7
U6
U5
U4
U3
LT-s
TB-pb
LT-pb,
LT-ng
LS-rg
LT-pb
T-d
LT-pb
LS-ng,
LS-rg
TB-cb,
TB-rg
T-pb
LS-pb,
LS-ng
T-pb,
T-rg
LS-pb

Figure 22B

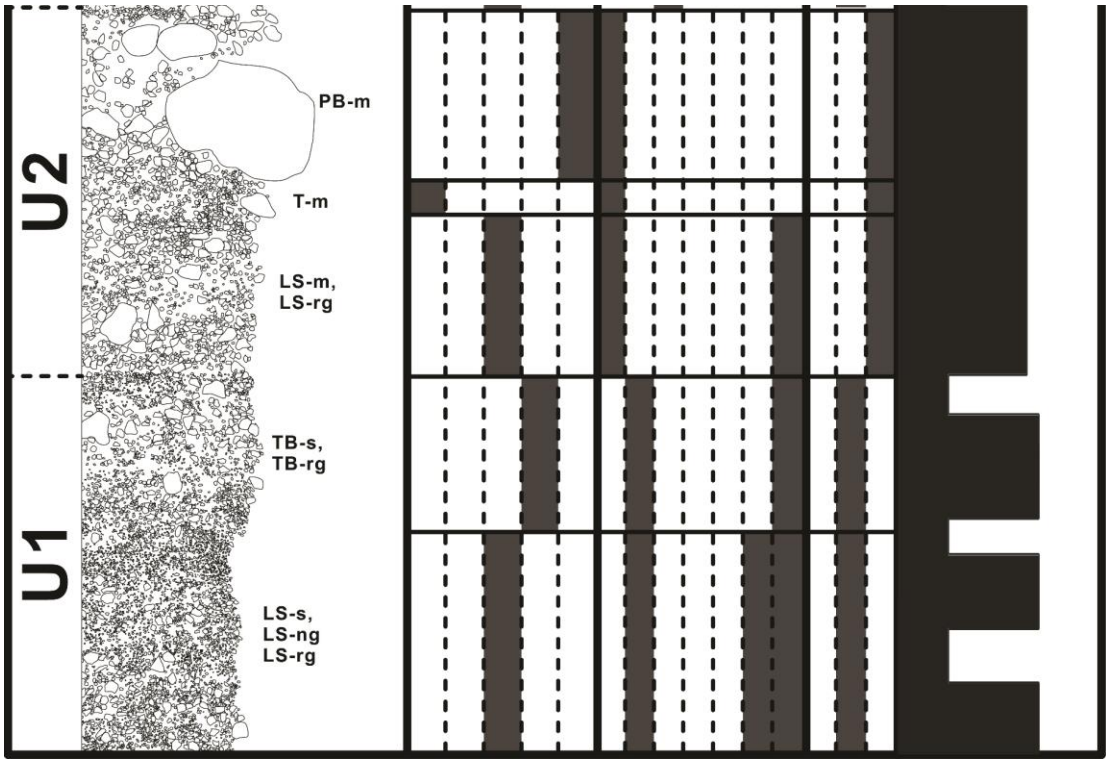

Figure 22C

Site 2 (S2):

Site 2 is located to the west of Tongxin Lake (N 47° 34’ 376”, E 121° 16’ 626”) and about 340 m from S1 on the north (Fig 18, green dot). S2 is located on the outer rim of the lake; a road runs between the two locations. S2 is approximately 30 m thick, making it the thickest continuously exposed outcrop with well-preserved pyroclastic units. The distinctive feature of S2, compared to S1, is the coarse-grained volcanic ash and clasts that dominate the deposits. (Fig 23A & C).

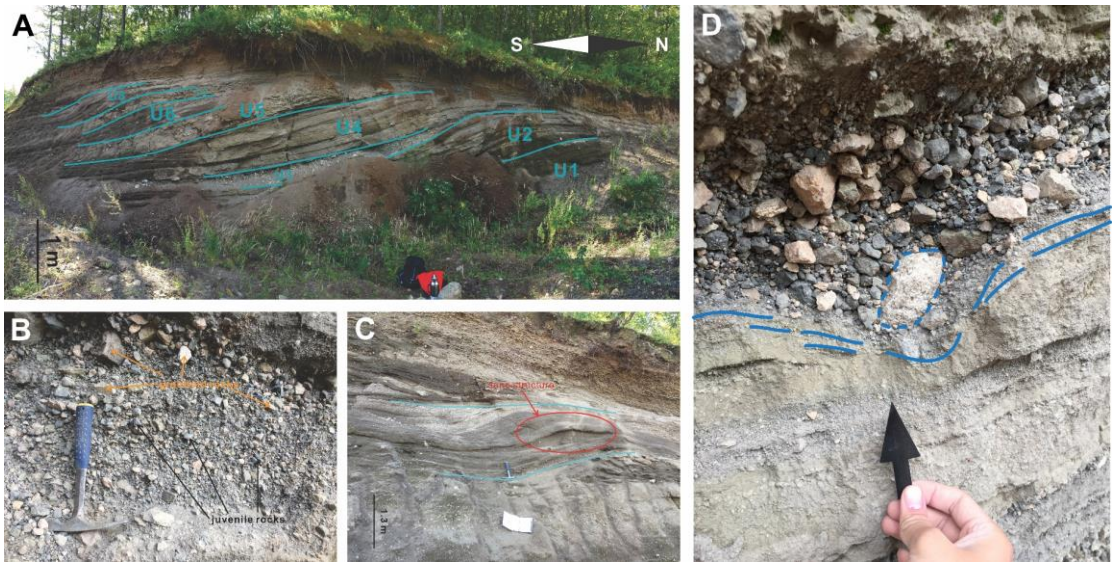

Figure 23: Photo A shows the lee side of site 2 (S2), deformed pyroclastic beddings (transportation suspected from right side to left side). Photo B depicts the beddings with clastic support property. Photo C reveals the dune structures with very fine grain sizes (transportation direction from right to left). Photo D is the sagging structure formed by ballistic projectiles (suspected impacting direction from top left to bottom right).

The S2 deposits are generally indurated, and the outcrop is steep, nearly 40 degrees. Thus, the overlying middle and upper sections of S2 are poorly exposed and difficult to access, so they had to be described from a distance and by collections of fallen hand samples which included volcanic clasts of very large grain size (coarse to very coarse lapilli). S2 successions are comprised of parallel bedded pyroclastic units consisting of intercalated coarse- and fine-grained beds.

Unit 1 and unit 2 are about 1.2 m thick and consist of fine-grained volcanic materials-generally, with ash-sized pyroclasts dominating the whole section. There are large numbers of accidental lithic clasts with no notable grading trend. Some fine-grained beds reach 15-20 cm in thickness. The intercalated coarse-grained beds are usually no more than 3 -5 cm thick and preserve angular accidental lithic clasts and subangular juvenile pyroclasts. In places, cross-bedding is well-developed. The thickness of the cross-bedded units is about 65 cm, with a foreset dip angle of 35-40 degrees. This section has been assigned to the LS and LT lithofacies (Fig 24E).

The thickness of unit 3 is estimated to be 35-45 cm. The deposits are dominated by the extremely high (60-75 vol% by visual estimate) very angular accidental lithic clasts up to 4 cm in diameter. Juvenile clasts are fewer and contain large numbers of

xenoliths derived from the surrounding country rock (olivine and pyroxene xenocrysts and mantle xenoliths) (Fig 23B). This section is massive, with no bedding observed and includes TB-m and PB-m facies based on the largest clastic size. At the top of the section, ballistic projectiles consisting of accidental lithic clasts or volcanic lithics from older volcanic units occur within fine to coarse-grained groundmass intercalated within the beddings. This section belongs to TB to PB lithofacies.

Unit 4 to unit 6 are dominated by fine-grained volcanic ash. In unit 4, there are at least five thin (up to 4 cm thick) interbeddings composed of coarse and fine sub-layers. These coarse units have the same components as the underlying coarse section. Coarse clast shapes range from very angular to subangular. The fine ash beds, up to 75cm thick, are parallel and cross-bedded and contain accidental lithic materials (75% by visual estimate). The grain size is under the millimetre scale (fine ash). The cross-bedding foreset is about 25 to 30 cm with a dip angle of 30-35 degrees toward the south. Elastic deformations, such as sag structures, are well preserved with the ballistic projectiles sitting in the sag as impact bodies (Fig 23D). One typical sag is approximately 15 cm long and 5 cm deep. Judging from the field, the impact direction forming the sagging structure is from the left to the right sides of the outcrop, which translates to a source location somewhere north of the outcrop. Unit 4 to unit 6 preserve interbedded coarse- and fine-grained beds and has been assigned as T, LT, LS and PB lithofacies.

Unit 7, composed of dune structures and cross-bedding, are both coarse and fine-grained units formed as interbedded units. Following the descriptions of the features mentioned above, the very fine-grained beds total about 50-65 cm in thickness, with intercalated thin coarse-sized sublayers of 4-7 cm in their thickness. On the lateral part of the dune structure, cross-bedding is well-developed. Also, the foreset part of the cross-bedding is pointing toward the downhill side, which is the south direction. The upper part of this unit, preserving the dune structure, is a generally coarse-grained lapilli deposit intercalated with about 2-4 cm thick fine-sized sandy sublayers. The average grain size of lapilli ranges from 2 to 4 cm in diameter, and cross-bedding is well-preserved. This unit is interpreted as T lithofacies (Fig 24D).

Unit 8 has one distinctive feature, a horizontal S-shaped deformation, and the dune structure is intercalating within it (Fig 23C). The fine-grained units consist of a fine-grained groundmass with coarse-grained clasts widely distributed within. The thickness is typically 75-80 cm. The S-shaped deformation is intercalated into the middle parts of the unit as a ductile and elastic property due to the non-cracking structures of the deformation. There are no significant features (dune and cross-bedding) on the lateral part. This section can be classified as LT and LS lithofacies (Fig 24C). The overlying 17-18 m thick succession consists of interbedded sand and lapilli sublayers. Large ballistic projectiles are dispersed throughout the deposits. These are large accidental lithic clasts and juvenile clasts in cauliflower shapes, with significant numbers of xenoliths, including peridotite lherzolite nodules up to 30 cm across. The average clastic size is 10-15 cm in diameter. The componentry is generally dominated by accidental lithic pyroclasts, with low numbers of juvenile pyroclasts (approximately 15-25% of total volume). There is an overall reverse grading trend in each bed. Cross-bedding on the onset partition of the S-shaped deformation is well-developed and can be traced over tens of metres. This section belongs to LT, LS and TB lithofacies (Fig 24C, unit 8).

The rest units of S2 are, in general, indurated with limited capacities of getting assessed into them. Thus, all possible descriptions are shown in the S2 stratigraphic column (Fig 24).

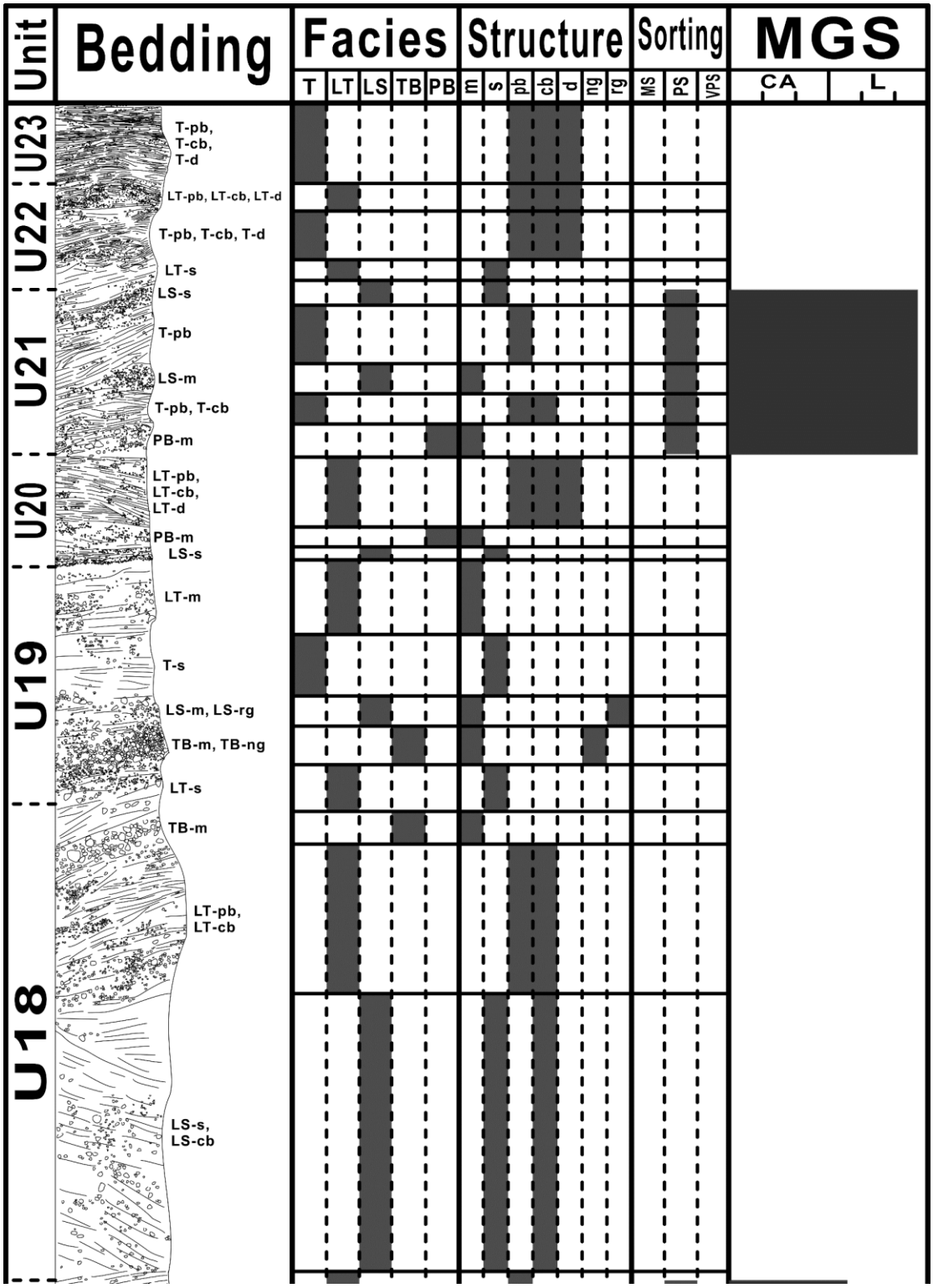

Figure 24A: The stratigraphy column of S2 deposits.

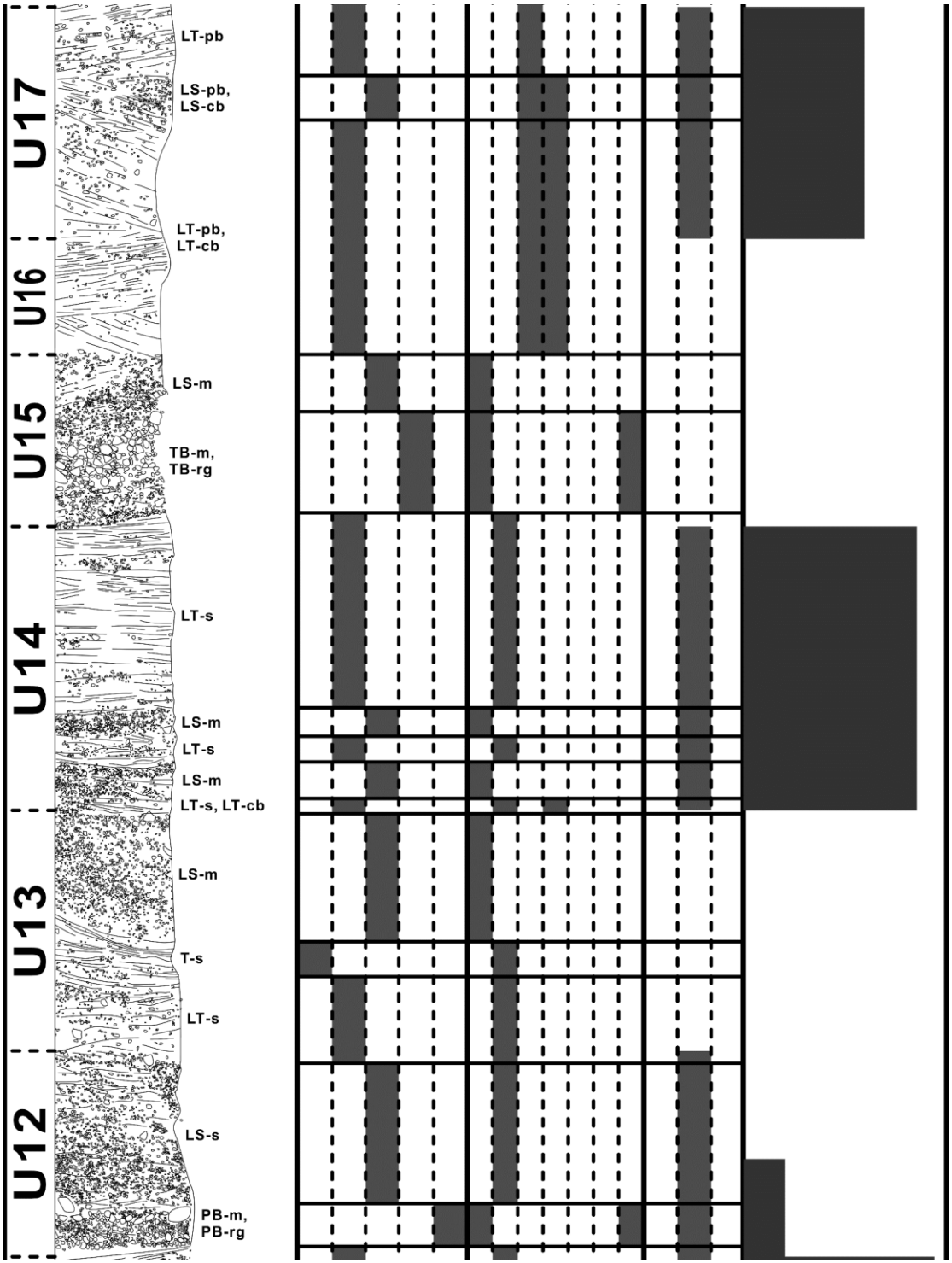
U17
U16
U15
U14
U13
U12
LT-pb
LS-pb,
LS-cb
LT-pb,
LT-cb
LS-m
TB-m,
TB-rg
LT-s
LS-m
LT-s
LS-m
LT-s, LT-cb
LS-m
T-s
LT-s
LS-s
PB-m,
PB-rg

Figure 24B

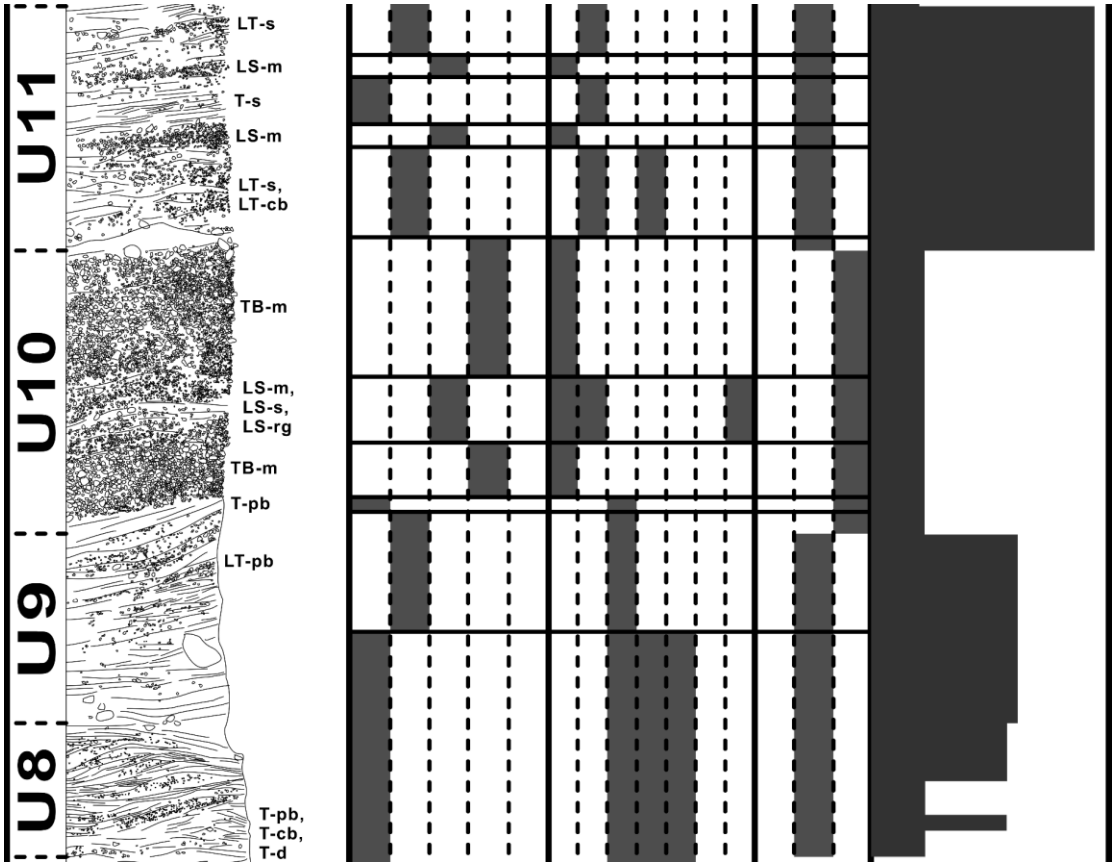
U11
U10
U9
U8
LT-s
LS-m
T-s
LS-m
LT-s,
LT-cb
TB-m
LS-m,
LS-s,
LS-rg
TB-m
T-pb
LT-pb
T-pb,
T-cb,
T-d

Figure 24C

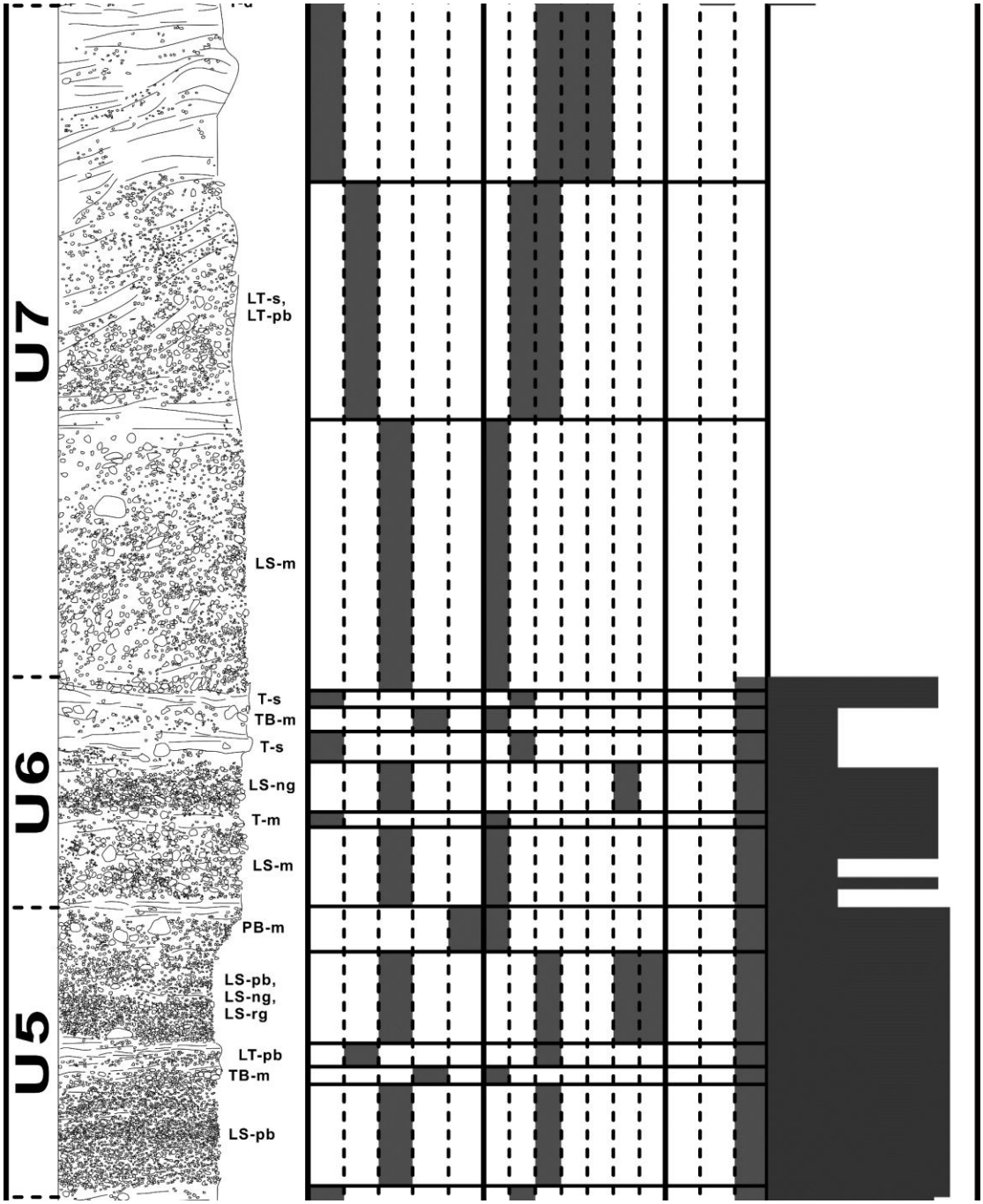
U7
U6
U5
LT-s,
LT-pb
LS-m
T-s
TB-m
T-s
LS-ng
T-m
LS-m
PB-m
LS-pb,
LS-ng,
LS-rg
LT-pb
TB-m
LS-pb

Figure 24D

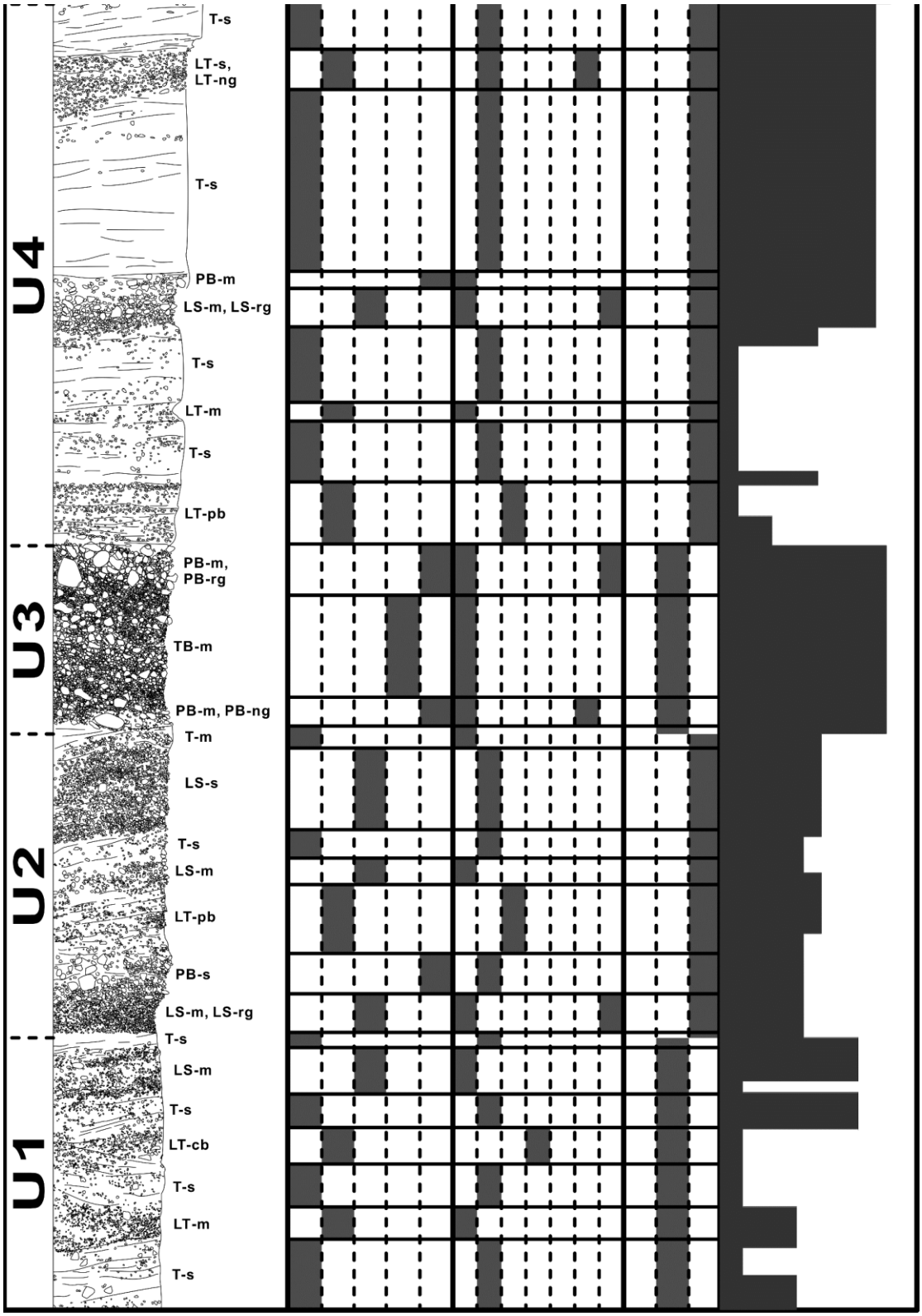

Figure 24E

Tongxin spatters deposit:

To the NNE of S1 and S2 (Fig 18, pink dot), the GPS location is N 47° 34’ 38.9”, E 121° 16’ 19.5”. Lava spatter sits directly on pre-volcanic granitoid bedrock. This is

interpreted as an indicator of an initially dry, mild explosive eruption phase, such as lava fountaining. The spatter unit has an undulating bed thickness and overall lentoid shape (Fig 25A). At its thickest, the spatter is about 150 cm.

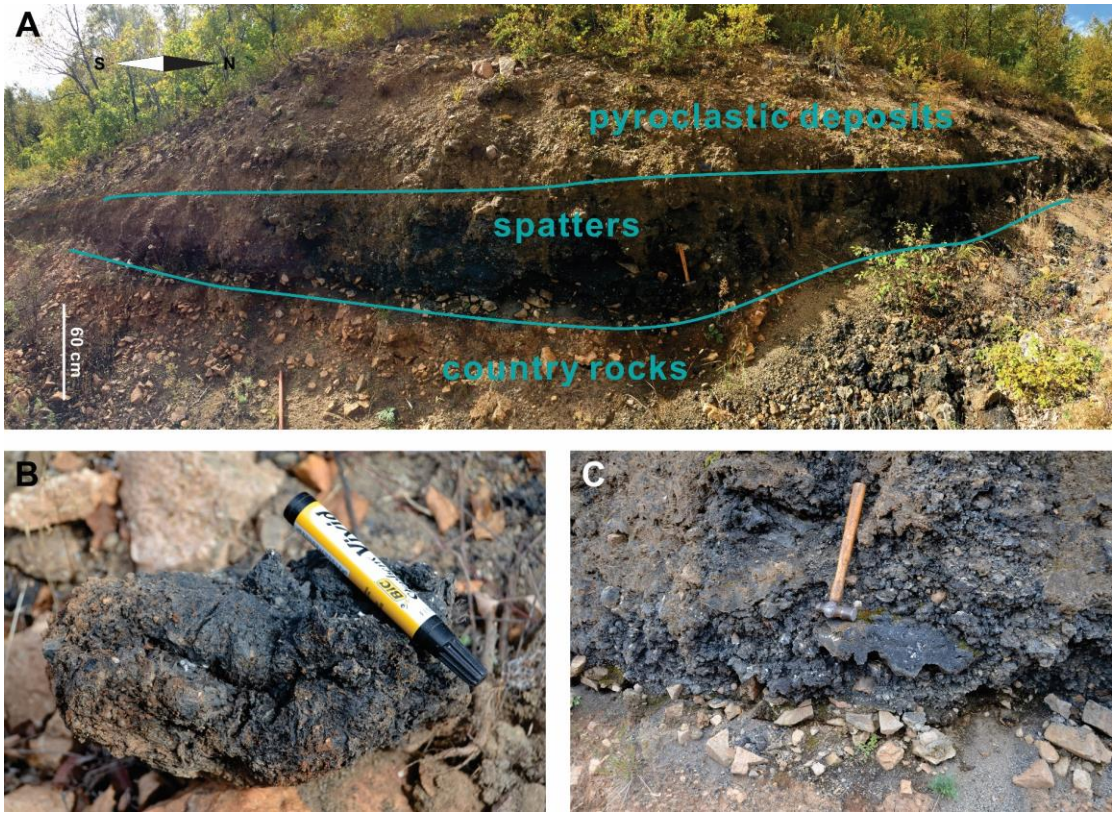

Figure 25: Spatter deposits of Tongxin Lake. Photo A shows the contacts of the spatters with the underlying country rock and overlying pyroclastic materials. Photo B shows the detail of one piece of spatter. Photo C depicts an overview of the spatters.

Above the spatter deposit, distinctive pyroclastic deposits with approximately 75 cm in thickness are preserved. The largest clasts, 1-4 cm in diameter, occur at the base of the deposit (Fig 26). The informal field names for the units c3, f2, and uf2, are shown in the stratigraphic column (Fig 27).

Figure 26: Details of the overlying pyroclastic deposits on spatters. Photo A shows the successions. Photo B depicts some details of the deposits. Note that the details of photo B are from the lp section of photo A. In photo A, the coarse layers are fairly wet, fine-depleted and rich in accidental lithic fragments. The spatter deposits are covered by some coarse scoriaceous beds. Subsequently, the overlying deposits quickly turned to be accidental lithic-rich fine lapilli and coarse ash beds, prior to maximum fragmentation, produced fine-grained accretionary lapilli rich massive, but the unsorted bed (f1).

Large ballistic projectiles can be found among the pyroclastic deposits. Clast shapes are commonly subrounded to subangular. The bedding is weakly developed, although some stratification is observed in the upper part of the section. The total exposed thickness is approximately 75 cm. In the lower part of this set of deposits, grain size ranges from fine lapilli to medium lapilli (c3, f2 and uf2, Fig 26A). In the lp section, the grain size changes abruptly to coarse lapilli, with the overlying c2 section consisting of medium lapilli. The f1 part contains coarse ash. The top section, c1, preserves coarse lapilli. Bedding boundaries are ambiguous to observe, slightly only marking them by significant variations of grain sizes and colour gradients. This section is assigned to TB, LS, and LT lithofacies. The middle section (c2 to f1) is more massive and fine-grained than the underlying unit; the grain sizes range from 0.5 to 3 cm. Thus, the lithofacies still belong to TB, LS, and LT. It contains more accidental lithic clasts than in the bottom section. The upper part of the deposits (c1) displays identical features to the middle part, except for the presence of clastic breccia with clasts 1-3 cm in diameter. This non-bedded part belongs to LS and LT lithofacies (Fig 27). In comparison to S1 and S2, the pyroclastic deposits in this location have no distinctive layering and boundaries for each unit are based on the type of volcanic materials.

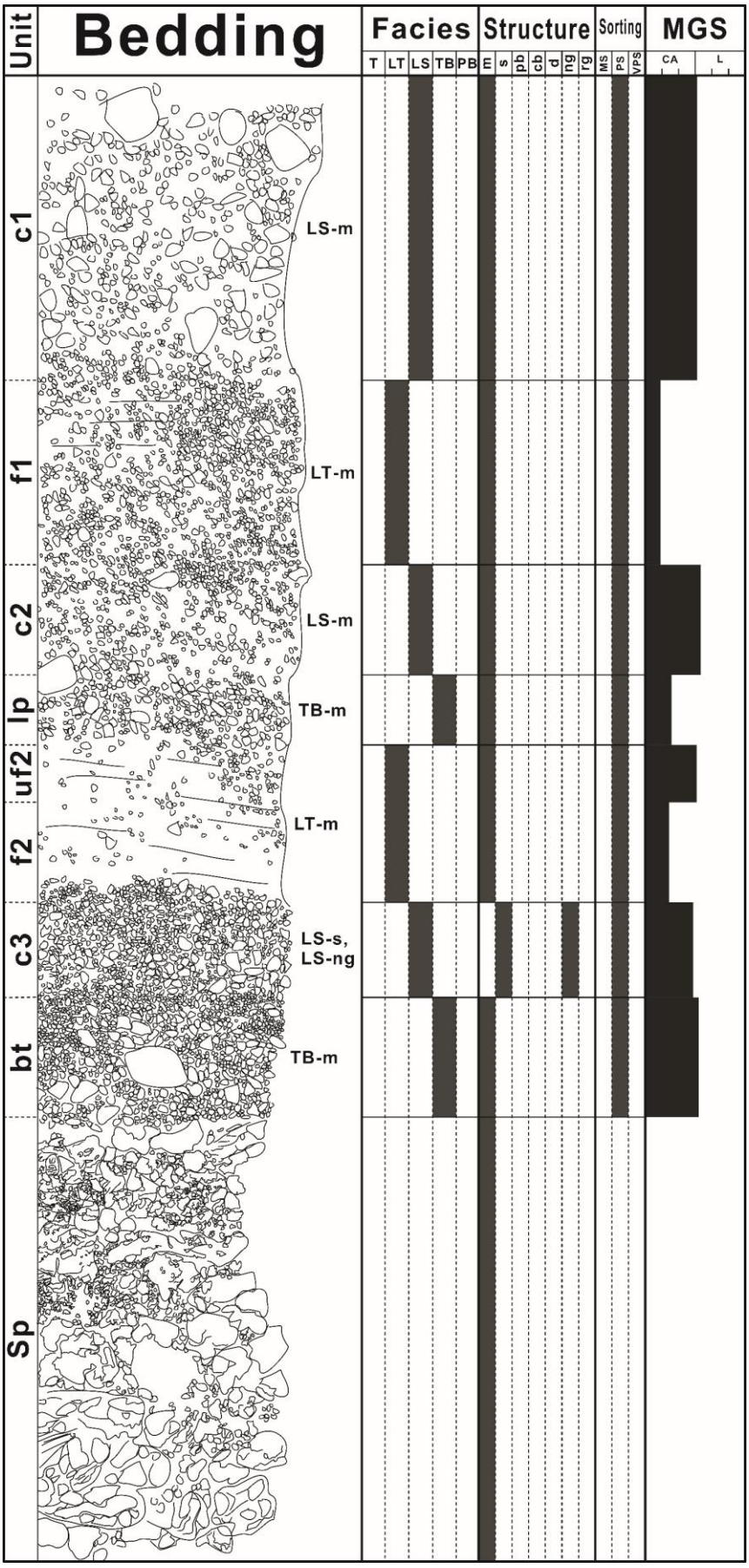

Figure 27: Stratigraphy column of the spatter deposits of Tongxin Lake.

Quarry on the southeast of the town (SE quarry, N 47° 32’ 58.14”, E 121° 18’ 59.04”):

This location is 1.2 km from Chaihe Town and 3.2 km southeast of the lake (Fig 18, red dot). The pyroclastic deposits lie on the original topography and dip approximately 45 degrees to the southwest (Fig 28A). The deposits consist of interbedded fine and coarse lapilli (1.5-4 cm in diameter) by eye-witnessed observations.

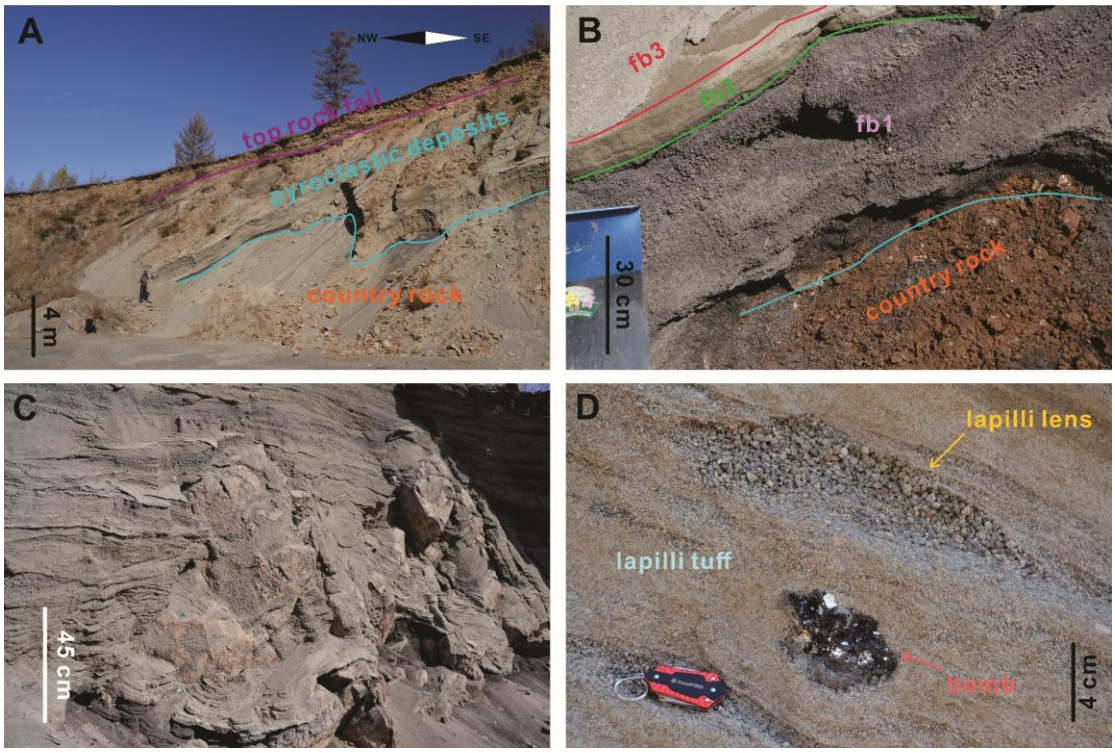

Figure 28: The quarry in the southeast direction of the town. Photo A shows the general view of the deposits. Photo B depicts the details of the bottom of the deposits contacting with the country rocks. Photo C reveals the structures of interactions between pyroclastic materials and bedrock. Photo D is a bomb intercalating within the deposits. There is no juvenile-rich basal unit, just a thin layer, which preserves less information than any other layers in this site. This location is probably far from the source, and those deposits were likely localised around the crater. The succession here represents the medial facies of the main eruption phase, dominated by PDC and drifted away eruption column from ash and lapilli fallout.

The total thickness of the exposed section is approximately 7 m. On the top of the deposits, rock debris overlies the topographic surface and shares the same dip angle. The blue line marks the contact between pyroclastic deposits and the underlying granitoid country rock (Fig 28A & B). This site preserves a set of deposits that may indicate the very first eruption phase. The dark-coloured deposits are about 15-20 cm thick and marked as fb1 (fabric 1) (Fig 29B). Grain size ranges from 0.5 to 2 cm. The fb1 section is massive and is assigned to LT and LS lithofacies. The overlying, slightly

indurated fb2 unit is about 3-5 cm thick with an average grain size of approximately 2 mm (Fig 29B). The facies assigned is T. From the base of fb3 to the top of the deposits, the sequence consists of interbedded coarse and fine units (Fig 29A). The basal pyroclastic deposits sitting on the country rocks show sedimentary features consistent with the pyroclastic deposits once flowing like liquid (Fig 28C). Within them, occasional ballistic juvenile bombs can be found (Fig 28D). Each unit (fb) can be assigned as LT for the relatively fine units and LS for the relatively coarse ones.

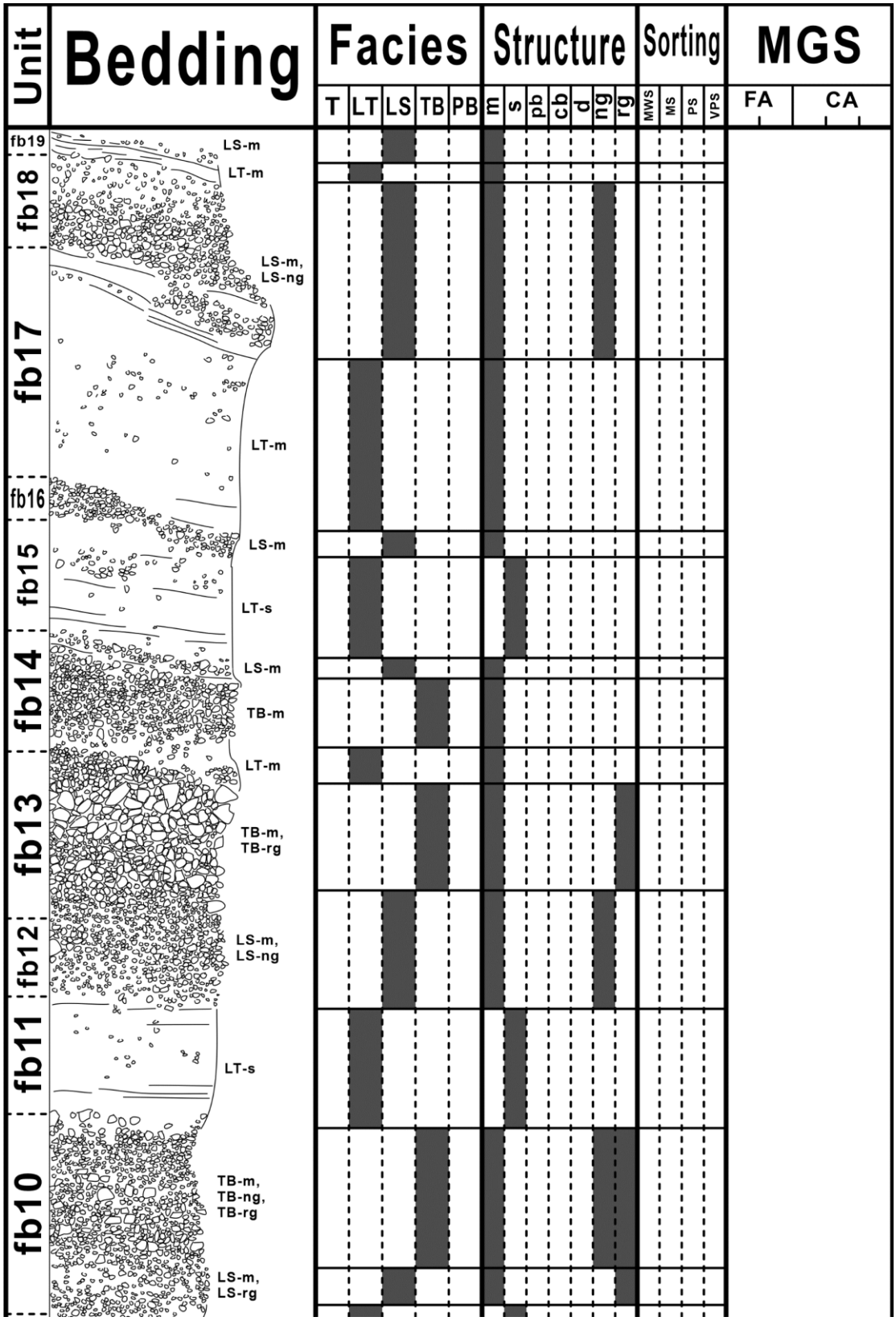

Figure 29A: The stratigraphy column of the quarry in the southeast direction of the town.

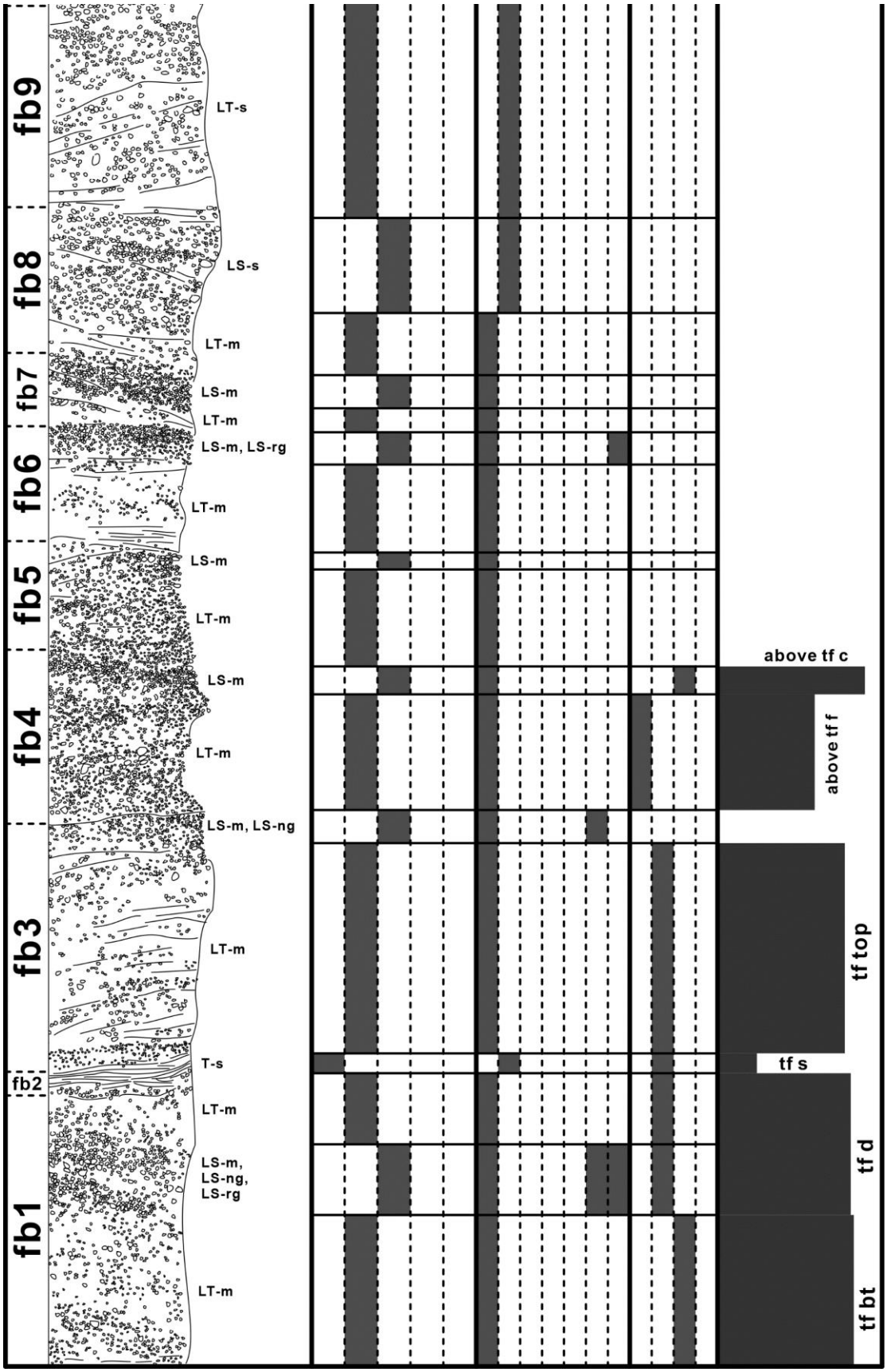
fb9
fb8
fb7
fb6
fb5
fb4
fb3
fb2
fb1
LT-s
LS-s
LT-m
LS-m
LT-m
LS-m, LS-rg
LT-m
LS-m
LT-m
LS-m
LT-m
LS-m, LS-ng
LT-m
T-s
LT-m
LS-m,
LS-ng,
LS-rg
LT-m
above tf c
above tf f
tf top
tf s
tf d
tf bt

Figure 29B

Far south of Tongxin Lake (N 47° 30’ 24.5”, E 121° 17’ 25.9”):

This site is located about 12 km to the south of Tongxin Lake (Fig 18, purple circle). Bedding dips at about 30 degrees toward the west following the slope of the country-rock basement, indicating the entire pyroclastic succession is a topography mantle. The deposits are most likely primary pyroclastic as there is no sedimentological evidence of syn-eruptive reworking. The bedding of the deposit within the outcrop is well preserved. At the base, the deposits are fine-grained (Fig 30A & B), consisting of 15-20 cm of ash. There is a weak-reversed grading trend. Compositions indicate that different pyroclastic successions represent the initial stages of the eruptive sequence at TX Lake due to accidental clasts in dominant quantities. Juvenile clasts are angular and subangular in shape with low to moderate vesicularity.

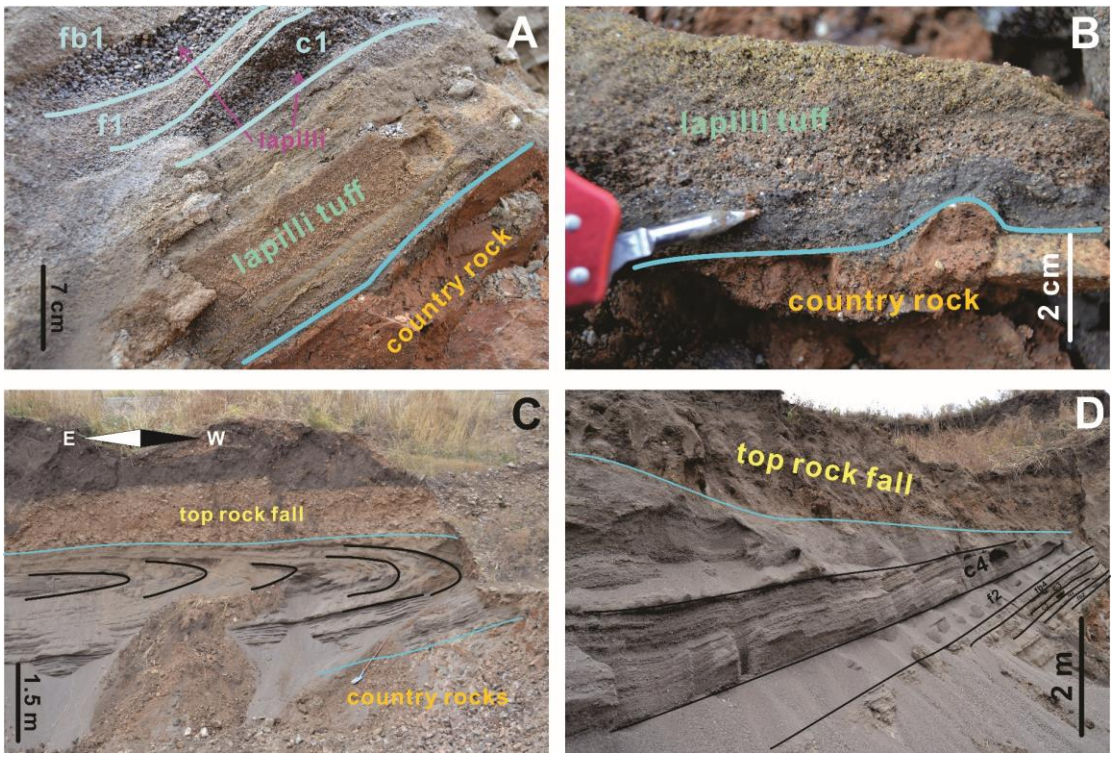

Figure 30: The main features of the pyroclastic deposits on the outcrop far south of Tongxin Lake. Photos A and B show the contact between pyroclastic deposits and country rocks. Photo C depicts the distinctive horizontal folding. The rockfall seems to wrap the topsoil and fold the underlying pyroclastic succession. Photo D indicates that somehow, the pyroclast accumulated in the steep slope, and the open cliff faces of granitoid rocks produced a talus over the tephra-covered lower slopes that gradually covered the pyroclastic deposits that are likely to slide and wrap the underlying layers, just like a carpet.

The pyroclastic deposits in the overlying section consist of fine lapilli, averaging 1-2 cm in diameter. The total thickness is about half a meter. This section preserves three distinctive sublayers (c2, c3 and fb4 belonging to LS, LT and TB facies). Within them, the grading trend is generally reversed. The unit is approximately 1.3 m bedded with coarse ashes and interbedded with fine-sized lapilli. Compositions are identical to the underlying ones. The shape of the clasts ranges between angular and sub-angular. This section is dominated by pyroclastics with many accidental lithics and fine lapilli to coarse lapilli in succession; the facies are LS and LT (Fig 31), with occasional TB facies between them. Both normal and reversed grading are observed; each unit has a sharp contact with the juxtaposing one. The most distinctive trend is the grading which changes up section, i.e., fine lapilli on the bottom, coarse lapilli in the intermediate sections, and again, fine lapilli on the top. The deposits are laterally uniform over the 5 m width of exposure. Besides, this is the first and only observation of a horizontal fold (compared with vertical ones) (Fig 30C), which preserves intact the structure in the volcanic deposits. The total thickness of the fold is approximately 1 m. The direction of the pinch-out partition is heading to the west. The axis is horizontal with the orientation of W-E. The hinge line can only be seen on the outcrop surface; thus, no signals of the true orientation. The angle between the two limbs is nearly 25-30 degrees. The deposits on both limbs are parallel-bedded with coarse ashes and interbedded with fine-sized lapilli.

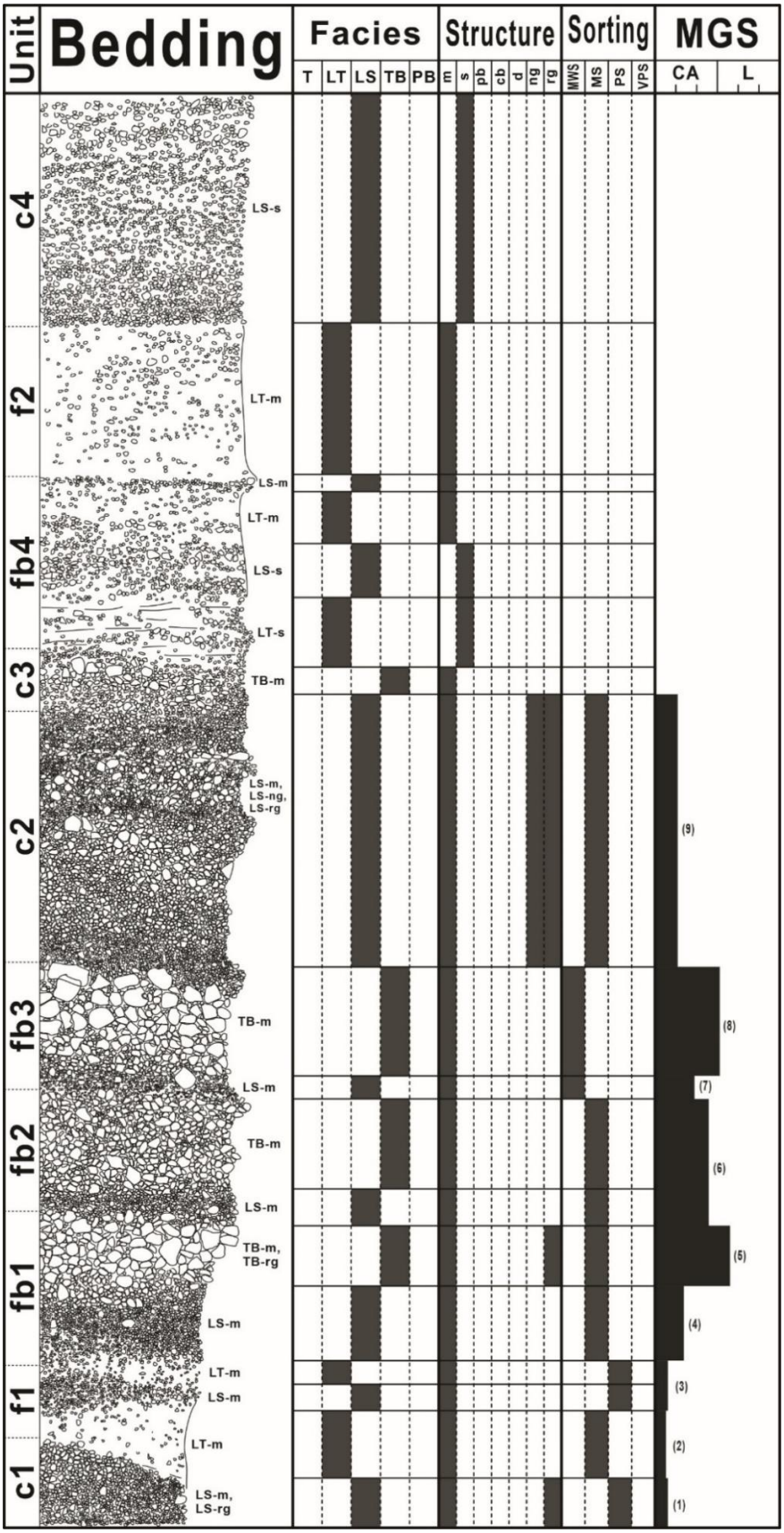

Figure 31: The stratigraphy column of the site far south of Tongxin lake. Please note that the numbers in the MGS section are the names corresponding to the subsequent sample names in the data presented.

3) Grain size distribution (GSD)

Grain size analyses have been undertaken with the aim of interpreting syn-eruptive behaviours by evaluating each sample from multiple field locations. Grain size analyses do not just sort the clasts present into size fractions; they also aid the interpretation of the transportation processes operating. Due to the large range of clastic sizes, the logarithmic phi scales (Krumbein, 1934) are used for data presentation and interpretation. The data presented utilises the Udden-Wentworth scale (Wentworth, 1922).

$$\phi = -\log_2 d \qquad (1)$$

Formula (1) indicates the relationship between arithmetic grain size values and logarithmic phi values, in which ϕ is the phi size and d is the diameters of the clasts in millimetres (Boggs Jr, 2014).

Commonly, the distributions of the grain size variations follow the standard normal distribution trend. In a statistical sense, if it is given a set of arbitrary numbers as the random variables, its mean value will perfectly follow a symmetric normal distribution curve in the probability distribution (McClave & Sincich, 2017), which is also called the bell-shaped curve.

$$f(x) = \frac{1}{\sigma\sqrt{2\pi}} e^{-\frac{1}{2}\left(\frac{x-\mu}{\sigma}\right)^2} \qquad (2)$$

In equation (2), the μ is the mean of the normal random variables; σ is the standard deviation; π is Archimedes' constant; e is Euler's number. Specifically, when the value of mean μ equals 0, and the standard deviation σ equals 1, equation (2) can be transformed into:

$$f(z) = \frac{1}{\sqrt{2\pi}} e^{-\frac{1}{2}z^2} \qquad (3)$$

Equation (3) is called standard normal distribution, denoted as the symbol z (McClave & Sincich, 2017).

Based on this theory, the samples of pyroclastic deposits found around Tongxin Lake are generally performed by the sieving processes, which utilise the US. Standard

techniques. There are 19 sieves with half phi values from -4.5 to 4, which means from 23 mm to 63 microns in clasts diametres. From the normal distribution curves, four parameters (median size, sorting, skewness and kurtosis) can be calculated by the following formulas, they are:

$$\bar{x}_{\phi} = \frac{\sum fm}{n} \qquad (4)$$

Equation (4) is the calculation for the mean, i.e., median value;

$$\sigma_{\phi} = \sqrt{\frac{\sum f\left(m - \bar{x}_{\phi}\right)^2}{100}} \qquad (5)$$

Equation (5) is the formula for the values of sorting, i.e., standard deviation of a single normal distribution;

$$Sk_{\phi} = \frac{\sum f\left(m - \bar{x}_{\phi}\right)^3}{100\sigma_{\phi}^3} \qquad (6)$$

Equation (6) leads to the outcomes of the skewness, i.e., tails of the distribution curves;

$$K_{\phi} = \frac{\sum f\left(m - \bar{x}_{\phi}\right)^4}{100\sigma_{\phi}^4} \qquad (7)$$

Equation (7) is the definition of kurtosis. It means the sharpness of a distribution curve.

In equations (4) to (7), f is the fraction of each grain size frequency; m is the median value of the whole range of grain size values; n is the total number of each size fraction, especially when the f values are in percentages, the value of n equals 100. Also, equations (4) to (7) are the moment methods for calculations of grain sizes (Krumbein & Pettijohn, 1938). By using this method, the outcomes are not constrained by the geometric deviations from the curves, and the data can be generated directly from the grain size data (Boggs Jr, 2014).

In order to correspond the GSD data to the up-mentioned stratigraphy columns in every site, the binary plots of the GSD data will be presented as multiple separated pictures on each location. Also, all the values on each data type are presented in logarithmic phi values rather than arithmetic ones.

Site 1:

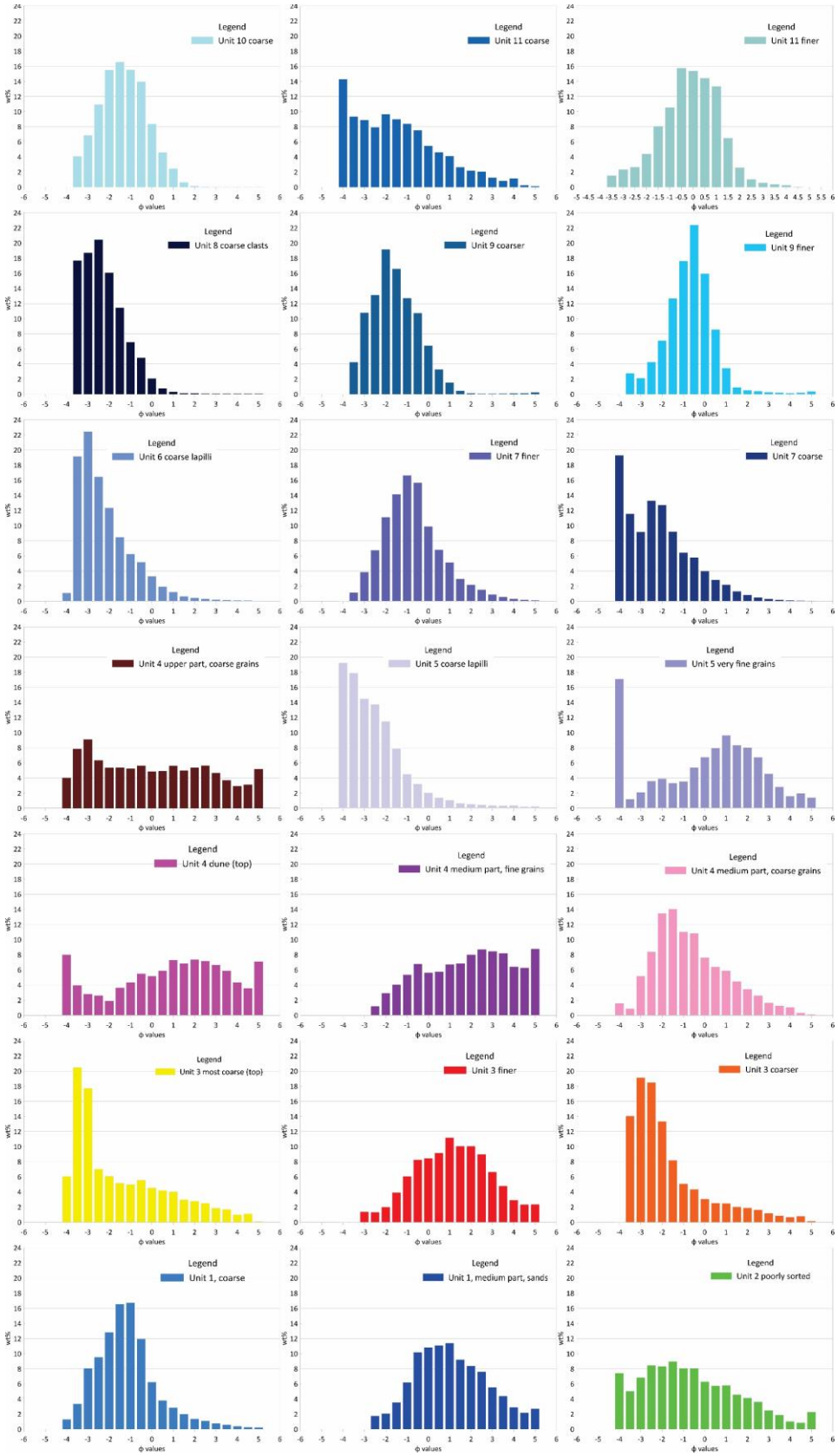

Figure 32: GSD data of S1 deposits. Each diagram is correlated with the above-mentioned descriptions of sedimentary stratigraphy.

Grain size distribution curves of S1 deposits (Fig 32) display a range of trends. Mean grain size values range between -2.5 and -0.43 (phi values) in all units, consistent with the majority of the material being coarse lapilli. Some units follow a unimodal bell curve, and others display bimodal and polymodal peaks. In the lower part of S1, the coarse samples from units 1 to 3 display very sharp peaks (high kurtosis) and are coarsely skewed, whereas the medium fraction has a lower kurtosis, and the sample is not skewed. Samples from units 5-8 presented a similar distribution trend to those in units 1-3. In the dune structure in unit 4, the curve shows a flattened trend with no clear mode. In contrast, the coarse fractions of that unit are strong to moderately coarse skewed and peaked. The fine fraction is weakly bimodal. Unit 1, 2 and the coarse materials in unit 4 reveal the fine-skewed trend with a long tail representing the fine grain sizes. The coarse fraction of unit 5 shows a gradual increase from -2ϕ to -4ϕ. In contrast, there is a huge increase of very coarse (-4ϕ) clasts in the very fine fraction of unit 5 in what is otherwise a largely normally distributed finer-grained sample due to the presence of ballistic projectiles in the sample. For most of the samples, sorting values range from 1.10 to 2, poorly sorted and very poorly sorted. An exception is Unit 8, which is moderately sorted (1.09). Among them, unit 4 is the exception where the fine grain size fraction ranges from -0.98 to 1.12 phi, which makes this unit the finest-grained unit in S1.

Site 2:

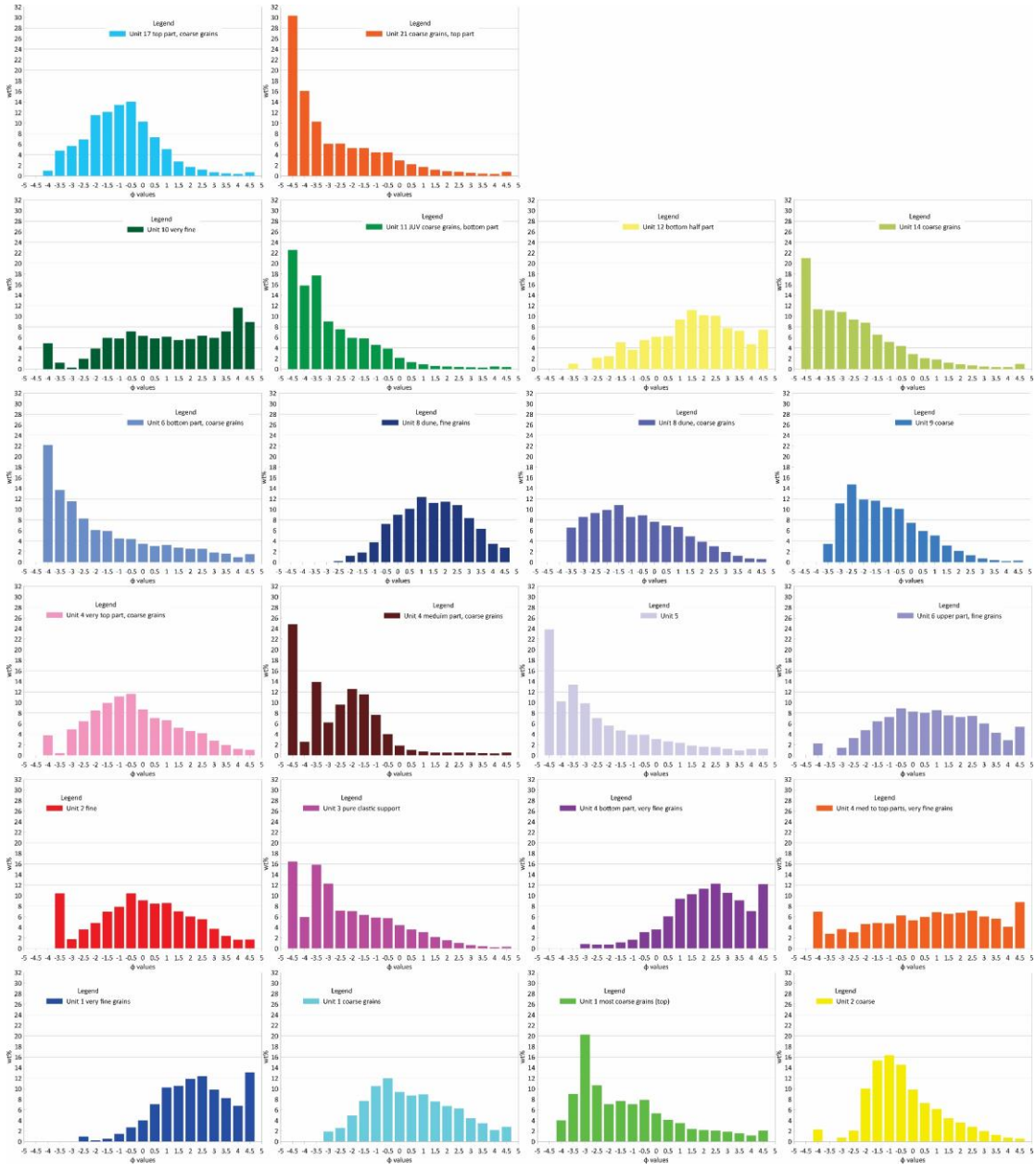

Figure 33: Plots of GSD on S2 deposits.

GSD of S2 deposits (Fig 24) are presented in Fig 33. The indurated nature of some of the S2 deposits means only the relatively loose materials, in specific units in the lower, intermediate and upper sections, were suitable for sieve analysis. As Fig 33 reveals, the total mean size ranges from -3.9 to 2 in phi values. Some plots show a total fine-skewed trend, which means a long tail marks the end of the curves, e.g., unit 1, unit 3 and unit 11. The sorting values range from 0.07 to 1.46, indicating poor and very poor sorting. Samples from unit 2 and unit 4 (the first one on the 5th row and the second one on the 4th row) show a sudden jumping between -4.5ϕ, -4ϕ and -3.5ϕ. In

comparison to the data from S1, the fine-skewed trend in S2 is more common than the same parameter in S1. Besides, S2 distribution curves are sharper than the curves of S1, which means large kurtosis values in comparison to the kurtosis of S1 data. Also, the median values are dispersed.

Pyroclastic deposits over the basal lava spatter:

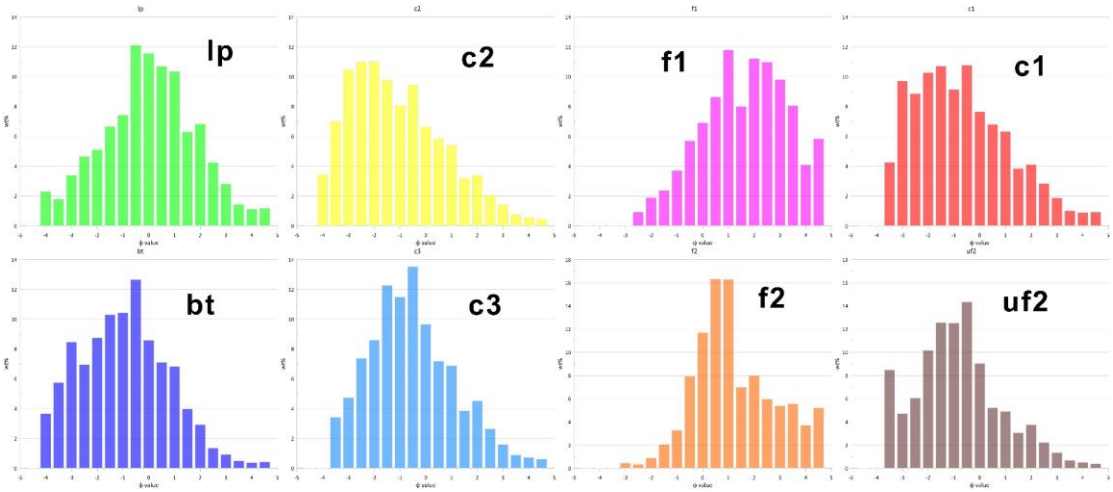

Figure 34: GSD binary diagrams of data from the pyroclastic deposits overlying the spatter.

GSD data from the spatter site shows a range of polymodal patterns. Some of them have more than three modes in the normal distribution trends. Median values range from -1.21 to 1.19, which indicates the MGS spanning fine gravel, coarse sand and medium sand. Fig 34 depicts that some samples have a fine-skewed pattern, e.g., c1, c2, c3 and uf2. The general sorting values have a very narrow range between 1.41 to 1.8, implying poor sorting. In comparison to the data of S1 and S2, the curvature sharpness of the data in Fig 34 is higher than the data trend in S1 and S2.

SE quarry, Tongxin Lake:

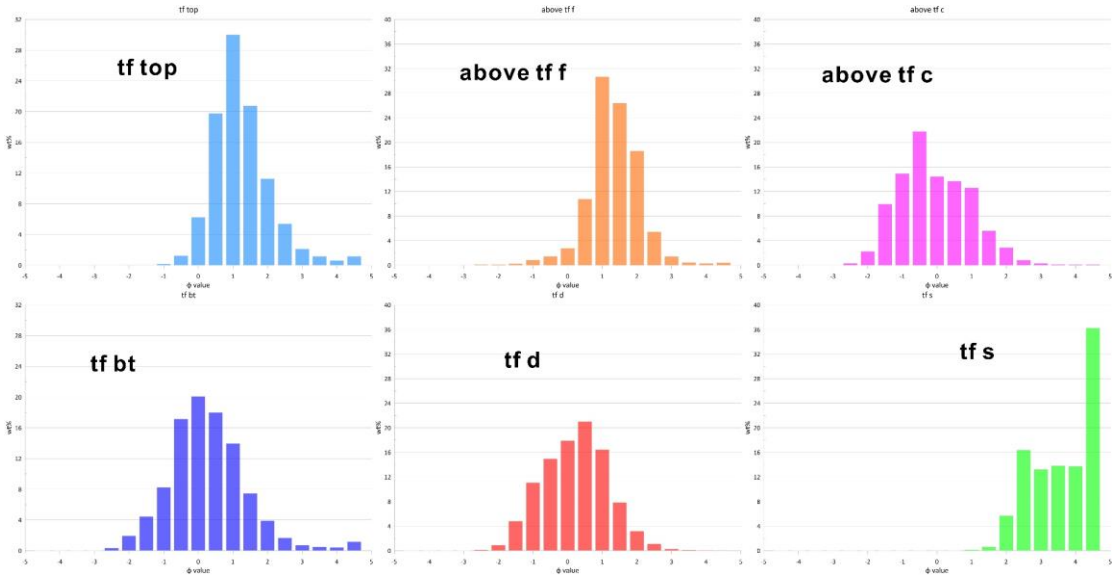

Figure 35: Normal distribution curves from the outcomes of analysing samples of the SE quarry of Tongxin Lake.

The data in Fig 35 is correlated to those in Fig 29B in the MGS section. The first erupted material occurs at the base of the deposits, in contact with country rocks. The total mean grain size spans from -2.15 to 2.8 in phi values. These are represented by four units, i.e., tf-bt, tf-d, tf-s and tf-top. Sample tf-s is bimodal, and the others are all unimodal. Mean grain sizes range from -0.01 to 2.82, which spans from fine ash to coarse ash. Sorting values are slightly different to sections S1 and S2. The values begin to be less than 1, which means moderate sorting, even moderate-well sorting. The skewness values have minor variations, with none of the fine-skewed trends that were found in S1 and S2 deposits. The tf-s deposit shows predominantly fine grain sizes.

Far south of Tongxin Lake:

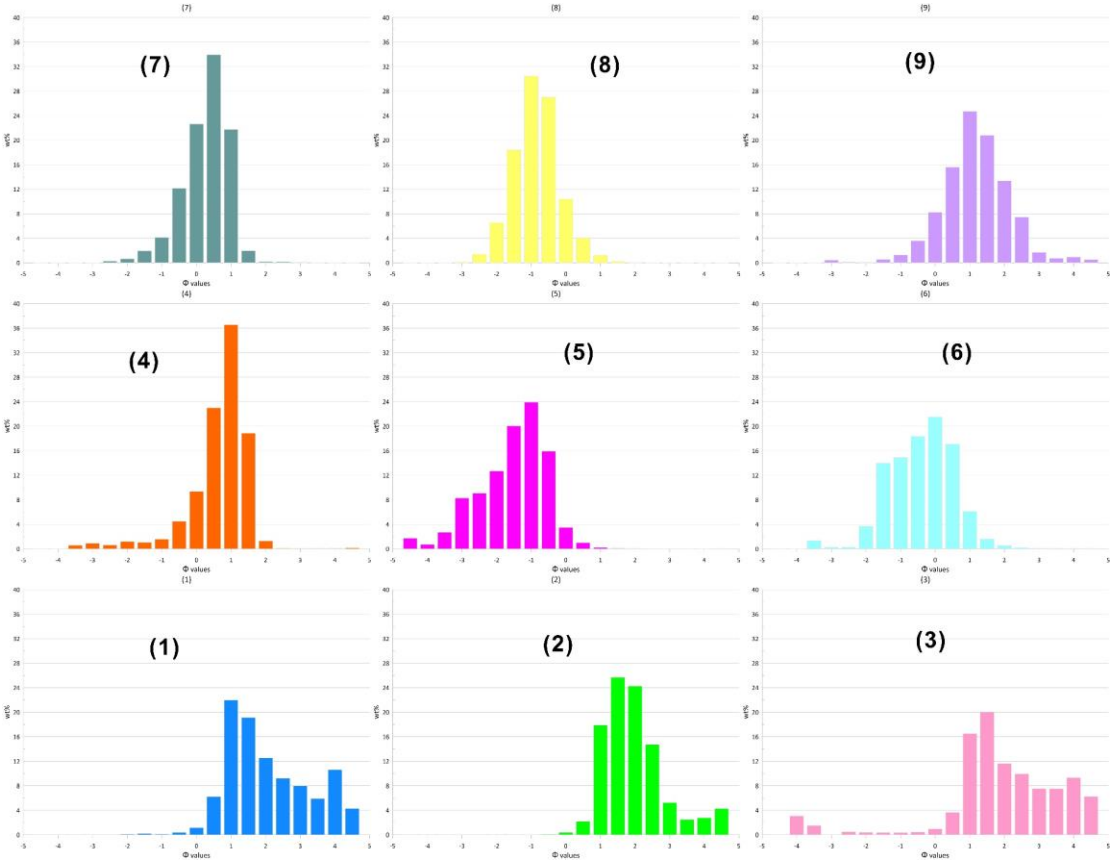

Figure 36: Statistical analyses of the GSD method on the deposits from far south of Tongxin Lake.

The names of each plot in Fig 36 correspond to the names in Fig 31 in the MGS section. This figure shows the values of mean grain sizes in intermediate variations from -1.78 to 1.71, which indicate fine gravels, coarse sands and medium sands. Only deposits (1) and (3) have sorting values larger than 1 (1.11 and 1.7, respectively), which means poor sorting. Other sorting values are generally smaller than 1 (ranging from 0.68 to 0.99), which indicates moderate sorting. Rather than the sorting values from S1 and S2 deposits, the deposits of this location are better sorted than the two major deposits (S1 and S2). Skewness is spreading on coarse skewness and symmetry; only sample (2) shows fine skewness. Most samples have the unimodal trend, except samples (1) and (3), i.e., bimodal and trimodal. Commonly, transportation models are separated by fallout and pyroclastic density current (PDC) behaviours. PDC has a normal uniformed distribution in GSD patterns; otherwise, the fallout has bimodal or polymodal patterns

of GSD due to the multiple phases of the accumulative processes during the syn-eruptive stages.

4) Point counting

The composition of the sediments was determined by the point-counting at least 300 grains on subsets of different size fractions. In order to carry out componentry analyses, seventy-seven samples were carefully analysed under the optical microscope. All the samples had been previously sieved, and grain size fractions, from -1.5ϕ to 2.5ϕ at half phi intervals, were selected. As some samples do not have coarse fractions due to lacking 300 grains to perform the point counting method, the data set obtained from clasts under 1.5ϕ represents the major distribution trend of point counting.

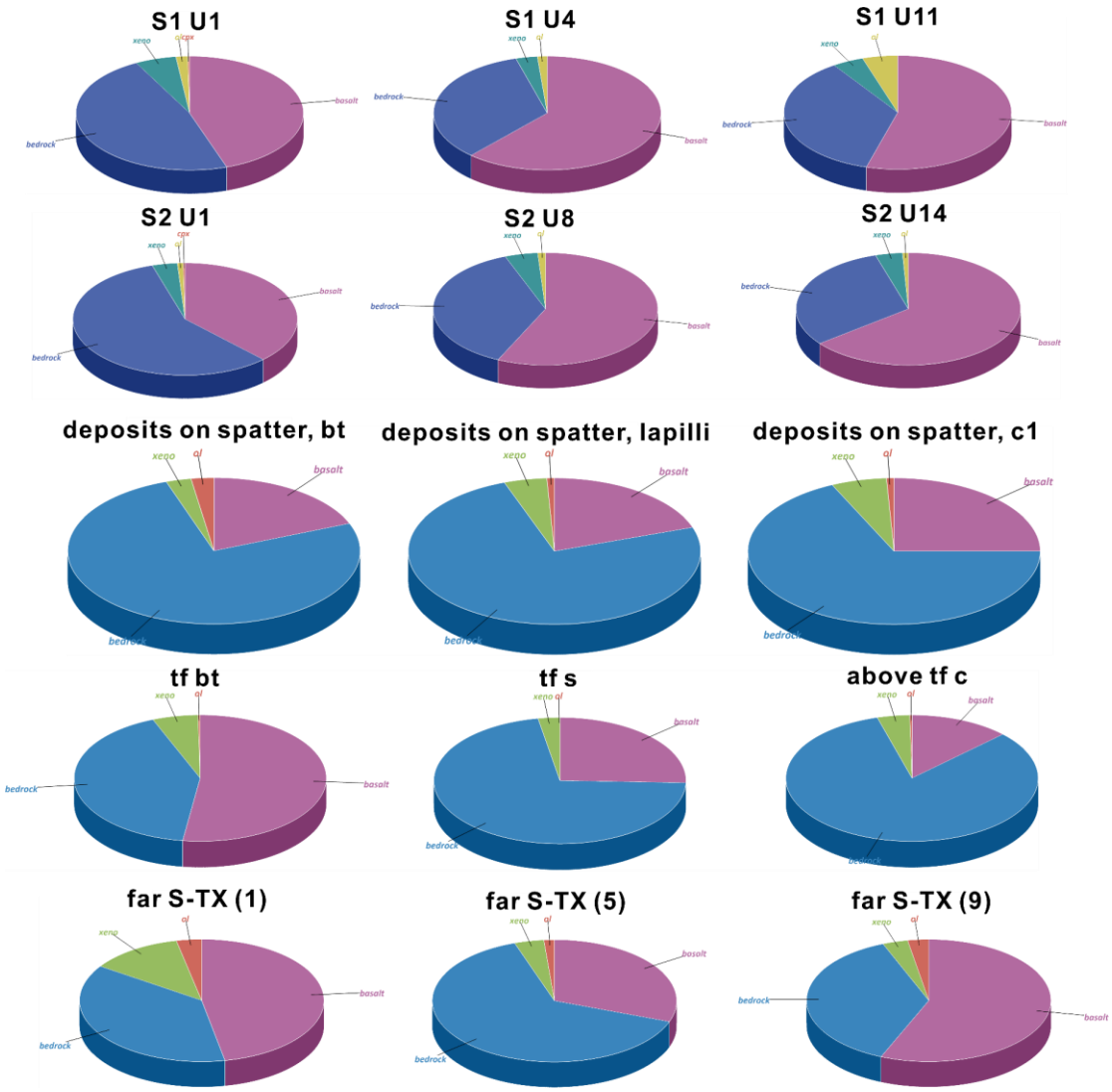

Figure 37: The composition data from the pyroclastic deposits around Tongxin lake. As this graph shows, the blue and deep blue colours represent the percentages of lithics (debris of country rocks); the red and yellow colours mark the percentages of olivine xenocrysts; the deep red colour shows the percentages of pyroxene xenocrysts; light and deep green colours reveal the percentages of mantle xenoliths (most of them are the lithics surrounded by juvenile materials); the pink colour is the indicator of the percentages of juvenile materials (commonly basalts).

Component analyses of Cenozoic eruptives from around Tongxin Lake have been undertaken. Seventy-seven samples were sieved, divided into nine different grain size fractions, and point counted under the petrographic microscope. The compositions of deposits in each site are presented in Fig 37. Judging by the anhedral shape of the olivine and pyroxene crystals present in many samples, all the mafic crystals in Tongxin deposits are deemed mantle-derived xenocrysts. Some xenoliths are classified as fragments of country rock with an outer coating of juvenile basaltic material. Pie

charts (Fig 37) show the mineral components of the different deposits. They present the results of analyses of Cenozoic eruptives, so volcanic materials from earlier eras are deemed as bedrock (country rock). The samples contained juvenile particles (basalt), country rock (bedrock), ol (olivine crystals and olivine xenocrysts), xenoliths, and CPX (pyroxene crystals). In general, country rock (bedrock) and juvenile debris dominate the samples (purple and blue colours). Xenocrysts such as olivine and pyroxene are present in secondary amounts. Vertical GSD variation trends reflect componentry fluctuations, i.e., juvenile clasts are rich in the bottom and top units of S1, but less is contained in the intermediate sections. No lateral variation trend was observed.

5) Density measurement

Density analysis of pyroclasts is a legit way to glimpse the reactions between the ascending lava batches and the surrounding environment (e.g., phreatomagmatic magma and water interaction), degassing processes (e.g., where, in what level, in what time). As mentioned above, two types of density (envelope and true density) have been carefully examined and converted into porosity calculation in order to interpret the interactions between magma batches and groundwater.

Especially the porosity calculation is based on the outcomes of the two types of density, which are Envelope density - the definition includes volumes of the solid materials, closed pores and open pores; true density - the definition is only including the volumes of the solid materials, excluding closed pores and open pores. Besides, bulk density is defined by the total volumes of solid materials, open pores, closed pores, and inter-clastic void spaces.

In the conventional concept, porosity can be calculated by:

$$n = \frac{V_V}{V_T} \qquad (8)$$

In formula 8, n denotes porosity; V_V is the volume of the void spaces; V_T is the volume of the bulk materials (Athy, 1930; Horgan, 1996).

Alternatively, the value of porosity is also defined by different types of density:

$$n = \frac{\rho_p - \rho_b}{\rho_p - \rho_f} \quad (9)$$

Where ρ_p is the particle density; ρ_b is the bulk density; ρ_f is the fluid density (Horgan, 1999; Horgan, 1998; Nelson, 2000; Rouquerol et al., 2011). Specifically, when the void spaces are filled with air rather than liquid, the formula nine can be transformed into:

$$n = 1 - \frac{\rho_b}{\rho_p} \quad (10)$$

Based on equation 10, if envelope density is measured from a single clast, then ρ_b is equal to the values of envelope density; ρ_b can be equal to the values of true density.

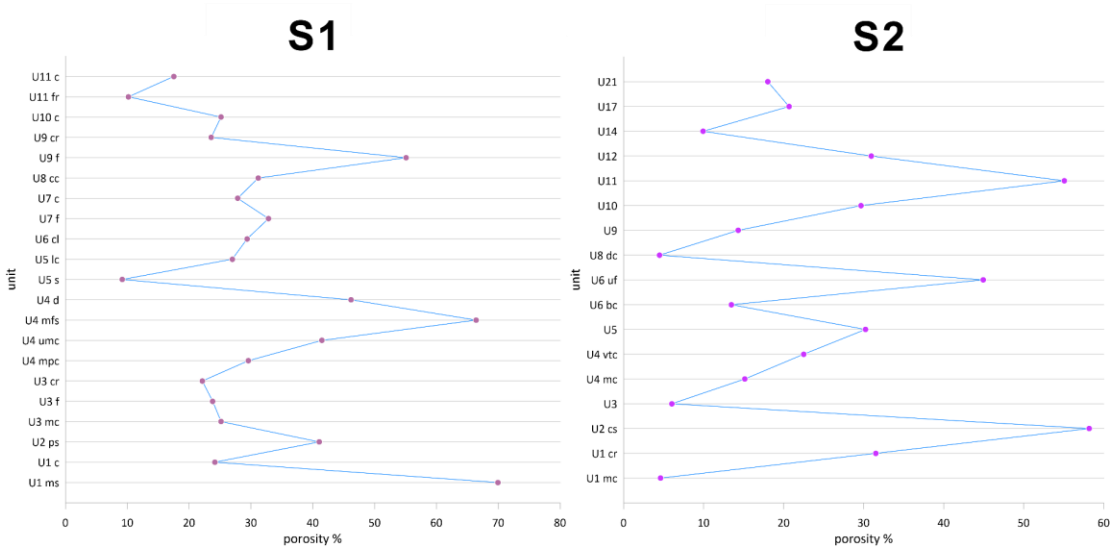

Figure 38: Porosity outcomes of S1 and S2. Please note that the units in each site are from the bottom to the top. Each porosity data was performed by measuring individual juvenile pyroclast in lapilli size ranges (64 mm to 2 mm).

The porosity calculations on each unit from S1 and S2 are shown in Fig 38. All the units correspond stratigraphically to those in Fig 22 and Fig 24, and all porosity data have been normalised by percentages. In general, the porosity of particles from S1 (range: <10% to nearly 70%) is greater than the porosity of particles from S2 (range: <<10% to 60%), and each plot shows at least three peaks. The lower units of S1 (name them here) show high values, the same as in intermediate sections (unit 4) and upper parts (unit 9). A similar trend occurs in the deposits of S2; upper unit 1 and unit 2 have the largest values; units 6 and 11 also demonstrate high porosity. Unit 5 has a moderately high value, giving S2 a fourth intermediate peak in porosity. To sum up, the porosity on both sites changes very rapidly with a large range of variation.

6) Pyroclast shape analyses and textures

Shapes of the pyroclasts are determined by several parameters, such as roundness and sphericity. Roundness refers to the sharpness of the corners of a single clast and how many edges a clast has. Surface texture indicates some features such as pits, scratches and ridges, as well as micro-crystals on a surface of a single clast (Boggs Jr, 2014). To interpret shapes and surface textures, scanning electron microscopy (SEM) and backscattered electrons (BSE) microscopy were performed on particles from S1, S2 and the -- quarry in the southeast of the town. Images taken during the microscopy were analysed, and it was found that roundness seems to be the most useful parameter in categorising clast shapes from the images (Boggs Jr, 2014; Fisher & Schmincke, 1984, 1994).

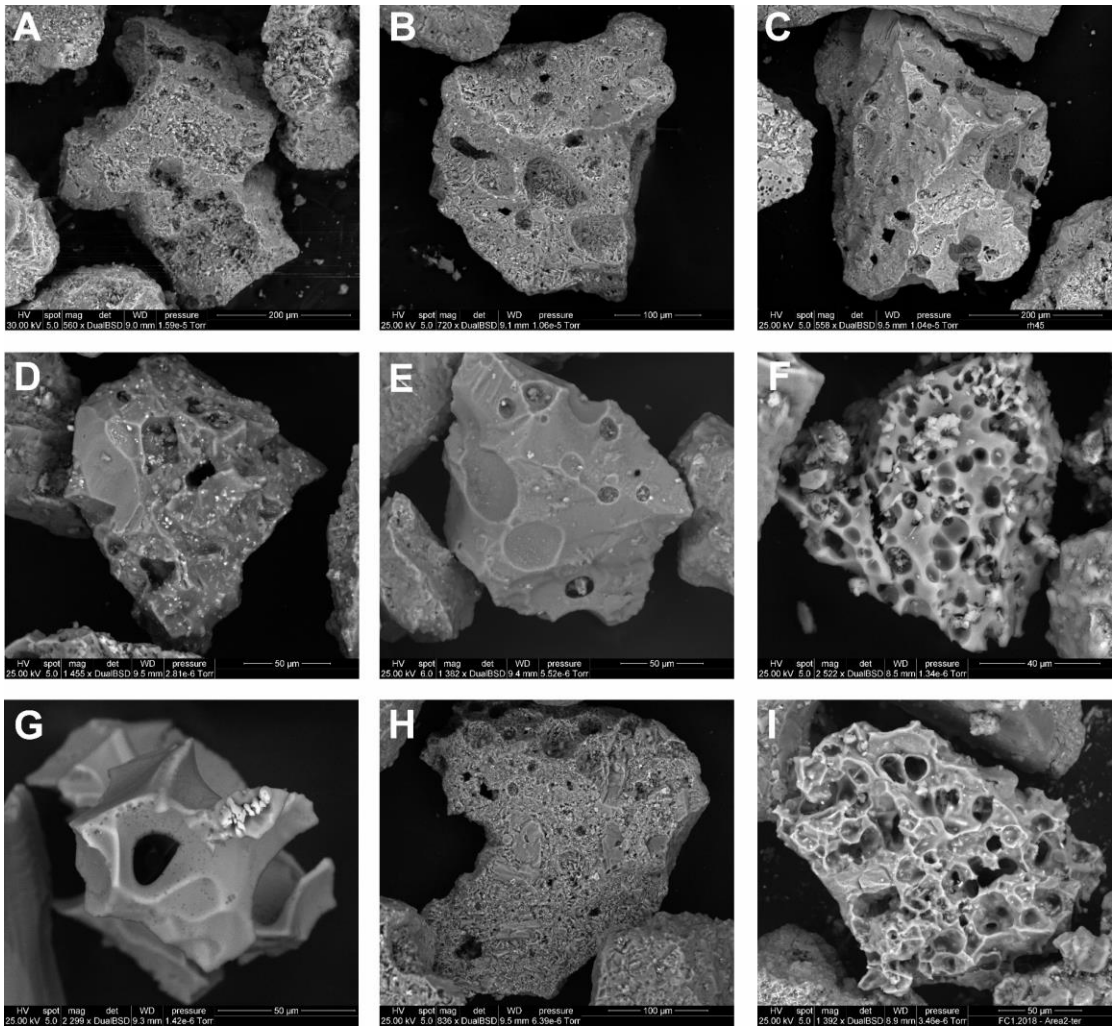

Figure 39: 3D SEM images of the pyroclastic particles from Tongxin Lake deposits. Photos A to I are the juvenile pyroclasts from S1, S2 and the quarry on the southeast of the town; the grain sizes range from 0.707 mm to 0.125 mm.

Clasts from S1 were chosen for three-dimensional SEM imagery (Fig 39) to show shape and surface features. All the grains are generally angular to sub-angular with a cauliflower-shaped boundary. Photos A, B and H are examples of juvenile particles displaying fully crystalline textures. On the surfaces, the feldspar-like and elongated bar crystals are very well-developed. Photo H also shows large xenoliths within a mass of microlites with euhedral to subhedral shapes (Winter, 2013). In photos C and D crystallisation is evident. Some of the microlites are in the early stages of crystal growth, whereas in others, crystallisation has progressed further. Photos E, F, G, and I show examples of glassy shards. There is no single piece of crystal formed on their surfaces, and the surfaces are very smooth. The grain in photo I also has a small number of crystals on its surface (tiny white dots with relatively high reflections compared to the greyish backgrounds of the groundmass), with most of the surface area quite smooth. The glassy grains F and I are also vesicular, with large numbers of "bubbles".

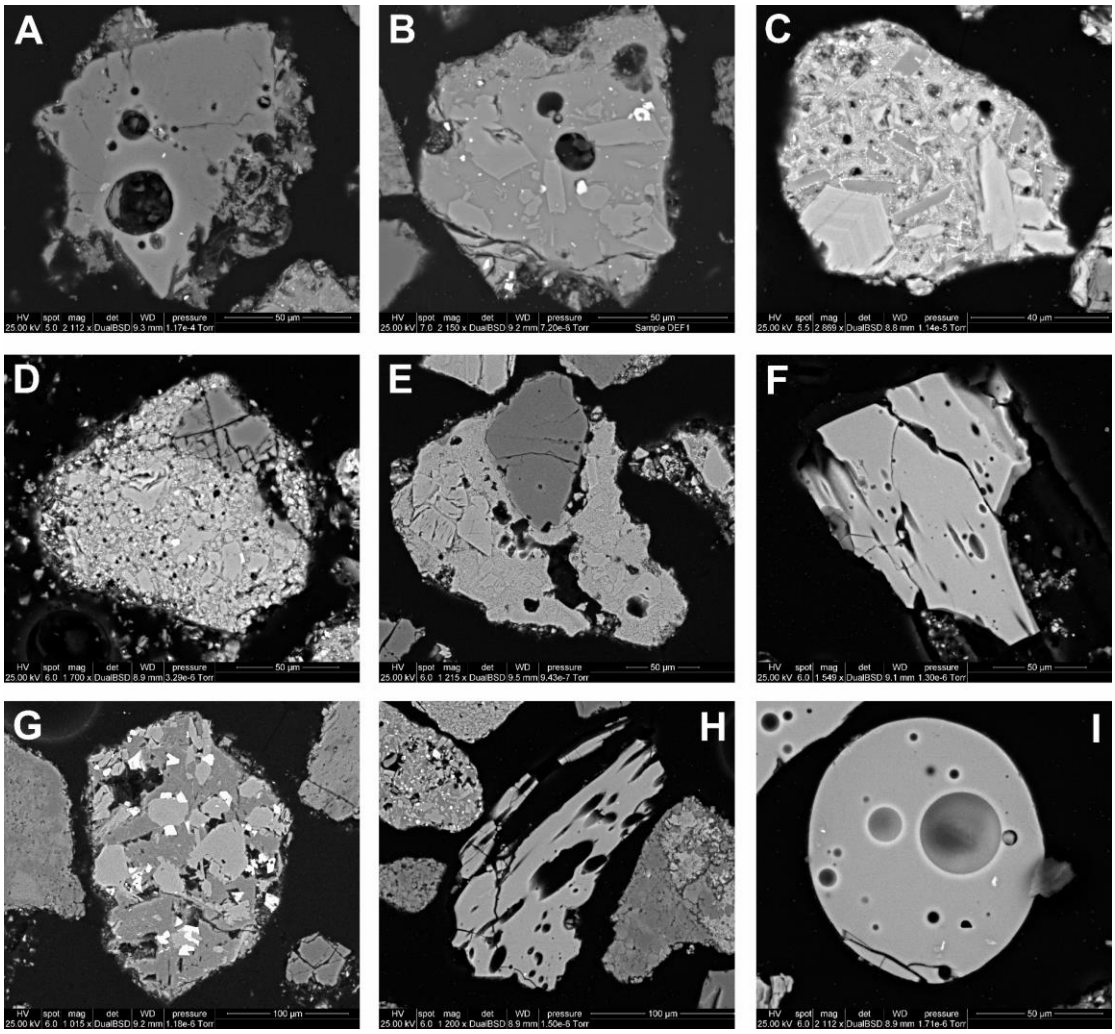

Figure 40: 2D BSE images of the pyroclastic particles from the deposits around Tongxin Lake. Photos A to I reveal the inner structures of the pyroclasts in S1 and S2, the two major locations. The grain sizes range from 2.83 mm to 0.177 mm.

Two-dimensional BSE imagery was undertaken on polished samples of pyroclastic grains from S1, S2 and the SE quarry. For each sample, nine different grain sizes were embedded in each of the nine holes in an epoxy plug that was ground and polished (Fig 40). Photos A and B from S1 show crystallisation at the early and medium stages. Photo A is actually a glassy shard, and the grain of photo B contains a few crystals within a glassy matrix. Photo C shows that crystals are highly developed and evolved, and in the bottom left corner, a zoned crystal is clearly visible. Photos D, E and G are from the deposits in contact with the country rock excavated from the quarry SE of Tongxin Lake. The particles in photos D and E contain large xenoliths of bedrock. Photo G shows the crystallisation of many different composition grains, such as plagioclase and olivine. Photos F, H, and I are also from the quarry location. Photos F and H depict

a “stretching” pattern on two glassy shards; note that the bubbles are stretched too. Photo I is a rounded glassy particle that contains rounded bubbles.

7) Bulk Geochemistry

Geochemistry was undertaken on the juvenile materials in the pyroclastic deposits and lava flows from Tongxin Lake and its surrounding areas with an aim to characterise the major, minor and trace element abundances of juvenile pyroclasts and coherent lava. Major, minor, and trace element data are presented as binary plots. Typically, the minor elements (such as sodium, magnesium, and aluminium) are treated as a subgroup or substitute for major elements. Thus, only the data of major and trace element data are presented. The major and minor elements are commonly expressed as oxides, e.g., SiO_2, Al_2O_3, MgO, and CaO in percentage values. The trace elements are expressed as elements in parts-per-million (ppm). The locations of samples taken from areas surrounding Tongxin Lake are shown in Fig 18 (yellow triangles).

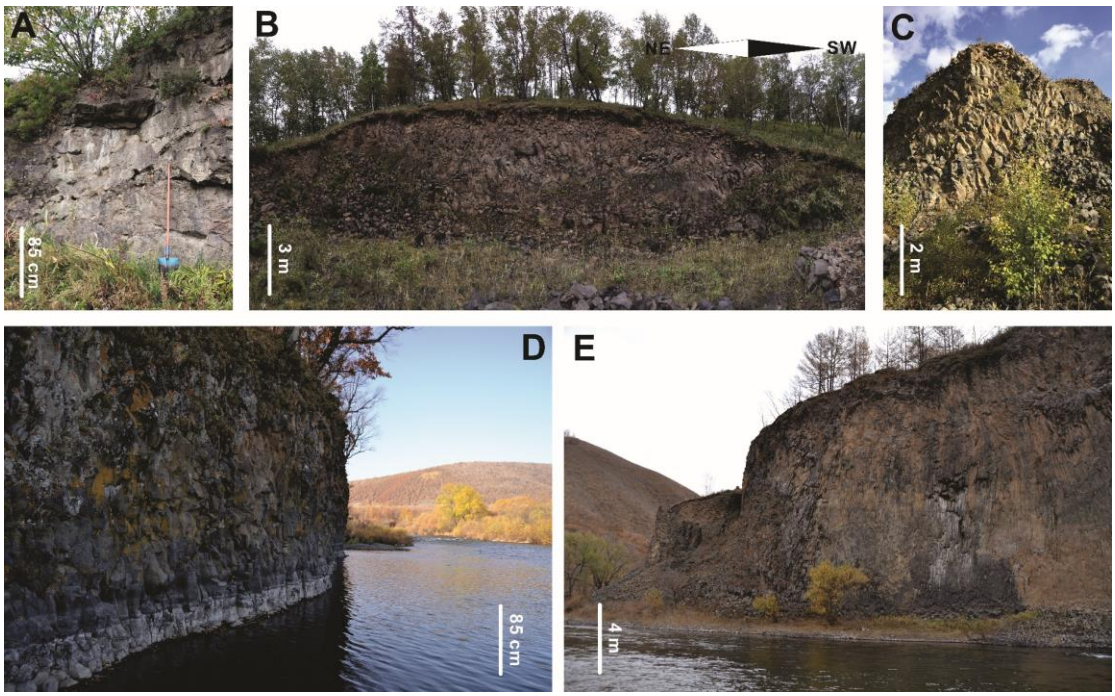

Figure 41: Lava flows observed in the field. A: Chaoer River, 2.75 km west of LakeTongxin (47°32'53.00"N, 121°17'20.00"E). B: turning point of the river, 2.5 km from the lake (47°33'17.60"N, 121°16'12.20"E). C: top of a dam, 1.7 km from the lake (47°33'51.10"N, 121°16'21.20"E). D: 3.3 km north of the lake (47°34'49.20"N, 121°14'54.70"E). E: 12.5 km south of the lake (near the location of the Far south of Tongxin).

The lava flows that preserve columnar jointing and fluidal structures (Fig 41) have been sampled (this does not include the locations in photos D and E) and analysed for elemental variations. Twenty-six samples were analysed by XRF using glass discs (Tables 6, 7 and 8) (see Appendix). Then the trace elements and REE data were extracted from the analyses of ICPMS at Waikato University (see Appendix).

	SiO_2 (%)	TiO_2 (%)	Al_2O_3 (%)	Fe_2O_3 (%)	MnO (%)	MgO (%)	CaO (%)	Na_2O (%)	K_2O (%)	P_2O_5 (%)	SO_3 (%)	LOI (%)	Sum (%)
S1U1	50.79	2.27	12.50	11.89	0.16	8.93	7.99	3.48	2.58	0.54	0.01	0.01	101.16
S1U2	52.84	2.37	12.87	11.48	0.16	7.61	8.01	3.64	2.73	0.53	0.01	0.03	102.28
S1U3	52.77	2.32	12.82	11.52	0.16	7.90	8.14	3.55	2.64	0.48	0.01	0.02	102.34
S1U4	52.68	2.24	12.70	11.34	0.16	8.40	7.86	3.52	2.59	0.48	0.01	0.01	101.99
S1U5	51.69	2.23	12.67	11.54	0.16	9.12	8.06	3.43	2.37	0.48	0.01	0.02	101.79
S1U6	51.86	2.13	12.30	11.60	0.16	9.94	8.51	3.19	2.26	0.43	0.01	0.02	102.41
S1U7	51.20	2.17	12.43	11.80	0.16	9.93	8.50	3.33	2.22	0.45	0.01	0.02	102.23
S1U8	53.08	1.98	12.91	10.93	0.15	8.54	7.26	3.56	2.43	0.41	0.01	0.02	101.28
S1U9	52.10	1.98	12.09	11.60	0.16	11.11	8.46	2.75	1.84	0.38	0.01	0.03	102.52
S1U10	51.35	1.93	12.10	11.60	0.17	11.28	8.80	2.78	1.76	0.36	0.01	0.00	102.14
S1U11	50.36	1.75	11.68	11.48	0.16	13.04	8.19	2.64	1.61	0.32	0.01	0.02	101.28
S2U5	52.25	2.25	12.63	11.95	0.17	6.65	8.75	3.47	2.44	0.57	0.01	0.05	101.19
S2U14	56.08	1.67	15.73	10.70	0.17	4.28	5.53	2.67	3.71	0.45	0.01	0.03	101.03
S2U15	53.17	2.13	13.07	11.58	0.16	7.43	7.75	3.41	2.60	0.56	0.01	0.03	101.92
S2U21	54.28	1.85	13.59	10.02	0.15	6.65	7.00	3.60	3.07	0.57	0.01	0.04	100.83
peridotite	45.61	0.34	4.38	8.63	0.13	37.57	3.22	0.75	0.38	0.09	0.00	0.15	101.25
LF2	50.25	1.92	13.23	11.69	0.17	9.18	9.69	3.19	1.23	0.31	0.00	0.05	100.92
LF1	48.42	2.10	13.12	11.62	0.17	10.12	9.62	2.99	1.64	0.46	0.00	0.30	100.54
SE quarry, bt	52.05	2.17	12.33	11.27	0.16	8.21	7.71	3.37	2.60	0.49	0.01	0.65	101.02
SE quarry, d	46.59	2.50	12.04	13.67	0.19	9.96	9.50	3.33	1.94	0.54	0.01	0.09	100.35
spatter2	49.14	2.53	12.93	12.76	0.17	6.53	8.82	3.89	2.57	0.83	0.01	0.06	100.24
spatter1	50.05	2.46	13.03	12.30	0.17	6.26	8.49	3.84	2.62	0.80	0.01	0.48	100.50
w-TX-d top, columnar	49.31	2.24	13.39	11.23	0.16	9.52	9.88	3.14	1.73	0.47	0.00	-	101.07
w-TX-d bottom LF	49.75	2.10	13.66	11.06	0.16	9.62	9.70	3.33	1.46	0.42	0.00	0.00	101.26
TX cornfield, LF	50.37	2.20	13.65	11.11	0.16	8.37	9.89	3.36	1.49	0.36	0.00	0.00	100.95
LF in Chaihe Town	49.00	2.24	12.95	11.46	0.16	10.09	9.71	3.28	1.72	0.49	0.00	-	101.09

Table 6: Data set of major elements of the deposits from the surrounding areas of Tongxin Lake. Note that "w-TX-d" means west Tongxin dam; LF = lava flow. All the sample names are correlated to the stratigraphic columns above. All the abbreviations have the same meaning in the following tables.

	Ba	Rb	Th	U	K	Nb	Ta	La	Ce	Sr	Nd	P	Sm	Zr	Ti	Tb	Y	Tm	Yb
S1U1	591	67.59	6.14	1.544	21850	59.6	5.26	36.6	70.92	615.4	36.71	2565	8.16	211.8	16310	1.154	28.35	0.3	1.59
S1U2	607.2	75.58	6.9	1.801	23270	65.27	5.49	36.3	68.55	573.2	34.94	2473	8.37	218.3	16970	1.248	28.89	0.48	2.14
S1U3	599.8	70.05	6.26	1.786	22150	62.67	4.5	33.27	62.92	570.2	33.02	2239	8.45	217	16520	1.314	27.71	0.523	1.96
S1U4	582.5	71.13	6.27	1.685	22090	62.19	4.61	33.84	64.61	553.9	33.98	2261	7.59	214	16120	1.1	27.89	0.35	1.99
S1U5	556.8	63.18	5.71	1.386	20160	56.82	5.18	34.24	65.78	561.6	33.3	2307	7.54	217.4	16150	1.024	27.36	0.331	1.91
S1U6	548.1	61.33	5.77	1.407	19380	56.85	4.27	31.5	59	542.8	30.3	2035	6.8	196.1	15820	1.028	26.65	0.287	1.73
S1U7	530.5	59.16	5.32	1.313	18860	55.4	4.15	30.74	59.61	506.7	30.76	2120	6.81	190.8	15910	1.016	26.42	0.319	1.92
S1U8	507.9	76.7	6.01	1.549	20720	52.56	4.58	30.73	58.89	489.2	30.06	1899	6.65	195.6	14570	1.018	27.87	0.382	2.09
S1U9	460.9	48.03	4.64	1.078	15630	45.84	3.605	25.32	48.9	549.9	24.79	1832	5.99	168.9	14770	0.838	23.3	0.292	1.74
S1U10	445.6	44.53	4.52	1.065	14989	45.27	3.68	25.56	47.35	522.6	24.16	1714	5.62	158.1	14559	0.895	23.98	0.309	1.91
S1U11	411.8	42.81	4.15	0.99	13689	38.58	2.988	23.82	42.1	408.6	22.59	1503	5.23	141.7	13196	0.817	23.79	0.305	1.77
S2U5	560.2	67.3	7.74	1.785	20740	72.2	5.11	37.75	76.53	597.5	39.27	2749	9.29	232.1	16670	1.297	30.43	0.349	1.94
S2U14	627.8	133.5	11.05	2.95	31490	42.63	3.78	40.52	83.54	377	44.1	2135	9.82	339.7	12490	1.539	48.55	0.699	4.61
S2U15	600.4	72.92	8.05	1.915	22800	62.32	4.55	38.7	76.44	605	39.22	2663	8.65	231.6	15940	1.166	29.36	0.351	1.84
S2U21	711.8	98.6	7.59	1.671	26430	56.35	4.43	41.25	81.25	774.8	39.87	2711	8.44	240.3	13980	1.106	26.98	0.306	1.69
peridotite	92.6	10.19	0.916	0.273	3204	7.5	1.5	5.82	10.23	81.22	5.34	387	1.22	32.81	3192	0.19	5.99	0.082	0.487
LF2	347.5	23.68	2.544	0.636	10435	34.17	2.567	18.12	35.36	359.9	17.75	1498	4.62	131.2	14450	0.722	19.68	0.275	1.57
LF1	473.8	30.59	3.53	0.873	14010	44.36	3.285	24.69	47.36	507.2	24.48	2154	5.7	164	15870	0.773	20.64	0.257	1.49
SE quarry, bt	583.9	66.94	7.88	2.08	22230	61.67	4.75	36.71	72.51	572.7	34.67	2297	7.47	203.5	16440	1.051	26.47	0.302	1.63
SE quarry, d	533.3	44.59	4.6	1.246	16820	62.81	4.76	34.92	68.69	599.6	35.75	2623	8.15	192.5	18820	1.2	30.56	0.347	1.95
spatter2	628.1	57.34	6.22	1.581	22000	83.54	6.29	45.15	93.08	752.4	49.96	3982	10.88	257.4	19010	1.417	32.33	0.326	1.67
spatter1	621.9	59.99	6.48	1.602	22550	80.8	5.98	43.79	90.5	717.6	47.66	3872	10.91	263.8	18340	1.404	31.91	0.334	1.65
w-TX-d top, columnar	507.1	30.89	3.88	0.772	14860	46.38	3.193	23.34	45.08	520.7	23.42	2251	5.42	177.4	16570	0.763	20.66	0.254	1.5
w-TX-d bottom LF	421.2	24.37	3.58	0.834	12620	41.21	2.712	21.21	40.78	543.6	21.28	2034	5.25	163.8	15500	0.697	18.77	0.232	1.33
TX cornfield, LF	452.4	23.5	3.48	0.296	12705	42.27	2.801	17.12	33.85	452.6	18.6	1733	4.43	164.2	16100	0.666	17.65	0.221	1.285
LF in Chaihe Town	505.3	33.66	3.88	0.831	14740	46.84	3.093	24.22	47.1	500	23.68	2348	5.67	174.8	16300	0.798	20.79	0.265	1.58

Table 7: Data set of trace elements with values in ppm. Sample locations and codes are the same as in Table 5.

	La	Ce	Pr	Nd	Sm	Eu	Gd	Tb	Dy	Ho	Er	Tm	Yb	Lu
S1U1	36.6	70.92	8.54	36.71	8.16	2.442	7.56	1.154	6.34	1.075	2.57	0.3	1.59	0.235
S1U2	36.3	68.55	8.35	34.94	8.37	2.419	7.8	1.248	6.52	1.267	2.81	0.48	2.14	0.377
S1U3	33.27	62.92	8.07	33.02	8.45	2.5	7.62	1.314	6.23	1.302	2.72	0.523	1.96	0.43
S1U4	33.84	64.61	8	33.98	7.59	2.438	7.2	1.1	6.01	1.043	2.54	0.35	1.99	0.302
S1U5	34.24	65.78	7.86	33.3	7.54	2.229	7.01	1.024	5.88	1.064	2.51	0.331	1.91	0.244
S1U6	31.5	59	7.22	30.3	6.8	2.171	6.92	1.028	5.67	1.051	2.43	0.287	1.73	0.255
S1U7	30.74	59.61	7.21	30.76	6.81	2.23	6.72	1.016	5.73	0.972	2.53	0.319	1.92	0.233
S1U8	30.73	58.89	7.03	30.06	6.65	1.948	6.75	1.018	5.86	1.048	2.64	0.382	2.09	0.296
S1U9	25.32	48.9	5.97	24.79	5.99	1.81	5.74	0.838	4.75	0.836	2.121	0.292	1.74	0.219
S1U10	25.56	47.35	5.84	24.16	5.62	1.78	5.8	0.895	5.2	0.927	2.31	0.309	1.91	0.226
S1U11	23.82	42.1	5.36	22.59	5.23	1.65	5.23	0.817	4.72	0.901	2.21	0.305	1.77	0.24
S2U5	37.75	76.53	9.38	39.27	9.29	2.62	8.23	1.297	7.02	1.138	2.75	0.349	1.94	0.268
S2U14	40.52	83.54	10.36	44.1	9.82	2.73	10.01	1.539	9.5	1.863	5.21	0.699	4.61	0.69
S2U15	38.7	76.44	9.17	39.22	8.65	2.56	8.39	1.166	6.45	1.097	2.66	0.351	1.84	0.258
S2U21	41.25	81.25	9.67	39.87	8.44	2.458	7.64	1.106	5.91	1.034	2.37	0.306	1.69	0.245
peridotite	5.82	10.23	1.194	5.34	1.22	0.397	1.39	0.19	1.15	0.221	0.601	0.082	0.487	0.08
LF2	18.12	35.36	4.102	17.75	4.62	1.571	4.78	0.722	4.18	0.783	2.05	0.275	1.57	0.224
LF1	24.69	47.36	5.61	24.48	5.7	1.829	5.4	0.773	4.63	0.804	2.04	0.257	1.49	0.225
SE quarry, bt	36.71	72.51	8.33	34.67	7.47	2.322	7.42	1.051	5.79	0.962	2.348	0.302	1.63	0.21
SE quarry, d	34.92	68.69	8.47	35.75	8.15	2.547	8.05	1.2	6.54	1.159	2.815	0.347	1.95	0.248
spatter2	45.15	93.08	11.53	49.96	10.88	3.41	9.95	1.417	7.64	1.255	2.75	0.326	1.67	0.202
spatter1	43.79	90.5	11.23	47.66	10.91	3.26	10.24	1.404	7.48	1.248	2.78	0.334	1.65	0.226
w-TX-d top, columnar	23.34	45.08	5.42	23.42	5.42	1.85	5.52	0.763	4.39	0.746	2.04	0.254	1.5	0.192
w-TX-d bottom LF	21.21	40.78	4.89	21.28	5.25	1.747	4.81	0.697	4.11	0.723	1.93	0.232	1.33	0.175
TX cornfield, LF	17.12	33.85	4.15	18.6	4.43	1.727	4.49	0.666	3.86	0.707	1.77	0.221	1.285	0.193
LF in Chaihe Town	24.22	47.1	5.49	23.68	5.67	1.844	5.56	0.798	4.65	0.797	1.94	0.265	1.58	0.202

Table 8: Data set of rare earth elements (REE) at each location in ppm at the same locations and samples as Tables 4 and 5.

The total alkaline vs silica (TAS) diagram has been chosen for classifications of the volcanic rocks (Cox et al., 2013; Maitre et al., 1989). In order to identify major trends across the sample analyses, the total alkali-silica diagram was employed. This diagram provides basic but vital information to recognise the major compositional trends and potential compositional clustering. The measured compositional data were also compared with data selected from Zhao and Fan (2012) from China and McGee et al. (2013) from AVF. Interestingly the samples derived from the basal pyroclastic successions revealed more evolved compositions (basaltic trachyandesite) in comparison to late-stage eruptive products that yielded to be more trachybasalt, basalt.

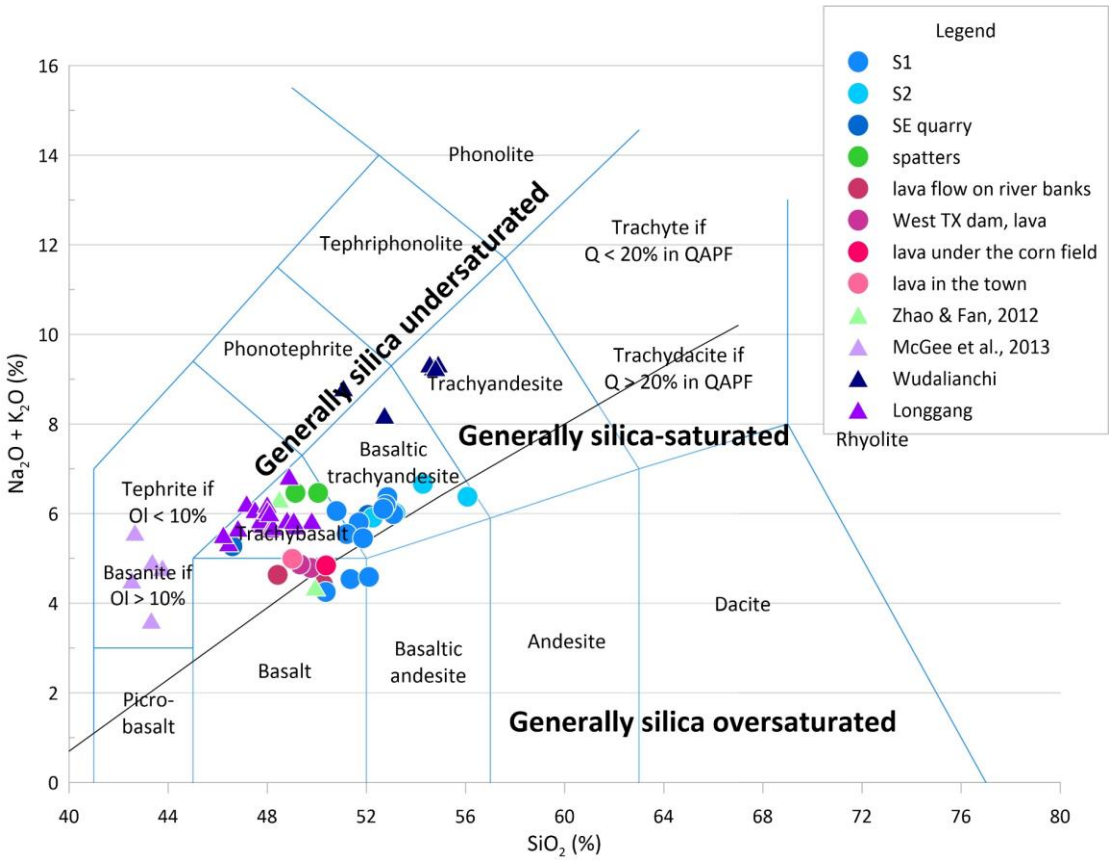

Figure 42: TAS diagram of Tongxin deposits (dots). Triangles are the data from previous research on Tongxin Lake (Zhao & Fan, 2012) and Auckland Volcanic Field (AVF) (McGee et al., 2013). Also, comparisons to the other two major monogenetic volcanic fields (Wudalianchi and Longgang) have been provided in this diagram (Fan et al., 1999; Hsu & Chen, 1998; Liu et al., 2009; Sui et al., 1999; Yu et al., 2003). For the location of ACVF, Wudaliuanchi and Longgang see Figure 1. Note that the order of the legend follows the real stratigraphic order from the S1 to the lava flows from top to bottom, respectively, and the same order is in the following diagrams.

The silica content of the Tongxin volcanic rocks ranges from 45% to 56%, from mafic to intermediate, with total alkalis ranging from 4% to nearly 7% (Fig 42). Generally, four types of volcanic rock fit these compositions: basalt, trachybasalt, basaltic andesite, and basaltic trachyandesite. S2 samples (yellow dots) are basaltic trachyandesite. Juvenile particles from S1 (red dot) span three fields (basalt, trachybasalt and trachyandesite), i.e., mafic and intermediate materials. The samples of spatters and lavas ("dry" eruptive materials) are mafic (trachybasalts and basalt). 95% of the samples lie within the silica-saturated field; only four samples reside in the silica-oversaturated field. Compared to the other datasets provided from New Zealand and a volcanic field near ACVF, volcanic materials from the Tongxin area have a wider compositional range in the major element perspective than those reported from the Auckland Volcanic Field spanning the mafic to intermediate rock types.

Based on the TAS, the trend visible from the more evolved compositions toward more primitive melt release raises the question of what caused this variation in a volcanic eruption that is inferred to take place in a short period of time. To have evolved compositions are commonly associated with some fractional crystallisation where mineral phases gradually escape the residual melt leaving it higher in silica content and gradually depleted in mafic minerals. The variations among the more primitive melts are commonly associated with variations in the degree of melts and the actual location of the melting anomaly of the deep source regions. To test these, further discrimination diagrams were used. Fractional crystallisation is one of the critical processes in the formation of volcanic rocks. It involves the separation of the solid phases from the liquid phases as the temperature drops (Winter, 2013). The partial melting process is the inverse trend to fractional crystallisation, i.e., equilibrium crystallisation. The binary phase diagrams show the trend of the oxides in the igneous rocks and indicate the cotectic and eutectic curves (Harker, 1900, 1909; Winter, 2013).

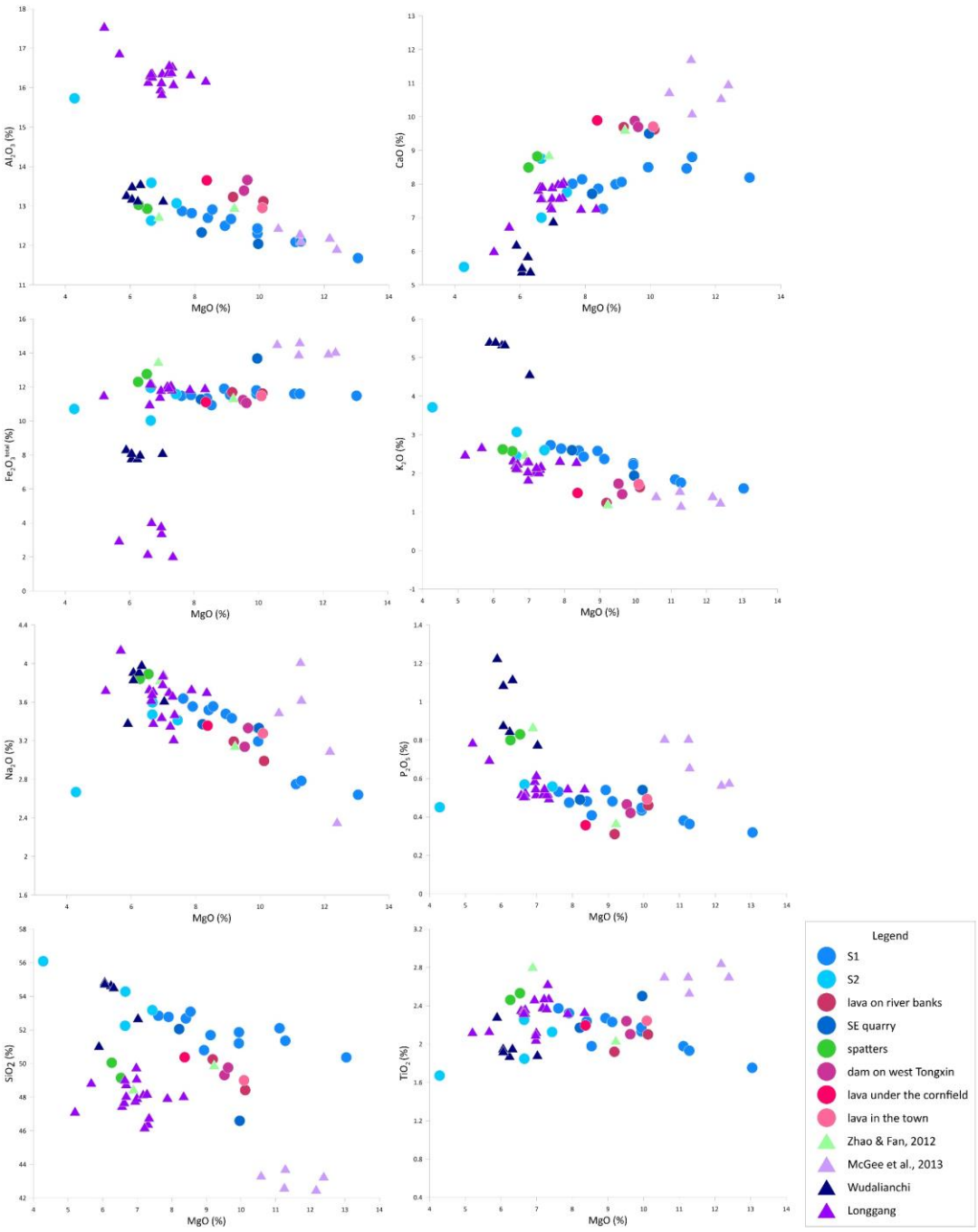

Figure 43: Binary plots of major elements on Tongxin locations (dots) and the comparisons to other pieces of research (triangles) (Hsu & Chen, 1998; Liu et al., 2009; McGee et al., 2013; Zhao & Fan, 2012). The whole spectrum of samples shows a typical trend expected within fractional crystallisation. It seems that the basal pyroclastic succession has a broad compositional spectrum covering nearly the entire compositional range (S1, blue dots), suggesting that this succession is already the result of a combination of various potential sources and fractional crystallisation.

When studying mafic magmatic systems, plotting magnesium oxide against other major element oxides is the fundamental way to observe the variations of a specific oxide representing a specific trend of fractional crystallisation (Winter, 2013). Thus, it

is sufficient to utilise the MgO content as the index to examine the trends between two oxides. Furthermore, the direction of fractional crystallisation, using the MgO concentration as a proxy, heads towards the decreasing direction of the numerical increase, which means the observer should have looked from the right side to the left side of the x-axis. As Fig 43 shows, an increasing trend occurs between magnesium oxide and alumina, potassium oxide, phosphorus oxide, sodium oxide, titanium oxide, and silica; decreasing trends occur between MgO and calcium oxide and total values of iron oxides (composed of Fe_2O_3 and FeO).

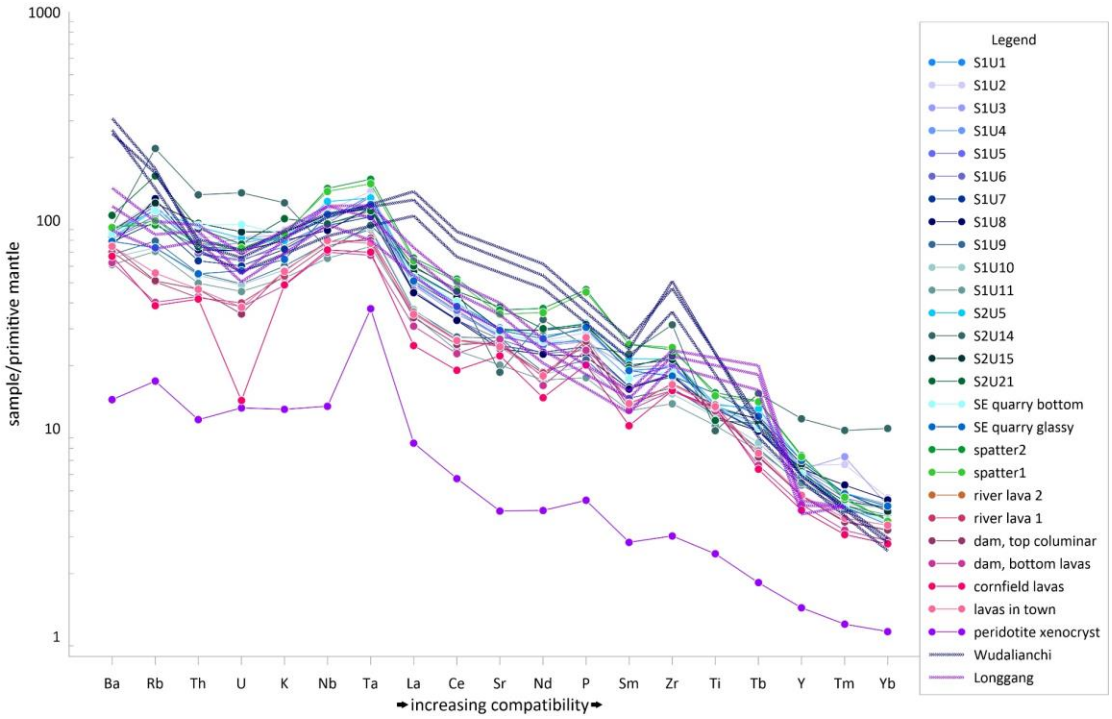

Figure 44: Multi-elements diagram with increasing compatibility from the left side to the right side of the x-axis of the trace elements. Note that the normalisation data is the ratio between the samples and primitive mantle data sets (Palme & O'Neill, 2003). Comparisons to the other two major monogenetic volcanic fields (Wudalianchi and Longgang) in NE China have been provided in this diagram (Hsu & Chen, 1998; Liu et al., 2009). This diagram indicates that every sample measured is nearly identical; hence the samples share a common petrogenetic province or feature that reflects their geodynamic position typical to intracontinental settings.

Fig 44 is the classic spider diagram of the multiple trace elements, which are incompatible on the left side and compatible on the right side. In general, the patterns of each sample are uniform. On the value of rubidium, values of lava flow show a negative trend in comparison to others; S2 deposits have the largest concentration of Rubidium with a positive trend. A similar situation occurs on the point of Strontium;

the lava flows show a positive trend; on the contrary, the deposits have a negative trend; this could mean that lavas are directly tapped from the source region fast, while the phreatomagmatic likely been tapped from different source regions from shallow storage; such storage may have proceeded fractionation processes already. The deposits on the bottom of S1 reveal a positive trend on thallium, compared to the negative trend on other sites. Specifically, unit 14 of S2 tells a non-uniform trend in general, with higher values on each element point. Also, the lava flows under the cornfield (47°33'9.20"N, 121°16'42.50"E) have an abnormality in the Uranium value, which is nearly identical to the one on the mantle peridotite xenocrysts.

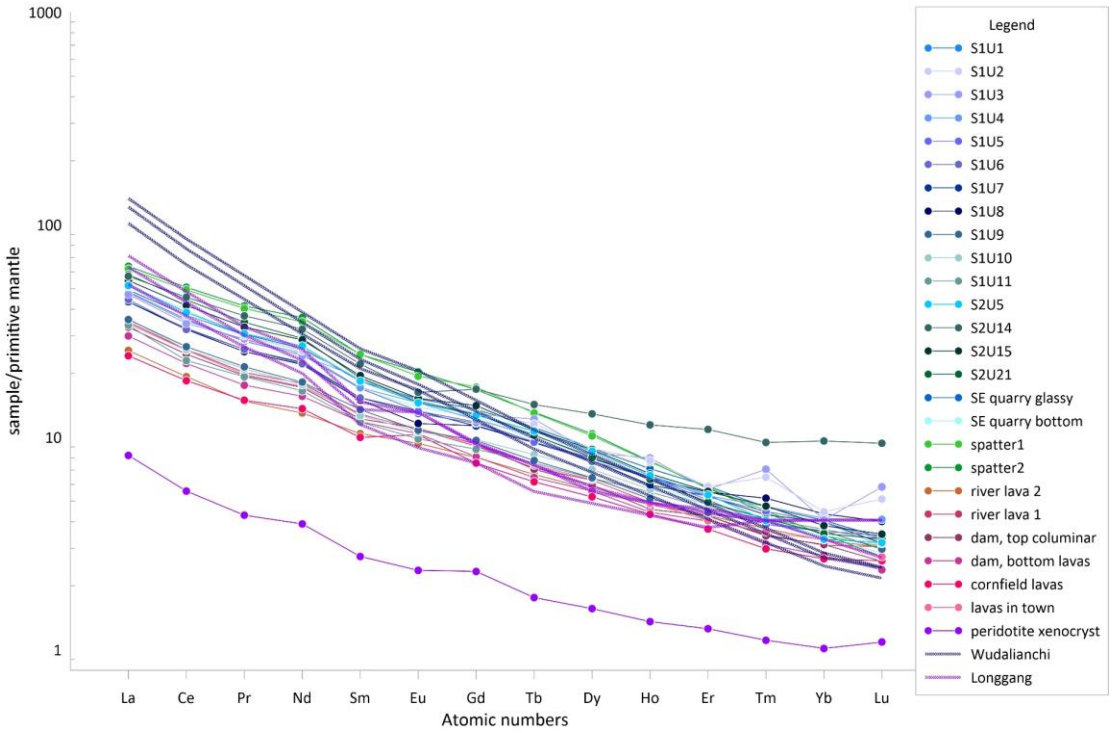

Figure 45: In the rare earth elements diagram, all data sets are normalised by primitive mantle data (McDonough et al., 1992). Comparisons to the other two major monogenetic volcanic fields (Wudalianchi and Longgang) in NE China have been provided in this diagram (Hsu & Chen, 1998; Liu et al., 2009). From this Fig, everything is very homogeneous, so the samples represent a common petrogenetic province. Also, the sample datasets are much higher than the mantle peridotite one; this could mean that melts may come from a shallow depth with evolved fractionation stages.

Fig 45 depicts the patterns of the rare earth elements (REE) with a homogeneous trend on each element. For Europium, the lava flows under the cornfield (Fig 18, orange dot) show a significant positive trend compared to the other REES. However, in thallium and Ytterbium, both positive trends (pyroclastic deposits) and negative trends (lava

flows) merge together. The values of Thulium from the bottom of S1 and the values of Lutetium from the same location yield an abnormality in comparison to others. Unit 14 of S2 generally has higher values from Terbium to Lutetium than other samples.

6. Discussion

1) Regional topography in relation to the distribution of volcanic deposits with subsequent lab analyses based on aspects of sedimentology

To the west of Tongxin Lake, hilly terranes and fluvial terraces developed a set of young topography, which represents post-eruptive hydrogeology. The Chaoer River, headwater sections in the north, is a fast-flowing river that transgresses through the flattened valleys as it goes south, bypassing the western flank of the lake. Serval turnings in the river have created a series of fluvial fans distributed on both sides of the river banks.

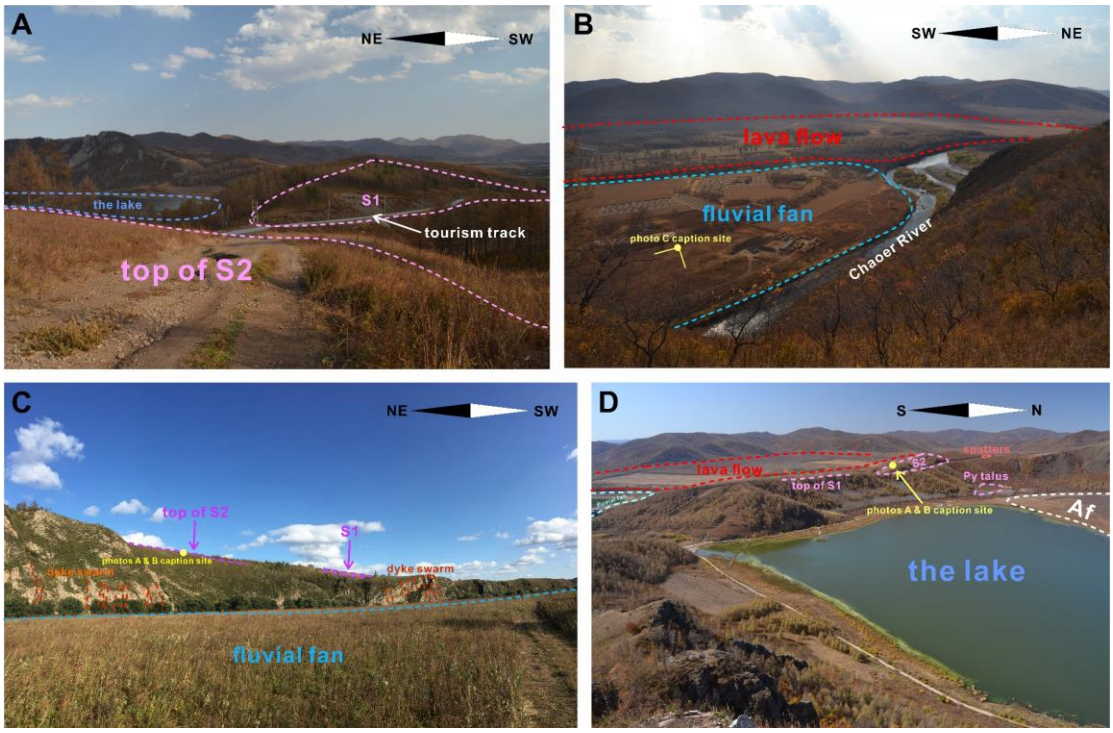

Figure 46: The geological and topographic features of the western sides of Tongxin Lake. Af = alluvial fan; Py = pyroclastic rocks, part of the tuff ring surrounding the maar crater. Photo A depicts the spacial relationships between S1 and S2 deposits. Photo B was captured on the top of the west flank of the lake rim. The caption site of photo C is shown in photo B; this photo shows the downhill trend from S2 to S1. Photo D is an overview of the western side of the lake; this one reveals further special relationships between the pyroclastic deposits and the adjacent situations (lava flows and topography).

On the western side of Tongxin Lake, the two major deposits, i.e., S1 and S2, lie on the top of the ring-shaped rim. As Fig 18 depicts, the two blocks of the deposits are separated from each other at about 350 m in distance. The elevations on both sites

are separated slightly by 705 m on S1 and 727 m on S2. This means that S2 is located on the upper-hilly trend in comparison to S1's location. Also, the dip angles of beddings in S2 show approximately 37-45 degrees toward the lower hill trend; this indicates that the beddings of S2 potentially dive into the surface of the top of the ridge and eventually intercalate under the beddings of S1. At least ten NE-SW striking vertical dykes up to 6m wide (but averaging 3m) and 4 m apart intrude the country rock (granite?) beneath the western outer rim of the Tongxin Lake tuff ring. (Fig 46C).

On the east flank of the lake (see Fig 19), the pyroclastic deposits cover the top of the ridge and extend downslope to the southeastern side of the town. The deposits nearly cover the whole southeast part of the ring rim. At least three spurs preserve pyroclastic deposits to the southeast until they stop at the point adjacent to an old valley filled up with earlier fluvial sediments. The spurs are approximately 300 to 500 m apart from each other. The deposits on the east ridge occupy the largest area.

In the north of the lake, the landscape is dominated by high-elevated ranges with intervening valleys (approximately 10.4 km^2). The area of the lake, valley and northern alluvial fan is about 16.3 km^2. The southern part of the valley is occupied by dispersed scoria boulders. In the upstream area, only country debris can be observed. On the western flank of the lake, spatter deposits, including dispersed scoria boulders, are present. These might be random fallout landings from the northern regions of the lake. The total area of the alluvial fan in the north is approximately 1.2 km^2. The area of the lake (about 1 km^2) is nearly identical to the area of the alluvial fan, and the average depth of the lake is about 5 m. Geomorphologically, the large volumes of the alluvial deposits are consistent with ongoing subsidence allowing for the accumulation of sediment. Based on this assumption, it is conceivable that the vent may lie beneath the alluvial fan. This would be consistent with the dykes mentioned above intruding from beneath the granites (country rocks). Thus, the magma batches might come into contact with the shallow aquifer systems associated with the fan to form a large crater due to magma-and-water explosive interaction, eventually creating a maar crater.

There is a distinctive breakage on the south of the ring-shaped lake rim. The country rocks are exposed on both sides of the breakage, which is covered by topsoil deposits. From the breakage to the lake's main entrance, there is no sign of lava flow in an

outcrop. Also, judging from the hydrogeology map, a small fluvial system has flowed from the south entrance to the town. The fluvial deposits formed the basement of the town's infrastructure, which is an area of approximately 1.1 km^2. No evidence of the lava flows near the breakage was found during fieldwork. It is possible that the outflow from the breakage is a remnant of an old fluvial system; the elevation is identical to that of the town, about 610 m. This elevation is lower than the elevation of the cornfield (approximately 620 m) to the south of the breakage. The cornfield appears to be a tiny plateau lying only 10m above the township. The riverbank deposits indicate that progressive fluvial deposits have been deposited to the south of the field. Quite steep slopes define the southern boundary of the field, approximately 50 degrees toward the south. To the north of the field, The slope is smooth and about 25 to 30 degrees heading in the north direction. An outcrop of lava flows was discovered on the southern margin of the field, which may imply that the lava flow is the basement of the cornfield. This corresponds to the relatively high elevation in this area in comparison to its surrounding areas.

The regional geology of Tongxin Lake is highly connected with the regional hydrological system. Chaoer River is one of the large fluvial systems in ACVF (Li et al., 2020). This river flows north to south, just west of Tongxin Lake. The area has been extensively modified by the Cenozoic volcanism in this region. The river reaches the southwest side of the town and makes a very sharp turn beside the cornfield in the south. Here the river curves away from the cornfield that has the lava flow as its basement. The elevation of the cornfield on the northern side is lower than that on the southern side (near the river), and analysis of the topography suggests the lava might have pushed the river to its south direction. The second turn is much sharper than the first. On both sides of the river channel, lava flows crop out on the riverbank, which indicates that the river is constrained by the flow. Also, this location is very near the pyroclastic deposits on the eastern flank of the lake, so it is presumed that the pyroclastic deposits played an important role in creating the syn-eruptive fluvial geomorphology.

Tongxin Lake and the surrounding Cenozoic volcanic materials lie on ancient country rocks, the Mesozoic plutonic rocks (Liu, 1989; Liu, 1993), which is the dominant

lithology of the Great Xing'an Range (Fig 2). The current volcanism preserves the old geomorphology and regional topography, enabling the calculation of the volumes of volcanic materials, thereby providing an estimate of the magnitude of the eruption and interpreting the volcanic evolution of Tongxin Lake. However, volume calculation is not straightforward for the deposits, even for bulk lavas. The first problem is determining where the basement lies beneath the deposits. Field observations (47°32'54.06"N, 121°17'34.62"E) along approximately 13 km of the Chaoer River have shown that the bottom of the river is filled with fresh fluvial deposits of boulders (up to 2 m in diameter); the river is no more than 7 m deep; hence the elevation of the river bottom is approximately 600 m above sea level. The bottom of the lava flows was not observed. The total estimated volume of lava flows is about 0.46 km^3 based on the surface area of the flow field and its estimated thickness

The volume of pyroclastic deposits is concentrated in the two major areas, the western and eastern flanks of the ring-shaped ridge. On the western flank, the two typical outcrops have been used to define the height of the deposits, 13 m and 30 m for S1 and S2, respectively. Due to the lack of exposure of the contact between the deposits and country rocks, an average height of 23 m has been applied. Thus, the volume of the deposits on the west flank of the lake is about 0.007 km^3, and the volume of the deposits on the east flank of the lake is about 0.044 km^3. The minimum volume of the pyroclastic deposits of Tongxin Lake is about 0.051 km^3 in proximal areas.

The lithofacies at each location are consistent with syn-eruptive sedimentation, such as fallout and base surge sedimentation processes. The lithofacies classified as T, LT, LS, TB, and PB (Table 4), are primarily based on grain size differences. In the proximal areas, T and LT indicate surge deposits due to the ash grain sizes; LS and TB represent air fallout deposits; PB is most likely to be bombs or ballistic projectiles due to their distinctively large grain size. However, in the intermediate and distal areas, the T or LT may indicate ashfall deposits (PDC do not travel such long distances); TB and PB are very rare in the pyroclastic deposits in such regions; TB tends to be the largest grain sizes found in the distal areas. Sedimentary structures are useful indicators of the processes and sedimentary environments present where the pyroclastic materials are

deposited during the syn-eruptive stages. Massive (m) beds indicate fallout or base surges in large ejected volumes; stratified (s) and pb may imply a typical channelling transportation behaviour; cb and d can reveal the shifting of the transportation directions and topography variations; ng and rg mean the continuous sedimentation and coarse-sediment transport lag during the settling processes of the coarse materials (Boggs Jr, 2014; Hand, 1997).

The grain size data using cumulative frequency curves of logarithmic weight percents vs grain sizes in ϕ values can provide insight into the distance from the vent location. When transportation occurs in a channel, and the transport medium is a Newtonian fluid, the cumulative probability curves are characteristical "S" shaped with three distinctive populations (slope intervals) representing traction, saltation, and suspension populations, respectively (Visher, 1969). However, volcanic eruptives can behave differently, especially where the sedimentation rates are high. The huge volumes of pyroclastic material being transported may not behave as a Newtonian fluid. The transportation processes are highly dependent on the type of edifice being built. For example, in the proximal areas, when the eruption starts, the initial deposits would immediately settle on the surface; the curve may plot as a series of straight lines. As the eruption proceeds, early deposits would create a tuff ring with a slope on the outer rim, and these transportation signals may emerge on the cumulative curves as a steep increasing line with a high slope value, which indicate the poor-sorted properties. In the intermediate and distal areas, reworked deposits from earlier eruptions might be present, and the shape of that accumulation will most likely reflect the distance they have travelled.

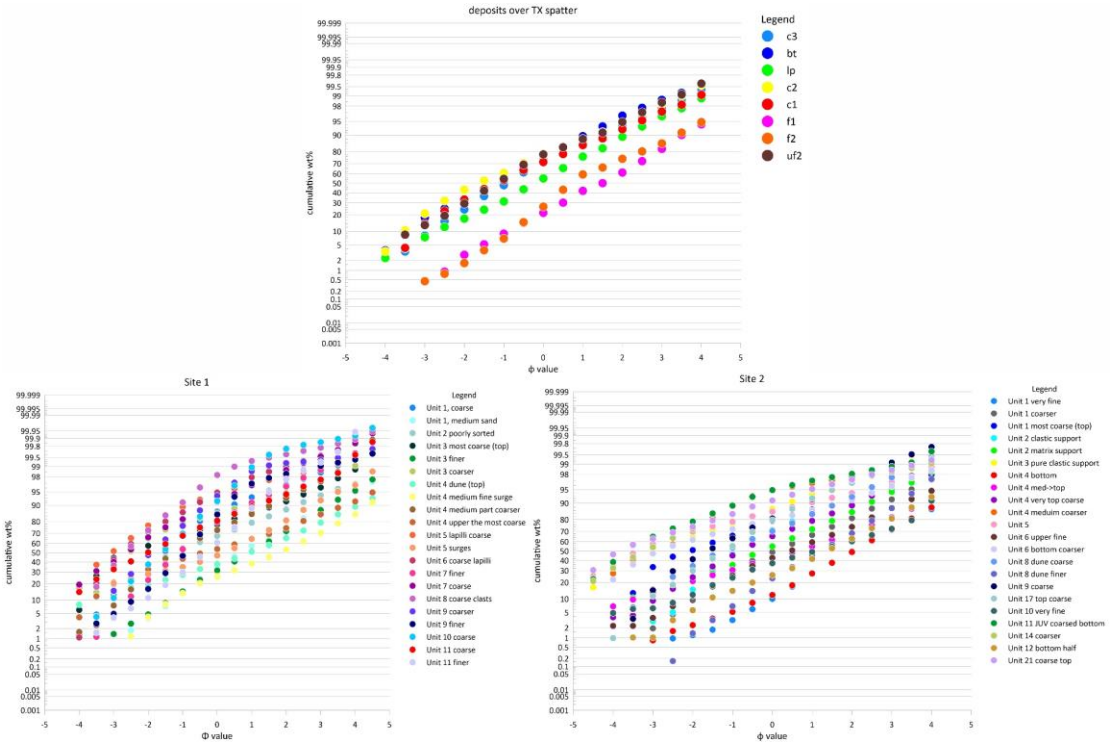

Figure 47: Cumulative frequency grain size curves of the deposits from the western flank of the partial tuff-ring (S1). Please note that the general trend is judged by the overall pattern rather than the trend of a single curve. These three plots show that the sorting is nearly identical due to the slope angle; this also means that the transportation behaviours are nearly none.

The cumulation distribution of the grain size of the deposits preserved on the western flank of the partial tuff-ring Tongxin Lake is shown in Fig 47. Most of the samples reveal a straight-line relationship meaning the deposits were most likely transported during the syneruptive sequences; it can be assumed that these deposits were settled immediately over the area without reworking or further transportation. If this interpretation is correct, then the proximal locations preserve primary pyroclastic deposits. Some of the samples from S1 and S2 show a two-population trend consistent with saltation and suspension populations. This is probably because the building of volcanic edifices formed a topographic slope, on which the subsequent deposits reworked to give a two-population trend. Also, the inner wall (S1) is likely to be more dominated by wet basal surge deposits rocketing up from the crater below.

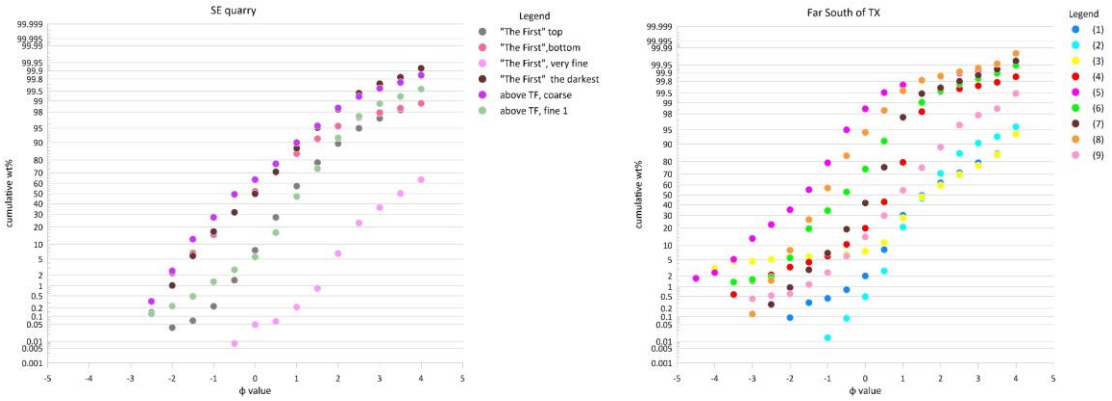

Figure 48: The cumulative curves from the SE quarry and the site far south of Tongxin Lake. The parameters are the same as in Fig 49, and please note that the legend of the far south of Tongxin deposits is correlated to Fig 31.

The deposits at locations (Fig 48) farther distant than S1, S2, and the spatters display the traction, suspension, and saltation populations that form the distinctive "S" shaped plot. The deposits from the SE quarry have moderated curvature compared to the ones of the far south of Tongxin Lake. Thus, the SE quarry should belong to the intermediate area, and the far south of Tongxin should belong to the distal areas. Also, this is surprising given that direct fallout could be expected because the PDCs were unlikely to travel this far.

Previous research has found that the slopes of the cumulative curves indicate variations in sorting (Friedman, 1962; Friedman, 1979; Khalaf et al., 1984; Seward-Thompson & Hails, 1973; Viard & Breyer, 1979). The sorting in the proximal areas (Fig 47) has a low value, whereas sorting comes from depositional processes in intermediate and distal areas (Fig 48) and shows large variations reflected by the different slopes of curves in each population. Obviously, the saltation part has the well-sorted property (lowest slope). The poor sorting of the proximal deposits always shows a similar wt% amount on each grain size fraction, suggesting the normal distribution curves have an "even" top (moderated kurtosis) and vice versa. In contrast, the "pointy" top (high kurtosis) of distribution curves indicates better-well sorting.

Facies in each pyroclastic deposit show a range of repeated sequences related to grain size variations. Each combination of facies and sedimentary structures reveals a typical syn-eruptive style and behaviour. Those facies signals may provide evidence that could lead to stratigraphic correlations at different locations. For example, S2 deposits (Fig

23) preserve the greatest amounts of primary pyroclastic materials (not reworked). From the bottom to the top, most of the units are composed of fine to very fine ash; and as mentioned above, S2 deposits are the ejecta from the proximal area on the inner wall of the partial tuff ring. Thus, facies T and LT can be deemed as the surge deposits, facies LS and TB are the fallout deposits, and facies PB can be classified both as fallout and ballistic projectiles. Thus, the lower section of U1, from S2, is formed by a range of surges (shockwave blasts). In the upper section of U1, the non-bedded lapilli (LS-m) represent small volume fallout materials erupted with the surges.

The spatter, and its overlying deposits, are found on the upper hill, indicating that the spatter underlies the S2 deposits. The spatter deposit contacts with underlying granite (country rock); thus, it can be imagined that the initial eruption was lava fountaining with subsequent phreatomagmatic explosions. In the intermediate and distal areas (SE quarry and far south of Tongxin, respectively), the T and LT facies consist of ashfall because the surge deposits can travel a long distance, the same as LS and TB (lapilli fall). There are no signs of PB facies. The bombs triggered by the eruptions only travel short distances; hence they are restricted to the proximal areas (Schmincke, 1977; Schumacher & Schmincke, 1991; Self & Sparks, 1978).

Compositional analyses, together with the ratios between the types of clasts from the deposits, reveal the type of volcanic structures forming. The S1 deposits (the first row of Fig 37) are primarily juvenile clasts (pink) with accidental lithics (deep blue) present in secondary amounts. Juvenile and lithics co-dominate, which means large volumes of accidental lithics come from the area surrounding the vent. The particles are angular to sub-angular (Fig 39), consistent with the particles being violently fragmented and transported by the significant eruptions. The large amounts of accidental lithics reveal excavation processes, which triggered the collapse of the wall of the vent, and then the bedrock materials mixed with the lava that subsequently erupted from the vent. The deposits overlying the spatter (the third row of Fig 37) also contain large amounts of lithics, which means the early eruption sequences resulted in excavation. The clasts in S2 are very angular (Fig 23B), suggesting the excavation processes were intense during the syn-eruptive stages.

The density (Fig 38) of the two major deposits (S1 & S2) show a similar frequency pattern. The sub-to-angular shapes of the clasts from field observations support that both deposits were formed by phreatomagmatic eruptions. Furthermore, there are large amounts of lithics, and these are the main components during explosive eruptions. Thus, the porosity of S1 and S2 deposits indicates the possibilities of water-magma interaction times. The values of the porosity are the calculations for the open pores and closed pores. A large number of pores of the lapilli deposits indicates the fractionation triggered by water-magma interaction (Agustín-Flores et al., 2021; Eichelberger et al., 2020; Geshi et al., 2019; Go & Sohn, 2021; Heap et al., 2021; Mueller et al., 2011; Ngwa et al., 2010). The U1, U4 and U9 of S1 are the peaks of the curve, which may imply the three times water injections from the aquifers, the same concepts for U2, U6 and U11 of S2. However, on average, the porosity values of S1 are higher than the values of S2. This could mean that the S1 deposits had experienced more fragmentation than the S2 deposits. The significant water-magma interactions occurred at least three times during the syn-eruptive phases.

Electron-microscope images with SEM and BSD reveal the external structure of the juvenile clasts. These images reveal magma fragmentation by water-magma interactions, e.g., high vesicular density, sub-rounded shapes and quench phenomenon. Figures 39A, B & C show relatively low magnitudes of fragmentation with highly evolved crystal systems. Photo H reveals similar crystallisation stages, in which the large anhedral xenoliths intercalated within the crystal groundmass. Photos E and G depict the non-crystallised phases. Those two clasts are basically glassy shards, which are a minor component of juvenile materials. There is no sign of crystals on the surfaces of the glassy shards, which means these particles may have experienced quench processes with insufficient time to form crystals, only mafic groundmass. Photo D depicts a glassy shard with fewer crystals than glassy shards, indicating the intermediate stages of the chilling procedures. Photos F and I show two glassy shards with high numbers of pores on the surfaces. This may imply that the magma had experienced a high magnitude of quenching with the abundance of water-triggered severe fragmentation subsequently.

2D BSD images (Fig 40) show the juvenile particles from another perspective. Photos C, D and E depict the evolved crystallisation phases, especially photo C, which shows crystal zonation on the bottom left, indicating the growth of a subhedral plagioclase crystal. Photos D and E also show the large accidental lithics enclosed by the juvenile materials. Photos A, F, H, and I represent glassy shards triggered by the quench processes. However, photos F and H reveal a distorted shape in a particular orientation. The deposits where photos F and H were taken were found in the SE quarry location, where the deposits are in contact with the country rock. Judging by the photos, the sheared shape is preserved, and the bubbles imply early eruption fuelled by the water-magma interactions resulting in rapid cooling processes. The magma batches were pushed out at high velocity, generating this sheared shape. This also may suggest that the cooling processes were prior to the eruption phases; in other words: the magma batches may have already been chilled at depth and then erupted. The zonation structure on the plagioclase crystal indicates long stages of magma evolution of the mixing procedures.

One possible conclusion is that the early eruption was triggered by the high magma ascent rate (quench), and then the following eruption phases were fuelled by the intermediate or even low magma ascent due to the high evolution and developments of crystallisation.

2) Discussion on chemical variations recorded

Major and trace elements of the juvenile materials from deposits and bulk lavas surrounding Tongxin Lake reveal the trends and distributions of the magma evolution. The TAS diagram (Fig 42) shows that the pyroclastic deposits from S1, S2 and the SE quarry are in the transitional zone between andesitic and basaltic composition S2 deposits lie within the areas of basaltic trachyandesite whilst S1 deposits cross three compositions of basaltic trachyandesite, trachybasalt, and basalt. S2 deposits are older than S1 deposits due to the depositional emplacements mentioned above; hence the early eruptions were andesitic and then became basaltic. The bulk lavas, based upon the mafic minerals, are trachybasalt and basalt. In comparison to other volcanic fields (AVF in New Zealand and Longgang Volcanic Field in NE China), the deposits from Tongxin Lake and bulk lavas are intermediate rather than mafic.

The lava flows around Tongxin Lake are thickest to the far south of Tongxin Lake (Fig 41E), reaching approximately 12 m. Photos B, C, D and E show the columnar jointing typically seen in outcrops. In general, the topsoil layers cover the top of the lavas with fully vegetated growth. Commonly, the young lava flows have pahoehoe or aa types of rough surfaces. For basaltic lavas, the erosional rate may take at least 0.14±0.09 km^3/kyr, which approximately equals 3 mm/kyr on average (Bablon et al., 2020; Büchner & Tietz, 2012; Uchman et al., 2020). Compared to the Yanshan-triple vent 55.6 km west of Tongxin Lake (0.162 ± 0.02 Ma) (Fan et al., 2011), the aa-type lava has created rough surfaces 25-35 cm thick, formed 2000 years ago (Bai et al., 2005). Furthermore, there is no sign of ejecta from dry-eruptive phases (scorias) on the top of the pyroclastic deposits.

The major element diagrams (Fig 43) show the possible processes that have occurred during magma evolution governed by the fractional crystallisation of the magma. Commonly, basaltic magma has large variations in magnesium values but small variations in silicate in elemental analyses (Wilson, 1989; Winter, 2013). On the diagrams of MgO vs SiO_2 and Fe_2O_3, the increasing and decreasing trends, respectively, indicate the crystallisation of olivine and/or pyroxene crystals from the melt. Also, the decrease of CaO commonly implies the removal of the calcic plagioclase crystals from the early-formed melt. This is correlated to the diagrams of SiO_2 and Fe_2O_3 (Fig 43). The plots of MgO vs Na_2O and K_2O show an increasing trend on both oxides, suggesting that calcic plagioclase compositions may settle down in the plagioclase crystals; otherwise, the potassium feldspar crystals may not form or only in a minor amount. The increasing trend of Al_2O_3 corresponds to the decreasing trend of CaO; this may indicate that the clinopyroxene (CPX) crystals crystallised from the early-formed melt.

The multi-element diagram (Fig 44) shows a pattern in which the high concentration of incompatible elements and a low concentration of compatible elements more or less correspond to the ocean island basalt (OIB) pattern (Weaver & Tarney, 1984). The uniform pattern of the analyses (blue and deep green gradients) indicates a heterogeneous mix from different sources due to the multiple peaks, i.e., Rb, Ta, P, Zr and Tb. From the plot, the two phases are represented by larger ion lithophile (LIL) elements, such as Rb, K and Ba, and fewer high field strength (HFS) elements (Zr, Ti

and Y). Thus, the LIL elements are concentrated within the glassy groundmass because LIL elements are in favour of liquid phases in equilibrium melts (Winter, 2013). Otherwise, the HFS elements might be crystallised and reshaped into microlites. Negative Nb implies that the crustal assimilation might evolve during the magma ascending. Concentrations of LIL elements indicate those elements were from the continental crust, which marks the contamination of the magmas. REE plot (Fig 45) shows an overall trend of highly enriched LREE and low concentration of HREE. This trend might indicate that the melt was mafic due to the depletions on the HREE side. The depletion of the HREE (Dy, Ho and Tm) may imply garnet-bearing sources. The negative Eu anomaly reveals the removal of the feldspar crystals from the melt. S2U14 has high concentrations of HREE (>10), which means the melt was felsic. This might suggest that the crustal materials are reinjected to the melt. S1U2 and S1U3 have positive Tm and Lu anomalies which denote that the magma batches ascended from different sources or were mixed with small volumes of felsic material.

The comparison of ACVF with two major monogenetic volcanic fields in NE China (Wudalianchi and Longgang) suggests that the mafic materials in ACVF are more primitive than the materials in Wudalianchi and Longgang by observation on binary plots of major elements. The three volcanic fields share a similar tectonic setting, but display differences in their geochemistry which deserve further investigation.

7. Conclusion

This paper documents the volcaniclastic geology of Tongxin Lake/Volcano in the NE corner of the ACVF. The major findings, combined with field observations and lab works in relation to sedimentology and geochemistry methods, are listed below.

1) Geomorphology and stratigraphy:

It is confirmed that Tongxin Lake is a volcanic lake, evidenced by the presence of abundant pyroclastic deposits and volcaniclastic talus on the east and west flanks in the vicinity of the lake basin.

The Chaoer River is the major fluvial system in the region. It has vastly modified the geomorphology and eroded volcanic materials over large areas, especially in the

southernmost region of the main depositional axis of Tongxin Volcano's phreatomagmatic successions. The river has exposed older lava flows emplaced in the ancestral fluvial system the modern Chaoer River occupied later, but no evidence was found to locate key deposits of TOngxin Volcano for more general stratigraphical correlation. This is interpreted as a sign of the complex geomorphological interaction between a large water flux fluvial system and the loose, easy-to-eroded pyroclastic succession of the tuff ring formed around the maar crater.

General reconnaissance mapping also revealed that older pre-Tongxin lava flows are complex in architecture and represent a long-lasting fluvial system succession of lava effusions occupied over a long time prior to the Tongxin Volcano explosive eruption. On the other hand, the distributions of the pyroclastic deposits associated with eh TOngxin Volcano concentrate on the southern part of Tongxin Lake, and there are no preserved pyroclastic deposits found in the north. This is interpreted as a sign that the eruption may have been very unidirectional, especially to release pyroclastic density currents toward the south where the ancestral Chaoer River broad fluvial channel was running through. The paleo-Chaoer River most likely existed in the time of the volcanism, and field relationships suggest the lava flows might have modified or controlled the fluvial channel and the course of the river.

Spatter deposits have been identified in the northern sector of the TOngxin crater rim in contact with the country rock, suggesting that the early eruptions included lava fountaining and Strombolian-style explosive events. The overlying pyroclastic deposits imply, however, that subsequent eruptions were phreatomagmatic. The changes in eruption style are inferred to be the result of subsequent magma batches interacting with available shallow water tables. This could have been achieved by the gradual shifting of actual eruption points along a fissure by moving it to more low-lying and water-saturated regions, such as the front of a prograding pre-volcanic fan within an intramountain depression.

The pyroclastic deposits identified were dominantly pyroclastic density current deposits as evidenced by the presence and abundance of sedimentary features such as parallel bedding, dune structures and cross-bedding, overlain by indurated fine ash.

The successions of interbedded fine and coarse materials indicate that multiple explosions took place.

2) Sedimentology:

Sequences of the different eruptive phases (T, LT vs LS, TB in lithofacies) have been described from five different locations (S1, S2, SE quarry, Spatter site and Far South of TX). A fifth lithofacies (PB) consists of ballistic projectiles (bombs).

The pyroclastic deposits are predominantly composed of accretionary lapilli juvenile and accidental lithic pyroclasts, all dominantly fine to coarse ash. Shape analyses from 3D SEM and 2D BSD images suggest that irregular shapes of those clasts are an indicator of forming under severe interactions of magma mixed with water. This also suggests that fractional crystallisation processes were taken place in different magnitudes. The pyroclastic rocks from each site are very poorly sorted. The GSD range from unimodal bimodal to trimodal and might denote deposits of PDC origin. Material from S1 and S2 and the deposits above the spatters represent areas proximal to the eruption; farther south, SE quarry and TX are distal deposits.

Most of the main pyroclastic succession is dominated by accidental lithic dominate most of the deposits. The excavation of accidental lithics from the conduit walls and crater zones is strong evidence that Tongxin Volcano is a maar volcano with a tuff ring.

Juvenile clasts contain large numbers of vesicles in various shapes, reflecting an enhancing role of the magmatic volatiles alongside the magma-water interaction, indicating that the eruptions were violent phreatomagmatic. It could also imply that intermediate compositions mean the magma is slightly more volatile-enriched. (maybe unlikely from such depth, still needed to prove this idea).

3) Geochemistry:

The magma batches, as determined by the TAS diagram, show that the eruptives are trachybasaltic materials, including some basaltic andesites. The products of Tongxin Volcano (PDC) present a range of crystal fractionation and mixing trends during the magma ascending processes. The volcano was most likely fuelled by different magma batches denoted by the multi-elemental enrichment and depletion trends. Early

ejecta, such as spatters, are found to be the most primitive materials among Tongxin eruptive products. The subsequently produced PDCs are more evolved. This could mean that after the initial deep-sourced magma batch erupted, the processed mobilized magma packets in shallower regions of the magmatic plumbing system; hence more evolved magma was evacuated. Eventually, the conduit and vent cleared, leading to fuel volcanism through an open conduit along repeated magma packets that were able to sustain explosive eruptions over hours, maybe days, and experience vent shifting.

MASSEY UNIVERSITY
GRADUATE RESEARCH SCHOOL

STATEMENT OF CONTRIBUTION
DOCTORATE WITH PUBLICATIONS/MANUSCRIPTS

We, the candidate and the candidate's Primary Supervisor, certify that all co-authors have consented to their work being included in the thesis and they have accepted the candidate's contribution as indicated below in the *Statement of Originality*.

Name of candidate:	Bo'xin Li
Name/title of Primary Supervisor:	Prof. Károly Németh
Name of Research Output and full reference:	
Geodiversity estimate of the Arxan-Chaihe Volcanic Field extending across two geoparks in Inner Mongolia, NE China	
In which Chapter is the Manuscript /Published work:	Chapter 4
Please indicate:	
• The percentage of the manuscript/Published Work that was contributed by the candidate:	Bo'xin Li, 80%
and	
• Describe the contribution that the candidate has made to the Manuscript/Published Work:	
Prof. Károly Németh, Dr. Vladyslav Zakharovskyi, Mrs Julie Palmer, Prof. Alan Palmer, and Prof. Jonathan Procter	
For manuscripts intended for publication please indicate target journal:	
Geological Society, London, Special Publications	
Candidate's Signature:	Bo'xin Li
Date:	
Primary Supervisor's Signature:	Prof Karoly Nemeth (Digitally signed by Prof Karoly Nemeth, DN: cn=Prof Karoly Nemeth, c=SA, o=Saudi Geological Survey, ou=National Earthquake and Volcano Program, email=nemeth.k@sgs.gov.sa, Reason: I am approving this document, Location: Jeddah, Kingdom of Saudi Arabia, Date: 2023.05.08 13:00:53 +03'00')
Date:	8 May 2023

(This form should appear at the end of each thesis chapter/section/appendix submitted as a manuscript/ publication or collected as an appendix at the end of the thesis)

Chapter 4: Geodiversity estimate of the Arxan-Chaihe Volcanic Field extending across two geoparks in Inner Mongolia, NE China

This chapter has been published, and the final version is on the website- https://www.lyellcollection.org/doi/10.1144/SP530-2022-130. The majority of the research was performed by the author, Bo'xin Li, who is under the supervision of Prof. Karoly Nemeth, Prof. Alan Palmer, and Mrs Julie Palmer. Also, it is much appreciated to Dr Vladyslav Zakharovskyi, who contributed to the GIS background.

1. *Abstract*

Arxan-Chaihe Volcanic Field is located southwest of the Great Xing'an Range in Inner Mongolia, NE, China. This monogenetic volcanic field formed in the Pleistocene, with its latest activity a fissure eruption about 2000 years ago. Here we present the first geodiversity estimate of the region, applying a method combining the geomorphological and geological elements into a grading system, weighting their rarity, significance, and uniqueness. In order to outline the geomorphological diversities, the geomorphon concept was used alongside watershed analysis of the theoretical fluvial network of the region. In addition, volcanic geomorphological elements were provided. Available geological maps, field surveys, and volcano geology classifications were utilised for the geological diversity estimates. Geology and geomorphology are the core parameters of the qualitative-quantitative assessment of geodiversity. Geographical Information Systems (GIS) have been used for calculations of geomorphological and geological parameters to provide geodiversity estimates for the region of ACVF. The variables used to estimate geodiversity include rock type, geomorphology, fluvial systems, slopes, and terrain (geomorphon). Our study assessed recent volcanic features and concluded they have high geodiversity and elevated geoheritage values. However, the uplifted and structurally complicated old terrains with mature fluvial networks provide high geomorphological diversity to the region, therefore keeping the overall geodiversity score high.

Keywords: geodiversity, geopark, geosite, monogenetic volcanic field, maar, scoria cone, lava, China, UNESCO

2. *Introduction*

Arxan-Chaihe Volcanic Field (ACVF), located in the southwest of the Great Xing'an Range, northwest China (Figs 49 & 50) (Sun et al., 2017), was formed within the Central Asian Orogenic Belt (CAOB) - through intraplate, continental monogenetic volcanism.

Here we selected the ACVF as a research subject on the basis of its superb recent to historic volcanic features that are unique in the region's geological context being far away from any active plate boundaries. In this context, its volcanic geoheritage is the main geological feature that stands out from other geological elements. In this study, we primarily focus on the characterisation of the study area from geology, geomorphology, and climatic conditions. We have not explored vegetation cover and the cultural aspects of the heritage elements of the region, as information is sporadic and uneven in these subjects. We, however, acknowledge that these heritage elements can be significant values mostly for geotourism aspects of the region and suggests exploring these values in future research. On the other hand, these values are commonly referred to as additional heritage elements and are not part of the core or main values of geoheritage. This is also under debate and a subject of global discussion; hence we kept our focus on the main geoheritage elements in this study.

The region occupied by ACVF was subject to convergence during the Paleozoic period when the Paleo-Asian Ocean plate was subducted beneath the rigid Asian platform. During the Mesozoic, the Paleo-Pacific Ocean plate in the east and the Mongol-Okhotsk Ocean plate in the northwest controlled the major tectonic movements in the region (Li et al., 2018). During the Mesozoic, metamorphism that shaped the mountain outlines took place, causing extensive deformation and magma emplacement forming batholiths and intrusive complexes. Great Xing'an Range is approximately 1200 km from north to south, made up of lowlands in the east and highlands in the west. The main elevation of the highest peaks of the Great Xing'an Range is about 1200 to 1300 metres above sea level (sources from: https://www.britannica.com/place/Da-Hinggan-Range). The Great Xing'an Range is

comprised predominantly of volcanic lithologies (basalt, andesite, dacite with minor rhyolite) generated by subduction of the Paleo-Asian Oceanic plate beneath a paleo-island-arc (Feng et al., 2018). In the Pleistocene, ACVF consists of continental basaltic volcanism that formed in response to weak rifting, causing intracontinental volcanism far from active plate margins.

Geodiversity is a relatively new concept that evaluates and assesses the abiotic nature of a region, including the geology, geomorphology and soil features and how the landscape has evolved—the most obvious geologic feature of ACVF volcanism. The annual precipitation in this area ranges from 30-50 mm in spring, 250-300 mm in the summer, and about 50 cm thick of snow covers in the winter time on average (source from:http://www.aesly.com/gotoaershan/ZRAeshan/Meteorological/20130725173056152.html). The mountains and hills of ACVF lie 200-300 m above the valley floor. The volcanic field includes lava-ponded lakes and crater lakes (Fig 49), with four main rivers and their tributaries located in the region's eastern part. These form a landscape dissected by river systems where the volcanic history and landscape development of ACVF can be studied. Hence, the region is well suited to establishing a logistics network of educational centres catering for geotourism and geoeducation. By using each of the geodiversity elements (geology, geomorphology and associated hydrology), the diversity of geosites can be established, and those with significant diversity can be identified, and the data used to promote their preservation through geoconservation.

3. *Aims and methods*

Utilising qualitative and quantitative assessment methods will highlight the most valuable geodiversity parameters and identify features to become potential geosites. In the geodiversity estimate, we followed the recently introduced method of applying the geomorphological and geological features recognised in the field to an 8-point grading system (Zwoliński, 2009; Zwoliński & Stachowiak, 2012) and measuring the average values across selected areas. The results were entered into GIS to model the region's geodiversity and identify the most significant places for potential geosites. In our research, we used the SRTM (Shuttle Radar Topography Mission) topographical database to create digital elevation models of the region. A Digital Elevation Model

(DEM) was then used to analyse the terrain for slope variations and morphological features to create a geomorphon distribution map. We employed QGIS freeware to provide tools for the readers to follow our methods in other regions and used available plugins and software packages (e.g., Grass GIS) compatible with the QGIS environments. For the geological data, we used available geological spatial information from the region and compiled them into a geological map. To outline the volcanic vents, we used the combination of satellite imagery derivative DEM maps (e.g., aspect ratio map) together with the available georeferenced geological maps. Locations were cross-checked in the field to validate the selected outline settings. Here we present the descriptions and interpretations of the geodiversity variables: geology, geomorphology, and hydrology. This information forms the database for assessing the geodiversity of the region, including identifying significant locations and documenting the attributes that make the locations unique geosites.

The main goal of this research is to identify important geosites in ACVF and to provide an accurate and reproducible evaluation of the diverse range of geology in the region. The geological, geomorphological, and hydrological descriptions were confirmed during field excursions of ACVF from 2017 to 2019. Identifying important and accessible outcrops and putting them into a geological (volcanic and tectonic) context will provide the foundation for establishing geosites.

4. Geopark context from volcanic geoheritage perspective

The study area is located in two independent geoparks that the Chinese National Tourism Institute established in Feb 2017. Arxan UNESCO Global Geopark (Fig 49) is located in the west, and Zalantun (Zhalantun) Geopark lies in the east (Fig 50). Both geoparks are part of the Chinese National Geopark Network.

1) Arxan UNESCO Global Geopark

The ACVF, its main geological entity, was officially approved as the 34th UNESCO Global Geopark of China and a member of the Global Geoparks Network by the 201st Session of the UNESCO Executive Board in 2017 (Németh et al., 2017a). At least 47 volcanic vents are identified in ACVF, covering approximately 2000 km^2. However, only 20 locations preserve distinctive volcanic features and have easy access. Furthermore,

only 9 locations have become scenic spots and are promoted by the geopark. There is potential to identify additional locations; hence geoheritage research should focus on studying and promoting additional geological landmarks. ACVF is divided into four different precincts: the Halaha Geo-region (Fig 49, No.1), the Tianchi Geo-region (Fig 49, No.2), the Hot Spring Geo-region (Fig 49, No.3), and the Haosengou Geo-region (Fig 49, No.4). About five significant (e.g., large and recognisable) vents are located in Tianchi Geo-region. These are commonly associated with volcanogenic lakes (e.g., crater lakes and lava-dammed lakes). The volcanism in the region is dated as Pleistocene to Holocene (Fan et al., 2011; Liu, 1987; Meng et al., 2018; Sun et al., 2017). However, older Miocene to Pliocene basalt lava flows from unknown sources are known along the Halaha River and other less-studied tributaries, indicating sporadic intracontinental basaltic volcanism at least since the Miocene (Fan et al., 2011). The Tianchi Lake (Heaven Lake) is a distinctive scoria cone formed by lava fountaining that subsequently built an agglutinated scoria cap on its top, which is now occupied by a lake. Earthly Pond, located south of Tianchi Lake, was most likely formed by a single explosive event triggered by the accumulation of gas beneath the lava flow (Boreham et al., 2020). Turtle Back Rock is formed by a 3 km long lava flow, and Arxan Grand Canyon is where lava flows have been incised by regional fluvial systems to form a V-shaped valley flanked by exposed columnar jointed basalts, and various rock falls formed due to the frigid northern zone of the region. The banks of the river expose basaltic lava flows with cracked talus/boulders and rough surfaces resembling blocky lava flow surface textures. Shitang Lin is a ponded lava flow with overgrown vegetation. The dominantly 'aā type lava flows followed the original topography, and lava tumuli formed in the foothills of the general westerly sloping terrain in the Halaha River valley, where four lava-dammed lakes were created. These spectacular tumuli formed when the lava emitted gas and created a range of small inverted cone structures (Anderson et al., 2012; Ollier, 1964). Tuofengling Lake (Camel Hump Lake) is another Cenozoic (most likely Late Pleistocene) vent, which is part of a scoria cone complex where phreatomagmatic pyroclastic deposits lie beneath the scoria cap. The lakes and vents described above are valuable geosites where a wide spectrum of geological features would make a valuable contribution to geoheritage and geoeducation in ACVF. Furthermore, the presence of non-volcanic geological

processes, both pre-and-post eruption, provides valuable geological context to the geopark and geoheritage of ACVF. The Arxan National Forest Park earns profitable income for economic growth. Tourism attracted 3.00, 4.31, and 2.60 million visitors to the region in 2016, 2018 and 2020, respectively (source: 2016 http://www.ce.cn/xwzx/gnsz/gdxw/201708/12/t20170812_24971554.shtml, 2018 https://www.mct.gov.cn/whzx/qgwhxxlb/nmg/201904/t20190424_843073.htm, 2020 https://baijiahao.baidu.com/s?id=1723175475603363833&wfr=spider&for=pc accessed on 15 August 2022). Promoting the geoheritage values of ACVF could greatly enhance the tourism earning potential of the region.

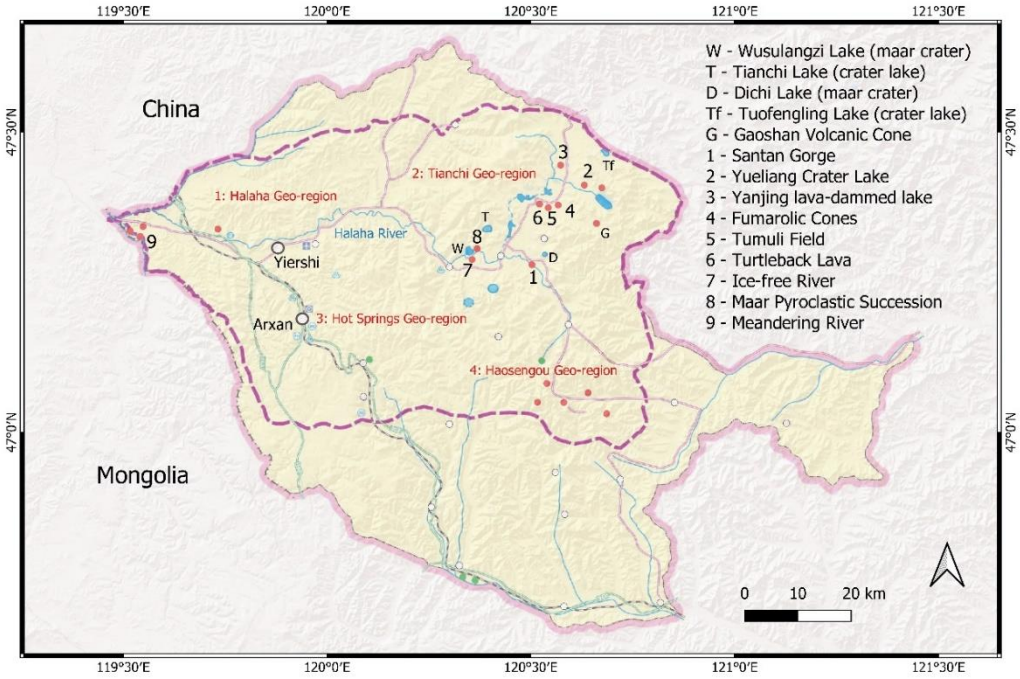

Figure 49: The overall outline map of administrative divisions in ACVF (data source from: https://www.chinadiscovery.com/inner-mongolia/hinggan-league/arxan-unesco-global-geopark.html). The pink line represents the administrative boundary of the Arxan Region. A dashed dark pink line shows the boundary of the Arxan UNESCO Global Geopark. Labels and numbers refer to key geosites (the most representative sets of geological features of the geopark) identified and fall under geoconservation management. Red dots mark other geosites outside the volcanic regions of the geopark. Main towns of Arxan and Yiershi function as major tourist centres, with an airport in Yiershi and geopark headquarters, as well as an information centre with interactive museums in Arxan. Geocultural sites are marked with green dots. The main road network and railroad (dark dashed line) are marked. Geospatial data is from ESRI Transportation and ESRI Shaded Relief database.

2) Zalantun/Zhalantun Geopark

The Zalantun, also transcripted as Zhalantun Geopark of the Chinese National Geopark Network (Fig 50), was established in 2017. This national park lies within the ACVF but is governed by different local authorities. This area is politically separate from Arxan. Zalantun National Forest Park contains several scenic spots. Among them is the Tongxin Volcano in Chaihe Town - a distinctive geological feature that represents the most valuable geodiversity prospect in ACVF. Currently, there are three classified geosites in Zalantun territory: Moon Lake, Bear Mountain and Tongxin Lake. All of these locations are related to post-Pliocene volcanism, which has a similar genesis to the vents in the Arxan area. Moon Lake is a scoria cone with a circular cone that hosts a shallow lake (Zhao et al., 2017). However, thick vegetation cover obscures much of the preserved pyroclastic successions. Bear Mountain is an older dissected scoria cone with an erosion-resistant crater rim covered by lava spatter. Its edifice is more voluminous than Moon Lake. Scoria deposits are distributed around the vent. Tongxin Lake is the largest vent in ACVF, formed by the most violent explosive eruptions (Németh et al., 2017a). Geological features with a high geodiversity value in the Zalantun region include eroded pahoehoe lava flows, spatter deposits, pyroclastic deposits, and a crater lake. Distinctive volcanic landforms in the Zalantun area are recognised at 14 locations. Most of them, which are found around Tongxin Lake, was formed by Strombolian-style explosive eruptions, fissure-fed lava-dominated processes, and maar-forming explosive activity. Volcanism around Tongxin Lake (including bulk lava flows and PDC-Pyroclastic Density Current deposits) distributes an area of about 40 km^2. Pyroclastic deposits indicate the occurrence of phreatomagmatic explosive eruptions. The associated landforms and deposits formed by these events are preserved on the west flank and to the south of Tongxin Lake. A maar crater is inferred in the current location of Tongxin Lake. The talus (deposited in the inner tuff ring structure) comes from the outer rim from the suspected collapse of a steep maar crater wall. The landforms that were created by the basaltic lava flows formed lava terraces, lava valleys, blocky lavas, and columnar jointing, as well as spatters (a unique feature of Tongxin Lake). The geodiversity of the Zalantun area, which has the highest number of volcanic vents in Inner Mongolia, NE China (Wang &

Tian, 2013), includes Cenozoic volcanism and Quaternary features, such as fluvial and lacustrine landforms.

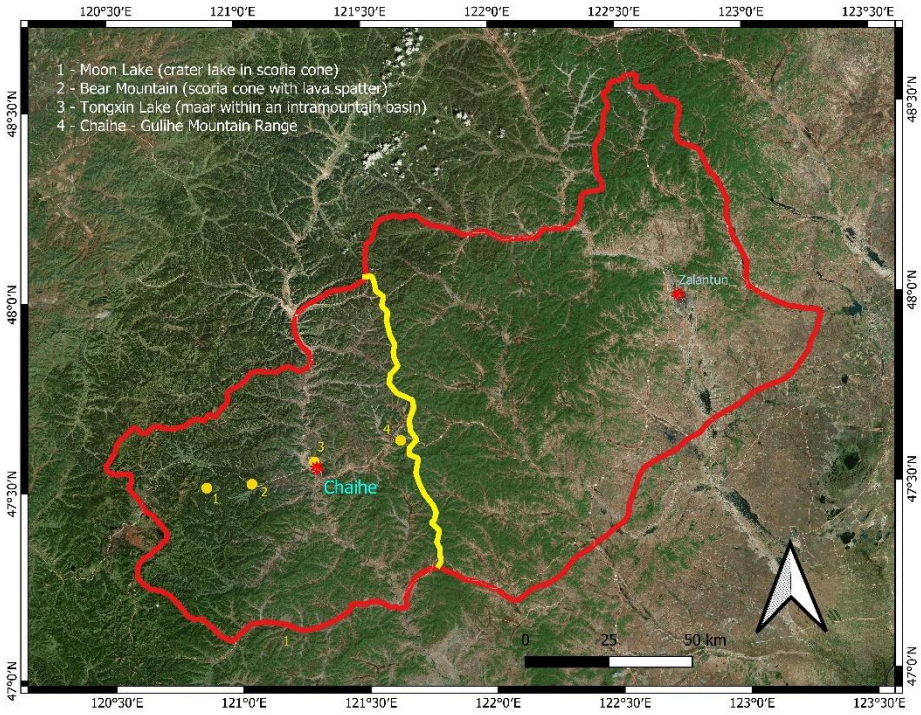

Figure 50: Outline map of administrative divisions in Zalantun/Zhalantun Province is marked with a red line over a Bing Aerial map (division boundaries based on data from: http://www.coolzou.com/Article_37144.html). The yellow line marks the ad-hoc boundary of the Zalantun Geopark. The main Geosites are marked with yellow dots. The geopark is in the volcanic region across the Great Xing'an Range and a tributary of the Chaoer River plus the Chaihe River through the centre of Chaihe township. Zalantun/Zhalantun is the administrative centre of the province and is located on the eastern side of the territory.

3) Geoparks summary

The majority of the volcanic features mentioned above are located within the boundaries of the Arxan UNESCO Global Geopark, while Zalantun Geopark has the highest number of volcanic vents but a smaller range of volcanic features. Furthermore, Zalantun Geopark has the most significant eruption locations in the volcanic field, giving it strong geoeducation and geoconservation relevance.

The volcanic features in ACVF include volcanic edifices as well as the landforms created by syn-eruptive processes such as pyroclastic density flows and lava flows. Scoria and spatter cones are evidence of strombolian-style explosive eruptions producing landforms with very steep slope angles and small volumes. The spatter

extrusives are welded, whereas the scoria occurs as loose materials. Tuff rings and tuff cones share the same type of ejecta, i.e., pyroclastic deposits formed by phreatomagmatic eruptions. A tuff cone is distinguished by its higher angle of repose (more than 45 degrees) than a tuff ring, whose angle of repose is generally no more than 35 degrees (Brand & Broz, 2015; Broz & Nemeth, 2015; Heiken, 1971). Due to the densities of the ejecta from different eruption types, dry eruption volcanoes have high preservation potential, and pyroclastic deposits are likely to be quickly eroded by the rivers. Lava flows can form totally different landforms compared to volcanic edifices. The 'aā type lavas have very rough surfaces, whereas the pahoehoe type displays twisted, fluid-shaped surfaces. In ACVF, lava flows have greatly altered the local geomorphology, especially the fluvial systems. On the Arxan side, aa lavas predominate and create a range of terraces. On the Chaihe side, lava flows changed the river courses, including the streams from the surrounding gullies, and lava flows followed the preexisting fluvial systems.

5. *Regional Geology*

The Great Xing'an Range is located in Inner Mongolia, NE China, in the Xing'an-Mongolian Orogenic Belt (Zhang et al., 2010b). The oldest rock succession has undergone ultra-high pressure metamorphism; intrusives, such as granite, emplaced during the Cenozoic, crop out along with Pleistocene extrusive volcanic rocks to form a basin and mountain range landscape in the study area (Zhang et al., 2009). The field is elongated from east to west. On the northeastern flank or side of the Great Xing'an Range is the Pleistocene to Holocene Wudalianchi Volcanic Field, which is a world-famous UNESCO Global Geopark conserving about 15 cinder cones in a 500 km^2 shield-shaped plateau created by lava flows in NE China (McGee et al., 2015). Field observations indicate that basement rocks of the Great Xing'an Range were deformed by the impact between the China Craton and West Pacific Plates, with a growth of 5.3 million km^2 during the Palaeozoic era (Li, 2006; Şengör et al., 1993; Sengor & Natalin, 1996). The old geomorphology was created by Mesozoic intrusives (mostly granitoid materials).

The young landforms of the ACVF are generally formed by Pleistocene to Holocene volcanism with Quaternary (Holocene) sediments capping them; those Holocene

sediments were generated by the local hydrological systems, such as fluvial and lacustrine networks. Each of these three major groups of rocks cropping out in the study area represents the geoheritage of the region and provides geotourism opportunities.

Cenozoic rocks have the highest geoheritage value of the three groups of rocks in the geopark. The reason is that the region is far from a present-day active volcanic region (e.g., far from an active plate margin), and visitors are fascinated to see first-hand the remains of young Quaternary volcanoes, including Holocene scoria cones, extensive lava fields and ash plains. The older Mesozoic rocks shape the regional landscape, and the younger volcanic landforms provide a spectacular contrast to the older rock-dominated hill country. The Mesozoic rocks are abundant on the surface in places forming large cliffs and gorges; their geological features include mineralisation and fold-fault zones. In terms of geoheritage, the least interesting rock type is the Quaternary sediments which tend to occur primarily in rivers and lakes. These young sediments have potentially preserved a Quaternary paleoenvironmental and paleoclimatic history of the area, especially the lacustrine sediments.

A regional geological map is compiled using GIS (Fig 51). The basement rocks present in the area are Mesozoic plutonic rocks (granites) and metamorphosed sandstones (Li et al., 2020). The oldest rocks, granite, occur in the North-East and South-West. Wang et al. (2014) mapped three volcanic events: old, middle, and young. The old-age lava (early Pleistocene) is found mainly in the South-West. The middle-age lava (Pleistocene) is widely distributed from the South-West to the North-East. The young lava flows (Holocene) primarily pond in the South-West (Fig 51). Sedimentary deposits accumulated in and adjacent to the regional fluvial systems. Later lava flows were emplaced in and adjacent to the fluvial network (Fig 49).

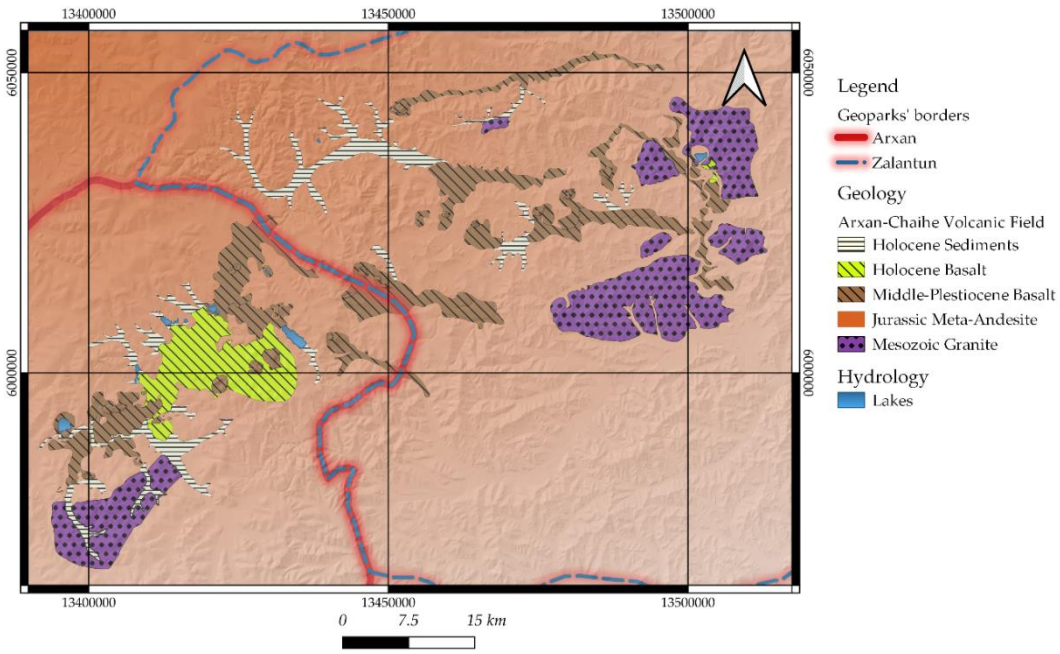

Figure 51: Geological model of ACVF based on geological map modified from the previous research with WGS 84/Pseudo-Mercator grid system (Wang et al., 2014). The background with orange gradient colour represents the basement of ACVF, i.e., Jurassic meta-andesite. The purple colour with dots reveals the distributions of the Mesozoic intrusive (mostly granitoid materials). The brown colour with diagonal lines marks the middle-Pleistocene volcanism (basalt). The light green colour with diagonal lines indicates the youngest volcanism in ACVF (formed in the Holocene era, basalt). The white colour with horizontal lines implies the capped Holocene sediments created by regional fluvial and lacustrine systems. Last but not least, the blue dashed line shows the boundaries of political regions between the Arxan geopark (left side) and Zalantun geopark (right side).

6. Geomorphology

The geomorphology of ACVF ranges from small-scale micro landforms to large-scale macro geographic sets. Macro landforms include mountain ranges and fluvial and lacustrine systems. ACVF has been highly dissected by local fluvial systems. Most streams headwater in the northwest, where elevation is > 1210 m, and flow southeastward to join the two main river systems (Halaha River and Chaoer River (Figs 49 & 50). The Chaoer River, located in the northeast of the region, originates from the eastern Great Xing'an Range and flows southeast of the volcanic field, collecting feeder tributaries from both the west and east. The catchment of the Chaoer River receives about 8.19 m of rain annually, with water levels of the mainstream from the lowest 849 mm to the highest 6.22 m in average values. The weather of ACVF is controlled by the frigid northern zone. The average temperature in winter ranges from

-16 to -37 °C, with 117 to 131 days annually (from Nov to Apr) experiencing frozen conditions (source from the survey of hydrology on Chaoer River, Inner Mongolia, China, 2015). The lowest altitude of the territory is about 480 m above sea level in the southwest and eastern parts of the river valley. The main channel of Chaoer River is broad and confined by the surrounding topography. In areas where the surrounding valleys connect, wide, flat terraces are incised and prone to flooding by meltwater in the spring. Spring flooding may have been more intense during Pleistocene interstadial/glacial climatic cycles when the water supply in the region was higher (Huang & Cao, 2015).

The region of the ACVF is highest in the northwest at up to 1700 m asl (Fig 52). The board valley floor of the Chaoer River, in the west, exposes ponded and channelised lava flows, which are, in places, covered by alluvium deposits (Fig 50). Tongxin and other lakes are located in elevated valleys around 1200 m asl (Figs 50 & 52).

The slope steepness of the land varies throughout the region ranging between 7.5 to 22.5 degrees (this range is just an average value only for the general assessments of diverse ranges of geology). By using the SRTM elevation model, a map showing slope variations in the region has been compiled (Fig 53).

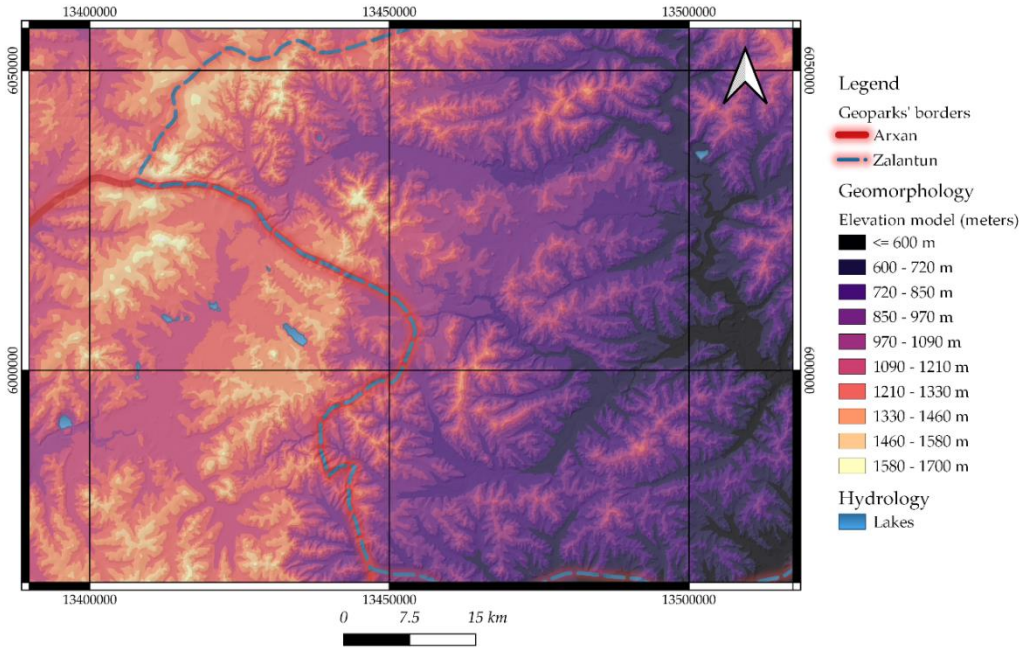

Figure 52: Elevation model of ACVF based on SRTM (with 30 m resolution of digital elevation database, sourced from: https://srtm.csi.cgiar.org/). This figure conveys the general altitude

variations in ACVF. Due to the limited resolution of the original SRTM data, the image indicates the trend of the elevation from high (up to 1700m asl) in the west, decreasing eastward to < 600m. The blue dashed line indicates the political region boundary between Arxan and Zalantun.

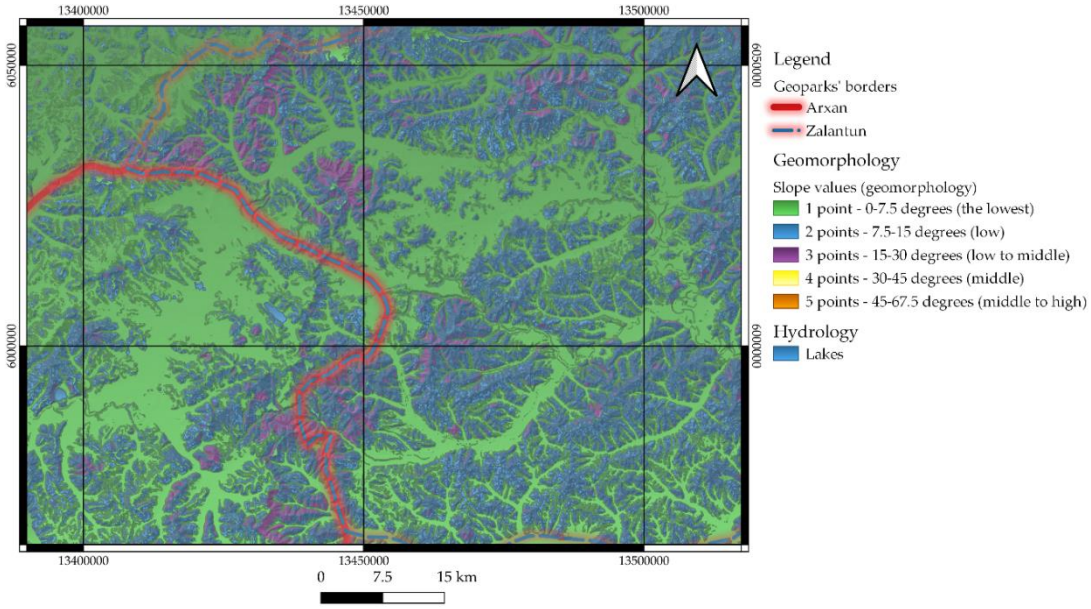

Figure 53: Slope model of ACVF generated using SRTM (Fig 56). The green shows the area with the gentlest slope; the blue through to brown colours show areas with a greater slope. Fluvial channels and mountain ridges tend to be flatter and hence have lower slopes, whereas the sides of the mountains have high slope values.

Another important geomorphological variable is the relief of the land. The "Geomorhon" tool applies an algorithm utilising raster images (in this research, the "SRTM model") that compare one-pixel parameters with parameters of other pixels around the targeted in 8 directions to generate a relief of the research area (Gioia et al., 2021; Luo & Liu, 2018; Swift & Kennedy, 2021). The method, first utilised on geomorphologic maps in Poland (Jasiewicz & Stepinski, 2013), analyses the local geologic and geographic features to make maps showing local morphological characteristics such as ridges, peaks, flats, pits, channels, and saddles (Fig 54).

Geomorphon analysis shows that the topography of ACVF is rough, with the high relief controlling the local hydrology. Slope (33.72%) is the most common type of landscape throughout the ACVF, followed by Valley (22.33%), Hollow (20.24%), and Spur (14.9%), while others are less than 5%, where Flat areas account for only 0.05% of the landscape.

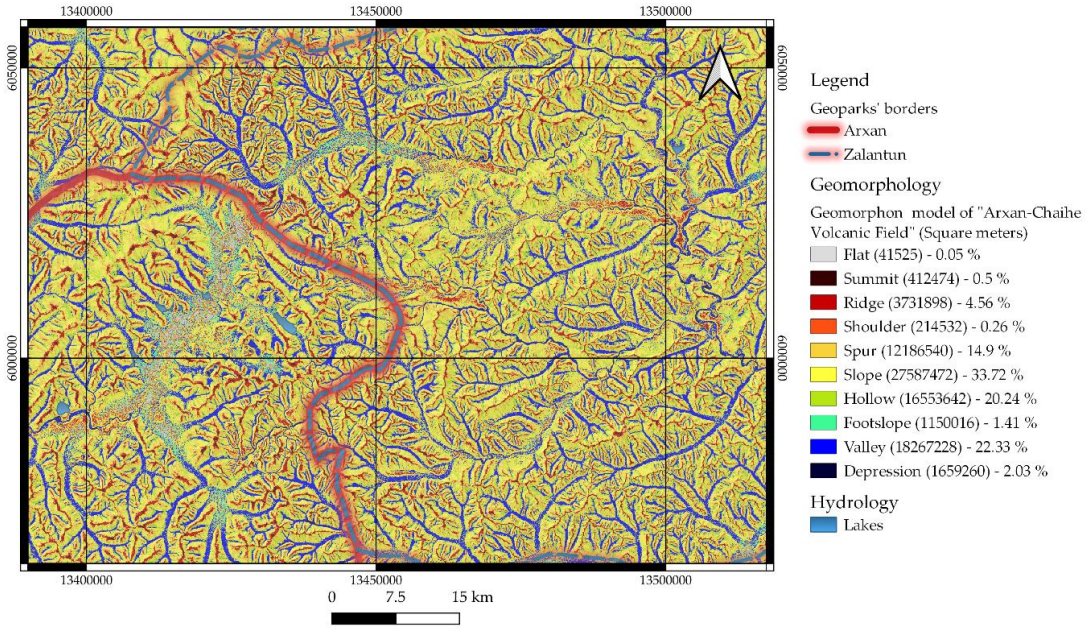

Figure 54: Terrains of ACVF generated using the Geomorphon tool. This map shows the variations of relief in the various landforms and the roughness of the area. The landforms include the slope, spur, ridge, flattened surface, and shoulder.

7. Hydrology

Halaha River in the southwest and Chaoer River in the east define the two main fluvial systems (Fig 55). The Halaha River, which has a number of tributaries flowing in from the central part of the study area, has no connection to any other major rivers. The Chaoer River is a much larger river with tributaries from all directions, especially the west. The Chaoer River flows into the Chai River. There are nine lakes present in the region; eight are located in the central to the western part of ACVF, and one in the northeast. Most of these lakes appear to occupy craters formed by volcanic activity.

The hydrological parameters of ACVF were analysed using the QGIS tool that generated a "Channel network and drainage basins" map of stream tributaries. The method, which uses a numerical measure of branching complexity to identify possible locations of streams, follows that developed by (Strahler, 1952; Strahler, 1957), where the stream from the source is the first order, then at the point where two streams merge is the beginning of the second order. The QGIS tool shows the direction of the flow of the streams, while lakes are highlighted as places without flow. These data are then amalgamated with the geomorphological and geological data to show ACVF's

hydrology. Fig 55 shows that the main fluvial systems, Halaha and Chaoer rivers, follow an NW-SE distribution from the Rose diagram.

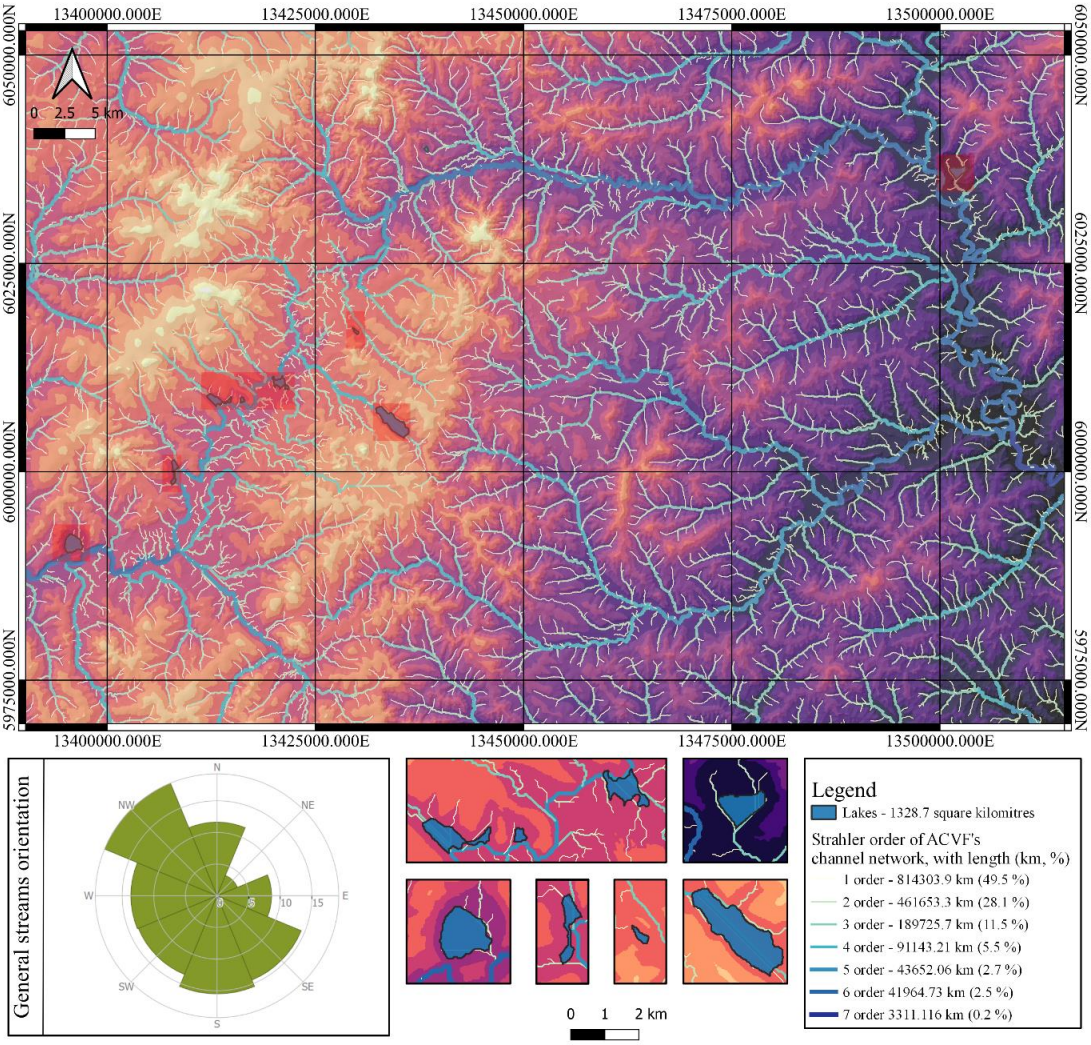

Figure 55: Map showing the major rivers and streams in ACVF on SRTM and generated using QGIS. The rose diagram shows the flow orientations of the branches of local streams (Rose Diagram Creator https://geographyfieldwork.com/RoseDiagramCreator.html). Detailed mini-maps show the lakes. These mini maps reveal how the lakes sit in the landscape and the inflow/outflow of the streams, which follow the gradient of the valleys.

8. Geodiversity

A qualitative-quantitative geodiversity assessment of ACVF is undertaken to highlight places with high abiotic value (Gray, 2008; Kozlowski, 2001; Kozłowski, 2004; Serrano & Ruiz-Flaño, 2007). The assessment considers the geology, geomorphology, hydrology, soils, weathering, and erosion that occur within a region. It takes into account all processes influencing the abiotic nature, including tectonism, solar

radiation, magnetic field variations, gravitational field variations, and the impact of climate and biology, including human activity. The objective is to generate a geodiversity map that reflects the features of the area in qualitative and quantitative ways (taking actual data and giving it a rating within the geodiversity points system).

Distinct geological and geomorphological parameters of the region are qualitatively assessed using an 8-point value scale, where 1 is the lowest value, and 8 is the highest (Zakharovskyi & Németh, 2021a). The geodiversity is quantified using the number of each of the parameters; in this study, we used geology and geomorphology. The model uses both qualitative and quantitative parameters to identify the significance of geosites in the territory rather than providing an accurate description of the geodiversity. The columns in Table 9 present the types of rocks exposed at the Earth's surface and their prevalence with respect to their geological age. The classes in Table 8 were then applied to the geology and geomorphology in ACVF using QGIS to generate a geodiversity model for specific areas (Table 9). For example, Precambrian intrusives formed the basement in ACVFand Mesozoic granitoid intrusives overlie it, particularly in eastern and southeastern parts of the volcanic field. Cenozoic volcanism represents the majority of rocks distributed across ACVF, and these are especially well-exposed in every scenic spot. The youngest materials are the Holocene topsoil, lacustrine deposits and fluvial sediments.

Eras	Crystalline				Sedimentary	No. of usable data points
	Extrusive	Intrusive	Metamorphic and "Precambrian"	Total		
Cenozoic	4	0	0	4	33	290
Mesozoic	2	1	1	4	18	177
Palaeozoic	1	1	<1	2	13	117
Precambrian	0	6	15	21	1	173
Age unknown	1	1	1	3	1	26
Total	8	9	17	34	66	783

Table 9: Percentage of rock types exposed on Earth's surface as a function of geological age (Blatt & Jones, 1975). According to the table, extrusive and intrusive rocks are the rarest type. Hence, they have the highest value from a geological perspective.

Main Values of Geodiversity			
Values (8-point system)	Elements of Geodiversity		
	Geomorphology	Geology	
	Slope angle (degrees)	Rock type and ages	Arxan – Chaihe Volcanic Field
1 (the lowest)	0-7.5	Sedimentary Cenozoic	Holocene Sediments
2 (low)	7.5-15	Sedimentary Mesozoic	-
3 (low to middle)	15-30	Sedimentary Paleozoic	-
4 (middle)	30-45	Metamorphic Precambrian	-
5 (middle to high)	45-67.5	Intrusive Precambrian	-
6 (high)	67.5-75	Extrusive Cenozoic	Holocene Basalt, Middle-Pleistocene Basalt
7 (the highest)	75-90	Extrusive Mesozoic	Jurassic Meta-Andesite
8 (the rarest)	Sedimentary (Precambrian), Metamorphic and Intrusive (Cenozoic, Mesozoic, Paleozoic), Extrusive (Paleozoic, Precambrian)		Mesozoic Granite

Table 10: The value of geodiversity for ACVF

A flowchart (Fig 56) outlines the steps used to create the geodiversity model. The method applies a standard arithmetic average equation through QGIS (Geographical Information Systems) software. The geological map (Fig 51) provided the geological rock units, and SRTM (Fig 52) provided the slope data imported into QGIS. Using the "union" tool, shapefiles, each with geological and geomorphological parameters, were generated to produce a value of geodiversity map (Fig 57).

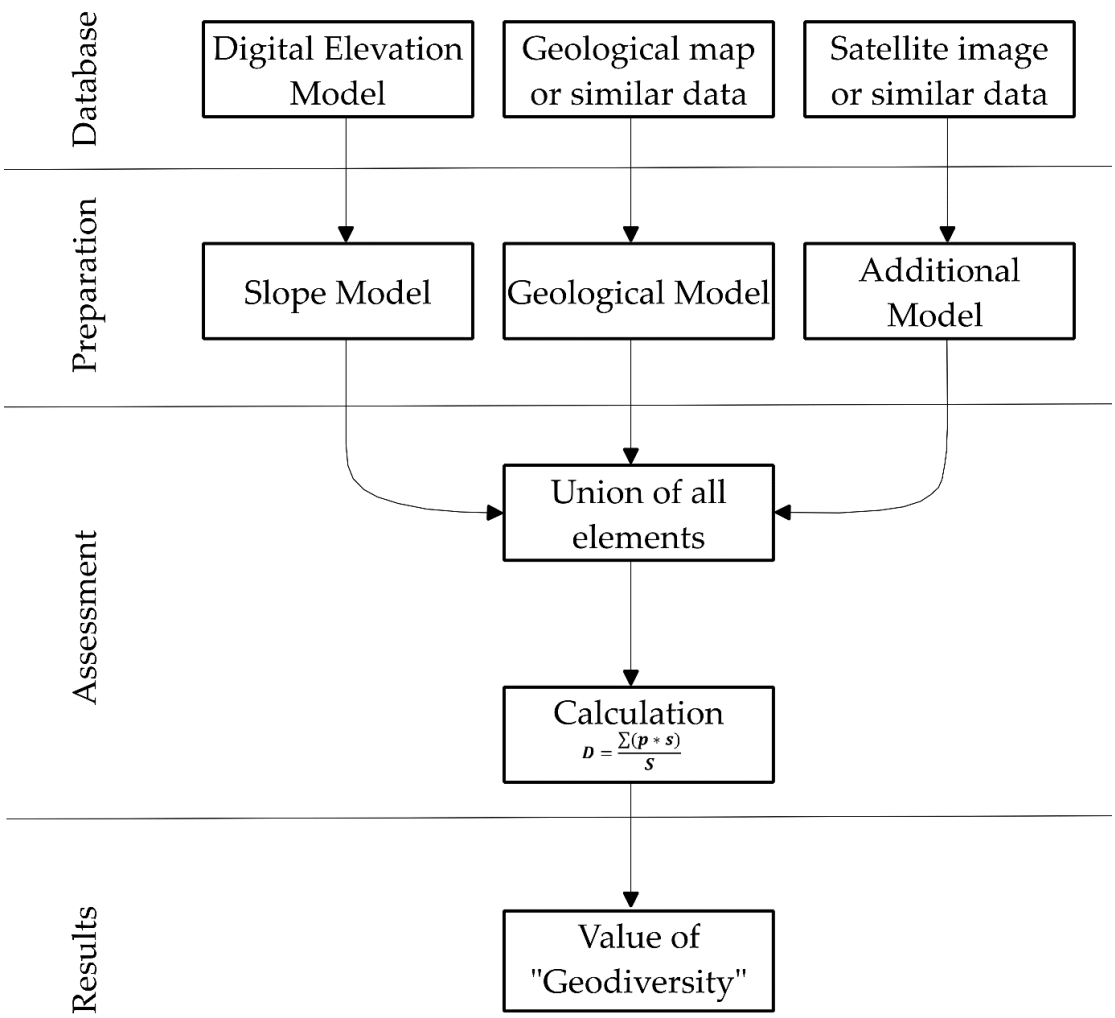

Figure 56: A flowchart of assessment procedures Zakharovskyi and Németh (2021a) - Qualitative-Quantitative Assessment of Geodiversity of Western Samoa). In this flowchart, the formula is the calculation of geological elements, such as topography, slope, and hydrology, against the whole area of the region. D is the value of diverse ranges of geology; p is the number of the elements mentioned above; s is the area that preserves those elements; S is the total area value of targeted locations.

Union (QGIS tool) and Calculation (Average arithmetic)

$$D = \frac{\sum(p * s)}{S}$$

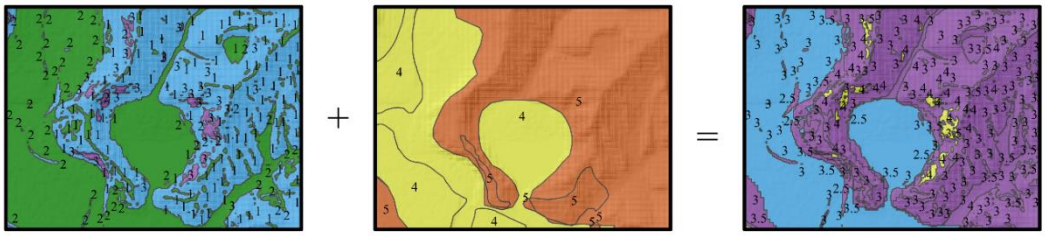

Figure 57: The "value" variables applied to calculating the geodiversity model. The numbers (8-point system mentioned above) are tiers of the importance of geodiversity. The geomorphological values highlight possible interesting locations, such as cliffs (light blue areas), PDC deposits, and spatter deposits; also, the green colour indicates the flattened areas; the geological values present the different rock types, such as granitoid materials (orange colour), lacustrine or fluvial deposits (yellow colour); the geodiversity values are the calculation (mentioned above in Fig 60) of each of the two parameters (Tongxin Lake, NE of ACVF). In the geodiversity value map, the yellow patterns indicate the highest geodiversity value, which might be the volcanic materials with distinctive topography; purple patterns indicate the secondary interests of the assessment, which are the country rocks with low topography values; blue patterns preserve the lowest values of geodiversity, which contain ordinary hydrological deposits on low-value topography.

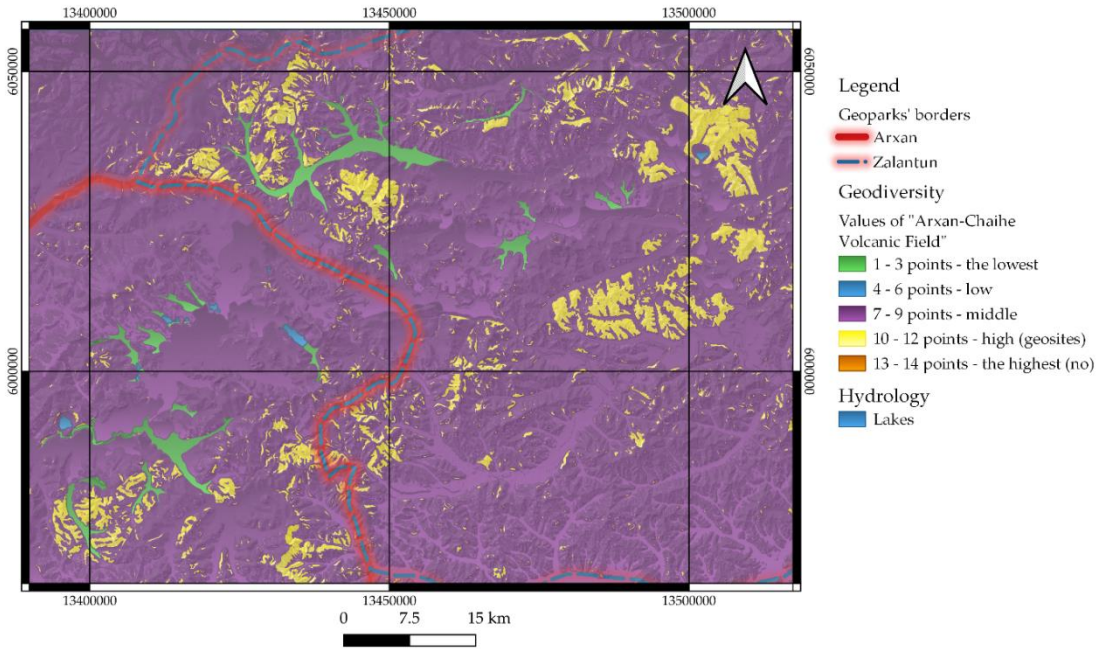

Figure 58: A map showing the qualitative-quantitative geodiversity of ACVF. The geodiversity is based on the values in Table 9: the highest values indicate the highest interest in geoheritage

research. The green colour indicates the locations of fluvial and lacustrine sediments distributed in ACVF have low geodiversity; the purple gradient shows the Mesozoic intrusives of ACVF have a middle geodiversity value. The same purple pattern encloses flat valley floors with lava flows of the Cenozoic volcanism of ACVF; the yellow gradient reveals the Mesozoic granitoid materials that are outcropping in ACVF have high geodiversity and the best candidates for key geosites.

As a result of assessments of ACVF's geodiversity (Fig 58), the majority of the territory is assessed as middle value with 7-9 points. These areas of predominantly Jurassic meta-andesites, which are under the score of 6 points for geological value. The locations of greatest geodiversity interest and potential geosites are the Mesozoic granite and places where it occurs together with Jurassic meta-andesites. The areas of lowest geodiversity are concentrated from the southeast to the central-north part study area, where the main rock type is Holocene Sediments. Features assessed with the highest value of geodiversity (13-14 points) are not present in the territory of ACVF. This likely reflects a low score for the geomorphological part of the assessments. The Cenozoic volcanism has the same geodiversity value as the Mesozoic background of ACVF (purple fields in Fig 58). Hence, while the geological value of ACVF is high, the overall qualitative-quantitative geodiversity assessment of the region gives it a middle value globally.

9. Discussion

ACVF is an area displaying a range of geodiversity values in Northeastern China. The high value of the existing scenic spots is undoubted, and this study shows that other areas within ACVF also have a potential for new geotourism endeavours and future research. Approximately 47 vents, including scoria cones and tuff rings/cones, are the major volcanic features recognised in ACVF. The variety of rock types and their distributions are shown in Fig 51. The base geological map is, at best, reconnaissance in some areas (with a resolution of only 30 m used in the STRM database), but recent geological fieldwork and mapping have increased the resolution around ACVF. The boundaries between the different geological units are inferred in places, sometimes resulting in irregular patterns representing the rock types. The geology of ACVF offers huge research potential. The elevation, which generally decreases from west to east, controls the flow directions of the local hydrology. Slope (Fig 53) is one of the key

values for the assessment of geodiversity and is best seen on the geomorphon map (Fig 54), which presents the morphological elements. Fig 52 shows that lowlands occupy the centre of ACVF (grey areas), while the surrounding ranges outline the shape of the volcanic field where the topography of the ranges encloses the volcanism. The regional hydrology map (Fig 55) shows the local river and lacustrine systems. The hydrological systems incise the surface and follow the lineaments created by the regional tectonic trend; thus, the ranges are shaped by them, and the plains preserve the Holocene sediments created by them. The geodiversity map (Fig 58) is the integration of geological and geomorphological aspects. Palaeozoic country rock dominates in most areas, whereas the Cenozoic volcanism, compared to the country rock, has minor status. Holocene deposits (light blue and green patterns) are constrained by the sides of the major fluvial channels. The locations preserving the rock types mentioned above are the targeted destinations of the ACVF research. The total area of ACVF is approximately 2000 km^2.

Geodiversity assessment of ACVF using the main geological elements (Table 9) in combination with geomorphology shows the area occupied by volcanic fields highly dissected by streams (Fig 55). Here, a qualitative-quantitative assessment was utilised because of the data limitation of the studied region. From a global perspective, the geological inventory of ACVF is high with its Jurassic meta-andesite and Mesozoic Granite. However, the geomorphological aspect of the region shows different values (Fig 54). Most slopes of the area are less than 40 degrees which means that throughout most of the territory, there are few good outcrop exposures for accurate observation, meaning these areas will have a low value of geodiversity. Meanwhile, in the northeast, northwest, and southwest parts of ACVF, the two old formations present, Jurassic meta-andesite and Mesozoic granite, are assessed to have a high value of geodiversity. Based on this geodiversity assessment, ACVF areas with high values (Fig 58) should be the focus of future geosites of the region as they will provide the best locations for future geoeducation and geotourism. This finding highlights the future attempt to explore those areas mostly formed on granite rocks as, under current geopark and geotourism programs, they are underrated. Their high geodiversity scores justify well the need to initiate new geological, geomorphological

and geoheritage mapping in those regions to explore what features exist on those unexplored granite terrains. This finding also highlights the potential geoeducation direction to design geoeducation strategy in which the old granite terrain evolution is a better fit.

Some future works should be concentrated on establishing high-resolution geological maps georeferenced to satellite images. These maps should include the location of possible geosites, currently within the two geoparks administered in the study area (Arxan and Zalantun Geoparks). They should provide key information such as access, protection of natural and artificial features, visitation values and geotourism elements of the region. Also, technical maintenance is needed to be considered, e.g., signs would be destroyed by foot traffic and the overgrowing vegetation. Finally, data-based recommendations and guidance on the usage of current geosites, and potential future directions to identify new geosites should keep interested in the region's diverse geology at a high level.

10. Conclusions

1) Our study presents the first detailed overview of the geodiversity estimate of ACVF. Geological mapping, which focuses on Cenozoic volcanism, has been integrated with regional topography, relief morphology and hydrology to model the geodiversity of ACVF. Results of the study show that the geodiversity of ACVF is complicated due to the range of different rock types over a wide area. The area is geologically and geomorphologically diverse and warrants further work to identify potential new geosites that can be developed for future geotourism and geoeducation.
2) The diverse range of geological parameters in ACVF reveals the potential values of volcanism, variations of hydrology, geomorphological diversity and geodiversity. The "8-point" system presented demonstrates a systematic approach to assessing diverse ranges of ACVF's geology. The combination of fieldwork and GIS analyses is essential to the precision of outcomes of geodiversity concepts.
3) The assessment and evaluation of the diverse range of geology in ACVF highlight the need for geoconservation. Recently, it has become clear that there are potential geosites in parts of ACVF that are currently not part of any

geoconservation strategy. The volcanism in ACVF has occurred in an intra-continent setting, some considerable distance away from a lithospheric plate boundary. More importantly, volcanism is not an ordinary feature in Inner Mongolia, so the volcanism in ACVF has enormous value for geotourism or tourism of local geological features in general. A geopark like ACVF could be a knowledge hub for intra-continental volcanism (monogenetic volcanic fields) and be aligned with a global geoeducation program that incorporates and promotes geodiversity.

MASSEY UNIVERSITY
GRADUATE RESEARCH SCHOOL

STATEMENT OF CONTRIBUTION
DOCTORATE WITH PUBLICATIONS/MANUSCRIPTS

We, the candidate and the candidate's Primary Supervisor, certify that all co-authors have consented to their work being included in the thesis and they have accepted the candidate's contribution as indicated below in the *Statement of Originality*.

Name of candidate:	Bo'xin Li
Name/title of Primary Supervisor:	Prof. Károly Németh
Name of Research Output and full reference:	
Eruption Scenario Builder Based on the most Recent Fissure-Feed Lava-Producing Eruptions of the Arxan-Chaihe Volcanic Field (ACVF), NE China	
In which Chapter is the Manuscript /Published work:	Chapter 5
Please indicate:	
• The percentage of the manuscript/Published Work that was contributed by the candidate:	Bo'xin Li, 80%
and	
• Describe the contribution that the candidate has made to the Manuscript/Published Work:	
Prof. Károly Németh, Mrs Julie Palmer, Prof. Alan Palmer, Dr. Vladyslav Zakharovskyi, and Mr Ilmars Gravis	
For manuscripts intended for publication please indicate target journal:	
IntechOpen	
Candidate's Signature:	Bo'xin Li
Date:	
Primary Supervisor's Signature:	Prof Karoly Nemeth (Digitally signed by Prof Karoly Nemeth, DN: cn=Prof Karoly Nemeth, c=SA, o=Saudi Geological Survey, ou=National Earthquake and Volcano Program, email=nemeth.k@sgs.gov.sa, Reason: I am approving this document, Location: Jeddah, Kingdom of Saudi Arabia, Date: 2023.05.08 13:01:27 +03'00')
Date:	8 May 2023

(This form should appear at the end of each thesis chapter/section/appendix submitted as a manuscript/ publication or collected as an appendix at the end of the thesis)

Chapter 5: Eruption scenario builder based on the most recent fissure feed and lava-producing eruptions of the Arxan-Chaihe Volcanic Field (ACVF), NE China

This chapter has been published as a paper on the InTech website (https://www.intechopen.com/chapters/86103). The majority of the work was carried out by the author, Bo'xin Li, who is under the supervision of Prof. Karoly Nemeth, Prof. Alan Palmer and Mrs Julie Palmer.

1. *Abstract*

Fissure eruption is the most prominent type of Pleistocene to Holocene volcanism in the Arxan-Chaihe Volcanic Field, recording vent migration along fissures. This research is examined Sentinel Satellite Images to outline the youngest lava flows in the region in conjunction with field observations. Also, GIS-based analyses were performed with the aim of calculating the volumes of lava flows to determine the length of the lava flow emissions. Topographic cross sections and various geomorphological parameters (e.g., geomorphon and topographic position index) were used to reconstruct the pre-eruptive geomorphology of the region to simulate lava flow inundation using Q-LAVHA plug in the QGIS package. Pre-eruptive topography was created, and various simulations were used to obtain the best-fit lava inundation. This process yielded to estimate of an average of 5 m lava flow thickness. The same parameters of the lava flow simulations were used to run on the post-eruptive topography to simulate future lava flow inundation. Results showed that the lava flows were best simulated if they emitted along a NE-SE trending fissure between two young vent zones or in an extensive elongated area following the NW-SE trending valley axis initiated from the Yanshan vents.

Keywords: scoria cones, pyroclastic, lava flow, fissure eruption, lava fountaining, strombolian eruption, satellite imagery, GIS

2. *Introduction*

Lava flows in every volcanic field represent the major volcanic events and significant phases of volcanism (Kilburn, 2000). The most distinctive characteristic of lava flows is their surface morphology. Such surface "shapes and patterns" not only represent the interests of tourism and scientific exhibitions but also reveal great value for interpretations of how volcanism occurred, potential indicators of petrogenesis, shifting of eruption phases, eruptive magnitudes (volumes and ejection pressures), and geochronology of how long an eruption last. In general, two types of the morphology of lava flows have been described in the literature: 'a'ā type and pāhoehoe (Kilburn, 2000). Pāhoehoe lava flows commonly emerge during events of Strombolian-style eruptions with low viscosity and high-temperature basaltic eruptions (Macdonald, 1953; Self et al., 1998). This type of lava flow is usually known for its smooth surfaces and gentle undulations, with occasional hummocky surfaces and tumuli. In general, pāhoehoe lava flows can extend tens of kilometres in distance from their sources (Self et al., 1998). Small outflows alternatively emerge from the chilled crust of the surface and can feed small "toes", which are approximately no more than a few decimetres thick, several m long, and dm-to-m wide. Pāhoehoe lava flows are associated with low outflux velocity; this means the volumetric flow rates are about 2-5 m^3/s, and slow flow front velocities are approximately 1-10 m/hr (Self et al., 1998). These behaviours of the emplacement are shown by the low flux velocity profile allowing the flows to develop a chilled crust keeping the melt able to move. Thus, the forehead of flows commonly proceeds moving slower than the lateral partitions of the flow body; this indicates that not only can the flow remain undisrupted with smooth and intact surfaces but also preserve "toe" structures while the flows keep moving. Like its counterpart, aa-type lava flows commonly present as extremely rough surfaces with spikes and swarmed gullies (Kilburn, 2000). The 'a'ā lava type generally has denser inner parts. The emplacement behaviour shows that the flows commonly have a thick (1–2 m) chilled shield surrounding the main lava body. The forehead of rough surfaces with clinkers can be broken while the flow moves (Kilburn & Lopes, 1988; Rossi, 1997; Sato, 1995). The fallen part will eventually be buried by the bottom of the flows. Topography can significantly affect how the flow

moves and facilitate ponding or cascading effects in steep steps or behind obstacles or valleys. Pāhoehoe lava can also become rubble where chilled crusts can be broken apart and carried rapidly further. In this case, morphotypes could work better to describe the flows (e.g., Murcia et al. (2014)).

Following the regional tectonic trends, fissure eruptions always generate large volumes of lava, which form the continental flood basaltic lava provinces (Thordarson & Self, 1993; Wylie et al., 1999). Commonly, the lava provinces can stretch into hundreds to thousands of km^2 areas. Due to the volumes of lava that ejected, a basaltic flood lava province usually was formed over a long time, extreme in a period of 1 to 2 million years (de Silva & Lindsay, 2015; Sheth, 2018). The fissure eruptions generally are related to the continental rift zones, such as the East African Great Rift (Hutchison et al., 2016). The stretching or rifting property usually produces large lava volumes. These geological settings are usually defined by monogenetic volcanic fields. They are defined by tens to hundreds of small vents formed due to mainly two eruptive styles, such as Strombolian, Hawaiian, and phreatomagmatic types (Smith & Németh, 2017). Those small vents usually swarm and confine in a large region (e.g., thousands of km^2). The occurrences of monogenetic volcanic fields are commonly shown by the linear trend of vents, clustering, or randomly distributing, all strongly influenced by the crustal structure of the region where they erupted (Le Corvec et al., 2013b; Mazzarini et al., 2016). In old continental crusts, inherited structural elements commonly influence the vent distribution of monogenetic volcanic fields and can be controlled by the regional fracture zones, which could subsequently form fissure-aligned volcanic systems (Le Corvec et al., 2013b).

The products of monogenetic volcanism are commonly revealed as scoria cones, cinder cones, tuff cones, tuff rings, lava flows, and pyroclastic materials (formations of ashes and density currents). Those straight-generated and primitive volcanic products can be easily affected by the local environments and climates, in other words, the surface processes (Kereszturi et al., 2011). When the surface processes influenced the young volcanism, it could vastly change the outlines of the topography and landforms (Murcia & Németh, 2020). Also, the pre-existed landforms play an

important role in forming subsequent volcanic landforms, such as hydrogeology-controlled lowlands and complexities of country rocks.

Modelling for lava flow emplacement is one of the interests of interpretations of lava eruptions in some ways that are beyond human records. Long lava flow commonly indicates flows extending approximately more than 100 km from their sources (Stephenson et al., 1998). In general, long flows can generate rapid and insulated emplacements. The rapid model can expect lava flows exceeding 100 km from sources (Stephenson et al., 1998), with less than 0.5°C/km of chilling stages under the transporting velocity of approximately 2–15 m/s. The insulated models prefer flows outfluxing under low velocities (Hutchison et al., 2016; Self et al., 1998; Stephenson et al., 1998), for example, 0.1–1.4 m/s. Also, insulated emplacements can be expected the thickness of flows to be no more than 23 m at the maximum, with effusive rates at about 8–7100 m^3/s (Self et al., 1998). Slope datasets are the essence of all the above-mentioned assessments. The flows that were emplaced by rapid aspect should be distinguished by the channel-fed structures, for example, lava channels on the surfaces of ‘a‘ā type, and expected as generated from short-lived lava fountaining. On the other hand, the insulated aspect can be expected to produce a range of inflated tube-feeding and sheet pāhoehoe flows within a long distance from their sources/vents. Such flows are also marked as an indicator of a long-lived ponding system (Self et al., 1998).

Volcanic eruptions commonly reveal themselves as multi-phases and prolonged event during the syn-eruptive stages. Also, building a range of eruption scenarios can allow researchers to have a better view of the complexities of volcanic eruptions and volcanic uncertainties (Kereszturi et al., 2014). In general, the eruption scenarios contain four major aspects: eruption locations, types of eruptive phases, duration of a single phase, and occurrence and frequency of hazards. Eruption locations indicate short-lived and small vents with their distributions and a single large composite volcano, which produces long-lived and complex volcanic events. The transitions between different eruptive types show that the diversities of volcanism are the current and future preceding states of volcanoes. Duration of eruptive phases analyze the potential magnitudes of local volcanism and are considered either discrete or

prolonged eruptions. Hazards' frequencies and occurrence are considered as the influences of erupted gas, blast styles, pyroclastic density current-triggered syn-eruptive disasters, and post-eruptive lahar events.

In NE China, numerous mafic monogenetic volcanic fields formed through the Cenozoic. Among these fields, there are volcanic fields that had historic volcanic eruptions, including lava effusions such as those known from Wudalianchi (Sun et al., 2018; Wei et al., 2003) and the Arxan-Chaihe Volcanic Fields (Bai et al., 2005). Two young volcanoes located in the southeast part of the Arxan-Chaihe Volcanic Field (ACVF), that is, Yanshan-the "triple vent" and Gaoshan (eastern side of YS), have been dated under the C14 method, which revealed the ages of those two vents about 1900–1990 cal a BP (Bai et al., 2005; Cui et al., 2021).

The major aim of this research is to focus on providing the best possible eruption model to understand the potential impact of a similar eruption in the future based on the youngest eruptive event in the region that occurred approximately 2000 years ago in ACVF. To constrain this, we employed satellite images that show the surface successions of lava flows as a range of typical indicators of how to build the possible chronicle of the vent onset events and the subsequent ponding processes in the volcanic histories of ACVF. Thus, we propose that the youngest eruption in the region took place along fissure-dominated vents. As the ACVF is part of the UNESCO Global Geopark network (Németh et al., 2017a), volcanic hazard needs to be treated seriously, and this work provides valuable geology-based information and lava flow simulation to envision the likely eruption scenario the region may face in a future volcanic eruption.

3. Geological settings

ACVF is located on the eastern side of Inner Mongolia, northeast of China (Figure 59a). The Great Xing'an Mountain is the basement holding ACVF's volcanism as a distinctive geomorphological outline, which vastly distracts and draws the interests of both tourism and commercial behaviours.

The volcanism of ACVF is the most targeted element of local interest, not only its rareness but also the value of research. ACVF is a distinctive volcanic field due to its

distance away from the Japan Subduction Zone, about 200 km. Such a long spatial span indicates that the general background of ACVF is mostly controlled by the intra-continental settings, which are influenced by a distant convergent plate margin (Li et al., 2020). ACVF is located on the western side of Song'liao Graben, which is an enormous geological and structural subsidence in the centre of NE China in consideration of a rifting-zone environment. One of the conventional concepts is that the delamination of supra-crustal layers takes place on the weak points so that the rifting processes can generate large subsidence areas, that is, grabens, on the local territories (Zhang et al., 2010a). The subduction zone fueled the delamination processes, which manifested the increasing activities of rifting. The basement of ACVF is approximately formed in the middle to late Mesozoic eras. Previous pieces of research show that the major components of the basement of the Great Xing'an Range are composed of Mesozoic volcanic and granitoid materials. The dwelling elements, such as zircon, whole-rock elements, and Hf isotopic composition, indicate the properties of the Great Xing'an Range. Geochronology (mostly K-Ar and Ar-Ar techniques) shows that there are at least three stages of the evolutionary histories of the ranges. The felsic volcanic rocks were formed in the Middle-Late Jurassic periods about 174–148 Ma; intermediate and intermediate-felsic volcanic rocks were created in the Early Cretaceous intervals about 142–138 Ma, with no later than 125 Ma; normal felsic volcanic

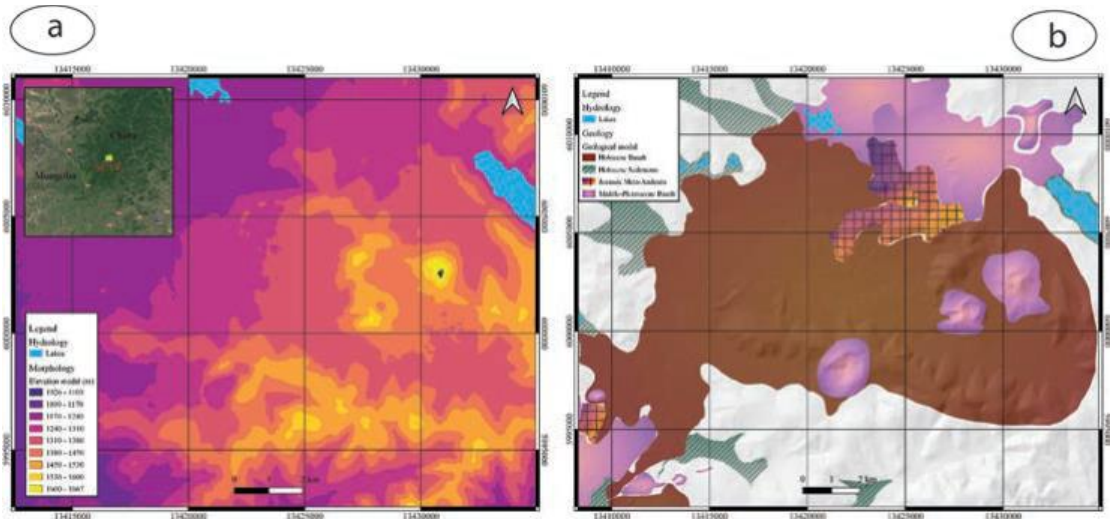

Figure 59: The general morphological aspect of the Arxan-Chaihe volcanic field (a) and its simplified geological architecture (b). Topography is based on SRTM 30 m resolution digital elevation model. Geology information is derived from (Wang et al., 2014). Please note that the

young lava flow extent is greatly overestimated. Reconnaissance mapping indicated that many regions shown on this map covered by the youngest lava flows are not accurate, and they are rather part of old lava flow fields. Maps are on the WGS84 projection using NE China local coordinate system.

rocks were generated in the Early Cretaceous at about 140–120 Ma, with the major volcanic events at 125 Ma. Upwelling mantle movements are the general factor of the compositions of Mesozoic volcanic rocks; this very well corresponds to the methods rifting system of Song'liao Graben (Zhang et al., 2010a).

The youngest activities of volcanism at ACVF occurred approximately 2000 years ago. Previous research shows that the lava flows cover the major areas of the Arxan UNESCO Global Geopark with several intervals of the ages. The k-Ar method (whole rock) reveals the ages of the bulk lava flows in multiple vent locations of AVCF. Lava flows on both riverbanks of the Halaha River erupted at about 0.587 ± 0.18 Ma (Bai et al., 2005; Liu et al., 2017). Among them, the youngest lava flows were generated from Yanshan's "triple vent" about 1990 to 2000 years ago. All these flow or bulk volcanic rocks are basalt or trachybasalt. The mafic property makes those flows follow the specific rheology and emplacement mechanisms of forming a range of young landforms of volcanism (Bai et al., 2005; Fan et al., 2011; Liu et al., 2017).

Up to now, 47 vents have been recognized by various field trips or satellite images (Li et al., 2020). The ACVF occupies an area of about 2000 km^2 in a hill country (Figure 59a). Those vents are aligned from southwest to northeast, especially along the study area (Figure 59b). For instance, on the eastern side of Tianchi Lake, two paralleled fissures indicate the propagation processes during the syn-erupted stages (Figures 60a-d). This feature is also found on the eastern side of Dichi Lake (Figures 60a-d). From the satellite images, the two ends of ACVF are marked by Wusulangzi Lake in the southwest corner (Figures 60a-d) and Tongxin Lake in the northeast corner. Between those two lakes, at least 15 vents are aligned through a distinctive orientation, which is SW-NE. Thus, vent distributions of ACVF show that the local tectonic trends, such as

fissure orientations, follow a general direction, which is SW-NE directed trend (Li et al., 2020; Németh et al., 2017a).

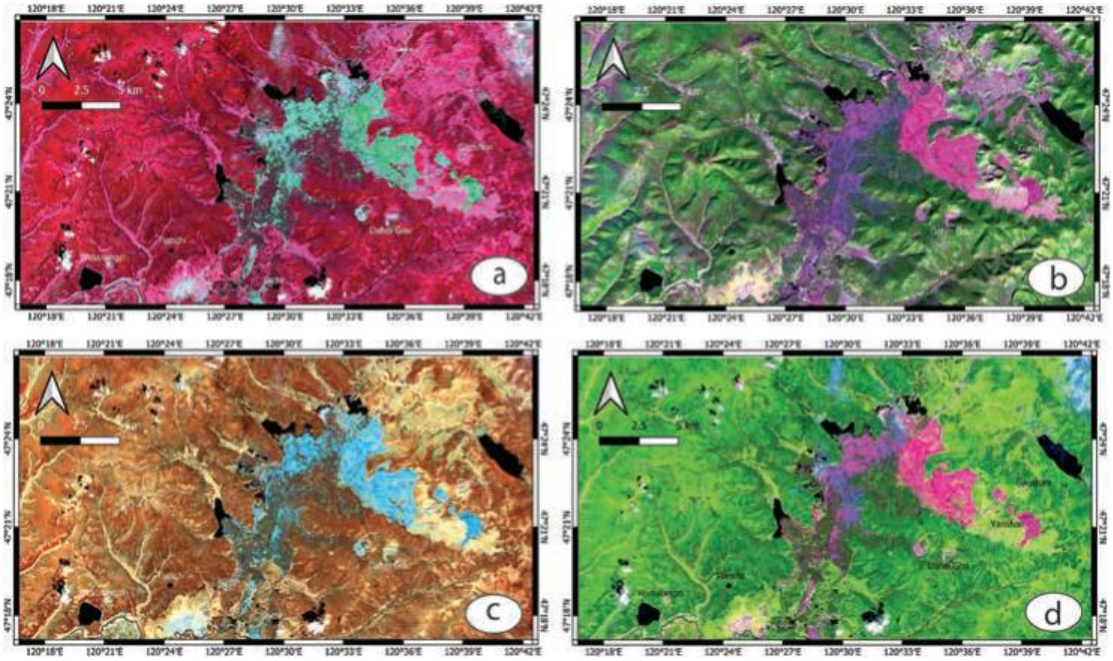

Figure 60: Sentinel satellite images of the Arxan – Chaihe volcanic field showing the distinct texture of the young lava flows. a) False colour image; b) SWIR image; c) geology – Band 8, 11, 12; d) geology – Band 12, 8, 2. Maps are in WGS84 projection using geographical coordinate systems.

Present-day geomorphology of the region of ACVF is revealed by a range of post-eruptive landscapes with volcanic products. The currently available geological map (Figure 59b) shows an extensive lava-covered region marked as Holocene basalt. Interestingly, in these maps, the three volcanic cone complexes, Gaoshan, Yanshan, and Da HeiGou, marked as Middle Pleistocene basalts distinctly separated from the young lava flows (Figure 59b). The targeted two vent complexes (Yanshan and Dahei Gou) are scoria cones with welded cores and various clastogenic lava units, indicating eruptions where Hawaiian and Strombolian-style eruptions alternated over the activity. On the present-day Halaha riverbanks, the youngest lava flows extend over 10 km on average and are suspected to reach about 16 km SW from their source following the paleo-Halaha River valley (Figure 60a-d). The surface structures of the flows represent the two distinctive pāhoehoe and ʻaʻā types. Also, pāhoehoe flows preserve a range of ponded fabrics such as ponded lakes, lave tubes, whalebacks, and

tumuli. Lava channels can be observed in a partially collapsed SW side of the Yanshan scoria cones.

4. *Methods*

Sentinel imagery is a ground-breaking aerospace technology which was carried out by the European Space Agency in 2014 (https://apps.sentinel-hub.com). The missions aim at the goals of agricultural monitoring, emergency management, land cover classification, and water quality. This research applies the satellite images depicted from the Sentinal-2 orbital system. The main reason for this research utilizing the Sentinel images is that lava flows or products of volcanism can vastly reveal a range of different textures or visual effects of imagery on the satellite photography system compared to the textures of surrounding areas. Yanshan (YS) and Dahei Gou (DHG) are the two vents that generated the youngest morphologies of lava flows, covering an area of at least about 70 km^2. Please note that on the geological map, the young lava flows are marked in an area significantly larger than the real extent of the lava flows suggested by our reconnaissance mapping. The images from the Sentinal-2 system reveal a series of flow textures under different observation methods (Figure 60a-d). Thus, the targeted two vents, that is, YS and DHG, and their eruptive products (mostly lava flows) might be outlined by systematical analyses of remote sensing and GIS methods in relation to the observed lava successions. DEM images downloaded from the ALOS-PALSAR dataset (https://asf.alaska.edu/data-sets/sar-data-sets/alos-palsar/) that offers digital elevation data with a resolution of 12.5 m. The accessed DEMs were reprojected to the WGS 84/UTM zone 51 N map datum and coordinate system. Using QGIS (version 3.26 – Tisler) and its SAGA and GrassGIS, we created slope maps, hill shades, and topography position index maps to check the general geomorphological details of the region. Cross-sections were utilized to understand the general trends of the morphology of the study area (Figure 61).

The Q-LAVHA plugin of QGIS software can provide a general model or a simulation with analyses of pre-eruptive and post-eruptive topography to interpret lava flow evolution histories and future hazard assessments (Mossoux et al., 2016; Rodriguez-Gonzalez et al., 2021). In general, the Q-lavHA program is a QGIS plugin that simulates

probabilities of ‘a‘ā lavas distributions from one or multiple distributed eruptive vents on a DEM satellite image (Mossoux et al., 2016). The inserted models, such as probabilistic and deterministic models, can

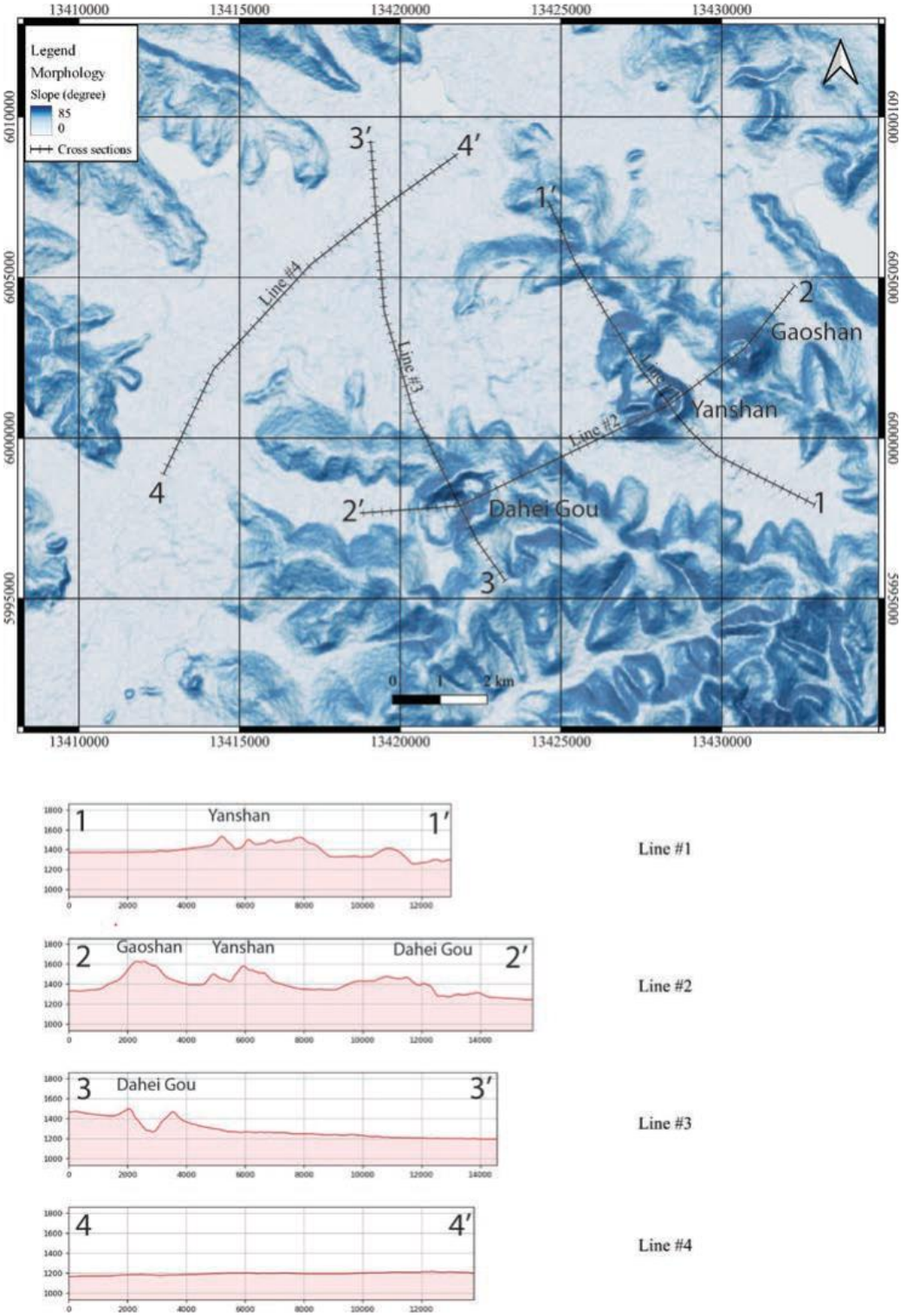

Figure 61: Slope map of the ACVF showing the characteristic texture of the region with scoria cones and extensive lava flows. Cross sections (lines with numbers on the map) revealed a very

gentle sloping landscape upon the lava emplaced. The map is on WGS84 projection using NE China local coordinate system.

provide a range of calculations in relation to probabilities for lava flow propagation and terminal length under spatial aspects (Harris & Rowland, 2001; Harris et al., 1998; Mossoux et al., 2016; Rodriguez-Gonzalez et al., 2021; Vilches et al., 2022). The confine of this program is the probabilistic steepest slope on parameters of spatial spreads. The corrective factors are the major algorithm to even the "pits," which may jeopardize the lava modelling processes by obstacles from DEM images. To overcome this issue, the DEM, upon the simulation runs, need to go through a prescribed preparation outlined in the plug-in manual. We have completed these steps. Moreover, we created a pre-eruptive topography by removing the lava flows on the current DEM. To do this, we created a contour map based on the ALOS-PALSAR 12.5 m resolution DEM and then we manually modified – in a supervised fashion – the contour lines fitting them to the general morphology unaffected by the youngest lavas (Figures 62a and b).

Based on the new contour lines, we recreated a new pre-eruptive DEM (Figure 62c) and visually compared it to the current DEM (Figure 62d). To see the validity of the pre-eruptive topography, we created slope maps for the pre-and post-eruptive scenario (Figures 63a and b) as well as aspect maps (Figures 63c and d) to have visual control over the process. We decided to follow this manual process, in spite of it being more time-consuming, as during the supervised process, we had a continuous connection to the landscape, and we were able to self-evaluate the scenes based on our own field experiences. In the end, we also created pre- and post-eruptive topographic position index maps just to see how the lava flow removal affects this

parameter (Figures 64a and b). Finally, we created a geomorphon map for the present-day situation (Figure 64c).

For the Q-LAVHA simulation, we tested all the in-built methods, and we found the Euclidian simulation performed the best due to the general low slope angle at our

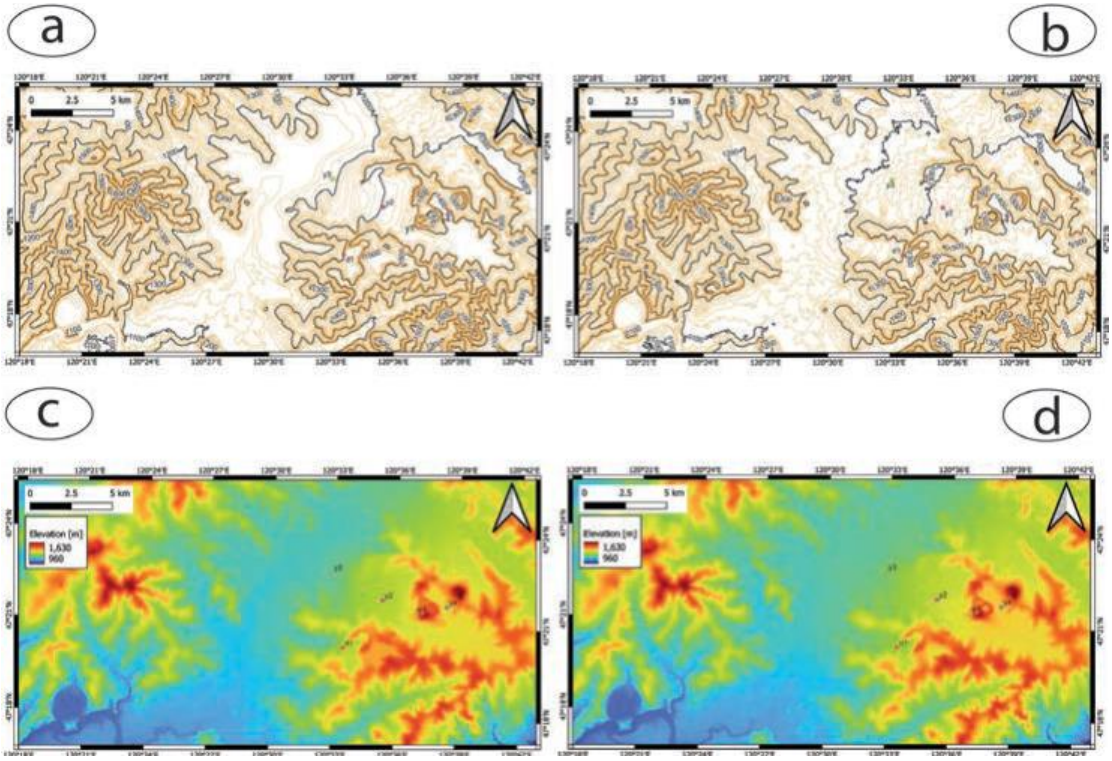

Figure 62: Contour map of the pre-eruptive (a) and post-eruptive (b) surface. Regenerated DEM of the pre-eruptive surface (c) was used to simulate lava flow emplacement. Post-eruptive DEM (d) was used to simulate future lava flow inundation. Maps are on WGS84 projection using a geographical coordinate system.

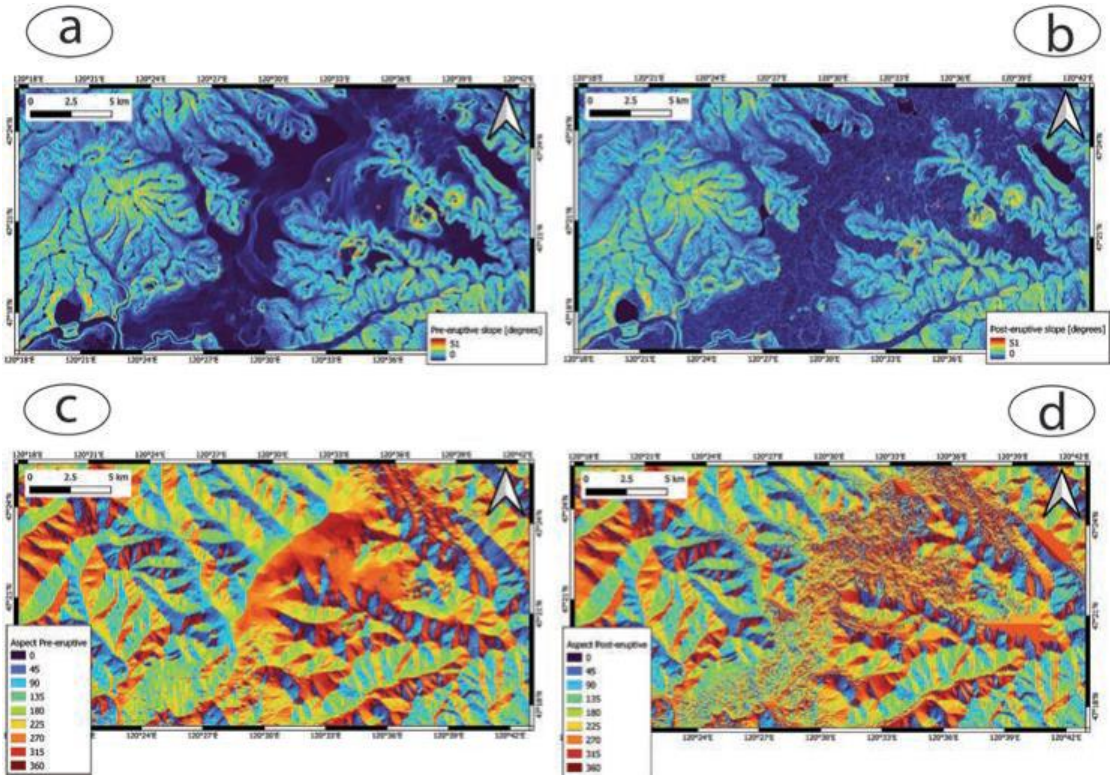

Figure 63: Pre-eruptive slope map (a) shows the general trend of the landscape, while the post-eruptive slope map demonstrates the rugged flow fields (b). Aspect maps of the pre-eruptive morphology (c) indicate a good trend to the general landscape characteristics. The aspect map of the post-eruptive surface (d) shows the rugged nature of the lava flow field. Maps are on WGS84 projection using a geographical coordinate system.

lava flows emplaced (an average of less than 1 degree). Within the simulations, we increased the simulation distances from the measured maximum lava flow runout distances. As other researchers used Q-LAVHA on regions of low slope angles (e.g., flat surface), such as Paricutin in Mexico (Becerril et al., 2021), we followed their recommendations to increase the simulation length well over ten times the measured lava flow length. In Paricutin, an even 50 times longer simulation length has been applied. In our work, we found the simulation distance about 25 times longer than the average lava flow runout distances provided good results, hence in our work, we followed this simulation distance (e.g., 250 km for a 10 km long, or 100 km for a 4 km long lava flow).

The terminal length is considered as FLOWGO Model (Harris & Rowland, 2001) through the definitions of fixed length values, a function of statistical length probabilities, and thermal-rheological properties of open-channel lava flows (Murcia et al., 2014). While Q-LAVHA offers the FLOWGO simulation, it requires numerous

physicochemical parameters (Sun et al., 2018). As we do not have most of those data, we have not explored the FLOWGO to the full extent; instead, we run some tests with likely parameters drafted from variable literature (Harris & Rowland, 2015; Rowland et al., 2005; Wantim et al., 2013). As field evidence indicates that the eruption, at least in the Yanshan vent complex, reached high intensity in times as evidenced by the presence of abundant clastogenic lava flows, we applied high magma mass flux rates, mafic composition, high-temperature conditions, and wide flow channel parameters.

The lava flow simulation method was performed by Q-LAVHA within QGIS. Three different modelling concepts have been carried out: points, a line, and a polygon (Mossoux et al., 2016).

A single point or multiple points are the envisions of vents that probably erupted flows around Yanshan areas. Lines are the simulations of fissure vents. Polygons

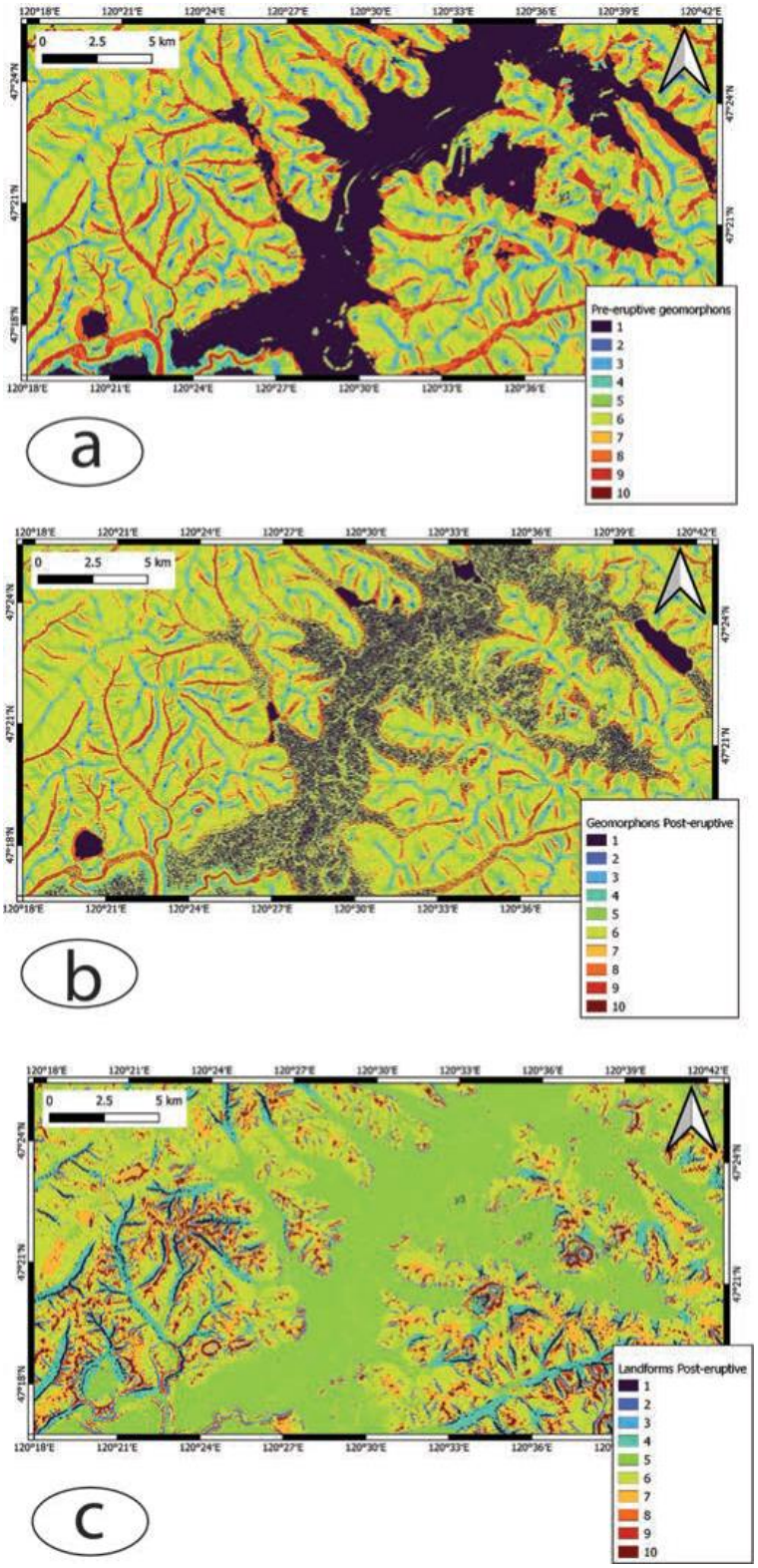

Figure 64: Pre-eruptive (a) and post-eruptive geomorphon maps show clearly the topographical differences the landscape received through the lava inundation. Codes refer to the following parameters: 1) flat; 2) summit; 3) ridge; 4) shoulder; 5) spur; 6) slope; 7) ho llow;

8) footslope; 9) valley; 10) depression. Topographic position index map (c) of the post-eruptive (present-day) landforms shows the variety of landforms the region has. Codes are 1) canyons, deeply incised streams; 2) midslope drainages, shallow valleys; 3) upland drainages, headwaters; 4) U-shaped valleys; 5) plains; 6) open slopes; 7) upper slopes, mesas; 8) local ridges, hills in valleys; 9) midslope ridges, small hills in plains; 10) mountain tops, high ridges. Maps are on WGS84 projection using a geographical coordinate system.

imply vent swarms. For the simulation processes, the preparation of DEM images is necessary. The resolution of a DEM image used is approximately 12.5 m in pixel sizes. Then, the contour map was treated in a supervised fashion, essentially adjusting the contours where the lava flow clearly acts as an addition to the morphology. Utilizing the GrassGIS plugin of QGIS is the next step to rebuilding a DEM image with a new corrected pre-eruptive contour line. It is also important that all the maps must be projected properly to UTM coordinate with the NE China sections.

In the end, we applied a 5 m average lava flow thickness and ran the flow simulation on the current topography to see potential lava inundation in case a similar eruption takes place in the same vent locations as those created in the 2000 AD lava flow fields. As mentioned above, several methods of Sentinel Imagery have been applied to the areas of YS and DHG.

False-colour imagery (Figure 60a) aims at observations of at least one non-visible wavelength to image Earth, which is generally composed of red and green bands in a very popular recognition of images. False colour imagery is most used to assess plant density and healthy conditions since plants reflect near-infrared and green light while they absorb red. Cities and exposed grounds are grey or brown, and water appears blue or black. In this image, the youngest lava flows appear as green colour regions with specific flow-banded patterns. Ash is shown in a smooth pink pattern that fills topography lows. From ash, loose alluvial deposits can be difficult to distinguish, but their surface pattern is slightly different.

Short wave infrared composite (SWIR) measurements (Figure 60b) can estimate how much water is present in plants and soil as water absorbs SWIR wavelengths in the optical spectrum. Shortwave-infrared bands are also helpful in distinguishing between cloud types (e.g., water clouds vs ice clouds), snow and ice, all of which appear to be white in visible light. In this classification, vegetation appears in green gradients, soils

and infrastructures are in brown gradients, and water appears to be black. Newly burned lands are strongly reflected in SWIR bands, making them visible for mapping fire events. Each rock type differently reveals shortwave infrared light, making it possible to map geology by comparing different colours of reflected SWIR light. Barren lava flow surfaces appear in pink tones reflecting the quick depletion of moisture from porous, dark lava surfaces.

Geology 8, 11, and 12 composite uses both shortwave infrared (SWIR) bands 11 and 12 to differentiate among different rock types (Figure 60c). Each rock and mineral type reflects shortwave infrared light differently, making it possible to map out geology by comparing reflected SWIR light. Near-infrared (NIR) band 8 highlights vegetation, contributing to the differentiation of ground materials. Vegetation in the composite appears red. The composite is useful for differentiating vegetation and land, especially geologic features that can be useful for mining and mineral exploration. In the Arxan region, young lava flows appear bright blue and differ significantly from the background brownish-reddish (mostly dry-vegetated) regions (Figure 60c).

Geology 12, 8, and 2 composites use shortwave infrared (SWIR) band 12 to differentiate among different rock types. Each rock and mineral type reflects shortwave infrared light differently, making it possible to map out geology by comparing reflected SWIR light. Near-infrared (NIR) band 8 highlights vegetation and band 2 detects moisture, both contributing to the differentiation of ground materials. The composite is utilized for finding geological formations and features (e.g., faults and fractures), lithology (e.g., granite and basalt), and mining applications. At Arxan, the image clearly shows the young lava surfaces against the vegetated background (Figure 64d).

5. *Results: lava flow morphology and the sources of the youngest AD2000 eruption*

Field observations have already determined that YS (Figure 65a) and DHG are the two large scoria cone complexes that generated significant morphologies of lava flows.

YS, The Triple Vent, preserves three distinctive scoria cones with visual successions from the observations of satellite images (Figures 60a-d). As Figures 64a-d depict, YS

composes of three distinct volcanic edifices overlapping each other with a total area of 2.2 km^2. Fieldworks indicate that the highest elevation (approximately 1597 m above sea level) is observed on the top of the jointing point between the southeast one and the southwest one (Figure 65b). Scoria caps cover the top of the triple vent. The steepest slope is located on the southern flank of the edifice, which is nearly 47 degrees due to the welded nature of the proximal scoria and spatter beds. A breakage merges on the southwestern cone with outpouring lava flows that form a range of influxes at least 3.77 km long into the broad fluvial valley of the Halaha River. Scoria ash and lapilli formed deposits that blanketed at least 1 m thick units in an area mostly to the east of the Yanshan vents (Figure 65c). The Sentinel images reveal that the ash plain extends about 4 km from the Yanshan volcanic complex, and traces of valley-accumulated ash up to 10 km from the source are likely based on the satellite image pattern. The eastern side of the Yanshan edifice is truncated, and a hummocky surface can be traced about a km from the cone flank, indicating an early collapse of the vent toward the east.

The rafted cone fragments were subsequently covered by the ash plain (Figure 60a, band d). Lava flows preserve a range of distinctive features of morphologies, such as

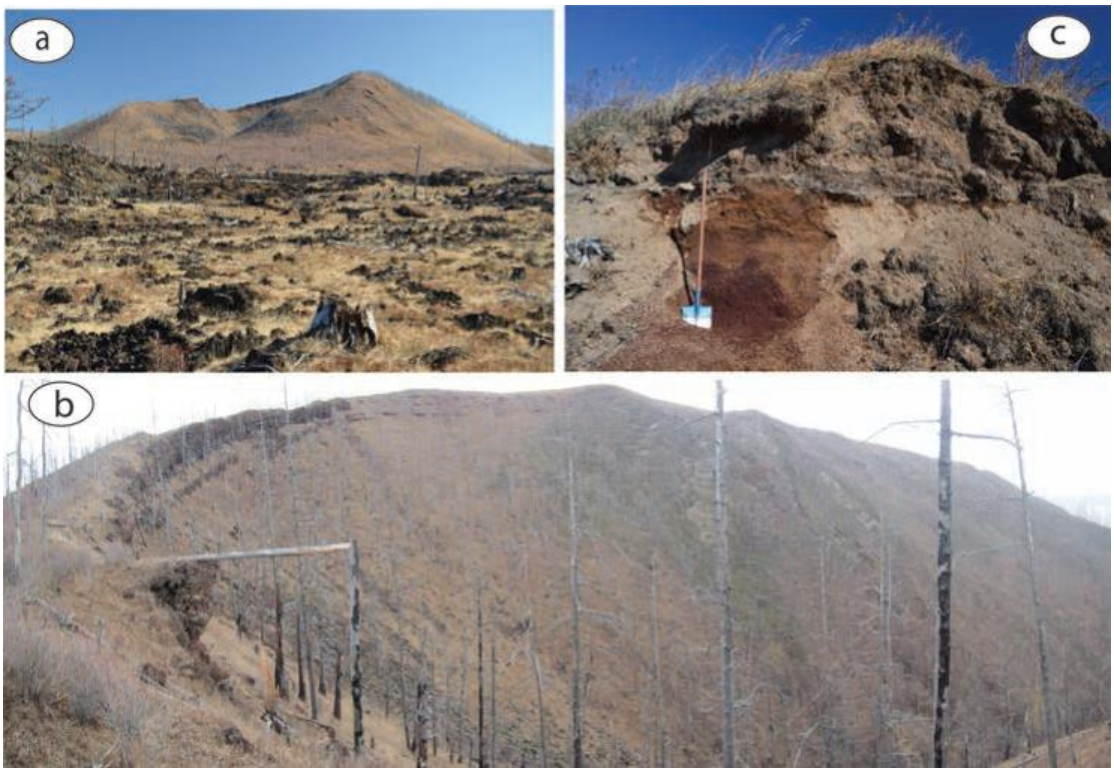

Figure 65: a) Yanshan complex scoria cone from the south. Note the steep slope and the wide-open crater toward the SW. b) the broad and deep crater of Yanshan is surrounded by a steep crater rim formed by clastogenic lavas. c) extensive ash plain over lava flows indicates that explosive eruption took place after the first effusive stage.

rubbly pāhoehoe (Figure 66a), rugged surface textures (Figure 66b), lava channels, and tumuli. Similar to YS, DHG is located in the southwest direction of YS, about 5 km.

The total area of the vent is approximately 2 km^2. In the areas of lava flows influenced by DHG, raft-shaped spatter sections and large slabs of lava that randomly pack in chaotic nature are shreds of evidence of the outpouring of lava from the vent. Inside the crater areas, individual tumuli, ramped-up lava rubble/talus, and large piles of ‘a‘ā lava blocks form a range of rough surface topography. Lava flows along the crater margin preserve several meter-long cracks parallel to the crater margin. These zones, as mentioned above, are represented as fractures along the inflated and ponded intra-crater, where ponded lava collapsed upon the partial evacuation of the large crater. DHG is composed of at least three major nested crater systems (Figures 60b and d), which indicate vent migration, crater infill, and sudden releases of lava, forming a pit-like crater system. Those extended lava fields and morphologies of the vents have drawn interest in eruption histories and geoconservation purposes (Li et al., 2020; Németh et al., 2017a).

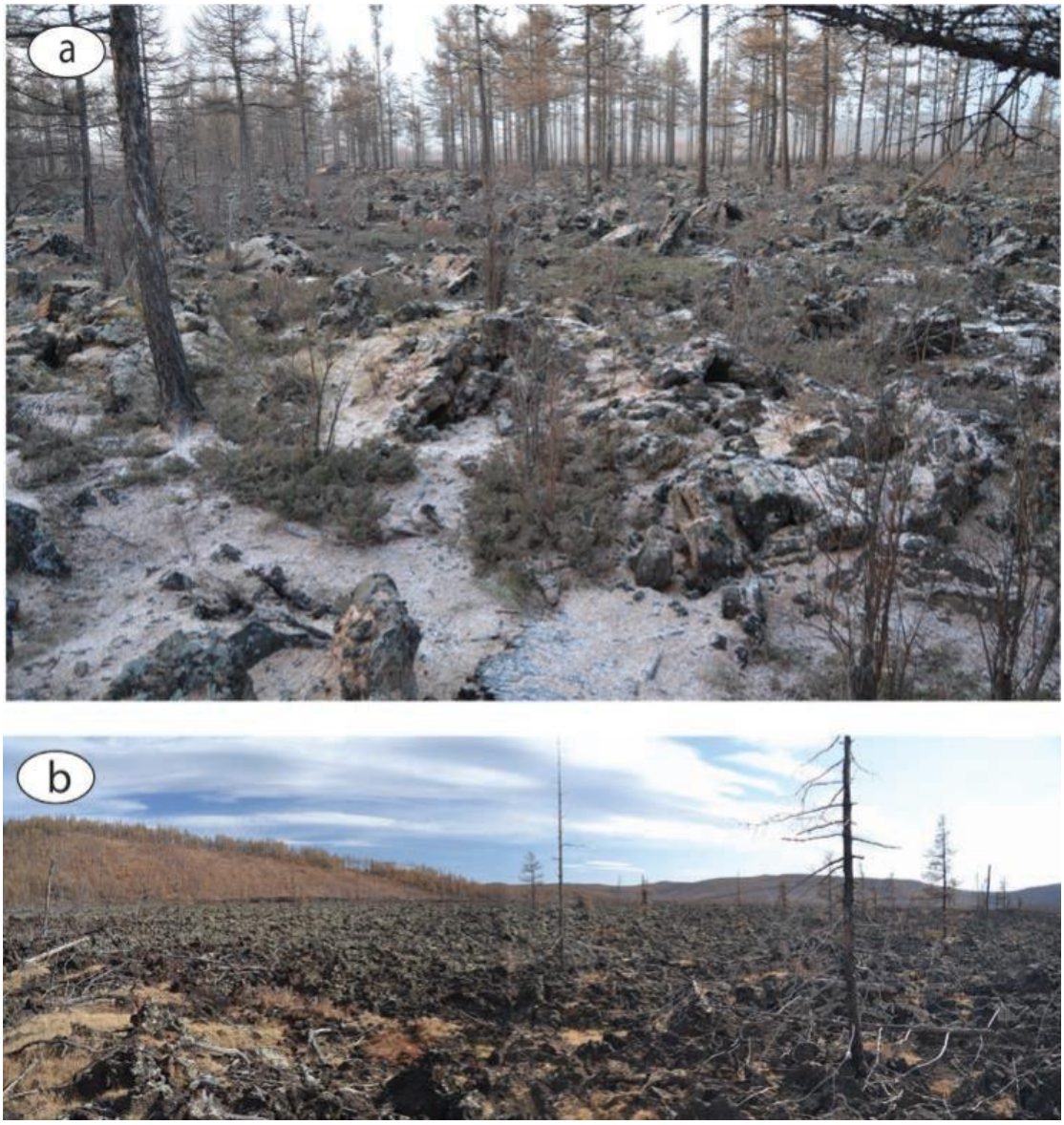

Figure 66: a) Typical distal lava flow field along the Halaha River valley, about 8 km from the source. b) Typical proximal lava flow field in the upper basin just east of the Yanshan volcano group.

General observations on satellite images such as the Sentinel image sets reveal a complex lava flow emplacement history. Three vents of the YS are clearly overlapping each other. On the basis of the overlap, a relative chronology can be established. The northern edifice formed first, followed by a new edifice grown in its southeastern flank. Later on, a third edifice was built on the western margin of the second cone. It is evident that the northern first cone likely suffered a collapse event, and a large part of the edifice was rafted away, forming a hummocky landscape in the eastern regions. It is also evident that the majority of the youngest lava flow is not covered by ash; hence the main ash-producing eruption, inferred to be sub-Plinian (based on the

estimated extent of its deposits), was followed by the main lava effusion toward the west and from a small fissure just NE from the first Yanshan cone.

The main lava flow can be distinguished into at least five satellite image patterns, not including the valley filling flow segment inferred to be derived from Dahei Gou (Figure 67a). The patterns are very similar in each sentinel image; hence they are likely to be reasoned from some geological feature. The main lava flow has a whirlpool-like pattern (Figures 67b and c), indicating flow movement and interaction with obstacles like tumuli; pressure ridges formed slightly earlier in the same flow field. All the sentinel images show that the main lava flow from YS made into the paleo valley of the Halaha River. They are not covered by ash; hence they clearly represent the youngest eruptive event in the region. The whirlpool-like pattern on the main flow indicates a higher portion of the lava margin on its N-NE side of the confining valley than on the S-SW side, suggesting that the flow likely made a curved move anticlockwise (Figure 67a). The elevation difference between the two edges of the flows (on profile 2) is about 40 m, which indicates a slightly westward inclined surface on what the lava emplaced (over 3660 m, about 40 m elevation difference yields a slope of no more than 1 degree, a very flat landscape). A low slope angle means that the lava is emplaced in a very gentle sloping landscape, so it is no wonder it generated some ponding once it entered the main flow channels of the paleo-Halaha River. On the NE-SW sections of the main YS lava flow, the flow thickness is estimated to be less than 10 m in proximal areas, but in the flow edges, the flow became thin, often only around 1–2 m thick. On the basis of the geological observation, a 5 m average flow thickness is a realistic estimate. In the thickest part of the lava flow fields and some ponded sections, the lava thickness may reach 20 m in localized sections. Topography profile from YS and to the far end of the lava field in the SE, over 16,000 m distances, 225 m drop has been recorded, yielding a less than 1° slope again. A low slope angle also indicates relatively thin lava coverage, especially in distal regions, which the direct observations confirmed. DHG longitudinal topography profile across the lava flow emitted from DHG also shows a clear drop of 94 m over 6638 m distance, yielding less than a 1° slope. This section forms the main DHG flow part. The satellite image pattern shows the textures of flows from DHG smoother than the ones of Yanshan flows,

indicating that the main DHG flow might predate YS. About 1186 m above sea level, a clear 2–4 m drop and a topography gap were recognized that separated a younger satellite image pattern suggesting that a young flow, probably of YS origin, formed the axis of the river valley fill flows.

Low thickness is estimated to be similar to YS and fixed to an average of 5 m. DHG topography profile perpendicular to the main flow axis indicates about 7 m higher lava surfaces on the N-NE side of the flow channel, suggesting that the flow slightly climbed in the southern valley margin, just as expected by the movement of the flow from DHG. YS lava flow initiated about 125 m higher than DHG (1381 m versus 1256 m). Judging that both flows are placed on flat areas with less than 1° slopes, it is

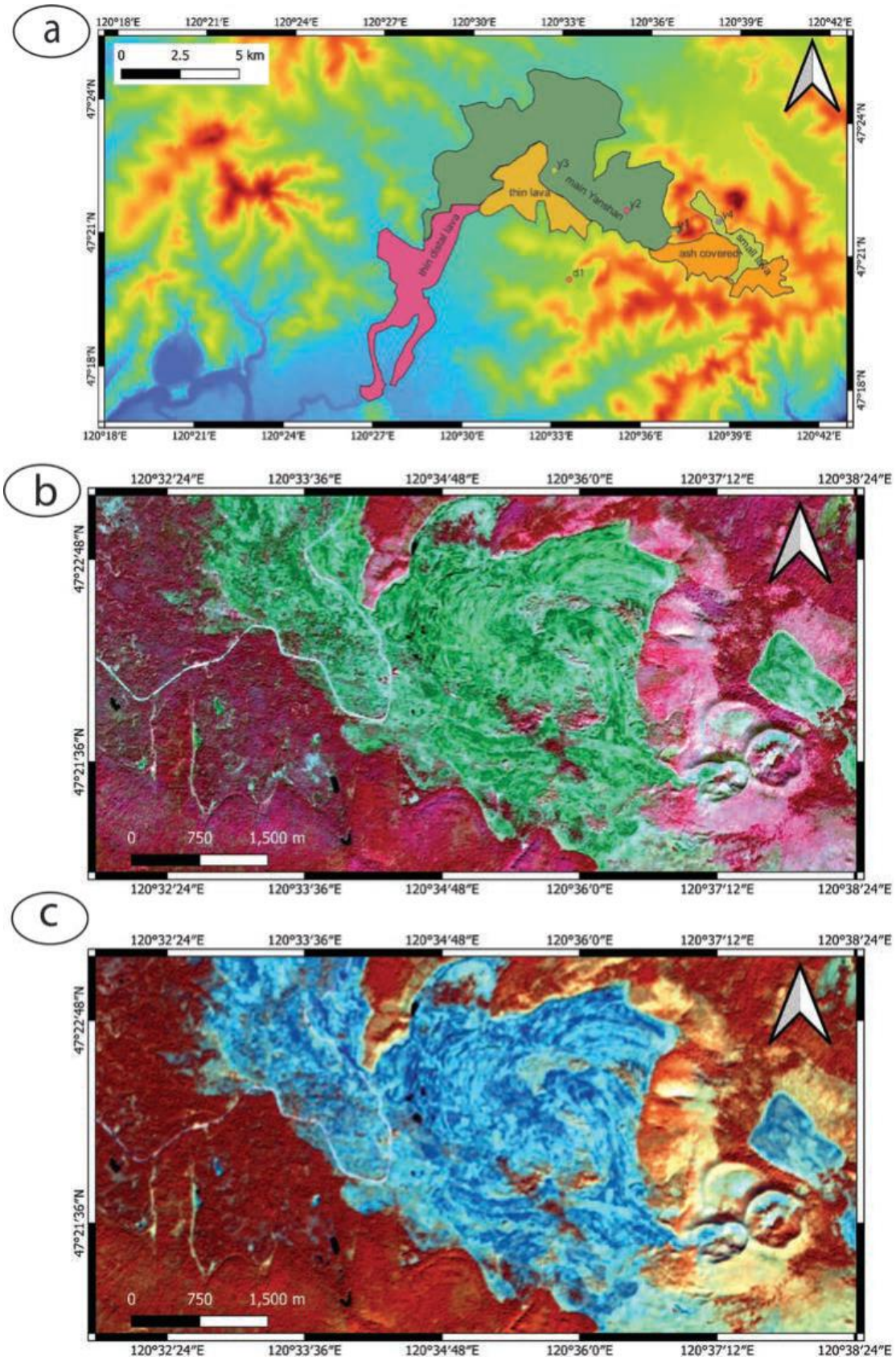

Figure 67: a) Distinct lava flow regions of the youngest lava flow of Arxan. b) Whirlpool-like lava flow pattern on false colour (c) and geology band 8, 11, 12 sentinel satellite images. Maps are on WGS84 projection using a geographical coordinate system.

expected that flows, if similar effusion rates are expected, will go further distances rather than higher elevations (16,000 m vs 6638 m, YS vs DHG, respectively). Following the above-mentioned logical steps, it can be assumed that at low lands, some mixing and interflow of lava flows take place, what we recognized as different satellite image textures. From field investigations, we can see that young lava flows are covered by an ash plain of about 2–4 m thick scoriaceous ash in the SE of YS. Light colour patterns on satellite images indicate that the ash covers are extensive in the SE of YS and likely reach over 10 km from their source. Field mapping confirms that beneath the ash cover, young lava flows to fill the valley in the SE of YS with a new channel of lava flow probably not thicker than 5 m. These lava flows formed before the ashfall. Satellite image textures indicate that lavas likely erupted and formed after the main ash fall events toward the NW, feeding main YS flows to the Halaha River valley. Thin ash coverages were recorded in NW of YS, in elevated regions and beneath some proximal flows. Satellite image textures indicate that young lava flow erupted from a fissure and filled the valley between YS and Gaoshan and some local lows SE from YS. As Gaoshan is fully covered by ash, following the points mentioned above, it can be stated that the fissure formed after the main ash fall event. In summary, Sentinel images reveal different textures from various methods of waveband observations. Those textures might be the indicators of lava successions and possible eruption histories of major territories of ACVF.

6. Discussion

1) Eruption scenarios and possible magnitudes of the vents

From the previous research, YS and DHG are two volcanoes formed by effusive or even violent Strombolian eruptions. Successions of lava flow distributed in surrounding areas of these two vents indicate a range of typical histories of syn-eruptive stages and volcanic edifice constructions.

DHG vent opened first in the youngest eruptive events and formed a scoria cone in the NE, gradually shifting fissures toward the SW. Lava outpour from the SW vent of DHG. At least three closely spaced vents/volcanoes formed, most of them still preserving young volcano morphology. Satellite image textures indicate that some

lava flows spill over the SW vent of DHG and feed the main DHG flow. It cannot be ruled out that the flow was not fed from some western flank fissure in the SW vent of DHG, but the satellite image pattern is more indicative of spillover. The dense vegetation cover over the main DHG flow indicates some soil formation over the lava flow surface. Some ash recorded on top of DHG flow indicates that subsequent, probably early Yanshan-sourced ash covered the main flow and the mixed flows in the far valley. The main SW crater is a 1 km wide and about 50 m steep pit crater filled with fresh lava that shows similar satellite image textures to the youngest lava flow and no sign of ash cover. This indicates that this fresh lava must have been emplaced after the main ash fell from YS.

Shortly after the emplacement of the DHG main flow, the complex YS vent system formed. While earlier Gaoshan was assigned to be part of the Yanshan vent system, based on the satellite image pattern and the general morphological architecture of the edifice, Gaoshan is clearly the oldest landform of the YS region as it has erosional gullies typical for older landforms in the region. It is also completely covered by ash inferred to come from YS.

The YS first vent y1 (Figure 68a) is the northern edifice, a scoria cone with relatively fine-grained deposits. It is not easy to establish if this vent sourced any lava or not. It seems that its SE side might have suffered some collapse as some hummocky surface was observed in the SE of this edifice about a km from its rim, which is in the right position to have some rafted cone there. In addition, in the same scar region, the second set of vents formed y2 (Figure 68b). This volcanic edifice reached about 100 m elevation and formed a steep scoria cone. The deepest point of the funnel-shaped crater is only about 25 m above the lava fields in the east. This cone must have been active for a long time to build such a substantial size of the cone. The cone also evolved in at least two phases, as magma withdrawal must have created a crater. After rejuvenation, it formed an intra-crater cone that nearly filled the original crater zone but never grew out of it. This eruption phase was also purely explosive, but its deposits were likely to form localized deposit piles within the major crater and probably the outer flank. This complex explosive activity produced ash plumes that deposited ash that covered earlier lava flows. Such flows are probably emitted due to magma

withdrawal during the main cone growth phase. The eruption subsequently built the third volcano just SW from the y2, defined as y3 (Figure 68c). The y3 built a scoria cone as well, forming an attached cone nearly as high as y2. Gradual SW-ward shift of the activity gradually built another edifice that subsequently changed its activity dominated by Hawaiian-style lava fountaining and building a complex spatter system. This side of the volcanic complex probably suffered some collapse and rafting, letting the magma find its way out toward the west, feeding the main lava flow of YS, reaching the Halaha River valley about 16 km away from the emission point.

At the time of the main lava emission, explosive activity was ceased or limited only to small lava fountains and/or localized ash emission toward the east, as the young lava flow surface has no ash cover. Probably at the same time (not really possible to establish relative chronology), a small fissure opened between YS and Gaoshan and emitted a flow that filled the depression just east of the YS system and between Gaoshan and YS. This event also postdates the ash fall event and is likely the youngest phase of the eruption. Interestingly, the Sentinel image textures in the DHG crater also exhibit very young lava morphology, raising the question that DHG probably had experienced an intermittent lava effusion phase that partially refilled the crater. Thus, a complex fissure is an aligned eruption sequence that puts DHG and YS on the same time horizon. Gaoshan is likely part of an older phase of eruptions. Thus, it can be assumed that this eruption was really an extensive event that occurred in a structural alignment (fissure or fault?) about 15 km in length.

The calculations of the estimated volumes of lava pouring can reveal how long the eruption events last. The lava flows are unlikely to form more than 20 m in thickness in ponded regions on valley floors. The estimated volumes of lava emplacements are calculated by a range of standards, such as the eruption types of other volcanic fields (e.g., Mt. Etna in 2001 and Hawaii in 1985). So far, the field identifications and observations, or even classifications, have already yielded an outcome that YS and DHG were formed by a series of violent lava fountaining or effusive eruption events. Also, the steps on the field are indicated that the slope of lava fields is relatively flattened. Thus, the simulations carried out on YS and DHG from the volcanoes with this similar eruptive style can be considered to be valid assumptions of eruption

scenarios. In Table 11, the rates of lava emplacements are based on different scenarios from varieties of volcanic fields in the world.

From Table 11, it can be assumed that probably about 14–30 m^3/s interval of the realistic one (green colour). These two values mean that the eruption periods lasted about half

Lava flow	Surface Area [m^2]	Average Estimated Thickness (m)	Volume (km^3)	Estimated Emplacement Time - Negros de Aras (Chile) (m^3/s): 14	Estimated Emplacement Time Negros de Aras (Chile) (m^3/s): 113	Estimated Emplacement Time Nyíamuragira 2006 (m^3/s): 145	Estimated Emplacement Time Mt Etna 2001 (m^3/s): 30	Estimated Emplacement Time Lentiscal (m^3/s): 100	Estimated Emplacement Time Hawaii 1985 (m^3/s): 2
Small YS (yv2)	2845217	3	0.00853565	7.056589782	0.874267761	0.68132591	3.293075231	0.987922569	49.39612847
Thin mixed lava (yd mix)	12014075	4	0.0480563	78.82095929	4.922187398	3.835911558	18.5402392	5.562071759	278.103588
Thin YS (y-d)	7363514	4	0.02945406	4.325035232	3.016844477	2.35105811	11.36344753	3.409034259	170.451713
Ash covered YS (yv1)	8537547	3	0.02561264	68.54108424	2.623385878	2.044431753	9.881420139	2.964426042	148.2213021
Major DHG (d)	10923970	8	0.08739176	14.7572615	8.951138971	6.975715198	33.71595679	10.11478704	505.7393519
Mayor YS (yv3)	37086705	8	0.29669364	232.6958946	30.38897493	23.68244253	114.4651389	34.33954167	1716.977083
Total	78771028		0.49574405	406.1968246 In realistic	50.77679941	39.57088506 In min	191.2592778 In realistic	57.37778333	2868.889167 In max

Table 11: Estimated eruption scenarios of YS and DHG that were calculated by different standards from similar volcanic fields.

a year to one and a half years with the continuous development of the entire flow field. However, considering the distinctive flow fields, it can be inferred that major effusive phases, either explosive phases or quiet time, have taken place. Overall, the possible assumption can be estimated that a similar eruption probably took a few years with distinctive explosive phases and separate lava effusion stages from vents along the main structural zones.

The 1983 eruption in Hawai'i was fed by effusion rates of up to 22–44 m^3/s and flows extended 7 km^2 to form a 6 km^2, 100 × 106 m^3 flow field (Trusdell, 1995). In contrast, the 1985 eruption (also in Hawai'i) was fed by effusion rates of 0.5–4.5 m^3/s, which resulted in flows extending 1.8 km to form a 2.2 km^2, 19 × 106 m^3 flow field (Harris et al., 1997). Effusion rate also appears to control the basic flow dynamics. In Hawaii, effusion rates determine the manner in which flows are emplaced. Effusion rates at 120 m^3/s produce rapidly advancing channelized 'a'ā lava flows, and effusion rates of approximately 20 m^3/s (but typically more than 5 m^3/s) produce slowly advancing tube-fed pāhoehoe flows (Rowland & Walker, 1990). The lava flows at ACVF are somewhere between. In the upper flow regime, they are more like a'a-type of lava flows with lots of slabs and rubbly pahoehoe; once they reach the valley floor, they slow down, inflate, and make whaleback features. Considering that the region is very flat, it can be imagined that the flow had to go at a reasonable speed (higher effusion rate) to retain heat to make the lava able to advance. In the end, the flow advanced over 16 km from its source, and even in DHG, the flow reached nearly 7 km. This is a large number and requires a relatively fast-moving flow.

2) Lava flow simulation

Sentinel images in different observation methods show the different textures of lava flows around YS and DHG. Those textures indicate the different lava batches, which were systematically emplacing and overlapped with each other. As mentioned above, the flow thickness is estimated to be about 5 m on average. While flows accumulate on a very flat surface (less than 1 degree), the program needs a substantial L value of simulation distance to put in as the measured lava runout distance (Becerril et al., 2021). If given a specific runout distance of the flows, for example, 10 km, the L value

would be 10 km. Thus, if given 25 times runout distance, the L value is actually 250 km. Eventually, the best simulation outcome is 250 km for the lava flow runout distance as the modelling pattern successfully covers the estimated flow areas (i.e., from YS). Field works have already proven that the slope of the flow areas is low, which might be no more than 1°. Such large volumes of flow can only be pushed on the flattened surface by a high effusion rate. Also, the low value of flow thickness with such an effusion rate that leads to large coverage areas of lava flows is approximately 5 m. Eventually, 5 m thickness of the flow pluses and 10 m of the given buffer thickness can help the modelling process switch on the quadrant, and the "16-point" aid makes sure that the simulation does not stop on flat surfaces (Mossoux et al., 2016). The best modelling pattern was created by Euclidean Length, which means that each iteration stops when the flowline reaches the specified Euclidean Length (m). The Euclidean represents the crow-fly distance between the point where the simulation starts and the front of the flow line. This calculation way can let flow patterns freely distribute in confined areas. From the above-mentioned modelling processes, geological implications can be:

- The flow thickness is probably the best to fix at 5 m, knowing that this might be higher up to 10 in proximal areas or far less in the far end of the flow lobes. This model envisions very well to correspond with geological observations in two seasonal field works.
- The lava flows probably cannot be in the 3 m range as they are too thin, and the model stops too early, whatever parameters are fitted in the program.
- The flows also cannot be more than 10 m range as that creates edifice-like flow patterns with far less lava flow runoff.

However, the problem is that this simulation cannot simulate the flow flowing through the Halaha River channel, which has a lower elevation than YS's. In order to solve this issue, one possibility is that those fields had been inundated by flows from DHG earlier.

The line simulation yields a distinctive outcome that may indicate YS and DHG were lying on the same fissure (Figures 69a and b). If the program is carried out YS and DHG within a 1 km wide, 7 km long fissure line, also let the program select random vents

along this assumed line with an average distance of about 500 m spacing. In this way, almost the entire lava flow area is covered by the simulated pattern. Thus,

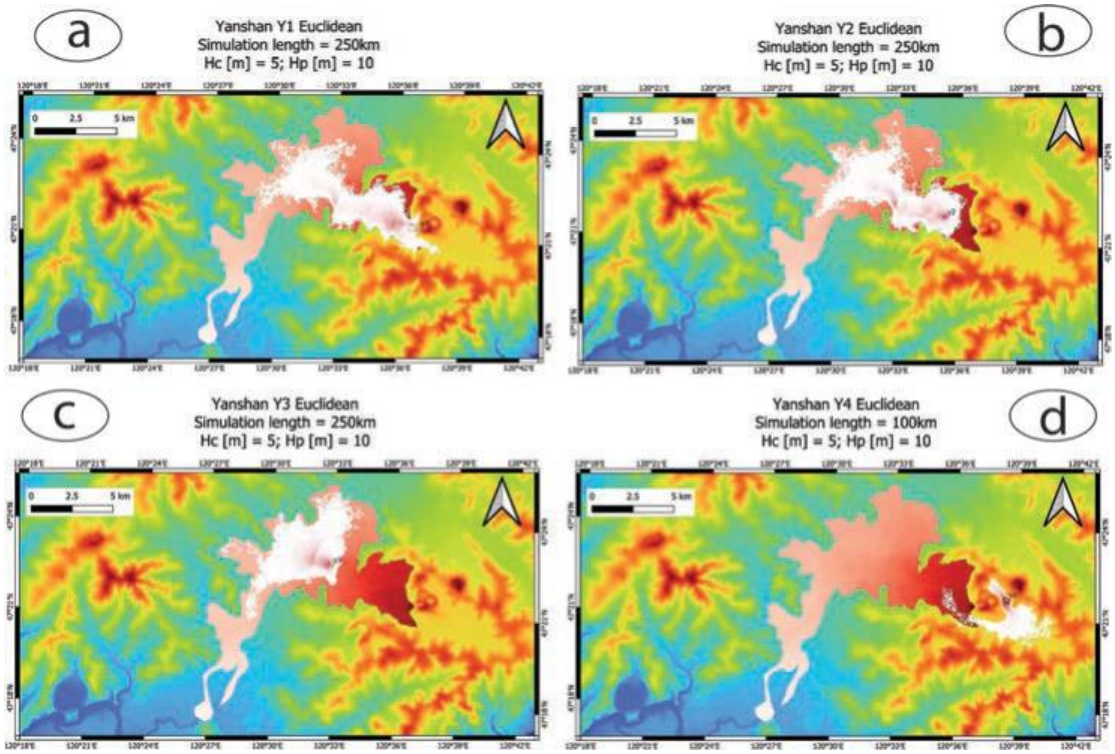

Figure 68: Lava flow simulations from four different point sources; a) from y1; b) from y2; c) from y3; d) from y4. Maps are on WGS84 projection using a geographical coordinate system.

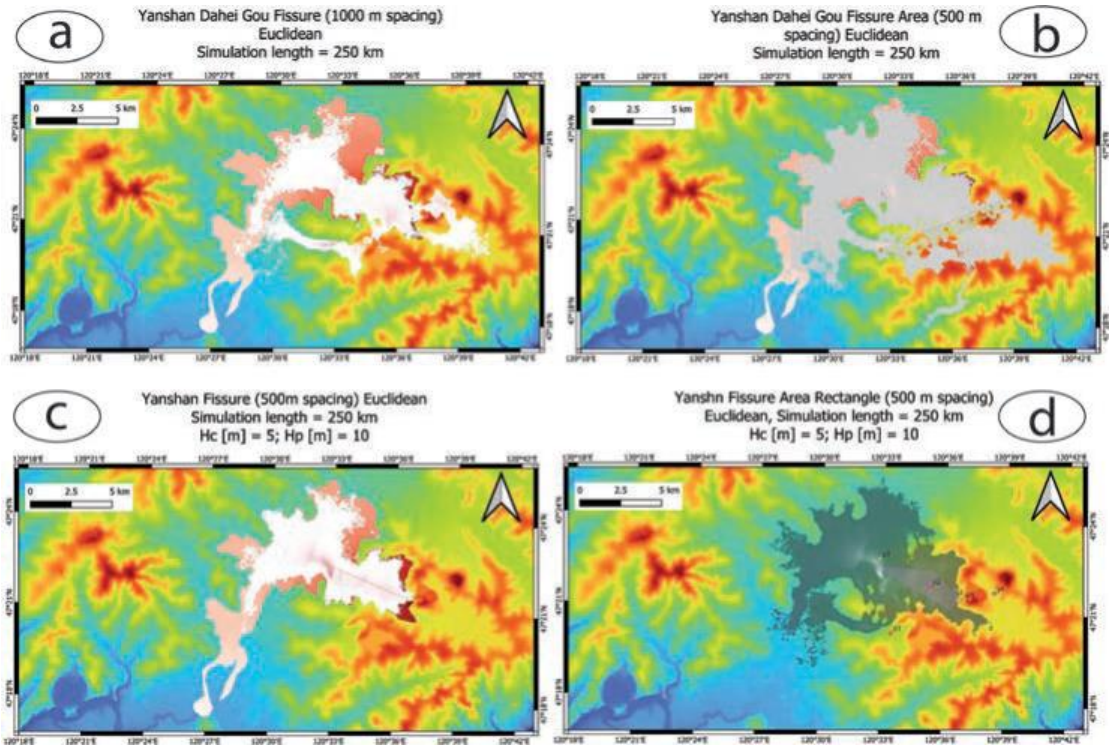

Figure 69: Lava flow simulation through a fissure between Dahei Gou and Yanshan (a) or a rectangle shape area of vents between Dahei Gou and Yanshan (b). Fissure eruption along an NW-SE axis valley centerline (c) and along a rectangle-shaped area (d) near Yanshan. Maps are on WGS84 projection using a geographical coordinate system.

the line simulation may imply that the Triple Vent and DHG probably erupted at the same time along a fissure about 1 km wide and 7 km long. Furthermore, flow thickness is no more than 5 m on average.

In addition, we explored the simulation if we envision a fissure from Yanshan toward the Halaha River valley and simulate a fissure eruption event (Figure 69c), treating the region as a potential vent zone within a rectangular region (Figure 69d). Both modellings were able to reproduce the upper flow fields of Yanshan. The vent area model, however, generated a potential scenario that lava may have overspilled from the Yanshan valley to Dahei Gou, which is a unique but apparently not impossible scenario (Figure 69d).

On the basis of the simulations, we fixed the lava flow thickness at 5 m and applied the same parameters we used on the current DEM to test how a lava flow would behave if future eruptions took place from the same vent. This is an unlikely situation within monogenetic volcanic fields, but not unknown. In addition, the two main vent complexes clearly show geological evidence that they are amalgamated complex

edifices where subsequent eruptions took place, at least in the vicinity of the previous vents.

The four-vent simulation on the current topography created a lava flow field that nearly completely covered the lava fields in the Yanshan and upper Halaha River Valley (Figure 70). It is clear that such eruptions would produce enough lava flow to disrupt the two main roads crossing the region.

3) Implications for the geopark

Applying the simulation to a theoretical fissure opening between Dahei Gou and Yanshan produced very extensive lava flow fields that clearly would be a devastating event for the operation of the geopark (Figure 71).

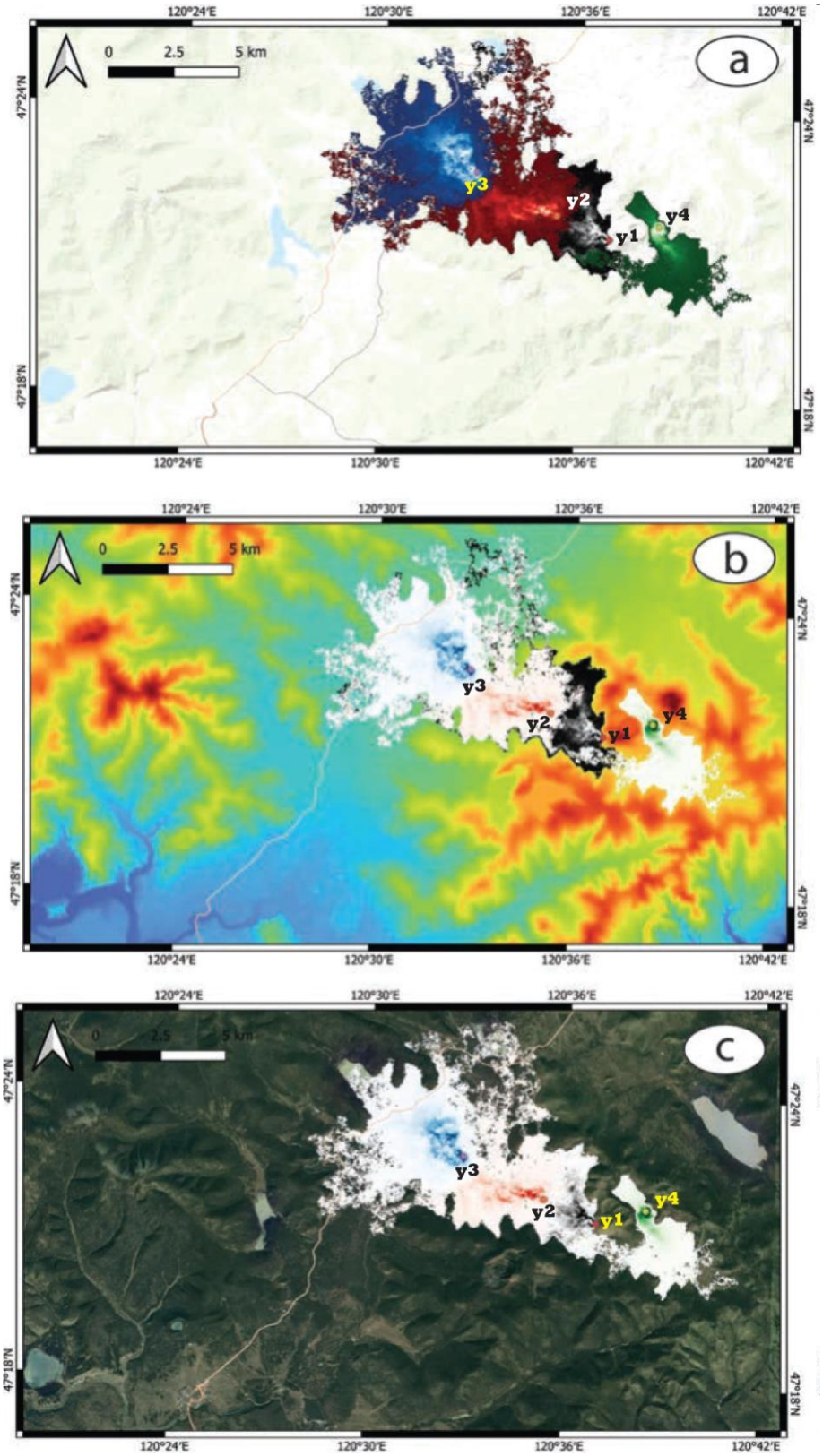

Figure 70: Set of lava flow simulations run over the current topography (post-eruptive), simulating lava effusion from the four vents along the NW-SE trending valley near Yanshan. Shaded relief map (a) with roading, post-eruptive DEM with roading (b), and GoogleEarth satellite imagery with roading show the potential inundation if effusive eruptions would take place from y1, y2, y3, and y4 vents in this time sequence.

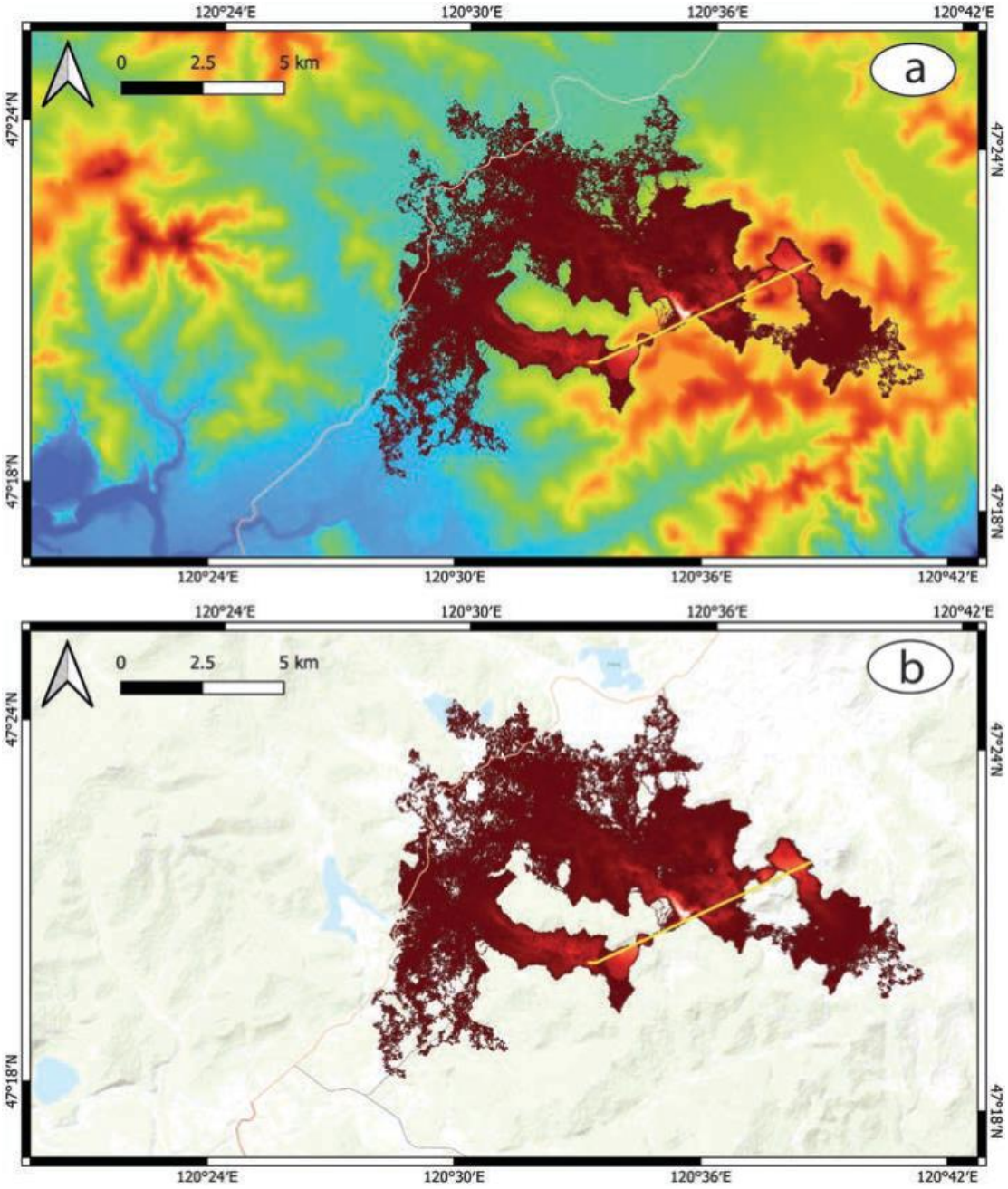

Figure 71: Simulating lava effusion along a fissure running between Dahei Gou and Yanshan on a post-eruptive DEM (a) and shaded relief (b) maps showing an extensive lava inundation that would fill the two parallel NE-SW valleys within Dahei Gou and the Yanshan group situated. Maps are on WGS84 projection using a geographical coordinate system.

Surprisingly, if we envision a vent swarm within a rectangle area in the Yanshan valley, it is likely that lava will enter the Dahei Gou valley and be able to produce extensive flow inundation, posing a substantial volcanic hazard for the geopark (Figure 72).

ACVF is located in a territory of a UNESCO Global Geopark, which was established in 2016 (Németh et al., 2017a). The annual tourism visitation rate is high, especially in

the high season and Chinese holidays; hence the volcanic risk is evident. The infrastructures of this geopark are mostly well constructed, but lava flow inundation simulations showed they are beyond the potential destruction zones. The current lack of volcanic hazard management consideration can be a critical issue not only for wealth engagements but also for the safety of local people.

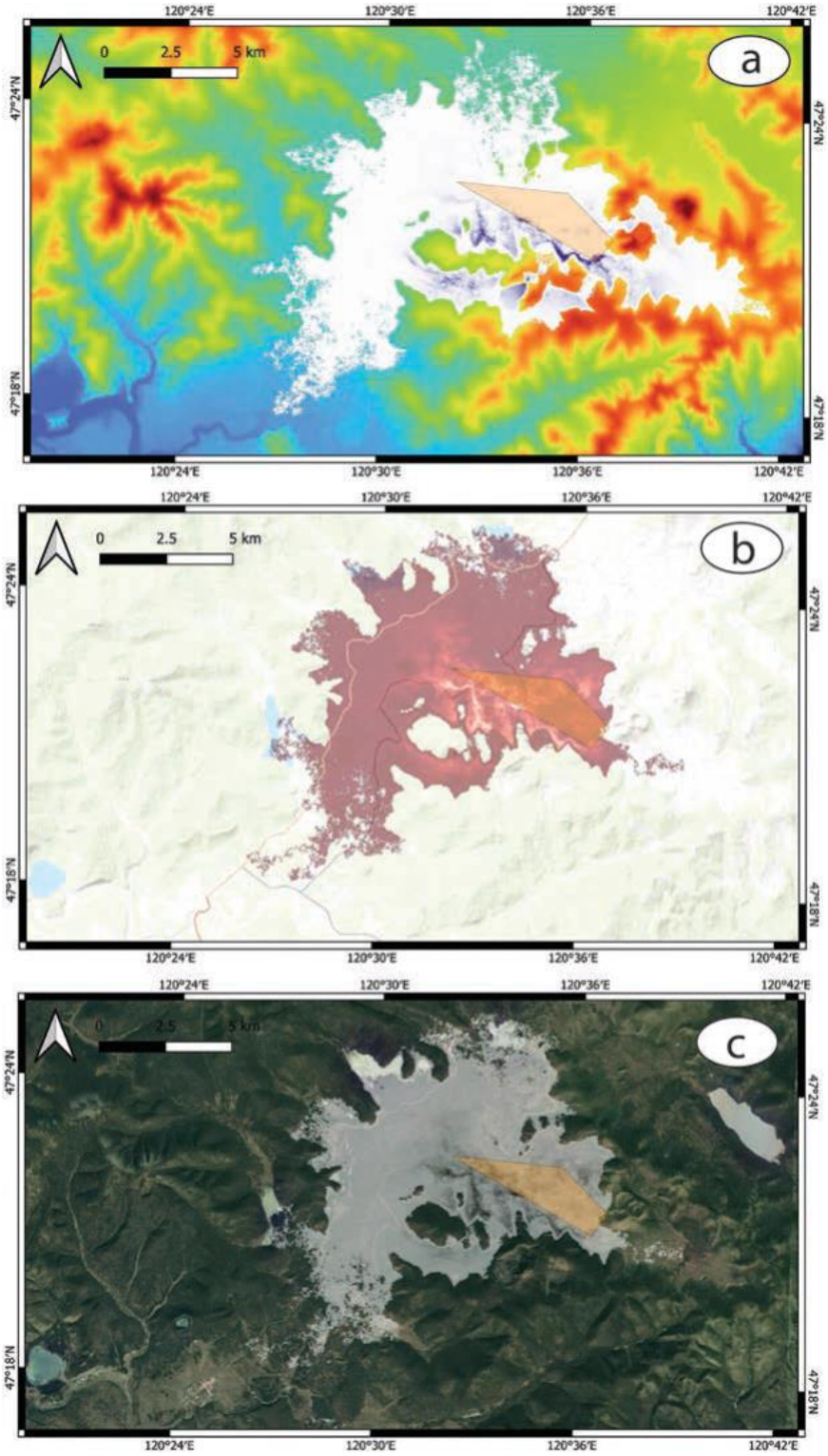

Figure 72: Lava flow inundation simulation applying rectangle shape vent zones along the NE-SW axis valley within the Yanshan group sits. On the digital elevation model (a), it is clearly visible that lava flows can reach the Dahei Gou valley and the maximum run-out distance of the flow can reach the broad alluvial valley near the local tourism centre of Tianchi township. On the shaded relief, (b) and Google earth satellite image (c) illustrates well the potential extent of the lava flows and their impact on the infrastructure. Maps are on WGS84 projection using a geographical coordinate system.

As mentioned above, ACVF is still an active volcanic field; YS and DHG are the two major vents in magnificent scales (e.g., volumes and areas). DHG and YS are observed from the Google satellite images and located from the main Tianchi Town, about 12.6 km and 17.3 km, respectively. From the observations of slope maps, the town is on the west side of these two vents, and elevations on the western side of ACVF are generally lower than the elevations on its east. Satellite images show that lava flows are the basement of constructions in relation to the town. The Halaha River cuts through from the western end of ACVF and then flows to the south, which is also the southern side of the town. Assessments and evaluations from Table 11 are sufficient indicators that a possible effusion rate of lava flows might be a significant parameter of local risk management. Under the relatively high effusion rates and considered flattened surfaces of local territories, basaltic flows always influenced tremendous areas surrounding the vents. The total area of flows in targeted destinations of ACVF is approximately 90 km^2. In comparison to the Hawaii eruptions in 2018, the flow areas generated from YS and DHG are less than the mentioned one, which was about 144 km^2. Another thing is that a 90 km^2 area of lava flows has already succeeded the total area of Wudalianchi flows, which is approximately 65 km^2 (Gao et al., 2013; Xiao & Wang, 2009); this could mean that the potential hazards from ACVF are needed to pay attention to most aspects of safety prospects. Local geomorphology shows that YS and DHG were formed in intra-mountainous settings. Valleys are the confines for the lava flowing. The low viscosity properties of basaltic lavas make the hazard areas even more dangerous than other areas with open topography; specifically, the town was built in the central part of the valley bottoms. ACVF is a national geopark in an active volcanic zone; this is very different from other volcanic geoparks that are commonly far away from the major vents. The low population in the region prevents generating primary interest in volcanic hazards within the community. In addition, people have little information and understanding of volcanic hazards; hence the Arxan UNESCO Global Geopark could be an excellent avenue to pass knowledge on the volcanic hazard to the local communities and visitors.

7. *Conclusion*

This preliminary research about lava flows erupted from YS and DHG tries to bring a new insightful result of lava evolutionary histories and subsequent hazard evaluations. Sentinel imagery plays an essential role in this research. Calculations for the lava volumes and effusion rates are the major outcomes of this research for the first time, providing geologically validated and modelled lava flow eruptive volumes for ACVF. GIS-based techniques provided new information on the nature and extent of lava flow inundation. Applying STRM and ALOS-PALSAR Digital Elevation Models and applying GIS techniques to analyze the morphological assets of the ACVF provided a complex framework to simulate lava flow inundation. Lava flow simulations, in concert with direct field observations, revealed that future lava flow effusion would generate significant lava flow infill along the NE-SW trending valley within Dahei Gou and Yanshan volcanoes sit. As these lava flow likely would reach the main transport routes of the region, complex volcanic hazard studies and probabilistic estimates are needed to mitigate future volcanic hazards. Future research is needed to concentrate on the chronologies of lava successions and predictions of future eruptions, along with the local fissures which formed the lava flows in ACVF.

MASSEY UNIVERSITY
GRADUATE RESEARCH SCHOOL

STATEMENT OF CONTRIBUTION
DOCTORATE WITH PUBLICATIONS/MANUSCRIPTS

We, the candidate and the candidate's Primary Supervisor, certify that all co-authors have consented to their work being included in the thesis and they have accepted the candidate's contribution as indicated below in the *Statement of Originality*.

Name of candidate:	Bo'xin Li
Name/title of Primary Supervisor:	Prof. Károly Németh
Name of Research Output and full reference:	
Geodiversity elements of a young fissure system as an immedi-ate precursory event of the youngest fissure-fed eruption within the Arxan UNESCO Global Geopark, Inner Mongolia in NE China	
In which Chapter is the Manuscript /Published work:	Chapter 6
Please indicate:	
• The percentage of the manuscript/Published Work that was contributed by the candidate:	Bo'xin Li, 80%
and	
• Describe the contribution that the candidate has made to the Manuscript/Published Work:	
Prof. Károly Németh	
For manuscripts intended for publication please indicate target journal:	
MDPI	
Candidate's Signature:	Bo'xin Li
Date:	
Primary Supervisor's Signature:	Prof Karoly Nemeth (Digitally signed by Prof Karoly Nemeth, DN: cn=Prof Karoly Nemeth, c=SA, o=Saudi Geological Survey, ou=National Earthquake and Volcano Program, email=nemeth.k@sgs.gov.sa, Reason: I am approving this document, Location: Jeddah, Kingdom of Saudi Arabia, Date: 2023.05.08 13:01:52 +03'00')
Date:	8 May 2023

(This form should appear at the end of each thesis chapter/section/appendix submitted as a manuscript/ publication or collected as an appendix at the end of the thesis)

Chapter 6: Geodiversity elements of a young fissure system as an immediate precursory event of the youngest fissure-fed eruption within the Arxan UNESCO Global Geopark, Inner Mongolia in NE China

This mini-chapter has already been published on the Sciforum website (https://sciforum.net/paper/view/13807). The data was analysed by the author, Bo'xin Li, who is under the supervision of Prof. Karoly Nemeth, Prof. Alan Palmer, and Mrs Julie Palmer. This chapter is also an extension of Chapter 5, about the young lava flows with respect to the concepts of fissure-eruptions.

1. *Abstract*

The Arxan-Chaihe Volcanic Field (ACVF) is a Pliocene to Recent intracontinental monogenetic volcanic field. Within the ACVF are preserved at least 47 vents in a 2000 km^2 area, forming two major NE-SW trending structural elements. The youngest eruptions took place about 2000 B.P., forming two distinct complex scoriaceous and lava spatter cone systems emitting low viscosity lava that invaded the paleo-Halaha River tributary, forming pahoehoe flow fields. This lava field forms the backbone of the geoheritage values of the Arxan UNESCO Global Geopark. The lava flow fields were believed to be almost exclusively sourced from a single vent complex around the Yanshan – Gaoshan region. However, a recent study has revealed that the flow field is a result of complex eruptions with an early phase from the nearby Dahei Gou vent complex. Here we provide evidence, based on Sentinel satellite imagery, ALOS-PALSAR-derived digital terrain model analysis, and direct field observations, that an even earlier fissure-fed eruption created another complex. This can be seen as a smaller lava flow field on the western side of the main flow field. The Dichi Lake is an iconic geosite of the geopark. It is a maar crater formed by a single explosion through an earlier lava field erupted from a network of fissures about 2.5 km long following a NE-SW trend. The Dichi Lake geosite provides an ideal example demonstrating the

effect of fissures opening in water-saturated lowlands resulting in phreatomagmatic eruptions. Moreover, our findings suggest that the youngest eruption in this region had at least three phases, probably not more than a few decades apart, along a 15 km-long fissure network propagated from the S.W. to N.E. We propose Dichi Lake as the centre of a geoheritage precinct, providing a hub of knowledge dissemination highlighting fissure eruptions as a key type of volcanic hazard to be taken seriously in the management of the geopark.

Keywords: geodiversity; volcanic geoheritage; volcanic hazard; monogenetic; scoria; lava

2. *Introduction*

The Arxan-Chaihe Volcanic field is in Inner Mongolia, in N.E. China and considered to be an active monogenetic (Németh & Kereszturi, 2015) volcanic field that evolved since the Pleistocene (Cui et al., 2021; Li et al., 2020; Németh et al., 2017a; Zhao et al., 2008). The latest eruption of the field took place about 2000 years ago, emitting over 20 km long, complex lava flows that filled the low-lying fault-bonded fluvial network of the region (Bai et al., 2005; Cui et al., 2021). The volcanic field hosts two geoparks, one of which is the Arxan UNESCO Global Geopark enjoys international recognition (Németh et al., 2017a). Volcanism and the eruptive products of monogenetic volcanism play a key role in the geopark geoeducation, geotourism and geo-conservation ventures (Németh et al., 2017a). The main attractions of the geopark mostly consist of lava surface features exhibiting various pāhoehoe lava, tumuli, and inflation/deflation features (Németh et al., 2017a; Wang et al., 2014). In addition, the geopark also highlights the power of young lava flows capable of blocking the entire fluvial network and creating a new lacustrine environment. While these are undoubtedly important geological and morphological features, the young volcanism offers far more to be explored and utilised in the geoeducation and geotourism program of the geopark. Here we provide a geological insight into the importance of fissure-fed volcanic eruptions that shaped the region's volcanic landscape that can be incorporated far more in future programs of the geopark.

3. *Materials and methods*

1) Study area

The study area is part of the Arxan-Chaihe Volcanic Field (Fig 73). It is a middle mountain area where Mesozoic basement rocks form fault-bounded ridges (Meng et al., 2018) (Figs 73 & 74). Between the ranges, broad flat-floored valleys are commonly filled with basaltic lava flows. The modern fluvial network gradually cut into the older lava surfaces forming canyons and broad alluvial fans in convulsions of major valley networks. The region has recognizable volcanic geoforms of scoria cones and maar craters filled with lakes (Li et al., 2020). Scoria cones commonly host shallow lakes that are also part of the main landscape elements of the region, such as the Arxan Tianchi near Tianchi township. Preserved volcanoes clearly form vent alignments following the main NE-SW trending structural elements of the region (Figs 73 & 74).

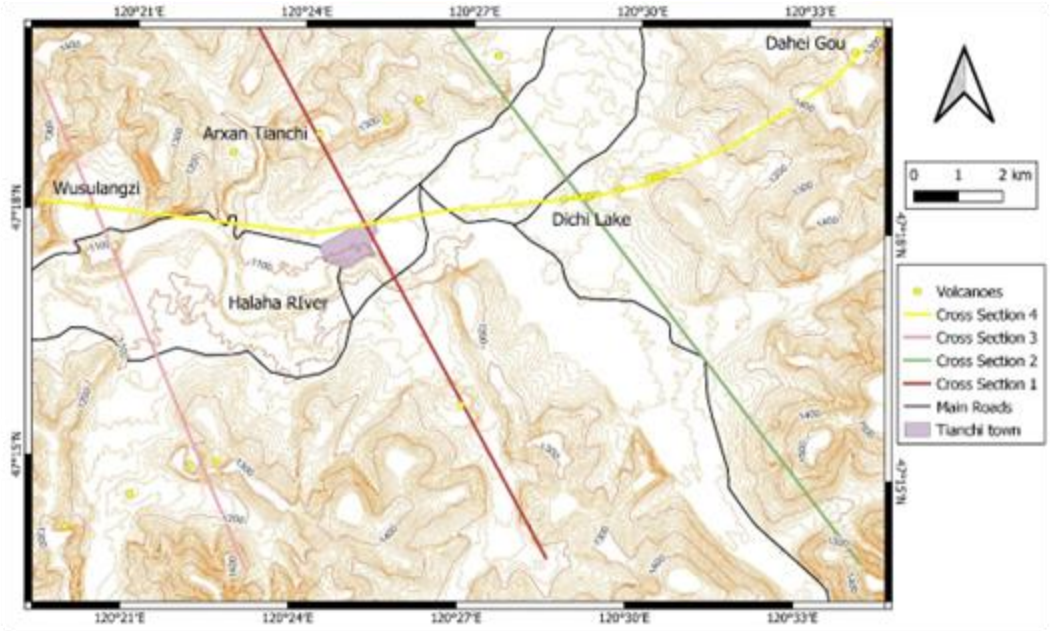

Figure 73: Contour map of the study area (10 m intervals) based on ALOS-PALSAR 12.5 m resolution digital elevation model (DEM). Lines representing cross-section lines. Note the aligned volcanoes following the main morphological escarpments of the region.

The region has a mountainous appearance despite the fact that the general trends of the relief are clearly simple and distinguishable to flat-floored lava flow-filled valleys, main fault-bounded basement blocks and a few elevated high landforms (Fig 74).

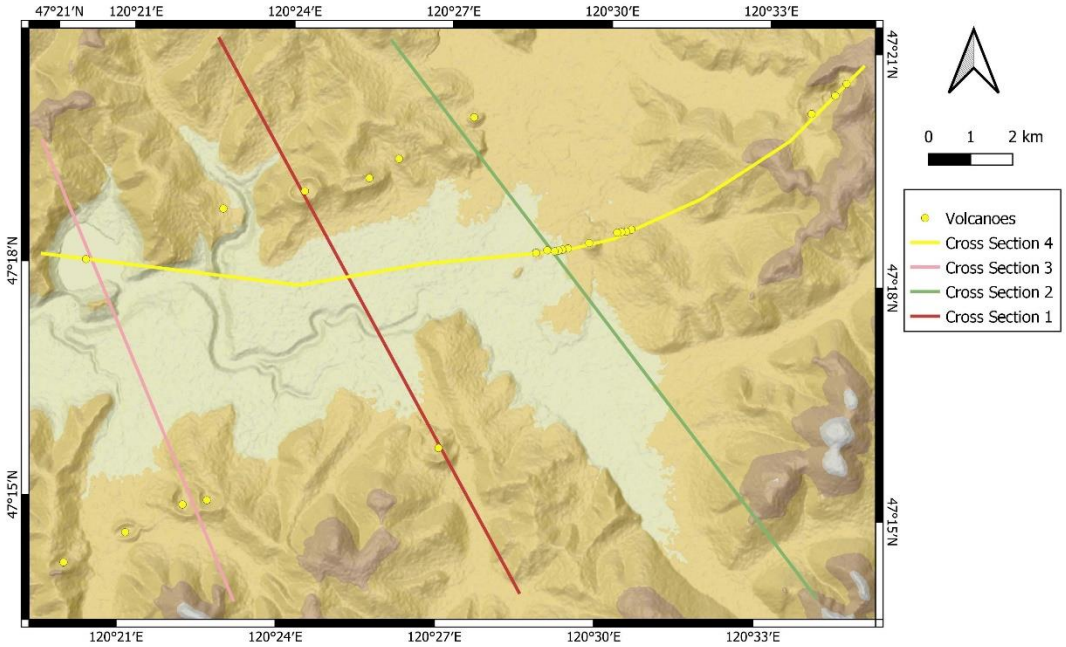

Figure 74: The relief map generated from the ALOS-PALSAR 12.5 m resolution digital elevation model demonstrates a simple morphological appearance of the study area.

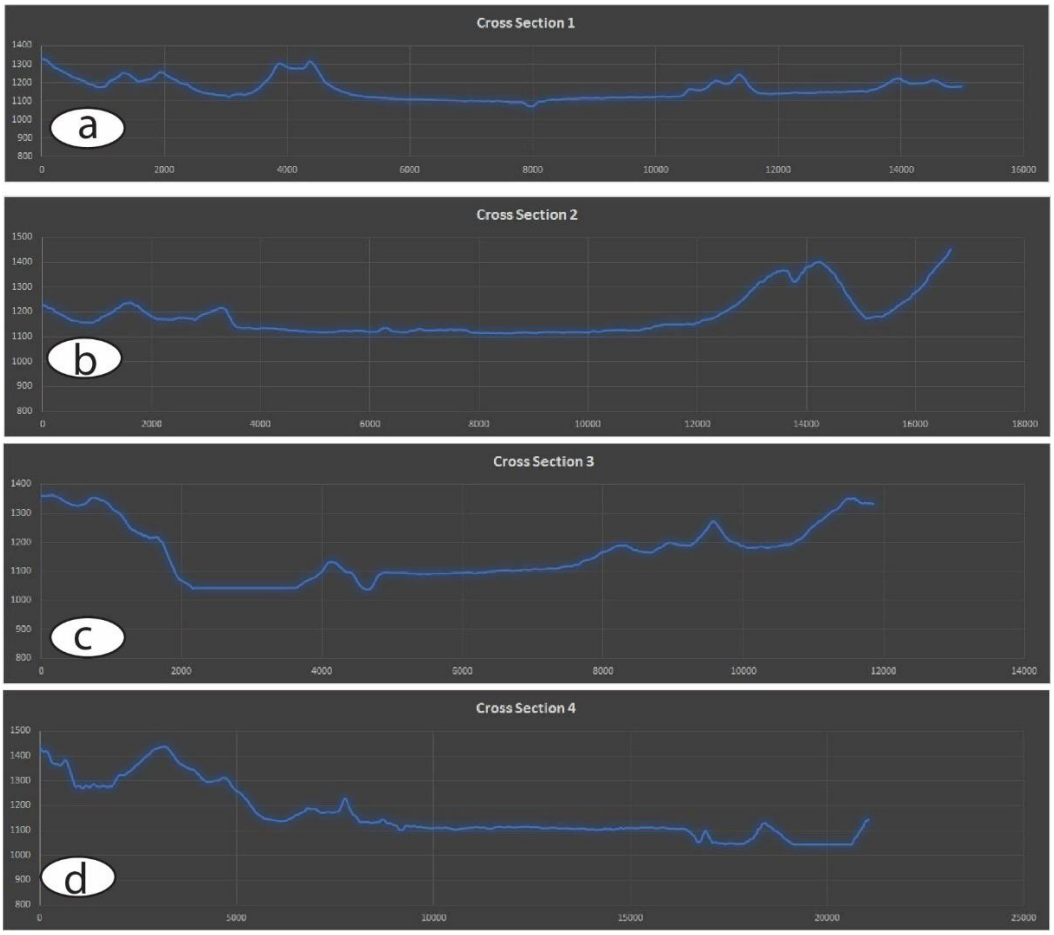

Figure 75: Four representative cross-sections across the study area clearly show the broad valley floors along phreatomagmatic volcanoes such as Wusulangzi and Dichi Lake formed. Cross-section lines are shown in Figures 77 & 78.

2) Satellite imagery and terrain analysis

To locate young volcanic geoforms such as scoria cones, maars and lava fields, satellite imagery from the Sentinel Hub (https://apps.sentinel-hub.com/eo-browser/) was used. For basic terrain analysis, the free ALOS-PALSAR 12.5 m digital elevation model (DEM) (https://search.asf.alaska.edu) was utilised.

In this study, we utilized four Sentinel satellite datasets, such as the True Colour Composite, False Colour composite and the Geology 8, 11, 12 and 12, 11, 2 composite images were used (Figs 67). Each of these images is sensitive to show young volcanic landforms, un-vegetated young lava flows, and a certain extent of volcanic ash-dominated regions.

For basic terrain analysis, the Q-GIS software and its accompanying software modules (e.g., Grass GIS) (https://qgis.org) were used on the available ALOS-PALSAR elevation

data. We generated slope, geomorphon and topographic position-based landform classification maps.

4. Results

Sentinel satellite imagery revealed that the young volcanic geoforms show up as distinct features on the images. Based on these maps, vents were identified (Figs 76a to d). It is evident that the lowermost elevation region, the main fluvial system within the Halaha River, hosts the youngest lava flow fields that erupted about 2000 years ago from the centre part of the ACVF and inundated the region by lava flows. The identified vents aligned in two separate lineaments, each following valley networks visible on the landscape. The two NE-SW aligned; parallel volcano rows composed of volcanic geoforms exhibit similar satellite image texture; hence they cannot be confidently assigned to a specific time order. It seems active volcanism was apparent at various times within both lineaments. The only exception from this trend is the centre part of the study area, where a short (<2.5 km) fissure-oriented volcano chain forms a slightly offset lineament (about 10 degrees offset from the main trends). Along this short fissure-aligned chain, scoria and lava spatter cones formed in the elevated part of the region, while a single explosion crater generated a maar that is currently one of the main geotouristic attractions of the area, the Dichi Lake. Dichi Lake is about 200 m in its diameter. Along its crater wall, lava flows exposed, while on its rim, large blocks of lava form some sort of ejecta ring. It is clear that the entire fissure system here predates the youngest lava flow emplacement of the Halaha River valley as it is associated with a relatively small lava field (about 4 km across) that functioned as a barrier against the youngest lava flows to move (Figs 75a to d).

A slope angle map generated from the 12.5 m resolution digital elevation data shows clearly the rugged but flat surface of the Halaha River Valley. The steepest slopes are in the SE-facing escarpment of basement rocks just on the true right side of the Halaha River N.W. from Tianchi Township (Figs 73 & 77). This escarpment is inferred to be a fault scarp, and the vents follow the same orientation in this region (Fig 77). The Dichi Lake area (Fig 73) and its lava flow field are marked by a morphological step in the S.E. edge of the Halaha River valley. This slightly elevated lava field diverted the main Halaha River lava flow. On the slope map, fissure-aligned vents are clearly visible, such

as the Arxan Tianchi scoria cone adjacent vents to the N.E. and S.W. (Fig 77). A similar trend of vent alignment is apparent at the Da Heigo (Fig 73), where three distinct volcanos formed within a 2 km fissure length. The closely spaced but small volcanic edifices built a volcano chain just N.E. from the Dichi Lake (Fig 77), where each small volcanic edifice amalgamated into a near-continuous crater row. This geomorphological aspect indicates that Dichi Lake vol-canoes must have erupted simultaneously due to a rapidly opening fissure. Such an eruption scenario is a likely cause of the formation of the crater chains just N.E. from Arxan Tianchi. However, this region is more vegetated and likely to represent slightly older eruptions than those forming the Dichi Lake system.

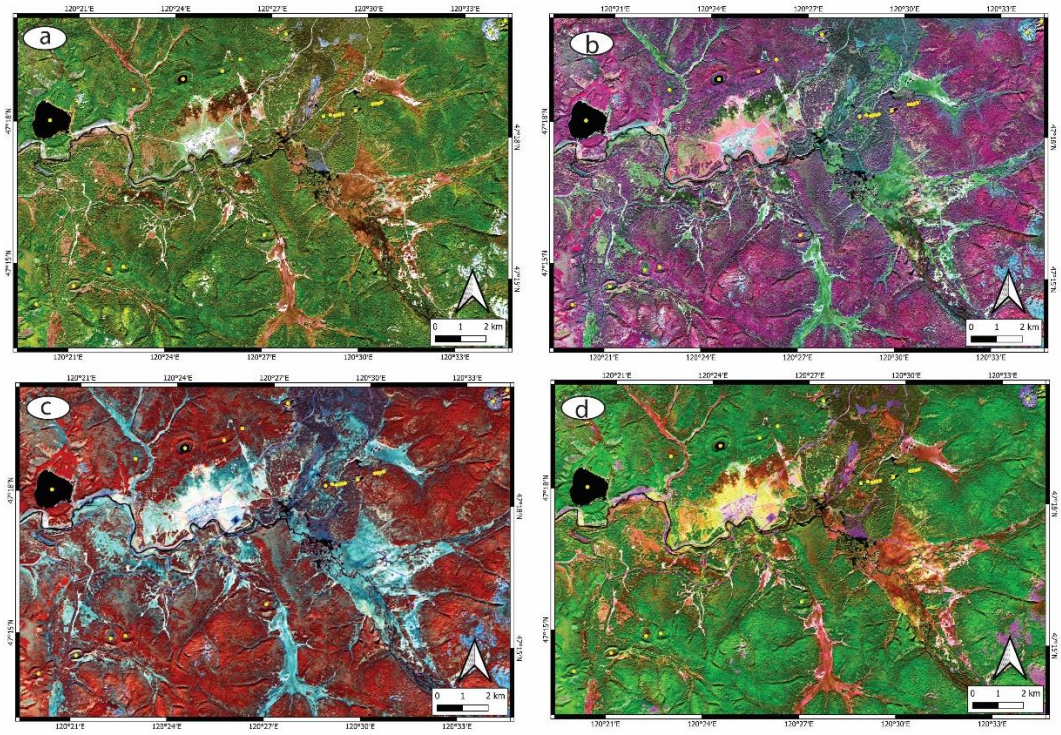

Figure 76: Sentinel satellite images of the study area such as true light (a) false colour (b), geology 8, 11, 12 band composite (c) and geology 12, 8, 2 composite images. Note, especially on the "c" and "d" images, the young lava flow that fills the Halaha River valley. The volcanic landforms are clearly recognizable, especially their NE-SW elongated fissure-oriented map view that is parallel with the main structural elements of the region.

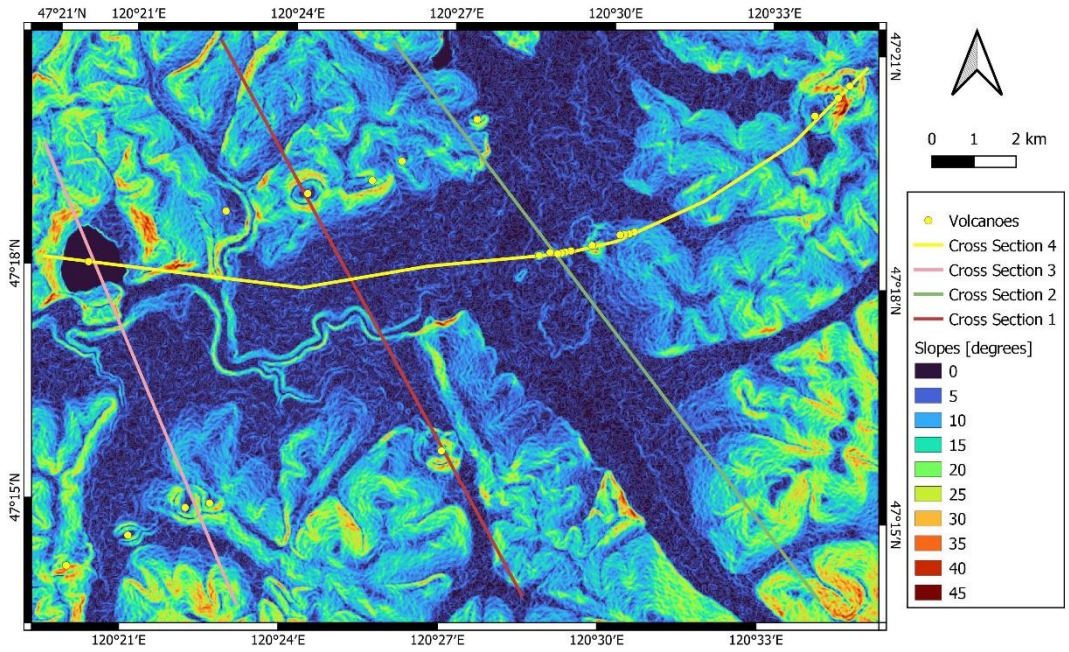

Figure 77: Slope map generated from the 12.5 m resolution ALOS-PALSAR digital elevation data. Note the broad flat floor valleys and the sharp morphological escarpment followed by the vent rows.

5. Discussion

Based on direct field observations and satellite imagery, it is evident that the young volcanic landforms are aligned. Their alignment is in good agreement with the recognized morphostructural elements of the region, indicating a strong structural control of the magma ascent that fed the dispersed volcanism in the region. Besides the field-wide vent alignments, the individual vents, as well as shorter groups such as the Dichi Lake system, follow the same NE-SW trends of elongation and alignments. The Dichi Lake, particularly a great example that fissures likely opened rapidly and simultaneously erupting vents produced mild explosive Hawaiian lava fountaining or Strombolian-style explosive eruptions. Once the feeder dike reached the low-lying and potentially water-saturated valley floors, a single explosive eruption took place to generate the Dichi Lake maar volcano. This eruptive mechanism that was revealed from the satellite imagery and morphological data accompanied by direct field documentation highlights the importance of the fissure-fed eruptions in the formation of this volcanic field. This information should play a more significant role in the geoeducation and geotouristic aspects of the Arxan UNESCO Global Geopark.

While the geopark has well-selected geosite "hotspots" (here we use this term to define regions that are key geosites within the conservation area), further analysis of the landscape by applying the geomorphon (Jasiewicz & Stepinski, 2013) (Fig 78) and the topographic position index-based landform classification (De Reu et al., 2013) methods (Fig 79) we can state that the area has far more to offer. On both maps (Figs 78 & 79), the fissure-aligned vents are clearly visible. Similarly, these landform classification methods captured well the general structural elements of the region. This information could be used to develop geoeducation materials for the visitors to help them to understand the landscape elements of the region. As the region has no characteristic landmarks other than some volcanic cones (that can be seen from distances only), generating landform classification maps could offer visitors a view to understand better the landforms and the potential geological and geomorphological processes standing behind their formations.

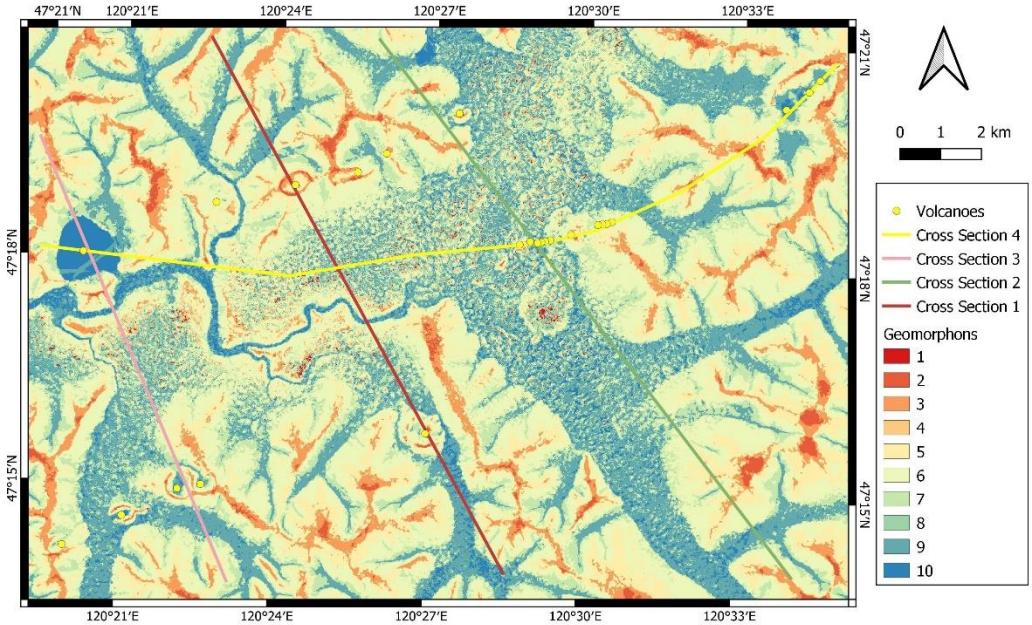

Figure 78: The geomorphon map (d) further demonstrates that the study area has monotonous landform classes within other landforms that are seemingly evenly distributed. Landform classes are 1) flat, 2) summit, 3) ridge, 4) shoulder, 5) spur, 6) slope, 7) hollow, 8) foot slope, 9) valley and 10) depression.

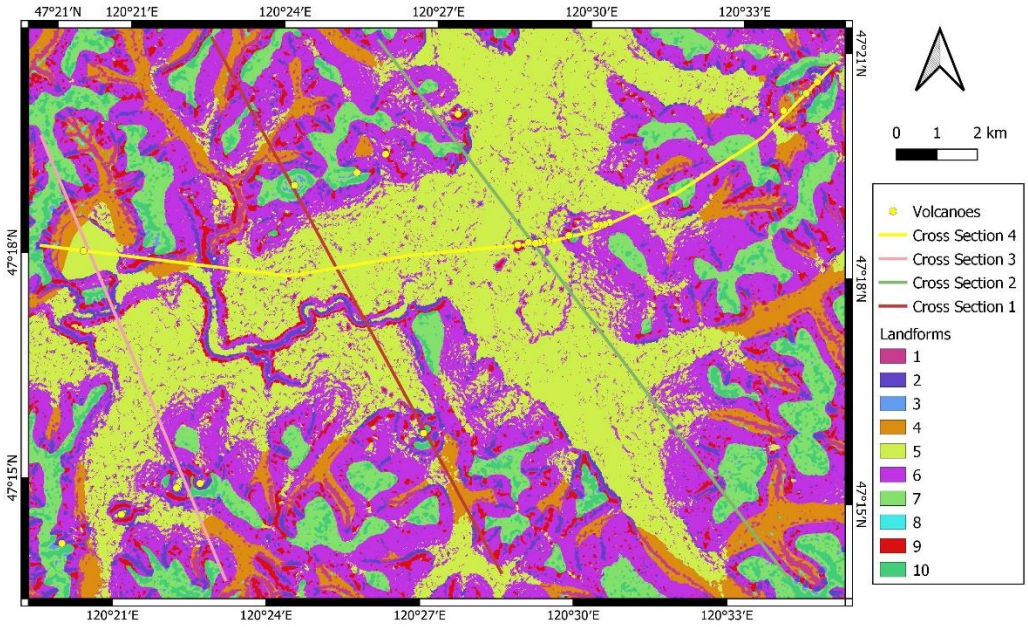

Figure 79: Topographic position index-based landform classification of the study area. Note the similar trends of the landforms captured by applying the geomorphon theory. 1) Canyons, deeply incised streams, 2) Mid-slope drainage and shallow valleys, 3) Upland drainage, headwaters, 4) U-shaped valleys, 5) Plains, 6) Open slopes, 7) Upper slopes/mesas, 8) Local ridges/hills in valleys, 9) Mid-slope ridges, small hills in plains, 10) Mountain tops and high ridges.

6. *Conclusion*

In this report, we provided clear evidence for fissure-dominated volcanic eruptions in volcano-to-volcanic field scales as one of the key characteristics of the volcanic geology of the Arxan-Chaihe Volcanic Field. Besides the direct field observations, the basic terrain and satellite image analysis demonstrated well that the volcanism in the region is restricted to narrow bands that are parallel with the main structural elements of the region. This is interpreted to be strong evidence that the volcanism in the region had strong structural control, and that will likely define future eruption locations and eruption styles. This information, alongside the advanced landform analysis of the region, could form a strong core of geoeducation within the geotourism aspects of the Arxan UNESCO Global Geopark, highlighting the firm link between volcanism and structural geology of the continental lithosphere of this monogenetic volcanic field.

Chapter 7: Synthesis

1) Geological setting overview

Arxan-Chaihe Volcanic Field (ACVF) is located southwest of the Great Xing'an Range on the eastern side of Songliao Graben (Fig 1). The Cenozoic volcanism in ACVF spans the early Pleistocene to Holocene (Fan et al., 2011) and covers approximately 2000 km^2. Major products from the volcanism are mafic materials (basalt).

2) Field relationships

This section will follow ACVF locations from the Arxan area (Fig 49) to the Zalantun area (Fig 50).

ACVF contains a range of typical volcanic features. The geomorphology includes plains of pāhoehoe and 'a'ā lava flows, ash plains composed of scoriaceous deposits, lava tubes, scoria cones, and complex cones. Scoria cones are concentrated on the western part of ACVF, including two major scenic spots, Wusulangzi Lake (which might be a crater lake) and Tianchi Lake (a scoria cone); the other two large vents are Yanshan (YS) and Da Heigou (DHG) (Fig 2). Fissure structures are located on both sides of Tianchi Lake (the west and the east). Dichi Lake, to the south of Tianchi Lake, is a small crater lake marking a single eruptive event. In the middle part of ACVF, Tuofengling (Camel Hump) Lake is a complex cone preserving pyroclastic deposits formed by phreatomagmatism and capped by scoria created during "dry" eruptions. In the east corner of ACVF, TX remains undated (because my third field season was cancelled due to Covid), but geomorphological relationships and the stage of development of soils in surficial deposits suggest a late Pleistocene or early Holocene age. There are pyroclastic deposits in proximal areas surrounding TX about 30 m thick.

The crater of Tongxin Lake can be separated into the inside crater and beyond the crater (Fig 18). The inner crater has a flat floor and is hypothesised to be a maar crater. The entire lake is believed to be the result of a maar-forming eruption. However, this was never explicitly demonstrated or proved. Tongxin Lake is no more than 14 m deep. In the northern part of the crater floor lies an alluvial fan covering an area of about 1.35 km^2. A small valley extends through the mountain range to the north of the lake. In this valley, the presence of several large cobbles of basaltic debris indicates the fallout of spatter ejecta spread this far. Interestingly, the volcanic clasts are rarely found inside the crater and have only been observed to the northwest and southeast

of the lake. Accessible pyroclastic deposits crop out on the western and southeast rim of the lake and adjacent areas (Fig 19). These deposits range from loose to moderately indurated and have been subjected to significant post-eruptive erosional processes in cold arid conditions by a complex fluvial network which has sculptured the current landscape over the last few thousand years or so. These deposits exhibit a young surface morphological fabric. Pyroclastic deposits that were found 12km south of the lake have undergone long-distance transportation by pyroclastic density currents, the deposits of which co-exist with some pumiceous pyroclastic fallout. Older lava flows surrounding Tongxin Lake are distributed over approximately 20 km^2. These flows include distinctive columnar jointed structures that pre-date the Tongxin pyroclastic deposits. The lava flows range from about 3 to 15 m in thickness, depending on how much the flows expose to the surface.

Tianchi (Heaven) Lake is located in the western part of ACVF (Fig 6). It consists of a scoria cone with a crater lake inside the cone structure (about 50 m high from the lake floor to the top of the cone). Eruption fissures are identified on the western and eastern sides of the lake. The fissure on the west of the lake reveals a succession of fissure-aligned pyroclastic rocks with clastogenic and layered structures (Fig 7C). Fissures on the eastern side of the lake form two parallel "walls" orientated W-E (Fig 7B). The presence of fissures on both sides of Heaven Lake is in keeping with a lake created by the fissure propagation during volcanism.

Tuofengling (Camel-Hump) Lake is located some 24 km to the northeast of Tianchi Lake. The lake is elongated with an area of approximately 0.25 km^2. Observations reveal that Tuofengling Lake may have experienced at least two eruptive stages. Fig 5A shows accretionary lapilli and explosive ejecta, indicating that the early eruptions were driven by phreatomagmatism. Scoriaceous materials forming a scoria cone on the top of the lake margin are deemed a later eruptive phase, most likely involving "dry" eruptions.

Yanshan (Triple Vent) in the southern part of ACVF (Fig 14) consists of three related and overlapping vents that are part of one larger volcano. Loose scoriaceous materials cover the slope of the cone edifice. The average thickness of scoria caps on each vent is about 3 m, with reddish and welded cinders on the top of vent 2 (Fig 16D). The slope

of the outer wall of each YS cone is steep, about 46 degrees and up to 48 degrees for vent 2.

Southwest of YS is DHG (Dahei Gou or Da Heigou), a basaltic crater (5 km in perimeter and 1.7 km in the long axis) (Fig 12C) consisting of at least five intermediate-sized and overlapping sub-craters. Field observations indicate that contemporary lava flows blanket filled the local topography (valley) as a continuous and undisturbed feature (Fig 12A &B), consistent with the voluminous productivity of lava out-pouring.

Lava flows around the fluvial plain of the Halaha River preserve a range of surface morphologies, including tumuli, tubes, nodules and bumps. The associated lakes indicate ponding occurred post-eruption. Channelised flows are present in YS, with a line of tumuli-orientated SW-NE. Lava flows near YS preserve intact 'a'ā-type lavas comprising rough and spiky surfaces.

The earliest basaltic lava flow in ACVF, to the south of TX, was about 1.365 Ma years ago (Fan et al., 2011). The largest maar in ACVF, Tongxin Lake, has subsidence over an area of about 2.8 km^2. The latest eruption in ACVF occurred about 2000 years ago at Yanshan-the "Triple Vent" (Bai et al., 2005).

In comparison to other monogenetic volcanism in the world, ACVF at 2000 km^2 is a comparable intraplate field with AVF (600 km^2) and NVP (15000 km^2, 7.5 times larger than ACVF). It has a lower density of volcanic features and an intermediary time span (2.3 Myr) compared to 0.29 Myr for AVF and 7.8 Myr for the NVP (Cas et al., 2017; Li et al., 2020).

In overview, ACVF is a hitherto poorly described monogenetic volcanic field, with a range of eruptive intensities ranging from extremely explosive phreatomagmatic (TX) to effusion of fissure-fed lava flows and scoria cone construction. The features are excellent examples of monogenetic volcanism in a developing rift within a continental craton.

3) Pyroclastic sedimentology

GSD can reveal processes operating during the deposition of pyroclastic deposits. Grain size analyses of samples from five locations around the TX site (two proximal

and three distal) are interpreted to represent fallout, surge, and flow processes. S1 and S2 on the TX crater wall show near-source deposits with distinctive sedimentary behaviours of surges and currents consistent with PDC properties. These pyroclastic deposits extend into distal areas (12 km), covering large areas of the downstream fluvial plains of the Chaoer River.

Using the GSD data, the syn-eruptive depositional characteristics of the PDC deposits are recognised. The proximal deposits of TX consist of interbedded coarse and fine-grained units consistent with channelised flow patterns, including cross-bedding and dune structures. Surge and fallout deposits are also recognised in the size data. An unimodal pattern in grain-size distribution demonstrates a single eruption episode within each bed, e.g., fallout and surges in a contemporaneous event. The S1 (inside the crater wall) deposits are dominated by unimodal-pattern deposits. Bimodal or polymodal patterns, as seen in S2 (outside the crater wall) deposits, indicate the mixing of multiple eruptive products and the transportation within shifting channels.

The composition of the pyroclastic deposits from five key locations shows that excavation of the surrounding bedrock material occurred during the syn-eruptive phases. A large number of xenoliths (granite) indicates that the excavation processes occurred in the shallow depth; xenoliths (peridotite/pyroxenite) are implied by the deeper sources within the lithosphere.

Density measurements on juvenile clasts reveal changes in the porosity for each accessible deposit of S1 and S2. The porosity of phreatomagmatic deposits can indicate how many times the presence of magma-water interactions occurred during the syn-eruptive episodes. At both S1 & S2, at least three major episodes of violent explosions from TX are preserved. Several minor fluctuations in the two plots (Fig 38) demonstrate different amounts of water influx (higher porosity equals more water input).

Electron microscopy provides 2D & 3D observations on the surface and inner structures of the pyroclastic clasts, specifically juvenile particles. The 3D images show that the surface structures of juvenile particles are highly fragmented by magma-water interactions and are comprised of a large number of open pores. 2D images

depict the magnitude of how much fractional crystallisation had taken place within the juvenile clasts, suggested by evolved microlites (zonations of plagioclase crystals).

The tuff deposits in proximal areas (S1 & S2) of Tongxin Lake are approximately 30 m in total thickness; also, the site in the far south of TX contains about 16 m thick pyroclastic deposits. Due to the talus cover on the top of S2, the thickness of proximal tuff deposits in TX could be greater than what was observed. In this case, the estimation of the total thickness of the pyroclastic deposits around TX proximal areas is about 30 m. Ballistic projectiles (bombs) intercalated within the deposits are found in TX's deposits. The accidental lithics comprise more than 65% (Fig 37) of TX's deposits. In this way, TX is larger than most explosion craters; compared to Lake Pupuke in AVF (4.2 km in perimeter and 1.1 km^2 in area), but deposits of TX are relatively poorly preserved; only parts of the tuff ring remain in comparison to comparable tuff features in the AVF or NVP.

Sedimentological studies on pyroclastic deposits of TX show that the deposits were highly eroded and poorly preserved, except in proximal areas and in some small distal areas. The poor preservation may be due to periglacial processes in the extremely cold winters of this region.

4) Geological diversity as revealed by GIS analysis

GIS-based evaluations using STRM satellite images provide an overview of the geological aspects of ACVF, including the distribution of basement and Cenozoic volcanism. Regional hydrology is assessed using stream outlines; local topography is revealed by the slope and regional geomorphology. Applying GIS software (QGIS), an elevation image is used to create a geological map for the entire ACVF. Without the GIS and relying solely on field observations, a reliable geological map would be limited only to areas visited during field seasons. The vastness of the ACVF (2000 km^2) meant only small areas were actually accessed and studied in detail during the two field trips; the planned third field season was cancelled due to Covid-19 travel restrictions. The other advantage of using the GIS approach is that systematic assessment of all aspects of the geology (the geodiversity) in ACVF can be undertaken and used for future geological modelling of the area.

As described in Chapters 2 & 3, the ACVF contains a range of geological diversity. Large areas of lava flows have modified the original topography, in which the lavas ponded and filled in the valleys; different morphologies of lava flows preserve distinctive values of geoheritage and tourism potential. Volcanoes provide scenic spots for geoconservation and research; the different types of vents represent the varieties of volcanism in ACVF. Regional fluvial systems have created a gigantic network of hydrological features. River shapes were greatly impacted by the lava flows, in which several ponded lakes form typical geological features indicating lava flows' behaviours in the past. In addition to the Cenozoic volcanism in ACVF, the TX crater exposes cliffs of hard granite, and the rivers have also carved interesting landforms through the country rock.

5) Lava flow characteristics and simulations

GIS-based analyses of satellite images enable the recognition of young lava flows exposed at the surface by the different surface textures. The Sentinel Satellite Imagery method provides a series of bands (visible light and infrared in most cases) that reveal differences in lava flows. Using the Q-LavHa program performed through QGIS, the succession of the young/surface lava flows can be assessed, and relative timing determined using regional topographical changes, such as elevation and coverage areas.

The different textures on the Sentinel satellite images indicate different infrared spectrums. Each spectrum reveals a specific mechanism and is interpreted as a specific environmental process. For instance, Figs 67 B & C show the images utilising geology band 8-11-12; the youngest lava flow from YS has a light-blue colour, which is distinguishable from the surrounding areas (older flows). Using Sentinel Imagery, at least four different episodes of eruptive activities can be recognised in lava flows around the Halaha River (Chapter 5, Fig 60).

6) Fissure-driven volcanism in ACVF

Cenozoic volcanism in ACVF is fissure-driven. The alignment of the vents and fissure structures can be seen on satellite images, and this alignment is supported by field observations.

There are at least three lineaments visible on the satellite images over ACVF. The first is Wusulangzi Lake, where fissure structures (Fig 7B and 7C) are evident on the eastern and western sides of Tianchi Lake, respectively; the estimated length of this fissure is about 7.7 km. The second fissure starts at Dichi Lake and trends across the eastern side of the lake through DHG and YS to Gaoshan, a distance of approximately 15.5 km (Fig 9A). The third from Bear Mountain to TX has only been studied using satellite images as the opportunity to visit Bear Mountain on a third field campaign was not possible due to COVID-19 travel restrictions. The third fissure so far is recognised by satellite images and at the TX site, a distance of about 17.5 km from the western TX; also, several dikes intrude the granite country rock on the true left bank of Chaoer River, adjacent to the TX crater. However, the latest field data suggests that TX resulted from fissure-propagation volcanism and dikes exposed on the west side of TX adjacent to Chaoer River may be the feeders.

Volcanism in NE China occurs in an intra-continental setting. Previous research has suggested that this volcanism followed local tectonic trends. This study proposes that ACVF is fissure-driven. The concept of "curtain of fire" (Macdonald, 1943) indicates that fissure-driven eruptions can generate large-volume basaltic flows. In ACVF, large areas of lava ponded on both sides of the Halaha River. The major body of the flow is concentrated on the southern side of ACVF, which contains Dichi, DHG and YS systems. Based on the local elevation changes, the flow from DHG extends about 7.7 km; from YS, about 9.5 km. The flows of ACVF follow the lineament of the Dichi-DHG-YS fissure and cover an area of approximately 70 km^2; this is consistent with ACVF being a volcanic field formed by fissure propagating processes.

There are a few characteristics of ACVF that differ from other fissure volcanism in the world. In Iceland, the fissures develop from the rifting processes on the divergent tectonic boundary of the Atlantic Mid-Ocean Ridge. The volcanism in Iceland involves the upwelling of magma in the rift forming during seafloor spreading. Volcanism in Hawaii occurs in another tectonic regime where magma makes its way to the surface through an intra-plate setting area where the oceanic crust is "thinner". This type of volcanism is referred to as "hotspot". The alignment of the volcanoes reflects how the magma erupts at different locations at different times as the Pacific Plate has moved

over time. Another aspect of hotspot volcanism is the ability to establish the rate and direction of movement of the lithospheric plate. In ACVF, fissure-propagation occurs in a rift zone within an intra-continent setting; such settings lie long distances from lithospheric plate boundaries, e.g., subduction zone but where the otherwise thick continental crust has thinned due to incipient rifting. The magma plumbing system follows a zone of weakness or cracks in the country rocks that extend to depth from the surface when the fissure-propagation occurs. The phreatomagmatism in TX has been triggered by the extrinsic water sources, such as rivers, because the local country rocks are not a good aquifer being composed of granitoid materials. Well-developed dikes are present within the country rocks. These dikes follow fractures and zones of weakness within the basement during magma ascension. Thus, this rising magma is likely to have encountered water at very shallow depths within the crust or even at the surface, and the most likely sources are the local rivers in the absence of porous country rock or thick mantling deposits such as loess, alluvium or glacial deposits.
Effusive/Strombolian eruption

Fissure-driven eruptions form linear volcanic systems that include spatter/cinder cones and elongated ramparts, which are like basaltic “walls” (Fig 7B). If the fissure propagation processes are confined to a small area, violent strombolian eruptions may be triggered. In ACVF, there is evidence of such volcanic events around the YS system. As mentioned in Chapter 2, the ash plain in the southern area around YS preserves at least a 3 m thickness of scoriaceous ash. The scoria capping the top of YS is about 3-5m thick on average. Fig 15D indicates that the strombolian-style eruptions ejected large amounts of basaltic materials covering an area of approximately 8.5 km^2, including the surface area of the YS edifice. At a location to the south of YS, about 1.7 km from the Triple Vent, three metres of loose scoria are exposed, but the deposit is likely to be much thicker (Fig 15D). It does, however, provide evidence that YS experienced lava-fountaining consistent with violent strombolian eruptions. The remaining areas of the young lava flow are without ash cover; this is interpreted to suggest the fall out from the eruption plume didn’t cover the area proximal to the volcano but drifted with the prevailing wind during the syn-eruptive episodes, or the lava flow post-dated the scoriaceous eruption (similar to Rangitoto in AVF).

Field observations suggest effusive eruptions from YS produced abundant lava tubes and tumuli consistent with the typical ponding and draining behaviours of lava flows. The possible extent of the youngest lava from YS is mapped using remote sensing in Chapter 5 to reach at least 8 km from the vent and cover 35 Km^2. To the southwest of YS, DHG produced flows that followed a valley before ponding on the Halaha River floodplain. As mentioned in Chapter 2, there are no loose scoria/cinder/spatter deposits around DHG; this means DHG is unlikely to have experienced explosive or even strombolian eruptions, only effusive or lava-fountaining events. The flows cover an area of approximately 50 km^2. The volume of DHG eruptives buried beneath the youngest lava flow from YS is unknown; however, the "older" flows can be recognised on the Sentinel images (Chapter 5). From these observations, it is likely that the "older" flow formed the modern topography of the local areas, with tumuli present as proof of the effusive eruptions.

Lava plateaus are a feature of ACVF; they were formed by fissures cutting through the broad country rock ridges between valleys. Yanshan-Triple Vent, which covers an area of about 2.4 km^2 with an elevation of about 1610 m above sea level, is one such volcanic feature.

Four scoria cones are recognised in ACVF. These scoria cones, in particular YS, display evidence of lava fountaining. Large areas surrounding YS are covered by scoriaceous ash falls overlying lava flows. At the DHG site, there is evidence of lava ponding within a crater as a lava lake. The significance of findings on YS and DHG is that these two vents are the largest and possibly longest-lived of the vents in the western Arxan end of ACVF but are not as large as TX in the east.

7) Phreatomagmatic eruption

There is evidence that highly explosive eruptions occurred in ACVF, e.g., Tuofengling (Camel Hump) Lake, Tianchi and TX. This research has found that Tuofengling Lake is a complex cone with a scoria/spatter cap overlying a tuff ring, which is evidence of a violent phreatomagmatic eruption followed by strombolian fire fountaining (Fig 5A). The thickness of the tuff ring deposit from Tuofengling is no more than 7 m; more fieldwork is required to establish the extent of pyroclastic deposits from this vent. It

can only be assumed that Tuofengling had experienced highly explosive eruption phases.

Tongxin (TX) Lake is another example of phreatomagmatism in ACVF. It is the largest vent, and intact pyroclastic deposits are sporadically preserved in the proximal, intermediate and distal areas (12 km away from TX), providing proof of violent explosive eruptions. Previous research proposed that TX might be a caldera-like crater with ring faults (Zhao, 2010). Although the effusive charging rate of TX is unknown, the thickness of the lava flows surrounding TX indicates that abundant volumes of magma have erupted from this area. Pyroclastic deposits found in distal areas suggest that air-fall deposits travelled long distances from the volcano, which implies large-magnitude eruptions. Any calculations of the volumes of the pyroclastic materials from TX could, at best, provide a minimum volume due to extensive erosion and re-transportation of these fragile and erosion-susceptible PDC and scoria deposits. However, the size of the crater (3 km in diameter) suggests that TX volcanism was large in magnitude.

PDC formation indicates that deconvolution behaviours occurred during the syn-eruption stages. Previous research (Schmincke et al., 1973; Schmincke, 1977) suggests that such a phenomenon is triggered by a topography-controlled mechanism in relation to friction changes within the flow channel shifting. The pyroclastic deposits around TX Lake show *in situ* sedimentological processes, which suggest no post-eruptive reworking affected the deposits.

The number of vents formed by phreatomagmatism is low. So far, only TX and Tuofengling(TFL/Camel-Hump) lake vents were identified as composed of tuff ring deposits. The reason for the low density of pheatomagmatism in ACVF is likely due to the lack of groundwater (mentioned earlier) and fissures rarely intersecting rivers (annual precipitation is 394-502 mm, concentrated from June to August).

8) The diverse range of geology in ACVF

By using GIS-based programs, the range of geology has been investigated, and its preservation/conservation potential has been assessed for the ACVF UNESCO Geopark. GIS techniques focus only on surface materials. In the case of ACVF, these include

young lava flows, hydrology, slope, and topography (elevation & geomorphology). Volcanism in ACVF is the most interesting aspect of geology for local tourism. A primary principle of a UNESCO Global Geopark is to develop and build the local economy and encourage tourism. ACVF was identified for its unique volcanic landscape in NE China. The secondary purpose of the ACVF UNESCO Geopark was to establish a "quintuplet A" (top-rated national park) national scenery spot. The diverse geology of ACVF, outlined in Chapter 4, fulfils the local geoconservation and geoheritage requirements and focuses primarily on the outstanding volcanic landscape of the geopark. Young geomorphologies of the young lava flow, multiple volcano types (tuff cone, tuff ring, and scoria/cinder cone), lava plateaus, and pāhoehoe/'a'ā lava have the potential to attract visitors and increase the profits from tourism. Geoconservation and geoheritage development is focused on social and economic improvements for the region. For instance, the local fluvial systems, dominated by two major rivers (Halaha and Chaoer Rivers), are under the protection of the local government, which is actively working on the quality of the water and its economic benefits - clean water for people and animals and water sources for irrigation for local agriculture; hence the importance of understanding and evaluating the hydrology. Geological education is an essential element in promoting the values of ACVF Geopark to the wider public. The Cenozoic volcanism in ACVF should form the basis for promoting the geopark to visitors. One aspect that warrants improvement is to introduce information about the park that is readily accessible and in multiple languages. The remoteness of ACVF is one of its attractions to visitors, so there is a need to provide new information about the genesis of this intra-continental region and the volcanic field.

9) Assessments of volcanic risks

Regional assessments and the management of volcanic risks in ACVF need upgrading. There appears to be no foresight into what might happen if an eruption were to occur. Cenozoic volcanism in ACVF (Chapter 5 and Chapter 6) has occurred within the last 2000 years, with a likelihood that further eruptions will occur.

In ACVF, 47 vents could indicate a high rate of volcanic activity. However, there is currently a paucity of dates, something that might have been addressed in a third field

season. More accurate dates are needed to determine when the activity began and the frequency of the following eruptions. The local geology (Chapter 4) is varied and complex, making it difficult to evaluate post-eruptive scenarios and potentially leaving the effects of future volcanic episodes underestimated. The United Nations International Strategy for Disaster Reduction (UNISDR), in developments on the Hyogo Framework for Action (HFA) in 2005, put out a statement on reducing risks from hazards that stated there needs to be a "*substantial reduction of disaster losses in lives and in the social, economic and environmental assets of communities and countries.*" (Jolly & de la Cruz, 2015). Defining the risk potential in ACVF is imperative. Practical "step-by-step" guidelines need to be established on how to deal with the risk for local residents and communities.

Monitoring volcanism can include visual surveillance, seismic monitoring, geodetic monitoring, geochemical monitoring, magnetism detections on magma and hydrometeorological monitoring. In ACVF, seismic monitoring is deemed sufficient because the volcanoes erupt infrequently. Two major rivers could be the most likely parameter of future eruptions; thus, hydrometeorological monitoring of these fluvial systems should have had the potential to mitigate the impact of any event. Local governing bodies and consultancies need to build a framework to collate and convey scientific advice informing the local communities. Little research has been undertaken on volcanism in ACVF. Most previous work has focused on the regional tectonic setting and structural geology. They provide useful information about tomography and stratigraphic successions, which help understand the regional setting. A few of them investigated the geomorphology of the Cenozoic volcanism with respect to cone structures, e.g., Tianchi Lake and Yanshan, and the morphology of lava flows (tumuli, a'ā, and pāhoehoe). Others have given insights into tourism trends. Despite the awareness of volcanic risk, the scientific suggestions about volcanism in ACVF do not appear to recognise it as a threat to the region. There is considerable research that could be undertaken to ascertain volcanic risk. One approach would be to undertake studies on microcrystals in volcanic deposits to model the rate of ascent of magma in the past. Estimating the rate of magma ascension is vital information once a seismic disturbance has been noted and gives volcanic risk managers the timeframe over

which decisions and possible evacuations must be made; it is this level of information that's required for hazard mitigation.

The geological features include fissure structures, which indicate what kind of mechanism generates the volcanoes. Volcanic cone structures, such as Tianchi and YS, mark the evolution and construction of volcanic features during eruptive stages and deposits from phreatomagmatism and strombolian volcanism (such as tuff and scoria). The emplacement of lava flows tells of the potential risk from lava flowing that might threaten and damage the local communities. Moreover, the explosive formation of maars and tuff rings has a greater likelihood of threatening life and infrastructure.

The major volcanic threats to ACVF are the pyroclastic flows from phreatomagmatic eruptions, and lava flows reaching local communities, especially during the high tourism season. There is also the possible propagation of fissures which means volcanic deposits could be farther reaching and occur in areas not previously recognized for volcanism. The risks are damage to the infrastructure, water sources and air routes. ACVF has a high-risk potential because the population of ACVF is relatively low compared to that in other parts of the world, such as Auckland, NZ, where the AVF presents a high hazard potential.

10) Global perspective

ACVF is a previously understudied monogenetic volcanic field in NE China. This field reveals a range of geological features which have value for geoconservation, education and tourism. ACVF shares features, eruptive styles and rock types with many other monogenetic fields in NE China and worldwide. However, ACVF has a distinctive orientation from SW-NE with various volcanic features scattered along a lengthy corridor controlled by basement faults.

Name	**ACVF**	**Longgang Volcanic Field**	**Wudalianchi Volcanic Field**	**Western Snake River Plain**	**Newer Volcanic Field**
Geological setting	Intraplate	Intraplate	Intraplate	Intraplate	Intraplate
Age	Pliocene to Quaternary	Neogene to Holocene	Pleistocene to Holocene	Miocene to Pleistocene	Tertiary to Holocene
Volcanic rock types	Basalts, trachybasalts, basaltic andesites	Basalts, trachybasalts, basanite	Trachybasalt and basaltic andesite	picro-basalt, tephrite basanite and basaltic trachyandesite	tephrite basanite, picro-basalt
Numbers of Vents	47	150	14	400	400
Total area	2000 km^2	1700 km^2	800 km^2	21000 km^2	15000 km^2
Volcanic features	Scoria cones, tuff rings, complex cones, pahoehoe and aa lava flows	Scoria cones and maars	Scoria cones	lava shields, pahoehoe lava fields, scoria cones, phreatomagmatic volcanoes	shield volcanoes, pyroclastic cones, tuff rings
Eruption types	Fissure eruption (SW-NE)	Probably fissure eruption (slightly SW-NE)	Fissure eruption (SW-NE)	Fissure eruptions (NW-SE)	Fissure eruptions (N-S)
Location	NE China	NE China	NE China	NW USA	SE Australia

Table 12: the comparisons between ACVF and other monogenetic volcanic fields in NE China and the world.

In NE China, there are two volcanic fields that have been more intensively studied, the Nuomin (NM) Volcanic Field and the Wudalianchi Volcanic Field.

The Longgang Volcanic Field is identified as a monogenetic volcanic field composed of about 150 scoria cones and maars (Bai et al., 2006). It is located near the boundary of China and North Korea (Fig 1, E). The total area is about 1700 km^2 (Zhao et al., 2021b; Zhao et al., 2022). The volcanic rock types are basalt, picro-basalt, trachybasalt, and tephrite Basanite (Liu et al., 2001). The K-Ar dating method indicated that this volcanic field erupted in the Neogene era, and then the ^{14}C method revealed that the activities continued in the Holocene (about 1500-1700 years ago) (Liu et al., 2009). Previous research shows that there are about 24 vents within this area (Liu et al., 2000). Most of the eruptive products are pyroclastic materials, loose scoria, bombs, and effusive lava flows. Those volcanic products erupted in the mid-late Pleistocene and early Holocene (Liu, 2000; Liu et al., 1999).

Wudalianchi Volcanic Field is the most studied monogenetic volcanic field in NE China (Fig 1, B), near the boundary of China and Russia. The name Wudalianchi in the Chinese language means a string of five lakes. The total area of Wudalianchi Volcanic Field is about 800 km^2 (Liu et al., 2001; Liu, 2000; McGee et al., 2015). There are 14 scoria cones lying on a sheld-like lava plateau. Those five lakes are lava-ponded lakes, which indicate five major eruptive sequences from the early Pleistocene until civilised history time (K-Ar dating method) (McGee et al., 2015). The volcanic rock types are trachybasalt and tephrite basanite (Wei et al., 2003).

As Table 12 shows, compared to other monogenetic volcanic fields, ACVF is the largest volcanic field in NE China, due to the largest area. The number of recognised vents in ACVF is in the mid-range among the volcanic fields in NE China. By contrast with Longgang and Wudalianchi fields, ACVF has a range of diversified volcanic edifices and landscapes. Longgang Volcanic Field is on the other side of Songliao Graben, near Mt. Changbai (the largest stratovolcano in China). The major fault orientation is almost the same as the fissure orientation in ACVF. Wudalianchi field is on the northern part of the Graben; the vent distribution also indicates the local fault orientation. All three volcanic fields in NE China reveal a similar fissure/fault orientation. The eruptive ages are different. The youngest eruption that occurred in ACVF was about 2000 years ago

(Bai et al., 2005). The latest eruption that was recorded in Wudalianchi happened in the year 1776 (Wei et al., 2003). The Longgang erupted in about the year AD 350 (Liu, 1999; Wei et al., 2003). Thus, the youngest feature in ACVF appears to be older than the youngest feature in the other two fields. The types of volcanic rocks in ACVF have similar compositions (mafic materials) compared to the rocks from Wudalianchi and Longgang.

A detailed comparison of ACVF with all the monogenetic volcanic fields on Earth would be very time-consuming, however, two have been selected for a brief comparison; the Snake River of monogenetic volcanic fields in previous studies is dedicated to the west Snake River Plain in Idaho, USA, as well as the Newer Volcanic Province in SE Australia.

The western Snake River Plain is composed of 400 monogenetic volcanoes within a 21000 km^2 area (Shervais et al., 2005; Wood & Clemens, 2002). This volcanic field is located in Idaho, west of the USA. The main features of monogenetic volcanism are lava shields, pahoehoe lava fields, scoria cones and several phreatomagmatic volcanoes (K. Németh & C. M. White, 2009). Those volcanic features were formed between the late Miocene and middle Pleistocene periods by the ^{40}Ar-^{39}Ar dating method (Godchaux & Bonnichsen, 2002; Godchaux et al., 1992). The rock types are mainly picro-basalt, tephrite basanite and basaltic trachyandesite (Bonnichsen & Godchaux, 2004).

The Newer Volcanic Province is a large voluminous volcanic field in SE Australia. The total area is approximately 15000 km^2 (Johnson, 1989; Lesti et al., 2008). There are 400 vents that are shield volcanoes and explosive volcanoes (Harries et al., 2006; Wellman & McDougall, 1974). The age ranges from Tertiary to Holocene periods (radiocarbon dating and ^{40}Ar-^{39}Ar methods) (Lesti et al., 2008). The major features of the volcanism are lava flows, small scoria cones, tuff rings, and maars. The rock types are tephrite basanite and picro-basalt. In comparison to these two well-known monogenetic volcanic fields, ACVF covers a smaller area and is of less total volume. Features are scattered along a long SW-NE trending corridor and are isolated from one another. Features such as the pyroclastic deposits near Tongxin Lake in ACVF contain a large proportion of granitoid country rock because of the interaction of the magma with surface water (rivers).

Putting ACVF on the global scale. The most recent eruptions on the Western Snake River Plain occurred about 400 thousand years ago (Shervais et al., 2002; Shervais et al., 2005). The latest eruption event happened in the Newer Volcanic Field was about 2900 BCE (Cas et al., 2017; Lesti et al., 2008; Vogel & Keays, 1997). Thus, ACVF is a young monogenetic volcanic field in comparison to those volcanic fields in the world. The rock types from ACVF are nearly the same as the volcanic rocks from those two fields, regardless of the minor numbers of rocks showing a signal of basaltic andesites in both ACVF and Western Snake River Plain. The total number of vents in ACVF is way less than those two volcanic fields, and the total area of ACVF compared to those fields belongs to the "small area". Thus, the ACVF is a young and small monogenetic volcanic field in the world. Due to the eruptive evolutions, ACVF does not contain shield volcanoes. The local orientation of the fissure/fault zone is totally different, due to the different local geological settings.

Chapter 8: Conclusion

Recognition of vent sites has revealed that ACVF experienced historical volcanism. Evidence includes multiple types of volcanic edifices, e.g., scoria cones, complex cones, and tuff rings. The exposed lava displays several morphologies of flow, such as tumuli, a'a and pāhoehoe. Vent edifices reveal eruptive types, e.g., effusive eruptions, strombolian eruptions and phreatomagmatic eruptions, with volcanism mainly controlled by fissure propagation that triggered the latest episodes of volcanism. The intra-continental setting raises interest as to the origins of ACVF volcanism and demonstrates that volcanism can be active even in areas with relatively thick continental crust and far away from active subduction zones; the asthenosphere upwelling and crustal thinning processes are the engines that most likely powered the Cenozoic volcanism in ACVF.

Pheatomagmatism in ACVF is represented by Tongxin Lake and its pyroclastic deposits. Three injections of magma into water-saturated sediments or free sub-surface water fueled the explosions. Five stratigraphic columns log the successions of the hydrovolcanic processes during syn-eruptive stages. The water that drives the

phreatomagmatic eruptions is of unknown source; country rocks are impervious and likely to be poor water sources, and the climate is arid. The local fluvial system (Chaoer River) is a highly likely source for water-triggering phreatomagmatism in TX. The absence of wide distributions of PDC deposits may be explained by the erosional processes that happened during post-eruptive stages; one reasonable assumption is that the environment was even more arid during the late Pleistocene. Erosion by periglacial processes during harsh winters is more likely to be the case, e.g., freeze-thaw. The lava flows flowed to the south of TX, meaning the flows covered large areas around Chaihe Town (about 30 km^2 in area).

ACVF contains a diverse range of geological features, such as evolved hydrogeology, complicated geomorphology, and potential values of geoconservation and geoheritage. The eastern part of ACVF has already been a national geopark, which means the preservation of young volcanic structures is under proper protection. Tongxin Lake and its surrounding areas are due to its distinctive volcanic features, especially the lava flows in the south and east of the lake with columnar jointing. The western part of ACVF is not yet under national geopark protection.

Lava flow simulations and cross-sections on the youngest lava flow from Da Heigou (DHG) and Yanshan-the Triple Vent (YS) suggest the areas of national geopark are on one of the major fissure trends, and future fissuring is likely to cause further eruptions , putting Geopark infrastructure and the local population at risk. The “whirlpool” structure of YS flow provides evidence of ponding after the lava effused from the vents with relatively high effusive rates judging from the flattened topography of the valley. Sentinal Satellite Imagery and GIS-based analysis support the assumption of flows erupting from vents in successive stages from Dichi Lake, DHG and YS. Vents aligned over several km support the idea of fissure-driven volcanism. This study concludes that ACVF was formed by fissure propagation where ascending magma broke through linear tectonic zones within the granitic and metasedimentary country rock.

Suggestions for future work:

- Systematic analyses on the loose scoria deposits in the south of YS. Those deposits may suggest the processes of how the strombolian eruptions

occurred, such as the initial stage, intermediate edifice constructions and the latter stages turning to effusive eruptions.

- Further detailed mapping of the lava flows is warranted. Huge volumes of lava dominate the eastern side of ACVF. The nature of the flows suggests that at least four vents might be the sources. In consideration of the flattened topography of the valley, if the flow can be ponded in such a large area, the rate of magma extrusion may be rapid.
- Modelling the ascent rate and supply of magma to inform emplacement dynamics is imperative to understanding volcanic risk and hazard in ACVF. The detailed chronology of eruptions from ACVF and TX, in particular, is poorly known. The latest dating information from previous research on ACVF is documented on the western part of the volcanic field, i.e., Yanshan (the triple vent). There has been no dating in TX.
- The preliminary analyses of geochemistry have been provided in the appendix part, this is so far the most detailed data on the five key outcrops of TX; those data follow the order of stratigraphic layout. However, the lack of mineral analyses, e.g. electron microprobe, are needed in the future, in order to take a glimpse of the petrogenesis of TX lava flows.
- Considering the sedimentary rate of PDC deposits in the world, e.g., the calculations from Patrick et al. (2007), there needs to be more work on the dynamics of PDC emplacement in the TX site in the future.
- It is complicated to distinguish lava flows from different vents in ACVF. At TX, the multi-elemental diagram and REE diagram reveal that lava flows could have originated from similar sources, which generated the juvenile particles in the PDC deposits. However, the source of each lava flow and its relation to PDCs atTX has yet to be determined because data from geochemistry only depicts the evolutionary processes of lava flows. Thus, further studies are needed to determine if it's possible to classify the lava flows from Tongxin Volcano. Mineralogical analyses (such as electron microprobe) are required in an effort to establish the evolutionary history of the magma.
- Only near-surface mafic materials had been dated by previous research (Bai et al., 2005; Fan et al., 2011; Liu, 1987; Meng et al., 2018; Sun et al., 2017)

mentioned in Chapter 2, Table 3; the real lifespan of the ACVF's volcanism is under debate, obviously, it is longer than what has been provided. Thus, in consideration of the sizes of both YS and DHG, a detailed chronology system is highly needed to help build a detailed evolutionary history of Cenozoic volcanism in ACVF.

- A more detailed geological map is required in the future to be able to see the geological variations of the region in higher resolution, and to a large extent, such work needs to be field-based. The Tongxin Volcano is located near the eastern end of ACVF, and 10 km farther east, there are three more vents. Also, the area to the west of ACVF is higher elevation than east of ACVF. Eventually, Chaihe Town may be in the path of future lava flows from TX or nearby eruptions. These relationships will be best determined by additional field mapping.
- Higher-resolution geospatial data are required for future works, including applications of LiDAR or drone survey-generated digital terrain models. STRM database has an intermediate spatial resolution (30 m). This resolution is only suitable for a first-order approach that identifies large-scale geodiversity elements and is not suitable for direct geosite identification and design of local geoconservation and geoeducation strategies. Higher resolution geospatial data would enable better resolution of lava flows And surface roughness, which could indicate the relative age of ash cover.
- The values of geodiversity (Table 10) need to be more specific than we have at present, e.g., more detailed information on rock types, natural resources, and level of risk assessments. The geodiversity of ACVF is complex due to the co-existence of multi-age and strikingly different rock types over a large area. Values are highly dependent on the perspectives of the viewer and the purpose of the geodiversity estimate (e.g., for geoeducation, geotourism, geoconservation or their various levels of combinations).
- Lava flow simulation using high-resolution satellite imagery GIS-based analyses is required. For example, at the Gaoshan site, it is necessary to investigate the relationships between each of the lava flows that ponded between YS and

Gaoshan in order to understand how ponding impacted the areas around and along the Halaha River.

- The volcanic risk assessment needs to consider many aspects. Not only should it address the issues of direct impacts from volcanic eruptions on a range of physical settings, but it should also include political, economic, and cultural obligations and prospects. The first awareness is pre-eruption preparation. In ACVF, long-term monitoring for volcanism needs to be routine (at least annual) and ongoing, e.g., seismograph network and heat flow studies. This is particularly important in areas with high population density and now that a national geopark has been established in areas with high visitor numbers. The scenic locations of Tianchi Lake and Tongxin Lake are popular with tourists and local residents, so they require frequent monitoring for seismic and/or volcanic activity. As described in Chapters 5 & 6, the emplacement of lava flows could cause ponding over a vast area; those areas contain local communities, including infrastructure, residences, medical facilities and businesses. More importantly, lava flows are relatively benign in terms of hazard to human life, but an explosion crater with PDCs out to a 3-5km radius could occur rapidly and be life-threatening. A hazard map is required; it should show the geology of fissure trends and evacuation routes in local areas and offer possible life-saving instructions.

References:

Affleck, D. K., Cassidy, J., & Locke, C. A. (2001). Te Pouhawaiki Volcano and pre - volcanic topography in central Auckland: Volcanological and hydrogeological implications. *New Zealand Journal of Geology and Geophysics*, *44*(2), 313-321. https://doi.org/10.1080/00288306.2001.9514940

Agustín-Flores, J., Siebe, C., Ferrés, D., Sieron, K., & González-Zuccolotto, K. (2021). Monogenetic volcanoes with initial phreatomagmatic phases in the Ceboruco graben, western Mexico: The cases of Potrerillo I, Potrerillo II, and San Juanito. *Journal of Volcanology and Geothermal Research*, *412*, 107184. https://doi.org/https://doi.org/10.1016/j.jvolgeores.2021.107184

Alvarado, G. E., Pérez, W., Vogel, T. A., Gröger, H., & Patiño, L. (2011). The Cerro Chopo basaltic cone (Costa Rica): An unusual completely reversed graded pyroclastic cone with abundant low vesiculated cannonball juvenile fragments. *Journal of Volcanology and Geothermal Research*, *201*(1), 163-177. https://doi.org/10.1016/j.jvolgeores.2010.11.010

Anderson, D. L. (2005). Large Igneous Provinces, Delamination, and Fertile Mantle. *Elements*, *1*(5), 271-275. https://doi.org/10.2113/gselements.1.5.271

Anderson, S. W., Smrekar, S. E., & Stofan, E. R. (2012). Tumulus development on lava flows: insights from observations of active tumuli and analysis of formation models. *Bulletin of Volcanology*, *74*(4), 931-946. https://doi.org/10.1007/s00445-012-0576-2

Aranda-Gómez, J., & Luhr, J. F. (1996). Origin of the Joya Honda maar, San Luis Potosí, México. *Journal of Volcanology and Geothermal Research*, *74*(1), 1-18. https://doi.org/10.1016/S0377-0273(96)00044-3

Aranda-Gómez, J. J., Luhr, J. F., & Pier, G. (1992). The La Breña — El Jagüey Maar Complex, Durango, México: I. Geological evolution [journal article]. *Bulletin of Volcanology*, *54*(5), 393-404. https://doi.org/10.1007/bf00312321

Athy, L. F. (1930). Density, Porosity, and Compaction of Sedimentary Rocks1. *AAPG Bulletin*, *14*(1), 1-24. https://doi.org/10.1306/3d93289e-16b1-11d7-8645000102c1865d

Auer, A., Martin, U., & Németh, K. (2007). The Fekete-hegy (Balaton Highland Hungary) "soft-substrate" and "hard-substrate" maar volcanoes in an aligned volcanic complex – Implications for vent geometry, subsurface stratigraphy and the palaeoenvironmental setting. *Journal of Volcanology and Geothermal Research*, *159*(1), 225-245. https://doi.org/10.1016/j.jvolgeores.2006.06.008

Bablon, M., Quidelleur, X., Samaniego, P., Le Pennec, J.-L., Santamaría, S., Liorzou, C., Hidalgo, S., & Eschbach, B. (2020). Volcanic history reconstruction in northern Ecuador: insights for eruptive and erosion rates on the whole Ecuadorian arc. *Bulletin of Volcanology*, *82*(1), 11. https://doi.org/10.1007/s00445-019-1346-1

Bacon, C. R. (1990). Calc-alkaline, Shoshonitic, and Primitive Tholeiitic Lavas from Monogenetic Volcanoes near Crater Lake, Oregon. *Journal of Petrology*, *31*(1), 135-166. https://doi.org/10.1093/petrology/31.1.135

Bai, Z., Tan, Q., Wang, D., & Wang, Y. (2012). Late Quaternary volcanic activity and neotectonics in the eastern Inner Mongolia. *Acta Petrologica Sinica*, *28*(4), 1099-1107.

Bai, Z., Tian, M., Wu, F., Xu, D., & Li, T. (2005). Yanshan, Gaoshan-Two Active Volcanoes of the Volcanic Cluster in Arshan, Inner Mongolia. *Earthquake Research in China*, *19*(4), 402-408.

Bai, Z., Xu, D., Zhang, B., Zhang, T., & Bu, J. (2006). Study on type and phase of Quaternary explosive volcanism in Longgang volcanic cluster. *Acta Geologica Sinica*(06), 1473-1480.

Becerril, L., Larrea, P., Salinas, S., Mossoux, S., Ferrés, D., Widom, E., Siebe, C., & Martí, J. (2021). The historical case of Paricutin volcano (Michoacán, México): challenges of simulating lava flows on a gentle slope during a long-lasting eruption. *Natural Hazards*, *107*(1), 809-829. https://doi.org/10.1007/s11069-021-04607-x

Begét, J. E., Hopkins, D. M., & Charron, S. D. (1996). The Largest Known Maars on Earth, Seward Peninsula, Northwest Alaska. *Arctic*, *49*(1), 62-69. http://www.jstor.org.ezproxy.massey.ac.nz/stable/40511986

Bemis, K. G., & Ferencz, M. (2017). Morphometric analysis of scoria cones: the potential for inferring process from shape. *Geological Society, London, Special Publications*, *446*(1), 61-100. https://doi.org/doi:10.1144/SP446.9

Blatt, H., & Jones, R. L. (1975). Proportions of Exposed Igneous, Metamorphic, and Sedimentary Rocks. *GSA Bulletin*, *86*(8), 1085-1088. https://doi.org/10.1130/0016-7606(1975)86<1085:Poeima>2.0.Co;2

Boggs Jr, S. (2014). *Principles of sedimentology and stratigraphy*. Pearson Education.

Bonnichsen, B., & Godchaux, M. M. (2004). Late Miocene, Pliocene, and Pleistocene geology of southwestern Idaho with emphasis on basalts in the Bruneau-Jarbidge, Twin Falls, and western Snake River Plain regions. *Idaho Geol. Surv. Bull.*, *30*, 229-312.

Boreham, F., Cashman, K., & Rust, A. (2020). Hazards from lava–river interactions during the 1783–1784 Laki fissure eruption. *GSA Bulletin*, *132*(11-12), 2651-2668. https://doi.org/10.1130/b35183.1

Brand, B. D., & Broz, P. (2015). Tuff Cone. In H. Hargitai & A. k. Kereszturi (Eds.), *Encyclopedia of Planetary Landforms* (pp. 2197-2204).

Brand, B. D., & White, C. M. (2007). Origin and stratigraphy of phreatomagmatic deposits at the Pleistocene Sinker Butte Volcano, Western Snake River Plain, Idaho. *Journal of Volcanology and Geothermal Research*, *160*(3-4), 319–339. https://doi.org/10.1016/j.jvolgeores.2006.10.007

Brenna, M., Cronin, S. J., Smith, I. E. M., Maas, R., & Sohn, Y. K. (2012). How Small-volume Basaltic Magmatic Systems Develop: a Case Study from the Jeju Island Volcanic Field, Korea. *JOURNALOF PETROLOGY*, *53*(5), 985-1018. https://doi.org/10.1093/petrology/egs007

Brenna, M., Cronin, S. J., Smith, I. E. M., Tollan, P. M. E., Scott, J. M., Prior, D. J., Bambery, K., & Ukstins, I. A. (2018). Olivine xenocryst diffusion reveals rapid monogenetic basaltic magma ascent following complex storage at Pupuke Maar, Auckland Volcanic Field, New Zealand. *Earth and Planetary Science Letters*, *499*, 13-22. https://doi.org/https://doi.org/10.1016/j.epsl.2018.07.015

Brenna, M., Németh, K., Cronin, S. J., Sohn, Y. K., Smith, I. E. M., & Wijbrans, J. (2015). Co-located monogenetic eruptions ~200 kyr apart driven by tapping vertically separated mantle source regions, Chagwido, Jeju Island, Republic of Korea. *Bulletin of Volcanology*, *77*(5), 43. https://doi.org/10.1007/s00445-015-0928-9

Browne, B. L., & Gardner, J. E. (2006). The influence of magma ascent path on the texture, mineralogy, and formation of hornblende reaction rims. *Earth and Planetary Science Letters*, *246*(3), 161-176. https://doi.org/https://doi.org/10.1016/j.epsl.2006.05.006

Broz, P., & Nemeth, K. (2015). Tuff Ring. In H. Hargitai & A. k. Kereszturi (Eds.), *Encyclopedia of Planetary Landforms* (pp. 2204-2210). https://doi.org/10.1002/jgre.20120

Büchner, J., & Tietz, O. (2012). Reconstruction of the Landeskrone Scoria Cone in the Lusatian Volcanic Field, Eastern Germany — Long-term degradation of volcanic edifices and implications for landscape evolution. *Geomorphology*, *151-152*, 175-187. https://doi.org/https://doi.org/10.1016/j.geomorph.2012.01.027

Burke, K., Kidd, W. S. F., & Wilson, J. T. (1973). Plumes and Concentric Plume Traces of the Eurasian Plate. *Nature Physical Science*, *241*(111), 128-129. https://doi.org/10.1038/physci241128a0

Buttner, R., Dellino, P., & Zimanowski, B. (1999). Identifying magma–water interaction from the surface features of ash particles. *NATURE*, *40*(6754), 688-690.

Büttner, R., & Zimanowski, B. (1998). Physics of thermohydraulic explosions. *Physical Review E*, *57*(5), 5726-5729. https://doi.org/10.1103/PhysRevE.57.5726

Camp, V. E., Roobol, M. J., & Hooper, P. R. (1991). The Arabian continental alkali basalt province: Part II. Evolution of Harrats Khaybar, Ithnayn, and Kura, Kingdom of Saudi Arabia. *GSA Bulletin*, *103*(3), 363-391. https://doi.org/10.1130/0016-7606(1991)103<0363:Tacabp>2.3.Co;2

Cañón-Tapia, E. (2016). Reappraisal of the significance of volcanic fields. *Journal of Volcanology and Geothermal Research*, *310*, 26-38. https://doi.org/https://doi.org/10.1016/j.jvolgeores.2015.11.010

Cañón-Tapia, E., & Walker, G. P. L. (2004). Global aspects of volcanism: the perspectives of "plate tectonics" and "volcanic systems". *Earth-Science Reviews*, *66*(1), 163-182. https://doi.org/https://doi.org/10.1016/j.earscirev.2003.11.001

Carrasco-Núñez, G., Ort, M. H., & Romero, C. (2007). Evolution and hydrological conditions of a maar volcano (Atexcac crater, Eastern Mexico). *Journal of Volcanology and Geothermal Research*, *159*(1), 179-197. https://doi.org/10.1016/j.jvolgeores.2006.07.001

Cas, R. A. F., Otterloo, J. v., Blaikie, T. N., & Hove, J. v. d. (2017). The dynamics of a very large intra-plate continental basaltic volcanic province, the Newer Volcanics Province, SE Australia, and implications for other provinces. *Geological Society, London, Special Publications*, *446*(1), 123-172. https://doi.org/doi:10.1144/SP446.8

Chough, S. K., & Sohn, Y. K. (1990). Depositional mechanics and sequences of base surges, Songaksan tuff ring, Cheju Island, Korea. *Sedimentology*, *37*(6), 1115-1135. https://doi.org/10.1111/j.1365-3091.1990.tb01849.x

Clague, D. A., & Jarrard, R. D. (1973). Tertiary Pacific Plate Motion Deduced from the Hawaiian-Emperor Chain. *GSA Bulletin*, *84*(4), 1135-1154. https://doi.org/10.1130/0016-7606(1973)84<1135:Tppmdf>2.0.Co;2

Connor, C. B., Conway, F. M., & Sigurdsson, H. (2000). Basaltic volcanic fields. *Encyclopedia of Volcanoes*, *1*, 331-343.

Cormier, V. F. (1975). Tectonics near the Junction of the Aleutian and Kuril-Kamchatka Arcs and a Mechanism for Middle Tertiary Magmatism in the Kamchatka Basin. *GSA Bulletin*, *86*(4), 443-453. https://doi.org/10.1130/0016-7606(1975)86

Cox, K. G., Bell, J. D., & Pankhurst, R. J. (2013). *The interpretation of igneous rocks*. Springer Science & Business Media.

Cui, Q., & Zhao, Y. (2019). Climatic abrupt events implied by lacustrine sediments of Arxan Crater Lake, in the central Great Khingan Mountains, NE China during Holocene. *Quaternary Sciences*, *39*(6), 1346-1356.

Cui, X.-g., Xu, J.-d., Yu, H.-m., Zhao, B., & Yang, W.-j. (2021). Understanding the Yanshan volcano eruption in the Chaihe–Arxan volcanic field, northeastern China. *Arabian Journal of Geosciences*, *14*(21), 2174. https://doi.org/10.1007/s12517-021-08368-6

De Reu, J., Bourgeois, J., Bats, M., Zwertvaegher, A., Gelorini, V., De Smedt, P., Chu, W., Antrop, M., De Maeyer, P., Finke, P., Van Meirvenne, M., Verniers, J., & Crombé, P. (2013). Application of the topographic position index to heterogeneous landscapes. *Geomorphology*, *186*, 39-49. https://doi.org/https://doi.org/10.1016/j.geomorph.2012.12.015

de Silva, S., & Lindsay, J. M. (2015). Chapter 15 - Primary Volcanic Landforms. In H. Sigurdsson (Ed.), *The Encyclopedia of Volcanoes (Second Edition)* (pp. 273-297). Academic Press. https://doi.org/https://doi.org/10.1016/B978-0-12-385938-9.00015-8

Decker, R. W., & Decker, B. B. (1999). *Volcano*. Encyclopedia Britannica. https://www.britannica.com/science/volcano

DeHon, R. (2015). Maar. In H. Hargitai & A. k. Kereszturi (Eds.), *Encyclopedia of Planetary Landforms* (pp. 1295-1299). https://doi.org/10.1007/978-1-4614-3134-3

Dellino, P., Isaia, R., & Veneruso, M. (2004b). Turbulent boundary layer shear £ows as an approximation of base surges at Campi Flegrei (Southern Italy). *Journal of Volcanology and Geothermal Research*, *133*(1-4), 211-228. https://doi.org/10.1016/S0377-0273(03)00399-8

Dellino, P., Isaia, R., Volpe, L. L., & Orsi, G. (2004a). Interaction between particles transported by fallout and surge in the deposits of the Agnano^Monte Spina eruption (Campi Flegrei, Southern Italy). *Journal of Volcanology and Geothermal Research*, *133*(1-4), 193-210. https://doi.org/10.1016/S0377-0273(03)00398-6

Dukhin, A., Swasey, S., & Thommes, M. (2013). A method for pore size and porosity analysis of porous materials using electroacoustics and high frequency conductivity. *Colloids and Surfaces A: Physicochemical and Engineering Aspects*, *437*, 127-132. https://doi.org/https://doi.org/10.1016/j.colsurfa.2013.01.018

Edwards, L., Lubin, M., & Marino, J. (2016). Improving the Repeatability of Coke Bulk Density Testing. In S. J. Lindsay (Ed.), *Light Metals 2011* (pp. 947-952). Springer International Publishing. https://doi.org/10.1007/978-3-319-48160-9_162

Eggins, S. M. (2003). Laser Ablation ICP-MS Analysis of Geological Materials Prepared as Lithium Borate Glasses. *Geostandards Newsletter*, *27*(2), 147-162. https://doi.org/https://doi.org/10.1111/j.1751-908X.2003.tb00642.x

Eichelberger, J., Kiryukhin, A., Mollo, S., Tsuchiya, N., & Villeneuve, M. (2020). Exploring and Modeling the Magma–Hydrothermal Regime. *Geosciences*, *10*(6), 234. https://www.mdpi.com/2076-3263/10/6/234

Eizenhöfer, P. (2020). Regional Geology Across the Solonker Suture Zone. In *Subduction and Closure of the Palaeo-Asian Ocean along the Solonker Suture Zone: Constraints from an Integrated Sedimentary Provenance Analysis* (pp. 13-40). Springer. https://doi.org/10.1007/978-981-32-9200-0_2

Fagents, S. A., & Thordarson, T. (2007). *Rootless volcanic cones in Iceland and on Mars*

Fan, Q., Liu, R., Wei, H., Sui, J., & Li, N. (1999). The petrology and geochemistry of Jinlongdingzi modern active volcano in Longgang area. *Acta Petrologica Sinica*, *15*, 584–589.

Fan, Q., Zhao, Y., Li, D., Wu, Y., Sui, J., & Zheng, D. (2011). Studies on Quaternary volcanism stages of Halaha river and Chaoer river area in the Great Xing'an Range: Evidence from K-Ar dating and volcanic geology features. *Acta Petrologica Sinica*, *27*(11), 2827-2832.

Fan, W.-M., Guo, F., Wang, Y.-J., & Lin, G. (2003). Late Mesozoic calc-alkaline volcanism of post-orogenic extension in the northern Da Hinggan Mountains, northeastern China. *Journal of Volcanology and Geothermal Research*, *121*(1), 115-135. https://doi.org/https://doi.org/10.1016/S0377-0273(02)00415-8

Fan, W.-M., Guo, F., Wang, Y.-J., & Zhang, M. (2004). Late Mesozoic volcanism in the northern Huaiyang tectono-magmatic belt, central China: partial melts from a lithospheric mantle with subducted continental crust relicts beneath the Dabie orogen? *Chemical Geology*, *209*(1-2), 27-48. https://doi.org/10.1016/j.chemgeo.2004.04.020

Farrand, W. H., & Singer, R. B. (1992). Alteration of hydrovolcanic basaltic ash: Observations with visible and near-infrared spectrometry. *Journal of Geophysical Research: Solid Earth*, *97*(B12), 17393-17408. https://doi.org/10.1029/92JB01075

Feng, M., G, K., & Wang, F. (1979). *Wudalianchi Volcanoes in China*. Shanghai Sci Tech Publishers.

Feng, M., & Whitford-Stark, J. L. (1986). The 1719–1721 eruptions of potassium-rich lavas at Wudalianchi, China. *Journal of Volcanology and Geothermal Research*, *30*(1), 131-148. https://doi.org/https://doi.org/10.1016/0377-0273(86)90070-3

Feng, Z., Liu, Y., Li, L., She, H., Jiang, L., Du, B., Liu, Y., Li, W., Wen, Q., & Liang, C. (2018). Subduction, accretion, and collision during the Neoproterozoic-Cambrian orogeny in

the Great Xing'an Range, NE China: Insights from geochemistry and geochronology of the Ali River ophiolitic mélange and arc-type granodiorites. *Precambrian Research*, *311*, 117-135. https://doi.org/https://doi.org/10.1016/j.precamres.2018.04.013
Fisher, R. V., & Schmincke, H. U. (1984). *Pyroclastic rocks*. Springer.
Fisher, R. V., & Schmincke, H. U. (1994). Volcaniclastic sediment transport and deposition. In *Sediment Transport and Depositional Processes* (pp. 351-388).
Fodor, E., & Németh, K. (2014). Spatter Cone. In *Encyclopedia of Planetary Landforms* (pp. 1-9). https://doi.org/10.1007/978-1-4614-9213-9_589-1
Fodor, E. k., & Broz, P. (2015). Cinder Cone. In H. Hargitai & A. Kereszturi (Eds.), *Encyclopedia of Planetary Landforms* (pp. 290-295).
Fornaciai, A., Behncke, B., Favalli, M., Neri, M., Tarquini, S., & Boschi, E. (2010). Detecting short-term evolution of Etnean scoria cones: a LIDAR-based approach. *Bulletin of Volcanology*, *72*(10), 1209-1222. https://doi.org/10.1007/s00445-010-0394-3
Foulger, G. R. (2007). The "plate" model for the genesis of melting anomalies. In *Plates, Plumes and Planetary Processes* (Vol. 430, pp. 0). Geological Society of America. https://doi.org/10.1130/2007.2430(01)
Foulger, G. R. (2011). *Plates vs plumes: a geological controversy*. John Wiley & Sons.
Foulger, G. R. (2021). The plate theory for volcanism. *Encyclopedia of Geology*, *3*, 879-890.
Foulger, G. R., & Natland, J. H. (2003). Is "Hotspot" Volcanism a Consequence of Plate Tectonics? *Science*, *300*(5621), 921-922. https://doi.org/doi:10.1126/science.1083376
Friedman, G. M. (1962). On Sorting, Sorting Coefficients, and the Lognormality of the Grain-Size Distribution of Sandstones. *The Journal of Geology*, *70*(6), 737-753. https://doi.org/10.1086/jg.70.6.30066373
Friedman, G. M. (1979). Address of the retiring President of the International Association of Sedimentologists: Differences in size distributions of populations of particles among sands of various origins. *Sedimentology*, *26*(1), 3-32. https://doi.org/https://doi.org/10.1111/j.1365-3091.1979.tb00336.x
Funiciello, R., Giordano, G., & De Rita, D. (2003). The Albano maar lake (Colli Albani Volcano, Italy): recent volcanic activity and evidence of pre-Roman Age catastrophic lahar events. *Journal of Volcanology and Geothermal Research*, *123*(1), 43-61. https://doi.org/10.1016/S0377-0273(03)00027-1
Gao, W., Li, J., Mao, X., & Li, H. (2013). Geological and Geomorphological Value of the Monogenetic Volcanoes in Wudalianchi National Park, NE China. *Geoheritage*, *5*(2), 73-85. https://doi.org/10.1007/s12371-013-0077-5
Gao, Y.-G., & Li, Y.-H. (2014). Crustal Thickness and Vp/Vs in the Northeast China-North China Region and Its Geological Implication. *CHINESE JOURNAL OF GEOPHYSICS*, *57*(2), 166-176. https://doi.org/https://doi.org/10.1002/cjg2.20094
Ge, W.-C., Chen, J.-S., Yang, H., Zhao, G.-C., Zhang, Y.-L., & Tian, D.-X. (2015). Tectonic implications of new zircon U–Pb ages for the Xinghuadukou Complex, Erguna Massif, northern Great Xing'an Range, NE China. *Journal of Asian Earth Sciences*, *106*, 169-185. https://doi.org/https://doi.org/10.1016/j.jseaes.2015.03.011
Gençalioğlu-Kuşcu, G., Atilla, C., Cas, R. A. F., & Kuşcu, İ. (2007). Base surge deposits, eruption history, and depositional processes of a wet phreatomagmatic volcano in Central Anatolia (Cora Maar). *Journal of Volcanology and Geothermal Research*, *159*(1), 198-209. https://doi.org/10.1016/j.jvolgeores.2006.06.013
Geshi, N., Németh, K., Noguchi, R., & Oikawa, T. (2019). Shift from magmatic to phreatomagmatic explosions controlled by the lateral evolution of a feeder dike in the Suoana-Kazahaya eruption, Miyakejima Volcano, Japan. *Earth and Planetary Science Letters*, *511*, 177-189. https://doi.org/https://doi.org/10.1016/j.epsl.2019.01.038

Gilder, S. A., Keller, G. R., Luo, M., & Goodell, P. C. (1991). Eastern Asia and the Western Pacific timing and spatial distribution of rifting in China. *Tectonophysics*, *197*(2), 225-243. https://doi.org/https://doi.org/10.1016/0040-1951(91)90043-R

Gioia, D., Danese, M., Corrado, G., Di Leo, P., Minervino Amodio, A., & Schiattarella, M. (2021). Assessing the Prediction Accuracy of Geomorphon-Based Automated Landform Classification: An Example from the Ionian Coastal Belt of Southern Italy. *ISPRS International Journal of Geo-Information*, *10*(11), 725. https://www.mdpi.com/2220-9964/10/11/725

Go, S. Y., & Sohn, Y. K. (2021). Microtextural evidence for vesiculated tuff formation in Songaksan tuff ring, Jeju Island, Korea. *Journal of Volcanology and Geothermal Research*, *417*, 107311. https://doi.org/https://doi.org/10.1016/j.jvolgeores.2021.107311

Godchaux, M., & Bonnichsen, B. (2002). Syneruptive magma–water and posteruptive lava–water interactions in the Western Snake River Plain, Idaho, during the past 12 million years. *Tectonic and magmatic evolution of the Snake River Plain Volcanic Province. Idaho Geol Surv Bull*, *30*, 387-434.

Godchaux, M. M., Bonnichsen, B., & Jenks, M. D. (1992). Types of phreatomagmatic volcanoes in the western Snake River Plain, Idaho, USA. *Journal of Volcanology and Geothermal Research*, *52*(1), 1-25. https://doi.org/10.1016/0377-0273(92)90130-6

Gong, J. (1997). Xiaogulihe-Keluo-Wudalianchi volcanic belt. *Heilongjiang Geology*, *8*(4), 29-39.

Gonnermann, H. M., & Manga, M. (2013). Dynamics of magma ascent. *Modeling volcanic processes: The physics and mathematics of volcanism*, *55*.

Gorbatov, A., Kostoglodov, V., Suárez, G., & Gordeev, E. (1997). Seismicity and structure of the Kamchatka Subduction Zone. *Journal of Geophysical Research: Solid Earth*, *102*(B8), 17883-17898. https://doi.org/https://doi.org/10.1029/96JB03491

Gray, M. (2008). Geodiversity: developing the paradigm. *Proceedings of the Geologists' Association*, *119*(3), 287-298. https://doi.org/https://doi.org/10.1016/S0016-7878(08)80307-0

Greeley, R., & King, J. S. (1977). Volcanism of the Eastern Snake River Plain, Idaho: A comparative planetary geology-guidebook. *vesr*.

Green, J., & Short, N. M. (1971). *Volcanic landforms and surface features: A photographic atlas and glossary*. Springer Science & Business Media.

Guilbaud, M.-N., Siebe, C., Layer, P., Salinas, S., Castro-Govea, R., Garduño-Monroy, V. H., & Le Corvec, N. (2011). Geology, geochronology, and tectonic setting of the Jorullo Volcano region, Michoacán, México. *Journal of Volcanology and Geothermal Research*, *201*(1-4), 97-112. https://doi.org/10.1016/j.jvolgeores.2010.09.005

Hamilton, C. W., Fagents, S. A., & Thordarson, T. (2010b). Explosive lava–water interactions II: self-organization processes among volcanic rootless eruption sites in the 1783–1784 Laki lava flow, Iceland [journal article]. *Bulletin of Volcanology*, *72*(4), 469-485. https://doi.org/10.1007/s00445-009-0331-5

Hamilton, C. W., Thordarson, T., & Fagents, S. A. (2010a). Explosive lava–water interactions I: architecture and emplacement chronology of volcanic rootless cone groups in the 1783–1784 Laki lava flow, Iceland [journal article]. *Bulletin of Volcanology*, *72*(4), 449-467. https://doi.org/10.1007/s00445-009-0330-6

Hand, B. M. (1997). Inverse grading resulting from coarse-sediment transport lag. *Journal of Sedimentary Research*, *67*(1), 124-129. https://doi.org/10.1306/d426850e-2b26-11d7-8648000102c1865d

Harker, A. (1900). Igneous Rock-Series and Mixed Igneous Rocks. *Journal of Geology*, *8*, 389. https://doi.org/10.1086/620830

Harker, A. (1909). *The natural history of igneous rocks*. Methuen & Company.

Harries, D., McHenry, M., Jennings, P., & Thomas, C. (2006). Geothermal energy in Australia. *International Journal of Environmental Studies*, *63*(6), 815-821. https://doi.org/10.1080/00207230601047008

Harris, A. J., & Rowland, S. (2001). FLOWGO: a kinematic thermo-rheological model for lava flowing in a channel. *Bulletin of Volcanology*, *63*(1), 20-44. https://doi.org/10.1007/s004450000120

Harris, A. J. L., Blake, S., Rothery, D. A., & Stevens, N. F. (1997). A chronology of the 1991 to 1993 Mount Etna eruption using advanced very high resolution radiometer data: Implications for real-time thermal volcano monitoring. *Journal of Geophysical Research: Solid Earth*, *102*(B4), 7985-8003. https://doi.org/https://doi.org/10.1029/96JB03388

Harris, A. J. L., Flynn, L. P., Keszthelyi, L., Mouginis-Mark, P. J., Rowland, S. K., & Resing, J. A. (1998). Calculation of lava effusion rates from Landsat TM data. *Bulletin of Volcanology*, *60*(1), 52-71. https://doi.org/10.1007/s004450050216

Harris, A. J. L., & Rowland, S. K. (2015). FLOWGO 2012: An Updated Framework for Thermorheological Simulations of Channel-Contained Lava. In *Hawaiian Volcanoes* (pp. 457-481). https://doi.org/https://doi.org/10.1002/9781118872079.ch21

Heap, M. J., Baumann, T., Gilg, H. A., Kolzenburg, S., Ryan, A. G., Villeneuve, M., Russell, J. K., Kennedy, L. A., Rosas-Carbajal, M., & Clynne, M. A. (2021). Hydrothermal alteration can result in pore pressurization and volcano instability. *Geology*. https://doi.org/10.1130/g49063.1

Heiken, G. H. (1971). Tuff rings: Examples from the Fort Rock-Christmas Lake Valley Basin, south-central Oregon. *Journal of Geophysical Research*, *76*(23), 5615-5626. https://doi.org/10.1029/JB076i023p05615

Hetényi, G., Taisne, B., Garel, F., Médard, É., Bosshard, S., & Mattsson, H. B. (2012). Scales of columnar jointing in igneous rocks: field measurements and controlling factors [journal article]. *Bulletin of Volcanology*, *74*(2), 457-482. https://doi.org/10.1007/s00445-011-0534-4

Hirano, N. (2011). Petit-spot volcanism: A new type of volcanic zone discovered near a trench. *GEOCHEMICAL JOURNAL*, *45*(2), 157-167. https://doi.org/10.2343/geochemj.1.0111

Hirano, N., & Machida, S. (2022). The mantle structure below petit-spot volcanoes. *Communications Earth & Environment*, *3*(1), 110. https://doi.org/10.1038/s43247-022-00438-1

Homrighausen, S., Geldmacher, J., Hoernle, K., & Rooney, T. (2021). Intraplate Volcanism. In D. Alderton & S. A. Elias (Eds.), *Encyclopedia of Geology (Second Edition)* (pp. 52-59). Academic Press. https://doi.org/https://doi.org/10.1016/B978-0-12-409548-9.12498-4

Horgan, G. W. (1996). A review of soil pore models. In: Citeseer.

Horgan, G. W. (1999). An investigation of the geometric influences on pore space diffusion. *Geoderma*, *88*(1), 55-71. https://doi.org/https://doi.org/10.1016/S0016-7061(98)00075-5

Horgan, V. (1998). Mathematical morphology for soil image analysis. *Eur. J. Soil Science*, *49*(2), 161-173.

Hsu, C.-N., & Chen, J.-c. (1998). Geochemistry of late Cenozoic basalts from Wudalianchi and Jingpohu areas, Heilongjiang Province, northeast China. *Journal of Asian Earth Sciences*, *16*(4), 385-405. https://doi.org/https://doi.org/10.1016/S0743-9547(98)00022-1

Huang, X., & Cao, G. (2015). Analyses and hydrology features of Chaoer River catchment. *Water conservancy and hydroelectricity in northeast China*, *33*(11), 2.

Hutchison, W., Pyle, D. M., Mather, T. A., Yirgu, G., Biggs, J., Cohen, B. E., Barfod, D. N., & Lewi, E. (2016). The eruptive history and magmatic evolution of Aluto volcano: new insights

into silicic peralkaline volcanism in the Ethiopian rift. *Journal of Volcanology and Geothermal Research*, *328*, 9-33. https://doi.org/https://doi.org/10.1016/j.jvolgeores.2016.09.010

Jackson, E. D. (1976). Linear Volcanic Chains on the Pacific Plate. In *The Geophysics of the Pacific Ocean Basin and Its Margin* (pp. 319-335). https://doi.org/https://doi.org/10.1029/GM019p0319

Jankovics, M. É., Harangi, S., Németh, K., Kiss, B., & Ntaflos, T. (2015). A complex magmatic system beneath the Kissomlyó monogenetic volcano (western Pannonian Basin): evidence from mineral textures, zoning and chemistry. *Journal of Volcanology and Geothermal Research*, *301*, 38-55. https://doi.org/10.1016/j.jvolgeores.2015.04.010

Jankovics, M. É., Sági, T., Astbury, R. L., Petrelli, M., Kiss, B., Ubide, T., Németh, K., Ntaflos, T., & Harangi, S. (2019). Olivine major and trace element compositions coupled with spinel chemistry to unravel the magmatic systems feeding monogenetic basaltic volcanoes. *Journal of Volcanology and Geothermal Research*, *369*, 203-223. https://doi.org/https://doi.org/10.1016/j.jvolgeores.2018.11.027

Jasiewicz, J., & Stepinski, T. F. (2013). Geomorphons — a pattern recognition approach to classification and mapping of landforms. *Geomorphology*, *182*, 147-156. https://doi.org/https://doi.org/10.1016/j.geomorph.2012.11.005

Ji, Z., Ge, W.-C., Yang, H., Wang, Q.-h., Zhang, Y.-l., Wang, Z.-h., & Bi, J.-H. (2018). Late Jurassic rhyolites from the Wuchagou region in the central Great Xing'an Range, NE China: Petrogenesis and tectonic implications. *Journal of Asian Earth Sciences*, *158*, 381-397. https://doi.org/https://doi.org/10.1016/j.jseaes.2018.03.011

Jia, H., Ji, H., Wang, L., Yang, D., Meng, P., & Shi, C. (2016). Tectono-sedimentary and hydrocarbon potential analysis of rift-related successions in the Dehui Depression, Songliao Basin, Northeastern China. *Marine and Petroleum Geology*, *76*, 262-278. https://doi.org/https://doi.org/10.1016/j.marpetgeo.2016.05.002

Johnson, R. W. (1989). *Intraplate volcanism in Eastern Australia and New Zealand*. Cambridge univ, Cambridge.

Jolly, G., & de la Cruz, S. (2015). Chapter 68 - Volcanic Crisis Management. In H. Sigurdsson (Ed.), *The Encyclopedia of Volcanoes (Second Edition)* (pp. 1187-1202). Academic Press. https://doi.org/https://doi.org/10.1016/B978-0-12-385938-9.00068-7

Jurado-Chichay, Z., Rowland, S. K., & Walker, G. P. L. (1996a). The formation of circular littoral cones from tube-fed pāhoehoe: Mauna Loa, Hawai'i [journal article]. *Bulletin of Volcanology*, *57*(7), 471-482. https://doi.org/10.1007/bf00304433

Jurado-Chichay, Z., Urrutia-Fucugauchi, J., & Rowland, S. K. (1996b). A paleomagnetic study of the Pohue Bay flow and its associated coastal cones, Mauna Loa volcano, Hawaii: constraints on their origin and temporal relationships. *Physics of the Earth and Planetary Interiors*, *97*(1), 269-277. https://doi.org/10.1016/0031-9201(95)03135-9

Kereszturi, G., Cappello, A., Ganci, G., Procter, J., Németh, K., Del Negro, C., & Cronin, S. J. (2014). Numerical simulation of basaltic lava flows in the Auckland Volcanic Field, New Zealand—implication for volcanic hazard assessment. *Bulletin of Volcanology*, *76*(11), 879. https://doi.org/10.1007/s00445-014-0879-6

Kereszturi, G., Csillag, G., Németh, K., Sebe, K., Balogh, K., & Jáger, V. (2010). Volcanic architecture, eruption mechanism and landform evolution of a Plio/Pleistocene intracontinental basaltic polycyclic monogenetic volcano from the Bakony-Balaton Highland Volcanic Field, Hungary [journal article]. *Central European Journal of Geosciences*, *2*(3), 362-384. https://doi.org/10.2478/v10085-010-0019-2

Kereszturi, G., & Nemeth, K. (2011). Shallow-seated controls on the evolution of the Upper Pliocene Kopasz-hegy nested monogenetic volcanic chain in the Western Pannonian Basin (Hungary). *GEOLOGICA CARPATHICA*, *62*, 535-546. https://doi.org/10.2478/v10096-011-0038-3

Kereszturi, G., & Németh, K. (2012a). Monogenetic Basaltic Volcanoes: Genetic Classification, Growth, Geomorphology and Degradation. In *Updates in Volcanology - New Advances in Understanding Volcanic Systems*. https://doi.org/10.5772/51387

Kereszturi, G., & Németh, K. (2012b). Structural and morphometric irregularities of eroded Pliocene scoria cones at the Bakony–Balaton Highland Volcanic Field, Hungary. *Geomorphology*, *136*(1), 45-58. https://doi.org/https://doi.org/10.1016/j.geomorph.2011.08.005

Kereszturi, G., & Németh, K. (2016a). Post-eruptive sediment transport and surface processes on unvegetated volcanic hillslopes – A case study of Black Tank scoria cone, Cima Volcanic Field, California. *Geomorphology*, *267*, 59–75. https://doi.org/10.1016/j.geomorph.2016.05.023

Kereszturi, G., & Németh, K. (2016b). Sedimentology, eruptive mechanism and facies architecture of basaltic scoria cones from the Auckland Volcanic Field (New Zealand). *Journal of Volcanology and Geothermal Research*, *324*, 41-56. https://doi.org/https://doi.org/10.1016/j.jvolgeores.2016.05.012

Kereszturi, G., Németh, K., Cronin, S. J., Agustín-Flores, J., Smith, I. E. M., & Lindsay, J. (2013). A model for calculating eruptive volumes for monogenetic volcanoes — Implication for the Quaternary Auckland Volcanic Field, New Zealand. *Journal of Volcanology and Geothermal Research*, *266*, 16-33. https://doi.org/10.1016/j.jvolgeores.2013.09.003

Kereszturi, G., Németh, K., Csillag, G., Balogh, K., & Kovács, J. (2011). The role of external environmental factors in changing eruption styles of monogenetic volcanoes in a Mio/Pleistocene continental volcanic field in western Hungary. *Journal of Volcanology and Geothermal Research*, *201*(1), 227-240. https://doi.org/https://doi.org/10.1016/j.jvolgeores.2010.08.018

Khalaf, F., Al-Bakri, D., & Al-Ghadban, A. (1984). Sedimentological characteristics of the surficial sediments of the Kuwaiti marine environment, northern Arabian Gulf. *Sedimentology*, *31*(4), 531-545. https://doi.org/https://doi.org/10.1111/j.1365-3091.1984.tb01818.x

Kilburn, C. R. (2000). Lava flows and flow fields. *Encyclopedia of Volcanoes*, 291-305.

Kilburn, C. R. J., & Lopes, R. M. C. (1988). The growth of AA lava flow fields on Mount Etna, Sicily. *Journal of Geophysical Research: Solid Earth*, *93*(B12), 14759-14772. https://doi.org/https://doi.org/10.1029/JB093iB12p14759

Kinoshita, O. (1995). Migration of igneous activities related to ridge subduction in Southwest Japan and the East Asian continental margin from the Mesozoic to the Paleogene. *Tectonophysics*, *245*(1), 25-35. https://doi.org/https://doi.org/10.1016/0040-1951(94)00211-Q

Kinoshita, O. (2002). Possible manifestations of slab window magmatisms in Cretaceous southwest Japan. *Tectonophysics*, *344*(1), 1-13. https://doi.org/https://doi.org/10.1016/S0040-1951(01)00262-1

Kokelaar, B. P. (1983). The mechanism of Surtseyan volcanism. *Journal of the Geological Society*, *140*(6), 939-944. https://doi.org/10.1144/gsjgs.140.6.0939

Kokelaar, P. (1986). Magma-water interactions in subaqueous and emergent basaltic [journal article]. *Bulletin of Volcanology*, *48*(5), 275-289. https://doi.org/10.1007/bf01081756

Kozlowski, S. (2001). Postepy prac nad ochrona georoznorodnosci w Polsce. *Kosmos*, *50*(1-2), 151-165.

Kozłowski, S. (2004). Geodiversity. The concept and scope of geodiversity. *Przegląd Geologiczny*, *Vol. 52, nr 8/2*, 833-837.

Kravchinsky, V. A., Cogné, J.-P., Harbert, W. P., & Kuzmin, M. I. (2002). Evolution of the Mongol-Okhotsk Ocean as constrained by new palaeomagnetic data from the Mongol-Okhotsk suture zone, Siberia. *Geophysical Journal International*, *148*(1), 34-57. https://doi.org/10.1046/j.1365-246x.2002.01557.x

Krumbein, W. C. (1934). Size frequency distributions of sediments. *Journal of Sedimentary Research*, *4*(2), 65-77. https://doi.org/10.1306/d4268eb9-2b26-11d7-8648000102c1865d

Krumbein, W. C., & Pettijohn, F. J. (1938). Manual of sedimentary petrography.

Kuritani, T., Kimura, J.-I., Ohtani, E., Miyamoto, H., & Furuyama, K. (2013). Transition zone origin of potassic basalts from Wudalianchi volcano, northeast China. *Lithos*, *156-159*, 1-12. https://doi.org/10.1016/j.lithos.2012.10.010

Lander, A. V., & Shapiro, M. N. (2007). The origin of the modern Kamchatka Subduction Zone. *Washington DC American Geophysical Union Geophysical Monograph Series*, *172*, 57. https://doi.org/10.1029/172gm05

Le Corvec, N., Bebbington, M. S., Lindsay, J. M., & McGee, L. E. (2013a). Age, distance, and geochemical evolution within a monogenetic volcanic field: Analyzing patterns in the Auckland Volcanic Field eruption sequence. *Geochemistry, Geophysics, Geosystems*, *14*(9), 3648-3665. https://doi.org/https://doi.org/10.1002/ggge.20223

Le Corvec, N., Spörli, K. B., Rowland, J., & Lindsay, J. (2013b). Spatial distribution and alignments of volcanic centers: Clues to the formation of monogenetic volcanic fields. *Earth-Science Reviews*, *124*, 96-114. https://doi.org/https://doi.org/10.1016/j.earscirev.2013.05.005

Leeman, W. P., Vitaliano, C. J., & Prinz, M. (1976). Evolved lavas from the Snake River Plain: Craters of the Moon National Monument, Idaho. *Contributions to Mineralogy and Petrology*, *56*(1), 35-60. https://doi.org/10.1007/BF00375420

Leng, C., Zhao, C., Cui, Q., Zhang, C., Sun, X., Yan, T., & Zhao, Y. (2021). Paleoclimatic changes recorded by n-alkanes from the lacustrine sediments of Arxan Crater Lake, in the central Great Khingan Mountains, Northeast China during the Holocene. *Quaternary Sciences*, *41*(4), 976-985.

Lesti, C., Giordano, G., Salvini, F., & Cas, R. (2008). Volcano tectonic setting of the intraplate, Pliocene-Holocene, Newer Volcanic Province (southeast Australia): Role of crustal fracture zones. *Journal of Geophysical Research: Solid Earth*, *113*(B7). https://doi.org/https://doi.org/10.1029/2007JB005110

Li, B., Németh, K., Palmer, J., Palmer, A., Wu, J., Procter, J., & Liu, J. (2020). Basic Volcanic Elements of the Arxan-Chaihe Volcanic Field, Inner Mongolia, NE China. In N. Károly (Ed.), *Updates in Volcanology* (pp. Ch. 10). IntechOpen. https://doi.org/10.5772/intechopen.94134

Li, F., & Guo, K. (1986). *Wudalianchi Volcanoes*. Geology Publishing House.

Li, J. Y. (2006). Permian geodynamic setting of Northeast China and adjacent regions: closure of the Paleo-Asian Ocean and subduction of the Paleo-Pacific Plate. *Journal of Asian Earth Sciences*, *26*(3), 207-224. https://doi.org/https://doi.org/10.1016/j.jseaes.2005.09.001

Li, Z.-Q., Chen, J.-L., Zou, H., Wang, C.-S., Meng, Q.-A., Liu, H.-L., & Wang, S.-Z. (2021). Mesozoic–Cenozoic tectonic evolution and dynamics of the Songliao Basin, NE Asia: Implications for the closure of the Paleo-Asian Ocean and Mongol-Okhotsk Ocean and subduction of the Paleo-Pacific Ocean. *Earth-Science Reviews*, *218*, 103471. https://doi.org/https://doi.org/10.1016/j.earscirev.2020.103471

Li, Z.-Z., Qin, K.-Z., Li, G.-M., Jin, L.-Y., & Song, G.-X. (2018). Neoproterozoic and Early Paleozoic magmatic records from the Chalukou ore district, northern Great Xing'an Range, NE China: Implications for tectonic evolution and Mesozoic Mo mineralization. *Journal of Asian Earth Sciences*, *165*, 96-113. https://doi.org/https://doi.org/10.1016/j.jseaes.2018.06.020

Lin, Q., Ge, W., Sun, D., Wu, F., Chong, K. W., Kyung, D. M., Myung, S. J., Moon, W., Chi, S. K., & Sung, H. Y. (1998). Tectonic significance of Mesozoic volcanic rocks in northeastern China. *Scientia Geologica Sinica*, *33*(2), 129-139.

Lin, W., & Wang, Q. (2006). Late Mesozoic extensional tectonics in the North China block: a crustal response to subcontinental mantle removal? *Bulletin de la Société Géologique de France*, *177*(6), 287-297. https://doi.org/10.2113/gssgfbull.177.6.287

Liu, J.-Q., Chen, L.-H., Wang, X.-J., Zhong, Y., Yu, X., Zeng, G., & Erdmann, S. (2017). The role of melt-rock interaction in the formation of Quaternary high-MgO potassic basalt from the Greater Khingan Range, northeast China. *Journal of Geophysical Research: Solid Earth*, *122*(1), 262-280. https://doi.org/https://doi.org/10.1002/2016JB013605

Liu, J.-Q., Erdmann, S., Chen, L.-H., Zhang, H.-L., Wu, B., Zeng, G., Wang, X.-J., Lei, Z.-L., & Yu, X. (2021). Petrological evidence for magma recharge and mixing beneath the Ma'anshan monogenetic volcano of Xiaogulihe in Northeast China. *Lithos*, *382-383*, 105928. https://doi.org/https://doi.org/10.1016/j.lithos.2020.105928

Liu, J. (1987). Study on geochronology of the Cenozoic volcanic rocks in Northeast China. *Acta Petrologica Sinica*, *4*, 21-31.

Liu, J. (1988). The Cenozoic volcanic episodes in northeast China. *Acta Petrologica Sinica*(1), 1-10.

Liu, J. (1989). On the origin and evolution of continental rift system in Northeast China. *Chinese Journal of Geology*, *3*, 209-319.

Liu, J. (1993). The northeast China rift system and opening of the Japan sea: a volcano-chronological review. *Sci. Geol. Sinica*, *2*(2), 157-162.

Liu, J. (1999). Volcanoes in China. In: Beijing: Science Press.

Liu, J., Chu, G., Han, J., Rioual, P., Jiao, W., & Wang, K. (2009). Volcanic eruptions in the Longgang volcanic field, northeastern China, during the past 15,000 years. *Journal of Asian Earth Sciences*, *34*(5), 645-654. https://doi.org/https://doi.org/10.1016/j.jseaes.2008.09.005

Liu, J., Han, J., & Fyfe, W. S. (2001). Cenozoic episodic volcanism and continental rifting in northeast China and possible link to Japan Sea development as revealed from K–Ar geochronology. *Tectonophysics*, *339*(3-4), 385-401.

Liu, J., Negendank, J. F. W., Wang, W., Chu, G., Mingram, J., Guo, Z., Luo, X., Chen, R., & Liu, T. (2000). The distribution and geological characteristics of maar lakes in China. *Quaternary Sciences*(01), 78-86.

Liu, M., Cui, X., & Liu, F. (2004). Cenozoic rifting and volcanism in eastern China: a mantle dynamic link to the Indo–Asian collision? *Tectonophysics*, *393*(1-4), 29-42. https://doi.org/10.1016/j.tecto.2004.07.029

Liu, R.-x. (2000). Active volcanoes in China. *Geological Review*, *45*, 1-15.

Liu, R., Fan, Q., Wei, H., & Li, N. (1999). Study on active volcanoes of China. *Geological Review*, *45*, 3-15. https://doi.org/10.16509/j.georeview.1999.s1.125

Liu, T., & Ding, Z. (1998). Chinese Loess and the Paleomonsoon. *Annual Review of Earth and Planetary Sciences*, *26*, 111. https://doi.org/10.1146/annurev.earth.26.1.111

Liu, W., Li, L., Chen, L., Wen, M., Wang, J., Yuan, L., Liu, Y., & Li, H. (2020). Testing a Comprehensive Volcanic Risk Assessment of Tenerife by Volcanic Hazard Simulations and Social Vulnerability Analysis. *ISPRS International Journal of Geo-Information*, *9*(4), 273. https://www.mdpi.com/2220-9964/9/4/273

Liu, Y., Jiang, S.-H., Bagas, L., Chen, C.-L., Han, N., & Wan, Y.-Y. (2019). Petrogenesis and metallogenic potential of the Wulanba granite, southern Great Xing'an Range, NE China: constraints from whole-rock and apatite geochemistry. *Geological Magazine*, *157*(3), 411-434. https://doi.org/10.1017/s0016756819000876

Lorenz, V. (1973). On the formation of maars [journal article]. *Bulletin Volcanologique*, *37*(2), 183-204. https://doi.org/10.1007/bf02597130

Lorenz, V. (1974). Vesiculated tuffs and associated features. *Sedimentology*, *21*(2), 273-291. https://doi.org/10.1111/j.1365-3091.1974.tb02059.x

Lorenz, V. (1975). Formation of phreatomagmatic maar-diatreme volcanoes and its relevance to kimberlite diatremes. *Physics and Chemistry of the Earth*, 17-27.
Lorenz, V. (1985). Maars and diatremes of phreatomagmatic origin; a review. *South African Journal of Geology*, *88*(2), 459-470. http://dx.doi.org/
Lorenz, V. (1986). On the growth of maars and diatremes and its relevance to the formation of tuff rings [journal article]. *Bulletin of Volcanology*, *48*(5), 265-274. https://doi.org/10.1007/bf01081755
Lorenz, V. (2003a). Maar-Diatreme Volcanoes, their Formation, and their Setting in Hard-rock or Soft-rock Environments. *GeoLines*, *15*, 72-83.
Lorenz, V. (2003b). Syn-and post-eruptive processes of maar–diatreme volcanoes and their relevance to the accumulation of post-eruptive maar–crater sediments. *Quaterly Journals of the Geological Survey of Hungary*, *40*, 13-22.
Lorenz, V. (2007). Syn- and posteruptive hazards of maar–diatreme volcanoes. *Journal of Volcanology and Geothermal Research*, *159*(1), 285-312. https://doi.org/10.1016/j.jvolgeores.2006.02.015
Lorenz, V., & Büchel, G. (1980). Zur Vulkanologie der Maare und Schlackenkegel der Westeifel. *Mitteilungen der Pollichia*, *68*, 29-100.
Lorenz, V., & Kurszlaukis, S. (2007). Root zone processes in the phreatomagmatic pipe emplacement model and consequences for the evolution of maar–diatreme volcanoes. *Journal of Volcanology and Geothermal Research*, *159*(1-3), 4-32. https://doi.org/10.1016/j.jvolgeores.2006.06.019
Lorenz, V., Mcbirney, A., & Williams, H. (1970). *An investigation of volcanic depressions. Part 3: Maars, tuff-rings, tuff-cones, and diatremes*. U. States.
Lorenzo-Merino, A., Guilbaud, M. N., & Roberge, J. (2018). The violent Strombolian eruption of 10 ka Pelado shield volcano, Sierra Chichinautzin, Central Mexico. *Bulletin of Volcanology*, *80*(3), 27. https://doi.org/10.1007/s00445-018-1208-2
Lu, J., Yao, Y., Zhu, Z., Sun, C., Wu, J., & Liu, J. (2021). Relationship between brGDGTs-based temperatures and volcanism record in the recent 300 years in Arxan region. *Quaternary Sciences*, *41*(1), 88-98.
Luo, W., & Liu, C.-C. (2018). Innovative landslide susceptibility mapping supported by geomorphon and geographical detector methods. *Landslides*, *15*(3), 465-474. https://doi.org/10.1007/s10346-017-0893-9
Luo, X., & Chen, Q. (1990). Preliminary study on geochronology for Cenozoic basalts from Inner Mongolia. *Acta Petrologica et Mineralogica*, *9*(1), 37-46.
Macdonald, G. A. (1943). The 1942 eruption of Mauna Loa, Hawaii. *American journal of science*, *241*(4), 241-256. https://doi.org/10.2475/ajs.241.4.241
Macdonald, G. A. (1953). Pahoehoe, aa, and block lava. *American journal of science*, *251*(3), 169-191. https://doi.org/10.2475/ajs.251.3.169
Macdonald, G. A. (1972). Composite Lava Flows on Haleakala Volcano, Hawaii. *GSA Bulletin*, *83*(10), 2971-2974. https://doi.org/10.1130/0016-7606(1972)83[2971:Clfohv]2.0.Co;2
Machida, S., Kogiso, T., & Hirano, N. (2017). Petit-spot as definitive evidence for partial melting in the asthenosphere caused by CO2. *Nature Communications*, *8*(1), 14302. https://doi.org/10.1038/ncomms14302
Maitre, R. W. L., Streckeisen, A., Zanettin, B., Bas, M. J. L., Bonin, B., Bateman, P., Bellieni, G., Dudek, A., Efremova, S., Keller, J., Lameyre, J., Sabine, P. A., Schmid, R., Sorensen, H., & Woolley, A. R. (1989). A classification of igneous rocks and glossary of terms. *Recommendations of the international union of geological sciences subcommission on the systematics of igneous rocks*, *193*. https://ci.nii.ac.jp/naid/10008204412/en/

Martí, J., Groppelli, G., & Brum da Silveira, A. (2018). Volcanic stratigraphy: A review. *Journal of Volcanology and Geothermal Research*, *357*, 68-91. https://doi.org/https://doi.org/10.1016/j.jvolgeores.2018.04.006

Martí, J., Planagumà, L., Geyer, A., Canal, E., & Pedrazzi, D. (2011). Complex interaction between Strombolian and phreatomagmatic eruptions in the Quaternary monogenetic volcanism of the Catalan Volcanic Zone (NE of Spain). *Journal of Volcanology and Geothermal Research*, *201*(1), 178-193. https://doi.org/10.1016/j.jvolgeores.2010.12.009

Martin, U., & Nemeth, K. (2005). Eruptive and depositional history of a Pliocene tuff ring that developed in a fluvio-lacustrine basin: Kissomlyo´ volcano (western Hungary). *Journal of Volcanology and Geothermal Research*, *147*(3-4), 342-356. https://doi.org/10.1016/j.jvolgeores.2005.04.019

Martin, U., & Németh, K. (2004). Mio/Pliocene phreatomagmatic volcanism in the western Pannonian Basin. *GEOLOGICA HUNGARICA*, *26*, 1-191.

Mattox, T. N., & Mangan, M. T. (1997). Littoral hydrovolcanic explosions: a case study of lava–seawater interaction at Kilauea Volcano. *Journal of Volcanology and Geothermal Research*, *75*(1), 1-17. https://doi.org/10.1016/S0377-0273(96)00048-0

Mazzarini, F., & Isola, I. (2010). Monogenetic vent self-similar clustering in extending continental crust: Examples from the East African Rift System. *Geosphere*, *6*(5), 567-582. https://doi.org/10.1130/ges00569.1

Mazzarini, F., Le Corvec, N., Isola, I., & Favalli, M. (2016). Volcanic field elongation, vent distribution, and tectonic evolution of a continental rift: The Main Ethiopian Rift example. *Geosphere*, *12*(3), 706-720. https://doi.org/10.1130/ges01193.1

McClave, J. T., & Sincich, T. T. (2017). *First Course in Statistics* (12 ed.).

McDonough, W. F., Sun, S. S., Ringwood, A. E., Jagoutz, E., & Hofmann, A. W. (1992). Potassium, rubidium, and cesium in the Earth and Moon and the evolution of the mantle of the Earth. *Geochimica et Cosmochimica Acta*, *56*(3), 1001-1012. https://doi.org/https://doi.org/10.1016/0016-7037(92)90043-I

McGee, L. E., McLeod, C., & Davidson, J. P. (2015). A spectrum of disequilibrium melting preserved in lava-hosted, partially melted crustal xenoliths from the Wudalianchi volcanic field, NE China. *Chemical Geology*, *417*, 184-199. https://doi.org/10.1016/j.chemgeo.2015.09.023

McGee, L. E., Smith, I. E. M., Millet, M.-A., Handley, H. K., & Lindsay, J. M. (2013). Asthenospheric Control of Melting Processes in a Monogenetic Basaltic System: a Case Study of the Auckland Volcanic Field, New Zealand. *Journal of Petrology*, *54*(10), 2125-2153. https://doi.org/10.1093/petrology/egt043

Meng, F.-c., Safonova, I., Chen, S.-s., & Rioual, P. (2018). Late Cenozoic intra-plate basalts of the Greater Khingan Range in NE China and Khangai Province in Central Mongolia. *Gondwana Research*, *63*, 65-84. https://doi.org/https://doi.org/10.1016/j.gr.2018.05.009

Molnar, P., & Atwater, T. (1973). Relative Motion of Hot Spots in the Mantle. *NATURE*, *246*(5431), 288-291. https://doi.org/10.1038/246288a0

Molnar, P., & Francheteau, J. (1975). The Relative Motion of 'Hot Spots' in the Atlantic and Indian Oceans During the Cenozoic*. *Geophysical Journal International*, *43*(3), 763-774. https://doi.org/10.1111/j.1365-246X.1975.tb06194.x

Mossoux, S., Saey, M., Bartolini, S., Poppe, S., Canters, F., & Kervyn, M. (2016). Q-LAVHA: A flexible GIS plugin to simulate lava flows. *Computers & Geosciences*, *97*, 98-109. https://doi.org/https://doi.org/10.1016/j.cageo.2016.09.003

Mueller, S., Scheu, B., Kueppers, U., Spieler, O., Richard, D., & Dingwell, D. B. (2011). The porosity of pyroclasts as an indicator of volcanic explosivity. *Journal of Volcanology*

and Geothermal Research, *203*(3), 168-174. https://doi.org/https://doi.org/10.1016/j.jvolgeores.2011.04.006

Murcia, H., & Németh, K. (2020). Effusive monogenetic volcanism. In *Updates in Volcanology-Transdisciplinary Nature of Volcano Science*. IntechOpen. https://doi.org/10.5772/intechopen.94387

Murcia, H., Németh, K., El-Masry, N. N., Lindsay, J. M., Moufti, M. R. H., Wameyo, P., Cronin, S. J., Smith, I. E. M., & Kereszturi, G. (2015). The Al-Du'aythah volcanic cones, Al-Madinah City: implications for volcanic hazards in northern Harrat Rahat, Kingdom of Saudi Arabia [journal article]. *Bulletin of Volcanology*, *77*(6), 54. https://doi.org/10.1007/s00445-015-0936-9

Murcia, H., Németh, K., Moufti, M. R., Lindsay, J. M., El-Masry, N., Cronin, S. J., Qaddah, A., & Smith, I. E. M. (2014). Late Holocene lava flow morphotypes of northern Harrat Rahat, Kingdom of Saudi Arabia: Implications for the description of continental lava fields. *Journal of Asian Earth Sciences*, *84*, 131-145. https://doi.org/10.1016/j.jseaes.2013.10.002

Murtagh, R. M., & White, J. D. L. (2013). Pyroclast characteristics of a subaqueous to emergent Surtseyan eruption, Black Point volcano, California. *Journal of Volcanology and Geothermal Research*, *267*, 75-91. https://doi.org/10.1016/j.jvolgeores.2013.08.015

Nakamura, K. (1977). Volcanoes as possible indicators of tectonic stress orientation — principle and proposal. *Journal of Volcanology and Geothermal Research*, *2*(1), 1-16. https://doi.org/https://doi.org/10.1016/0377-0273(77)90012-9

Nelson, J. R. (2000). Physics of Impregnation. *Microscopy Today*, *8*(1), 24-24. https://doi.org/10.1017/S1551929500057114

Nemeth, K. (2001). Long-term erosion-rate calculation from the Waipiata Volcanic Field (New Zealand) based on erosion remnants of scoria cones, tuff rings and maars / Calcul de la vitesse d'érosion à long terme dans la zone volcanique de Waipiata (Nouvelle-Zélande) fondé sur les formes résiduelles de cônes de scories, d'anneaux de tuf et de maars. *Geomorphologie-relief Processus Environnement - GEOMORPHOLOGIE*, *7*, 137-152. https://doi.org/10.3406/morfo.2001.1097

Németh, K. (2010a). Volcanic glass textures, shape characteristics and compositions of phreatomagmatic rock units from the Western Hungarian monogenetic volcanic fields and their implications for magma fragmentation. *Open Geosciences*, *2*(3). https://doi.org/10.2478/v10085-010-0015-6

Németh, K. (2010b). Monogenetic volcanic fields: Origin, sedimentary record, and relationship with polygenetic volcanism. *What Is a Volcano?*, 43-66. https://doi.org/10.1130/2010.2470(04) (Geological Society of America Special Papers)

Németh, K. (2012). An Overview of the Monogenetic Volcanic Fields of the Western Pannonian Basin: Their Field Characteristics and Outlook for Future Research from a Global Perspective. *Updates in Volcanology-A Comprehensive Approach to Volcanological Problems*.

Németh, K. (2016). Introductory Chapter: Updates in Volcanology – From Volcano Modeling to Volcano Geology. In N. Karoly (Ed.), *Updates in Volcanology* (pp. Ch. 1). IntechOpen. https://doi.org/10.5772/64734

Németh, K., Casadevall, T., Moufti, M. R., & Marti, J. (2017b). Volcanic Geoheritage. *Geoheritage*, *9*(3), 251-254. https://doi.org/10.1007/s12371-017-0257-9

Németh, K., & Cronin, S. J. (2011). Drivers of explosivity and elevated hazard in basaltic fissure eruptions: The 1913 eruption of Ambrym Volcano, Vanuatu (SW-Pacific). *Journal of Volcanology and Geothermal Research*, *201*(1), 194-209. https://doi.org/10.1016/j.jvolgeores.2010.12.007

Németh, K., Cronin, S. J., Smith, I. E. M., & Agustin Flores, J. (2012). Amplified hazard of small-volume monogenetic eruptions due to environmental controls, Orakei Basin,

Auckland Volcanic Field, New Zealand. *Bulletin of Volcanology*, *74*(9), 2121-2137. https://doi.org/10.1007/s00445-012-0653-6

Németh, K., Goth, K., Martin, U., Csillag, G., & Suhr, P. (2008). Reconstructing paleoenvironment, eruption mechanism and paleomorphology of the Pliocene Pula maar, (Hungary). *Journal of Volcanology and Geothermal Research*, *177*(2), 441-456. https://doi.org/10.1016/j.jvolgeores.2008.06.010

Nemeth, K., & Kereszturi, G. (2013). *On the variety of Mio-Pleistocene root zones of monogenetic volcanoes of the Pannonian Basin*.

Németh, K., & Kereszturi, G. (2015). Monogenetic volcanism: personal views and discussion. *International Journal of Earth Sciences*, *104*(8), 2131-2146. https://doi.org/10.1007/s00531-015-1243-6

Németh, K., & Kósik, S. (2020). Review of Explosive Hydrovolcanism. *Geosciences*, *10*(2), 44. https://www.mdpi.com/2076-3263/10/2/44

Németh, K., Manville, V., & Kano, K. (2009). Source to sink — Volcaniclastic sedimentation in and around the Pacific. *Sedimentary Geology*, *220*(3), 135. https://doi.org/10.1016/j.sedgeo.2009.04.012

Németh, K., & Martin, U. (1999). Late Miocene paleo-geomorphology of the Bakony-Balaton Highland Volcanic Field (Hungary) using physical volcanology data. *Zeitschrift fur Geomorphologie*, *43*(4), 417-438. http://hdl.handle.net/10179/9631

Németh, K., Martin, U., & Csillag, G. (2003a). Calculation of erosion rates based on remnants of monogenetic alkaline basaltic volcanoes in the Bakony–Balaton Highland Volcanic Field (Western Hungary) of Mio/Pliocene age. *Pliocene age, Geolines*, *15*, 93-97.

Németh, K., & Moufti, M. R. (2017). Geoheritage Values of a Mature Monogenetic Volcanic Field in Intra-continental Settings: Harrat Khaybar, Kingdom of Saudi Arabia. *Geoheritage*, *9*(3), 311-328. https://doi.org/10.1007/s12371-017-0243-2

Németh, K., & Moufti, M. R. (2023). Lava Flow Hazard and Its Implication in Geopark Development for the Active Harrat Khaybar Intracontinental Monogenetic Volcanic Field, Saudi Arabia. *Land*, *12*(3), 705. https://www.mdpi.com/2073-445X/12/3/705

Németh, K., Risso, C., Nullo, F., & Kereszturi, G. (2011). The role of collapsing and cone rafting on eruption style changes and final cone morphology: Los Morados scoria cone, Mendoza, Argentina. *Central European Journal of Geosciences*, *3*(2), 102-118. https://doi.org/10.2478/s13533-011-0008-4

Németh, K., & White, C. M. (2009). Intra-vent peperites related to the phreatomagmatic 71 Gulch Volcano, western Snake River Plain volcanic field, Idaho (USA). *Journal of Volcanology and Geothermal Research*, *183*(1), 30-41. https://doi.org/https://doi.org/10.1016/j.jvolgeores.2009.02.020

Németh, K., & White, J. D. L. (2009). Miocene phreatomagmatic monogenetic volcanism of the Waipiata Volcanic Field, Otago, New Zealand: Field Guide. Oamaru Conference, 2009, Oamaru, New Zealand.

Nemeth, K., White, J. D. L., Reay, A., & Martin, U. (2003b). Compositional variation during monogenetic volcano growth and its implications for magma supply to continental volcanic fields. *Journal of the Geological Society*, *160*(4), 523–530.

Németh, K., Wu, J., Sun, C., & Liu, J. (2017a). Update on the Volcanic Geoheritage Values of the Pliocene to Quaternary Arxan–Chaihe Volcanic Field, Inner Mongolia, China. *Geoheritage*, *9*(3), 279-297. https://doi.org/10.1007/s12371-017-0224-5

Ngwa, C. N., Suh, C. E., & Devey, C. W. (2010). Phreatomagmatic deposits and stratigraphic reconstruction at Debunscha Maar (Mt Cameroon volcano). *Journal of Volcanology and Geothermal Research*, *192*(3), 201-211. https://doi.org/10.1016/j.jvolgeores.2010.02.012

Nieto-Torres, A., & Martin Del Pozzo, A. L. (2019). Spatio-temporal hazard assessment of a monogenetic volcanic field, near México City. *Journal of Volcanology and Geothermal*

Research, *371*, 46-58. https://doi.org/https://doi.org/10.1016/j.jvolgeores.2019.01.006

Ollier, C. D. (1964). Tumuli and Lava Blisters of Victoria, Australia. *NATURE*, *202*(4939), 1284-1286. https://doi.org/10.1038/2021284a0

Ouyang, H., Mao, J., Zhou, Z., & Su, H. (2015). Late Mesozoic metallogeny and intracontinental magmatism, southern Great Xing'an Range, northeastern China. *Gondwana Research*, *27*(3), 1153-1172. https://doi.org/https://doi.org/10.1016/j.gr.2014.08.010

Palme, H., & O'Neill, H. S. C. (2003). Cosmochemical Estimates of Mantle Composition. *Treatise on Geochemistry*, *2*, 568. https://doi.org/10.1016/b0-08-043751-6/02177-0

Pan, B., de Silva, S. L., Xu, J., Chen, Z., Miggins, D. P., & Wei, H. (2017). The VEI-7 Millennium eruption, Changbaishan-Tianchi volcano, China/DPRK: New field, petrological, and chemical constraints on stratigraphy, volcanology, and magma dynamics. *Journal of Volcanology and Geothermal Research*, *343*, 45-59. https://doi.org/https://doi.org/10.1016/j.jvolgeores.2017.05.029

Pardo, N., Macias, J. L., Giordano, G., Cianfarra, P., Avellán, D. R., & Bellatreccia, F. (2009). The ~1245 yr BP Asososca maar eruption: The youngest event along the Nejapa–Miraflores volcanic fault, Western Managua, Nicaragua. *Journal of Volcanology and Geothermal Research*, *184*(3), 292–312. https://doi.org/10.1016/j.jvolgeores.2009.04.006

Patrick, M. R., Harris, A. J. L., Ripepe, M., Dehn, J., Rothery, D. A., & Calvari, S. (2007). Strombolian explosive styles and source conditions: insights from thermal (FLIR) video. *Bulletin of Volcanology*, *69*(7), 769-784. https://doi.org/10.1007/s00445-006-0107-0

Qiu, L., Yan, D.-P., Xu, H., Shi, H., Dong, W., & Sun, S. (2020). Late Cretaceous mud volcanism in the southwestern Songliao basin records slab rollback of the subducted paleo-Pacific Plate underneath NE China. *Journal of Asian Earth Sciences: X*, *3*, 100028. https://doi.org/https://doi.org/10.1016/j.jaesx.2020.100028

Ramos, F. C., Wolff, J. A., Buettner, J. E., Wei, H. Q., & Xu, J. (2019). Ra/Th ages of sanidine in young trachytes erupted at Changbaishan Volcano, China. *Journal of Volcanology and Geothermal Research*, *374*, 226-241. https://doi.org/https://doi.org/10.1016/j.jvolgeores.2019.02.006

Raue, H. (2004). A new model for the fracture energy budget of phreatomagmatic explosions. *Journal of Volcanology and Geothermal Research*, *129*(1), 99-108. https://doi.org/10.1016/S0377-0273(03)00234-8

Ren, J., Li, S., & Lin, C. (1997). Late Mesozoic intracontinental rifting and basin formation in eastern China. *Journal of China University of Geosciences*, *8*(1), 40-44.

Ren, J., Tamaki, K., Li, S., & Junxia, Z. (2002). Late Mesozoic and Cenozoic rifting and its dynamic setting in Eastern China and adjacent areas. *Tectonophysics*, *344*(3-4), 175–205.

Rittmann, A. (1962). *Volcanoes and their activity*.

Rodriguez-Gonzalez, A., Aulinas, M., Mossoux, S., Perez-Torrado, F. J., Fernandez-Turiel, J. L., Cabrera, M., & Prieto-Torrell, C. (2021). Comparison of real and simulated lava flows in the Holocene volcanism of Gran Canaria (Canary Islands, Spain) with Q-LavHA: contribution to volcanic hazard management. *Natural Hazards*, *107*(2), 1785-1819. https://doi.org/10.1007/s11069-021-04660-6

Rossi, M. J. (1997). Morphology of the 1984 open-channel lava flow at Krafla volcano, northern Iceland. *Geomorphology*, *20*(1), 95-112. https://doi.org/https://doi.org/10.1016/S0169-555X(97)00007-X

Rouquerol, J., Baron, G., Denoyel, R., Giesche, H., Groen, J., Klobes, P., Levitz, P., Neimark, A. V., Rigby, S., Skudas, R., Sing, K., Thommes, M., & Unger, K. (2011). Liquid intrusion and alternative methods for the characterization of macroporous materials (IUPAC

Technical Report). *Pure and Applied Chemistry*, *84*(1), 107-136. https://doi.org/doi:10.1351/PAC-REP-10-11-19

Rowland, S. K., Garbeil, H., & Harris, A. J. L. (2005). Lengths and hazards from channel-fed lava flows on Mauna Loa, Hawai'i, determined from thermal and downslope modeling with FLOWGO. *Bulletin of Volcanology*, *67*(7), 634-647. https://doi.org/10.1007/s00445-004-0399-x

Rowland, S. K., & Walker, G. P. L. (1990). Pahoehoe and aa in Hawaii: volumetric flow rate controls the lava structure. *Bulletin of Volcanology*, *52*(8), 615-628. https://doi.org/10.1007/BF00301212

Russell, J. K., Porritt, L. A., Lavallée, Y., & Dingwell, D. B. (2012). Kimberlite ascent by assimilation-fuelled buoyancy. *NATURE*, *481*(7381), 352-356. https://doi.org/10.1038/nature10740

Rutherford, M. J. (2008). Magma Ascent Rates. *Reviews in Mineralogy and Geochemistry*, *69*(1), 241-271. https://doi.org/10.2138/rmg.2008.69.7

Rutherford, M. J., & Hill, P. M. (1993). Magma ascent rates from amphibole breakdown: An experimental study applied to the 1980–1986 Mount St. Helens eruptions. *Journal of Geophysical Research: Solid Earth*, *98*(B11), 19667-19685. https://doi.org/https://doi.org/10.1029/93JB01613

Sato, H. (1995). Textural difference between pahoehoe and aa lavas of Izu-Oshima volcano, Japan — an experimental study on population density of plagioclase. *Journal of Volcanology and Geothermal Research*, *66*(1), 101-113. https://doi.org/https://doi.org/10.1016/0377-0273(94)00055-L

Schmincke, H.-U., Fisher, R. V., & Waters, A. C. (1973). Antidune and chute and pool structures in the base surge deposits of the Laacher See area, Germany. *Sedimentology*, *20*(4), 553-574. https://doi.org/10.1111/j.1365-3091.1973.tb01632.x

Schmincke, H. (1977). Eifel-Vulkanismus östlich des Gebietes Rieden-Mayen. *Fortschritte der Mineralogie*, *55*, 1-31.

Schumacher, R., & Schmincke, H.-U. (1991). Internal structure and occurrence of accretionary lapilli — a case study at Laacher See Volcano [journal article]. *Bulletin of Volcanology*, *53*(8), 612-634. https://doi.org/10.1007/bf00493689

Self, S., Keszthelyi, L., & Thordarson, T. (1998). The Importance Of Pāhoehoe. *Annual Review of Earth and Planetary Sciences*, *26*(1), 81-110. https://doi.org/10.1146/annurev.earth.26.1.81

Self, S., & Sparks, R. S. J. (1978). Characteristics of widespread pyroclastic deposits formed by the interaction of silicic magma and water [journal article]. *Bulletin Volcanologique*, *41*(3), 196. https://doi.org/10.1007/bf02597223

Şengör, A. M. C., Natal'in, B. A., & Burtman, V. S. (1993). Evolution of the Altaid tectonic collage and Palaeozoic crustal growth in Eurasia. *NATURE*, *364*, 299. https://doi.org/10.1038/364299a0

Sengor, A. M. C., & Natalin, B. (1996). Paleotectonics of Asia : fragments of a synthesis. *The Tectonic evolution of Asia*, 486-640. https://ci.nii.ac.jp/naid/10004123427/en/

Serrano, E., & Ruiz-Flaño, P. (2007). Geodiversity : a theoretical and applied concept. *Geogr. Helv.*, *62*(3), 140-147. https://doi.org/10.5194/gh-62-140-2007

Seward-Thompson, B. L., & Hails, J. R. (1973). An appraisal of the computation of statistical parameters in grain size analysis. *Sedimentology*, *20*(1), 161-169. https://doi.org/https://doi.org/10.1111/j.1365-3091.1973.tb01612.x

Shao, J., Zhang, L., & Mou, B. (1998). Thermo-tectonic evolution in middle and south part of Dahinggan. *Sci. China, Ser. D*, *28*, 194-200.

Shao, J., & Zhang, W. (2008). The evolving rift belt—Wudalianchi volcanic rock belt. *Earth Science Frontiers*, *15*(6), 241-250.

Sheridan, M. F., & Wohletz, K. H. (1981). Hydrovolcanic Explosions: The Systematics of Water-Pyroclast Equilibration. *Science*, *212*(4501), 1387-1389. https://doi.org/10.1126/science.212.4501.1387

Shervais, J., Shroff, G., Vetter, S., Matthews, S., Hanan, B., & McGee, J. (2002). Origin and Evolution of the Western Snake River Plain: Implications From Stratigraphy, Faulting, and the Geochemistry of Basalts Near Mountain Home, Idaho. *Idaho Geological Survey Bulletin*, *30*, 343-361.

Shervais, J. W., Kauffman, J. D., Gillerman, V. S., Othberg, K. L., Vetter, S. K., V., R. H., Zarnetske, M., Cooke, M. F., Matthews, S. H., Hanan, B. B., & Dehler, C. M. (2005). Basaltic volcanism of the central and western Snake River Plain:A guide to field relations between Twin Falls and Mountain Home, Idaho. In *Interior Western United States* (pp. 0). Geological Society of America. https://doi.org/10.1130/2005.fld006(02)

Sheth, H. (2018). Morphology and Architecture of Flood Basalt Lava Flows and Sequences. In *A Photographic Atlas of Flood Basalt Volcanism* (pp. 33-79). Springer International Publishing. https://doi.org/10.1007/978-3-319-67705-7_3

Siebert, L. (2008). Volcanoes of the world : an illustrated catalog of Holocene volcanoes and their eruptions. *http://www.volcano.si.edu/world/*. https://cir.nii.ac.jp/crid/1570572700935995136

Smith, I. E. M., Blake, S., Wilson, C. J. N., & Houghton, B. F. (2008). Deep-seated fractionation during the rise of a small-volume basalt magma batch: Crater Hill, Auckland, New Zealand. *Contributions to Mineralogy and Petrology*, *155*(4), 511-527. https://doi.org/10.1007/s00410-007-0255-z

Smith, I. E. M., Brenna, M., & Cronin, S. J. (2021). The magma source of small-scale intraplate monogenetic volcanic systems in northern New Zealand. *Journal of Volcanology and Geothermal Research*, 107326. https://doi.org/https://doi.org/10.1016/j.jvolgeores.2021.107326

Smith, I. E. M., & Németh, K. (2017). Source to surface model of monogenetic volcanism: a critical review. *Geological Society, London, Special Publications*, *446*(1), 1-28. https://doi.org/10.1144/sp446.14

Sohn, C., & Sohn, Y. K. (2019a). Distinguishing between primary and secondary volcaniclastic deposits. *Scientific Reports*, *9*(1), 12425. https://doi.org/10.1038/s41598-019-48933-4

Sohn, C., & Sohn, Y. K. (2019b). Volcaniclastic tide-modulated tempestite in a coastal tuff ring, Jeju Island, Korea. *Scientific Reports*, *9*(1), 3561. https://doi.org/10.1038/s41598-019-39784-0

Sohn, Y. K. (1996). Hydrovolcanic processes forming basaltic tuff rings and cones on Cheju Island, Korea. *GSA Bulletin*, *108*(10), 1199-1211. https://doi.org/10.1130/0016-7606(1996)108<1199:HPFBTR>2.3.CO;2

Sohn, Y. K., & Park, K. H. (2005). Composite tuff ring/cone complexes in Jeju Island, Korea: possible consequences of substrate collapse and vent migration. *Journal of Volcanology and Geothermal Research*, *141*(1-2), 157-175. https://doi.org/10.1016/j.jvolgeores.2004.10.003

Sottili, G., Palladino, D. M., Gaeta, M., & Masotta, M. (2012). Origins and energetics of maar volcanoes: examples from the ultrapotassic Sabatini Volcanic District (Roman Province, Central Italy) [journal article]. *Bulletin of Volcanology*, *74*(1), 163-186. https://doi.org/10.1007/s00445-011-0506-8

Stephenson, P. J., Burch-Johnston, A. T., Stanton, D., & Whitehead, P. W. (1998). Three long lava flows in north Queensland. *Journal of Geophysical Research: Solid Earth*, *103*(B11), 27359-27370. https://doi.org/https://doi.org/10.1029/98JB01670

Strahler, A. (1952). Hypsometric (area altitude) analysis of erosional topology. *Geol Soc Am Bull*, *63*, 1117-1142.

Strahler, A. N. (1957). Quantitative analysis of watershed geomorphology. *Eos, Transactions American Geophysical Union*, *38*(6), 913-920. https://doi.org/https://doi.org/10.1029/TR038i006p00913

Straub, S. M., LaGatta, A. B., Martin-Del Pozzo, A. L., & Langmuir, C. H. (2008). Evidence from high-Ni olivines for a hybridized peridotite/pyroxenite source for orogenic andesites from the central Mexican Volcanic Belt. *Geochemistry, Geophysics, Geosystems*, *9*(3). https://doi.org/10.1029/2007gc001583

Sui, J., Fan, Q., & Cao, J. (1999). A preliminary study of eruption features and petrochemistry of volcanic rocks from the Longgang volcanoes. *Geological Review*, *45*, 319-324.

Sulpizio, R., Bonasia, R., Dellino, P., Di Vito, M. A., La Volpe, L., Mele, D., Zanchetta, G., & Sadori, L. (2008). Discriminating the long distance dispersal of fine ash from sustained columns or near ground ash clouds: The example of the Pomici di Avellino eruption (Somma-Vesuvius, Italy). *Journal of Volcanology and Geothermal Research*, *177*(1), 263-276. https://doi.org/10.1016/j.jvolgeores.2007.11.012

Sulpizio, R., & Dellino, P. (2008). Chapter 2 Sedimentology, Depositional Mechanisms and Pulsating Behaviour of Pyroclastic Density Currents. In J. Gottsmann, Mart, iacute, & Joan (Eds.), *Developments in Volcanology* (Vol. 10, pp. 57-96). Elsevier. https://doi.org/10.1016/S1871-644X(07)00002-2

Sun, C., Liu, Q., Wu, J., Németh, K., Wang, L., Zhao, Y., Chu, G., & Liu, J. (2016). The first tephra evidence for a Late Glacial explosive volcanic eruption in the Arxan-Chaihe volcanic field (ACVF), northeast China. *Quaternary Geochronology*, *40*, 109-119. https://doi.org/10.1016/j.quageo.2016.10.003

Sun, C., Liu, Q., Wu, J., Németh, K., Wang, L., Zhao, Y., Chu, G., & Liu, J. (2017). The first tephra evidence for a Late Glacial explosive volcanic eruption in the Arxan-Chaihe volcanic field (ACVF), northeast China. *Quaternary Geochronology*, *40*, 109-119. https://doi.org/https://doi.org/10.1016/j.quageo.2016.10.003

Sun, C., Németh, K., Zhan, T., You, H., Chu, G., & Liu, J. (2018). Tephra evidence for the most recent eruption of Laoheishan volcano, Wudalianchi volcanic field, northeast China. *Journal of Volcanology and Geothermal Research*. https://doi.org/10.1016/j.jvolgeores.2018.03.014

Sun, W., Chi, X.-G., Zhao, Z., Pan, S.-Y., Liu, J.-F., Zhang, R., & Quan, J.-Y. (2014). Zircon geochronology constraints on the age and nature of 'Precambrian metamorphic rocks' in the Xing'an block of Northeast China. *International Geology Review*, *56*(6), 672-694. https://doi.org/10.1080/00206814.2014.883183

Swift, T. P., & Kennedy, L. M. (2021). Beaver-Driven Peatland Ecotone Dynamics: Impoundment Detection Using Lidar and Geomorphon Analysis. *Land*, *10*(12), 1333. https://www.mdpi.com/2073-445X/10/12/1333

Takada, A. (1994). The influence of regional stress and magmatic input on styles of monogenetic and polygenetic volcanism. *Journal of Geophysical Research: Solid Earth*, *99*(B7), 13563-13573.

Tang, J., Wang, J., Chen, X., Zhao, G., & Zhan, Y. (2005). A Preliminary Investigation on Electric Structure of the Crust and Upper Mantle in Arxan Volcanic Area. *CHINESE JOURNAL OF GEOPHYSICS*, *48*(1), 214-221.

Tang, J., Xu, W.-L., Wang, F., Wang, W., Xu, M.-J., & Zhang, Y.-H. (2014). Geochronology and geochemistry of Early–Middle Triassic magmatism in the Erguna Massif, NE China: Constraints on the tectonic evolution of the Mongol–Okhotsk Ocean. *Lithos*, *184-187*, 1-16. https://doi.org/https://doi.org/10.1016/j.lithos.2013.10.024

Taran, Y. A. (2009). Geochemistry of volcanic and hydrothermal fluids and volatile budget of the Kamchatka–Kuril subduction zone. *Geochimica et Cosmochimica Acta*, *73*(4), 1067-1094. https://doi.org/https://doi.org/10.1016/j.gca.2008.11.020

Thorarinsson, S. (1953). The crater groups in Iceland [journal article]. *Bulletin Volcanologique*, *14*(1), 3-44. https://doi.org/10.1007/bf02596003

Thordarson, T., Miller, D. J., Larsen, G., Self, S., & Sigurdsson, H. (2001). New estimates of sulfur degassing and atmospheric mass-loading by the 934 AD Eldgjá eruption, Iceland. *Journal of Volcanology and Geothermal Research*, *108*(1), 33-54. https://doi.org/https://doi.org/10.1016/S0377-0273(00)00277-8

Thordarson, T., & Self, S. (1993). The Laki (Skaftár Fires) and Grímsvötn eruptions in 1783–1785 [journal article]. *Bulletin of Volcanology*, *55*(4), 233-263. https://doi.org/10.1007/bf00624353

Thordarson, T., & Self, S. (2003). Atmospheric and environmental effects of the 1783–1784 Laki eruption: A review and reassessment. *Journal of Geophysical Research: Atmospheres*, *108*(D1), AAC 7-1-AAC 7-29. https://doi.org/10.1029/2001jd002042

Trusdell, F. A. (1995). Lava Flow Hazards and Risk Assessment on Mauna Loa Volcano, Hawaii. In *Mauna Loa Revealed: Structure, Composition, History, and Hazards* (pp. 327-336). https://doi.org/https://doi.org/10.1029/GM092p0327

Turcotte, D. L., Oxburgh, E. R., Thompson, R. N., Brown, G. M., apos, Hara, M. J., & Oxburgh, E. R. (1978). Intra-plate volcanism. *Philosophical Transactions of the Royal Society of London. Series A, Mathematical and Physical Sciences*, *288*(1355), 561-579. https://doi.org/doi:10.1098/rsta.1978.0034

Uchman, A., Johnson, M. E., Ramalho, R. S., Quartau, R., Berning, B., Hipólito, A., Melo, C. S., Rebelo, A. C., Cordeiro, R., & Ávila, S. P. (2020). Neogene marine sediments and biota encapsulated between lava flows on Santa Maria Island (Azores, north-east Atlantic): An interplay between sedimentary, erosional and volcanic processes. *Sedimentology*, *67*(7), 3595-3618. https://doi.org/https://doi.org/10.1111/sed.12763

Uslular, G., Le Corvec, N., Mazzarini, F., Legrand, D., & Gençalioğlu-Kuşcu, G. (2021). Morphological and multivariate statistical analysis of quaternary monogenetic vents in the Central Anatolian Volcanic Province (Turkey): Implications for the volcano-tectonic evolution. *Journal of Volcanology and Geothermal Research*, *416*, 107280. https://doi.org/https://doi.org/10.1016/j.jvolgeores.2021.107280

Valentine, G. A., & Gregg, T. K. P. (2008). Continental basaltic volcanoes — Processes and problems. *Journal of Volcanology and Geothermal Research*, *177*(4), 857-873. https://doi.org/10.1016/j.jvolgeores.2008.01.050

Valentine, G. A., & van Wyk de Vries, B. (2014). Unconventional maar diatreme and associated intrusions in the soft sediment-hosted Mardoux structure (Gergovie, France). *Bulletin of Volcanology*, *76*(3). https://doi.org/10.1007/s00445-014-0807-9

Valentine, G. A., & White, J. D. L. (2012). Revised conceptual model for maar-diatremes: Subsurface processes, energetics, and eruptive products. *Geology*, *40*(12), 1111-1114. https://doi.org/10.1130/g33411.1

Van Otterloo, J., Raveggi, M., Cas, R. A. F., & Maas, R. (2014). Polymagmatic Activity at the Monogenetic Mt Gambier Volcanic Complex in the Newer Volcanics Province, SE Australia: New Insights into the Occurrence of Intraplate Volcanic Activity in Australia. *Journal of Petrology*, *55*(7), 1317-1351. https://doi.org/10.1093/petrology/egu026

Vazquez, J. A., & Ort, M. H. (2006). Facies variation of eruption units produced by the passage of single pyroclastic surge currents, Hopi Buttes volcanic field, USA. *Journal of Volcanology and Geothermal Research*, *154*(3-4), 222-236. https://doi.org/10.1016/j.jvolgeores.2006.01.003

Viard, J. P., & Breyer, J. A. (1979). Description and hydraulic interpretation of grain size cumulative curves from the Platte River system. *Sedimentology*, *26*(3), 427-439. https://doi.org/https://doi.org/10.1111/j.1365-3091.1979.tb00918.x

Vilches, M., Ureta, G., Grosse, P., Németh, K., Aguilera, F., & Aguilera, M. (2022). Effusion rate estimation based on solidified lava flows: Implications for volcanic hazard assessment

in the Negros de Aras monogenetic volcanic field, northern Chile. *Journal of Volcanology and Geothermal Research*, *422*, 107454. https://doi.org/https://doi.org/10.1016/j.jvolgeores.2021.107454

Visher, G. S. (1969). Grain size distributions and depositional processes. *Journal of Sedimentary Petrology*, *39*, 1074-1106. https://doi.org/10.1306/74D71D9D-2B21-11D7-8648000102C1865D

Vogel, D. C., & Keays, R. R. (1997). The petrogenesis and platinum-group element geochemistry of the Newer Volcanic Province, Victoria, Australia. *Chemical Geology*, *136*(3), 181-204. https://doi.org/https://doi.org/10.1016/S0009-2541(96)00142-8

Wan, L., Lu, C., Zeng, Z., Mohammed, A. S., Liu, Z., Dai, Q., & Chen, K. (2019). Nature and significance of the late Mesozoic granitoids in the southern Great Xing'an range, eastern Central Asian Orogenic Belt. *International Geology Review*, *61*(5), 584-606. https://doi.org/10.1080/00206814.2018.1440645

Wang, F., Zhou, X.-H., Zhang, L.-C., Ying, J.-F., Zhang, Y.-T., Wu, F.-Y., & Zhu, R.-X. (2006). Late Mesozoic volcanism in the Great Xing'an Range (NE China): Timing and implications for the dynamic setting of NE Asia. *Earth and Planetary Science Letters*, *251*(1-2), 179-198. https://doi.org/10.1016/j.epsl.2006.09.007

Wang, H., Fan, T., & Wu, Y. (2015). The subsurface structure and stratigraphic architecture of rift-related units in the Lishu Depression of the Songliao Basin, China. *Journal of Asian Earth Sciences*, *99*, 13-29. https://doi.org/https://doi.org/10.1016/j.jseaes.2014.11.026

Wang, L., & Tian, M. (2013). Tourism resources types and development of Zalantun Geopark in Inner Mongolia [J]. *Journal of Arid Land Resources and Environment*, *10*.

Wang, L., Tian, M., & Bai, Z. (2013). Volcanic geological relics and their features in Arshan-Chaihe area in Inner Mongolia. *Resources & Industries*, *15*(01), 89-95. https://doi.org/10.13776/j.cnki.resourcesindustries.2013.01.002

Wang, L., Tian, M., Wen, X., Zhao, L., Song, J., Sun, M., Wang, H., Lan, Y., & Sun, M. (2014). Geoconservation and geotourism in Arxan-Chaihe Volcano Area, Inner Mongolia, China. *Quaternary International*, *349*, 384-391. https://doi.org/10.1016/j.quaint.2014.06.024

Wang, P.-J., Mattern, F., Didenko, N. A., Zhu, D.-F., Singer, B., & Sun, X.-M. (2016). Tectonics and cycle system of the Cretaceous Songliao Basin: An inverted active continental margin basin. *Earth-Science Reviews*, *159*, 82-102. https://doi.org/https://doi.org/10.1016/j.earscirev.2016.05.004

Wang, P., Liu, W., Wang, S., & Song, W. (2002). 40Ar/39Ar and K/Ar dating on the volcanic rocks in the Songliao basin, NE China: constraints on stratigraphy and basin dynamics. *International Journal of Earth Sciences*, *91*(2), 331-340. https://doi.org/10.1007/s005310100219

Wang, T., Guo, L., Zhang, L., Yang, Q., Zhang, J., Tong, Y., & Ye, K. (2015b). Timing and evolution of Jurassic–Cretaceous granitoid magmatisms in the Mongol–Okhotsk belt and adjacent areas, NE Asia: Implications for transition from contractional crustal thickening to extensional thinning and geodynamic settings. *Journal of Asian Earth Sciences*, *97*, 365-392. https://doi.org/https://doi.org/10.1016/j.jseaes.2014.10.005

Wang, Y. (1979). Volcanic geology and volcanic landform of Wudalianchi area. *Heilongjiang Geol*, *1*(3), 33-43.

Wang, Y., & Chen, H. (2005). Tectonic controls on the Pleistocene–Holocene Wudalianchi volcanic field (northeastern China). *Journal of Asian Earth Sciences*, *24*(4), 419-431. https://doi.org/10.1016/j.jseaes.2003.12.010

Wang, Y., Li, C., & Chen, H. (1999). Tectonic settings of Cenozoic volcanism in northeastern China. *Geological Review*, *45*, 180-189. https://doi.org/10.16509/j.georeview.1999.s1.146

Wang, Y. Z., & Sun, J. Z. (1980). A preliminary division on the episodes of Cenozoic volcanism in Jilin Province. *Jilin Geol*, *3*, 6-25.

Wantim, M. N., Kervyn, M., Ernst, G. G. J., del Marmol, M. A., Suh, C. E., & Jacobs, P. (2013). Numerical experiments on the dynamics of channelised lava flows at Mount Cameroon volcano with the FLOWGO thermo-rheological model. *Journal of Volcanology and Geothermal Research*, *253*, 35-53. https://doi.org/https://doi.org/10.1016/j.jvolgeores.2012.12.003

Ward, J. F., Rosenbaum, G., Ubide, T., Wu, J., Caulfield, J. T., Sandiford, M., & Gürer, D. (2021). Geophysical and geochemical constraints on the origin of Holocene intraplate volcanism in East Asia. *Earth-Science Reviews*, *218*, 103624. https://doi.org/https://doi.org/10.1016/j.earscirev.2021.103624

Watson, B. F. (1985). Tectonic evolution of Kamchatka and the Sea of Okhotsk implications for the Pacific Basin. *Tectonostratigraphic Terranes of the Circum-Pacific Region*, *1*, 333-348. https://ci.nii.ac.jp/naid/10030364925/en/

Weaver, B. L., & Tarney, J. (1984). Empirical approach to estimating the composition of the continental crust. *NATURE*, *310*(5978), 575-577. https://doi.org/10.1038/310575a0

Webb, P. A. (2001). Volume and density determinations for particle technologists. *Micromeritics Instrument Corp*, *2*(16), 01.

Wei, H., Liu, G., & Gill, J. (2013). Review of eruptive activity at Tianchi volcano, Changbaishan, northeast China: implications for possible future eruptions. *Bulletin of Volcanology*, *75*(4), 706. https://doi.org/10.1007/s00445-013-0706-5

Wei, H., Sparks, R. S. J., Liu, R., Fan, Q., Wang, Y., Hong, H., Zhang, H., Chen, H., Jiang, C., Dong, J., Zheng, Y., & Pan, Y. (2003). Three active volcanoes in China and their hazards. *Journal of Asian Earth Sciences*, *21*(5), 515-526. https://doi.org/https://doi.org/10.1016/S1367-9120(02)00081-0

Wei, W., Hammond, J. O. S., Zhao, D., Xu, J., Liu, Q., & Gu, Y. (2019). Seismic Evidence for a Mantle Transition Zone Origin of the Wudalianchi and Halaha Volcanoes in Northeast China. *Geochemistry, Geophysics, Geosystems*, *20*(1), 398-416. https://doi.org/https://doi.org/10.1029/2018GC007663

Wellman, P., & McDougall, I. (1974). Cainozoic igneous activity in eastern australia. *Tectonophysics*, *23*(1), 49-65. https://doi.org/https://doi.org/10.1016/0040-1951(74)90110-3

Wentworth, C. K. (1922). A scale of grade and class terms for elastic sediments. *J. Geol.*, *30*(5), 377-392. https://doi.org/citeulike-article-id:14211954

White, J. D. (1991). Maar-diatreme phreatomagmatism at Hopi Buttes, Navajo Nation (Arizona), USA [journal article]. *Bulletin of Volcanology*, *53*(4), 239-258. https://doi.org/10.1007/bf00414522

White, J. D. L. (1990). Depositional architecture of a maar-pitted playa: sedimentation in the Hopi Buttes volcanic field, northeastern Arizona, U.S.A. *Sedimentary Geology*, *67*(1-2), 55-84.

White, J. D. L. (1996a). Pre-emergent construction of a lacustrine basaltic volcano, Pahvant Butte, Utah (USA) [journal article]. *Bulletin of Volcanology*, *58*(4), 249-262. https://doi.org/10.1007/s004450050138

White, J. D. L. (1996b). Impure coolants and interaction dynamics of phreatomagmatic eruptions. *Journal of Volcanology and Geothermal Research*, *74*(3), 155-170. https://doi.org/https://doi.org/10.1016/S0377-0273(96)00061-3

White, J. D. L., & Ross, P. S. (2011). Maar-diatreme volcanoes: A review. *Journal of Volcanology and Geothermal Research*, *201*(1), 1-29. https://doi.org/https://doi.org/10.1016/j.jvolgeores.2011.01.010

White, J. D. L., & Schmincke, H.-U. (1999). Phreatomagmatic eruptive and depositional processes during the 1949 eruption on La Palma (Canary Islands). *Journal of*

Volcanology and Geothermal Research, *94*(1), 283-304. https://doi.org/10.1016/S0377-0273(99)00108-0

Winter, J. D. (2013). *Principles of igneous and metamorphic petrology*. Pearson Education.

Winterer, E. L. (1973). Sedimentary Facies and Plate Tectonics of Equatorial Pacific1. *AAPG Bulletin*, *57*(2), 265-282. https://doi.org/10.1306/819a4268-16c5-11d7-8645000102c1865d

Wohletz, K. H. (1986). Explosive magma-water interactions: Thermodynamics, explosion mechanisms, and field studies [journal article]. *Bulletin of Volcanology*, *48*(5), 245-264. https://doi.org/10.1007/bf01081754

Wohletz, K. H., & McQueen, R. G. (1984a). Experimental studies of hydromagmatic volcanism. *Explosive volcanism: inception, evolution, and hazards*, 158-169.

Wohletz, K. H., & McQueen, R. G. (1984b). Volcanic and stratospheric dustlike particles produced by experimental water-melt interactions. *Geology*, *12*(10), 591-594. https://doi.org/10.1130/0091-7613(1984)12<591:VASDPP>2.0.CO;2

Wohletz, K. H., & Sheridan, M. F. (1983). Hydrovolcanic explosions II. Evolution of basaltic tuff rings and tuff cones. *American journal of science*, *283*(5), 385-413.

Wood, C. A. (1979). *Morphometric studies of planetary landforms: impact craters and volcanoes* Harvard].

Wood, C. A. (1980). Morphometric evolution of cinder cones. *Journal of Volcanology and Geothermal Research*, *7*(3-4), 387-413. https://doi.org/10.1016/0377-0273(80)90040-2

Wood, S. H., & Clemens, D. M. (2002). Geologic and tectonic history of the western Snake River Plain, Idaho and Oregon. *Tectonic and Magmatic Evolution of the Snake River Plain Volcanic Province: Idaho Geological Survey Bulletin*.

Wood, S. H., & Clemens, D. M. (2004). Tectonic and magmatic evolution of the Snake River Plain volcanic province. In B. Bonnichsen, M. McCurry, & C. White (Eds.), (Vol. 30, pp. 69-103). Idaho Geological Survey.

Wu, F.-Y., Lin, J.-Q., Wilde, S. A., Zhang, X. O., & Yang, J.-H. (2005). Nature and significance of the Early Cretaceous giant igneous event in eastern China. *Earth and Planetary Science Letters*, *233*(1), 103-119. https://doi.org/https://doi.org/10.1016/j.epsl.2005.02.019

Wu, J., Zhu, Z., Sun, C., Rioual, P., Chu, G., & Liu, J. (2019). The significance of maar volcanoes for palaeoclimatic studies in China. *Journal of Volcanology and Geothermal Research*, *383*, 2-15. https://doi.org/https://doi.org/10.1016/j.jvolgeores.2018.09.004

Wylie, J. J., Helfrich, K. R., Dade, B., Lister, J. R., & Salzig, J. F. (1999). Flow localization in fissure eruptions. *Bulletin of Volcanology*, *60*(6), 432-440. https://doi.org/10.1007/s004450050243

Xiao, L., & Wang, C. (2009). Geologic features of Wudalianchi volcanic field, northeastern China: Implications for Martian volcanology. *Planetary and Space Science*, *57*(5), 685-698. https://doi.org/https://doi.org/10.1016/j.pss.2008.08.005

Xiao, W., Windley, B. F., Hao, J., & Zhai, M. (2003). Accretion leading to collision and the Permian Solonker suture, Inner Mongolia, China: Termination of the central Asian orogenic belt. *Tectonics*, *22*(6), n/a-n/a. https://doi.org/10.1029/2002TC001484

Xiao, W. J., Windley, B. F., Huang, B. C., Han, C. M., Yuan, C., Chen, H. L., Sun, M., Sun, S., & Li, J. L. (2009). End-Permian to mid-Triassic termination of the accretionary processes of the southern Altaids: implications for the geodynamic evolution, Phanerozoic continental growth, and metallogeny of Central Asia [journal article]. *International Journal of Earth Sciences*, *98*(6), 1189-1217. https://doi.org/10.1007/s00531-008-0407-z

Yang, W., Yongkang, L., & Ruiqi, G. (1985). Formation and Evolution of Nonmarine Petroleum in Songliao Basin, China1. *AAPG Bulletin*, *69*(7), 1112-1122. https://doi.org/10.1306/ad462b8c-16f7-11d7-8645000102c1865d

Yarmolyuk, V., & Kovalenko, V. (2004). The Mesozoic-Cainozoic of Mongolia. In *Tectonics, Magmatism and Metallogeny of Mongolia* (pp. 201-241). Routledge.

Yu, F., & Cong, L. (2006). Trace element characteristics of Cenozoic basalts and their mantle xenoliths selected from Aershan area in Inner Mongolia. *China. Journal of Mineralogy and Petrology*, *26*(1), 29-34.

Yu, F., Yuan, W., Han, S., Ma, Z., & Jin, K. (2003). U-series component dating for Late Pleistocene basalt of Longgang, Jilin Province1. *High energy and nuclear physics*, *27*(11), 1039-1043.

Zakharovskyi, V., & Németh, K. (2021a). Qualitative-Quantitative Assessment of Geodiversity of Western Samoa (SW Pacific) to Identify Places of Interest for Further Geoconservation, Geoeducation, and Geotourism Development. *Geographies*, *1*(3), 362-380. https://www.mdpi.com/2673-7086/1/3/20

Zarazúa-Carbajal, M. C., & De la Cruz-Reyna, S. (2021). Digital Elevation Model resolution: Effects on the chronometry-oriented morphological analysis of monogenetic scoria cones in the Sierra Chichinautzin, central Mexico. *Geomorphology*, *389*, 107842. https://doi.org/https://doi.org/10.1016/j.geomorph.2021.107842

Zhang, C., Quan, J.-Y., Zhang, Y.-J., Liu, Z.-H., Li, W., Wang, Y., Qian, C., Zhang, L., & Ge, J.-T. (2020). Late Mesozoic tectonic evolution of the southern Great Xing'an Range, NE China: Evidence from whole-rock geochemistry, and zircon U-Pb ages and Hf isotopes from volcanic rocks. *Lithos*, *362-363*, 105409. https://doi.org/https://doi.org/10.1016/j.lithos.2020.105409

Zhang, J.-H., Gao, S., Ge, W.-C., Wu, F.-Y., Yang, J.-H., Wilde, S. A., & Li, M. (2010b). Geochronology of the Mesozoic volcanic rocks in the Great Xing'an Range, northeastern China: Implications for subduction-induced delamination. *Chemical Geology*, *276*(3), 144-165. https://doi.org/https://doi.org/10.1016/j.chemgeo.2010.05.013

Zhang, S.-H., Zhao, Y., Liu, X.-C., Liu, D.-Y., Chen, F., Xie, L.-W., & Chen, H.-H. (2009). Late Paleozoic to Early Mesozoic mafic–ultramafic complexes from the northern North China Block: Constraints on the composition and evolution of the lithospheric mantle. *Lithos*, *110*(1), 229-246. https://doi.org/10.1016/j.lithos.2009.01.008

Zhang, S., Gao, R., Li, H., Hou, H., Wu, H., Li, Q., Yang, K., Li, C., Li, W., Zhang, J., Yang, T., Keller, G. R., & Liu, M. (2014). Crustal structures revealed from a deep seismic reflection profile across the Solonker suture zone of the Central Asian Orogenic Belt, northern China: An integrated interpretation. *Tectonophysics*, *612-613*, 26-39. https://doi.org/https://doi.org/10.1016/j.tecto.2013.11.035

Zhang, Z., Mao, J., Wang, Y., Pirajno, F., Liu, J., & Zhao, Z. (2010a). Geochemistry and geochronology of the volcanic rocks associated with the Dong'an adularia–sericite epithermal gold deposit, Lesser Hinggan Range, Heilongjiang province, NE China: Constraints on the metallogenesis. *Ore Geology Reviews*, *37*(3), 158-174. https://doi.org/https://doi.org/10.1016/j.oregeorev.2010.03.001

Zhao, B., Xu, D., Bai, Z., & Chen, Z. (2021b). Volcanism in the Longgang volcanic field of NE China: insights from eruption history, volcano types and geochemical characteristics. *Geological Society, London, Special Publications*, *510*(1), 27-39. https://doi.org/doi:10.1144/SP510-2020-60

Zhao, B., Xu, D., Bai, Z., & Chen, Z. (2022). Hydro-Volcanism in the Longgang Volcanic Field, Northeast China: Insights from Topography, Stratigraphy, Granulometry and Microtexture of Xidadianzi Maar Volcano. *Minerals*, *12*(9), 1113. https://www.mdpi.com/2075-163X/12/9/1113

Zhao, C., Li, X., Zhou, X., Zhao, K., & Yang, Q. (2016). Holocene vegetation succession and responses to climate change in the northern sector of Northeast China. *Science China*

Earth Sciences, *46*(1674-7240), 870. https://doi.org/https://doi.org/10.1360/N072015-00180

Zhao, Y.-W., Zou, H., & Li, N. (2021a). Geomorphology and geochemistry of the Late Cenozoic volcanoes in the Halaha River–Chaoer River volcanic fields, western Greater Hinggan Mountain Range, NE China. *Geological Society, London, Special Publications*, *510*, SP510-2020-2082. https://doi.org/10.1144/SP510-2020-82

Zhao, Y. (2010). *Study on Geology and geochemistry of Quaternary volcanoes in the Da Hinggan Ling Mountains* [Ph.D thesis, Institute of Geology China Earthquake Administration, Beijing].

Zhao, Y., & Fan, Q. (2010). Yanshan and Gaoshan volcanoes in the Daxingan Mountain Range-a new eruption style. *Seismology and Geology*, *32*(01), 28-37.

Zhao, Y., & Fan, Q. (2012). Mantle sources and magma genesis of Quaternary volcanic rocks in the Halaha River and Chaoer River area，Great Xing'an Range. *Acta Petrologica Sinica*, *28*(4), 1119-1129.

Zhao, Y., Fan, Q., Bai, Z., Sun, Q., Li, N., Sui, J., & Du, X. (2008). Preliminary study on Quaternary volcanoes in the Halaha River and Chaoer River area in Daxing'an Mountain range. *Acta Petrologica Sinica*, *24*(11), 2569-2575.

Zhao, Y., Fan, Q., Li, N., & Gong, L. (2017). Study on volcanic geology characteristics and magma feeding fractures of Late Quaternary volcanoes in Dalinor volcanic field, Inner Mongolia. *Acta Petrologica Sinica*, *33*(3), 127-136.

Zheng, Y., Shen, W., Zhou, L., Yang, Y., Xie, Z., & Ritzwoller, M. H. (2011). Crust and uppermost mantle beneath the North China Craton, northeastern China, and the Sea of Japan from ambient noise tomography. *Journal of Geophysical Research: Solid Earth*, *116*(B12). https://doi.org/https://doi.org/10.1029/2011JB008637

Zhou, J., Wang, B., Zeng, W., & Cao, J. (2014). Detrital Zircon U–Pb dating of the Zhalantun metamorphic complex and its tectonic implications, Great Xing'an, NE China. *Acta Petrolei Sinica*, *30*(7), 1879-1888.

Zhou, X., & Armstrong, R. L. (1982). Cenozoic volcanic rocks of eastern China — secular and geographic trends in chemistry and strontium isotopic composition. *Earth and Planetary Science Letters*, *58*(3), 301-329. https://doi.org/https://doi.org/10.1016/0012-821X(82)90083-8

Zhou, X. M., & Li, W. X. (2000). Origin of Late Mesozoic igneous rocks in Southeastern China: implications for lithosphere subduction and underplating of mafic magmas. *Tectonophysics*, *326*(3), 269-287. https://doi.org/https://doi.org/10.1016/S0040-1951(00)00120-7

Zimanowski, B. (1998). Phreatomagmatic explosions. In A. Freundt & M. Rosi (Eds.), *From magma to tephra* (pp. 25-53).

Zimanowski, B., & Buttner, R. (2002). Dynamic mingling of magma and liquefied sediments. *Journal of Volcanology and Geothermal Research*, *114*(1-2), 37-44. https://doi.org/10.1016/S0377-0273(01)00281-5

Zimanowski, B., Büttner, R., & Lorenz, V. (1997). Premixing of magma and water in MFCI experiments [journal article]. *Bulletin of Volcanology*, *58*(6), 491-495. https://doi.org/10.1007/s004450050157

Zimanowski, B., Fröhlich, G., & Lorenz, V. (1995). Experiments on steam explosion by interaction of water with silicate melts. *Nuclear Engineering and Design*, *155*(1), 335-343. https://doi.org/10.1016/0029-5493(94)00880-8

Zimanowski, B., & Wohletz, K. H. (2000). Physics of phreatomagmatism; Part 2: Eruption physics. *Terra Nostra*, *6*, 535-544.

Zwoliński, Z. (2009). The routine of landform geodiversity map design for the Polish Carpathian Mts. *Landform Analysis*, *11*, 77-85.

Zwoliński, Z., & Stachowiak, J. (2012). Geodiversity map of the Tatra National Park for geotourism. *Quaestiones Geographicae*, *31*(1), 99-107.

Appendix:

Major element geochemistry can be utilised to classify and identify igneous rocks and their processes, and can also reveal the chemical controls on the physical essences such as crystallisation and melting processes (Winter, 2013). In advance, the major element analyses can represent the processes of magma evolution (Winter, 2013). The data of both sample groups (the key five locations of TX, Figs 21, 23, 25, 28 & 30) is followed by the XRF analyses at Massey University, and ICPMS analyses at Waikato University. In the powder preparation, the Tungsten ring mills and the crusher facilitated the procedures, thus the dried rocks and soil can be crushed as homogeneous powders (Fig 80). After the powder making, the samples were kept in a desiccator for about 12 hours. After the cooling procedure, the samples contained in the crucibles were heated up to 900 °C within the Muffle Furnace (Fig 81) for about 30 minutes in terms of the LOI (loss of ignition). Only by using this step could the samples get rid of the volatile contents, even the water of the crystallisation. Thus, the weight of LOI can be measured through the difference between the sample weight before 900° and after this temperature.

Figure 80: The ring mill for grinding the rocks into powder

Figure 81: The Muffle Furnace in the soil lab of Massey University

After the procedures mentioned above finished, the powder will be mixed with an XRF flux (Fig 82A), which contains 35.3% lithium tetraborate, and 64.7% lithium metaborate. Each rock powder was taken at 0.8 g, and the flux that was mixed with rock powder was measured at 8 g. Once the mixing processes are finished, each mixed sample will be put into an XrFuse 2 machine (Fig 82C) for fusion into glass beads (Fig 82B).

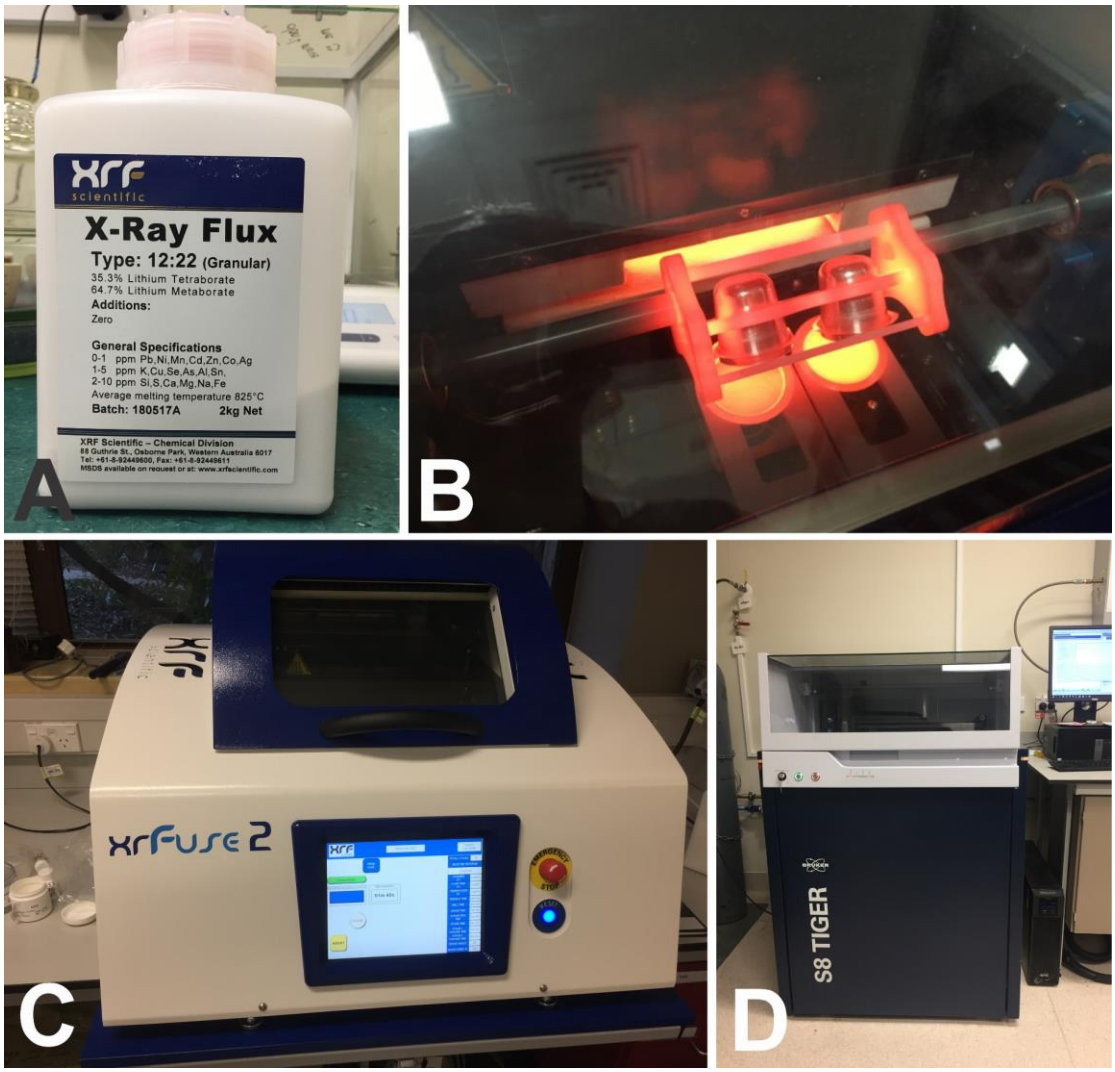

Figure 82: the fusion processes of XRF analyses

When the fusion process is finished, the samples will be kept in the desiccator for one night. Then the next morning, those glass beads will eventually be put into a machine called BRUKER S8 TIGER from Massey University (Fig 82D) for analyses of major elements.

The analyses for trace elements and REE were taken place at Waikato University in Hamilton NZ. In order to meet the requirements of the test, all the glass beads are glued to each other into a stack. The techniques are theoretically following the article from Stephen M. Eggins about the *"Laser Ablation ICP-MS Analysis of Geological Materials Prepared as Lithium Borate Glasses"* (Eggins, 2003). In this method, the samples made by XRF (glass beads) must be stacked and set in epoxy. Then, samples

were cut in half and the section surfaces had to be polished; those procedures were prior to the analyses.

The major analyses utilised the instruments, including Agilent 8900 Triple Quadrupole ICP-MS coupled with a Laurin Technic S155 SE ablation cell and a RESOlution 193 nm ArF excimer laser, in the School of Science, University of Waikato. The data was extracted by using Iolite 3.32, and the NIST612 glass standard was utilised as an external standard.

The general information of ICP-MS analyses is as follows:

- ICP-MS:

Model	Agilent Technologies QQQ 8900
Gas flows	Plasma (Ar) 15 L.min Auxiliary (Ar) 0.9 L.min Carrier (He) 0.37 L.min Nebuliser 0.95 to 1.05 optimised range
Shield torch	Used for most analyses
Vacuum pressure	1 x 10^{-5} Torr
Software	MassHunter 4.5 V.C.01.05

Table 13: The information about the ICP-MS instrument

- Laser:

Model	RESOlution SE series excimer laser
Wavelength	193 nm
Laser repetition rate	10 Hz
Pre-ablation laser warm-up	Laser fired continuously
Spot size	100 µm
Incident pulse energy	c. 0.04 mJ
Energy density on sample (fluence)	c. 5 J.cm^2
Software	Geostar v8.50

Table 14: The information on laser beams with related supplementary software

❖ Data Acquisition Parameters

Data acquisition protocol	Time-resolved analyses
Scanning mode	Peak hopping, 1 point per peak
Detector mode	Pulse counting, dead time correction applied
Isotopes measured	
Dwell time per isotope	10 ms (Al, Si) and 50 ms (all other elements)
Quadrapole settling time	c. 2 ms
Data acquisition	85 s (40 s background, 45 s ablation)
Software	MassHunter 4.5 V.C.01.05

Table 15: The details of data extraction, please note there were no isotope measures during the whole process.

ICP-MS is a supported technique in relation to the analyses of typical elements within the materials. The utilisation of ICP-MS Laser Ablation instruments at Waikato University is to identify trace elements for a diverse range of samples. Typical element analyses concentrate on those elements: Ag, Al, As, Ba, Cd, Co, Cr, Cu, Mg, Mn, Ni, Pb, Se, Sr, U, V, Zn, Ca, Fe, K, Na, P, S, Si, Hg, Mo, Sb. There are two types of techniques for both liquid and solid materials. The equipment called the New Wave 213-A/F laser ablation system is for the laser analyses.

MASSEY UNIVERSITY
TE KUNENGA KI PŪREHUROA
UNIVERSITY OF NEW ZEALAND

GRADUATE RESEARCH SCHOOL

STATEMENT OF CONTRIBUTION
DOCTORATE WITH PUBLICATIONS/MANUSCRIPTS

We, the student and the student's main supervisor, certify that all co-authors have consented to their work being included in the thesis and they have accepted the student's contribution as indicated below in the Statement of Originality.

Student name:	Bo'xin Li
Name and title of main supervisor:	Prof. Károly Németh
In which chapter is the manuscript/published work?	Chapter 2

Describe the contribution that the student and members of the supervisory team have made to the manuscript/published work:[1]

Prof. Károly Németh conceptualization, supervision, funding
Mrs Julie Palmer revision supervision
Prof. Alan Palmer revision supervision

Please select one of the following three options:

- (●) **The manuscript/published work is published or in press**

  Please provide the full reference of the research output:

  Li, B., Németh, K., Palmer, J., Palmer, A., Wu, J., Procter, J., & Liu, J. (2020). Basic Volcanic Elements of the Arxan-Chaihe Volcanic Field, Inner Mongolia, NE China. In N. Károly (Ed.), Updates in Volcanology (pp. Ch. 10). IntechOpen. https://doi.org/10.5772/intechopen.94134

- ( ) **The manuscript is currently under review for publication**

  Please provide the name of the journal:

- ( ) **It is intended that the manuscript will be published, but it has not yet been submitted to a journal**

Student's signature:	Bo'xin Li	Main supervisor's signature:	Karoly Nemeth Digitally signed by Karoly Nemeth Date: 2024.02.27 03:47:18 +13'00'

This form should be placed at the beginning of each relevant thesis chapter.

[1] Refer to the Massey University Publishing and Authorship guidelines (OneMassey for staff, Stream for students) and/ or Contributor Roles Taxonomy (CRediT) guidelines for guidance.

MASSEY UNIVERSITY
TE KUNENGA KI PŪREHUROA
UNIVERSITY OF NEW ZEALAND

GRADUATE RESEARCH SCHOOL

STATEMENT OF CONTRIBUTION
DOCTORATE WITH PUBLICATIONS/MANUSCRIPTS

We, the student and the student's main supervisor, certify that all co-authors have consented to their work being included in the thesis and they have accepted the student's contribution as indicated below in the Statement of Originality.

Student name:	Bo'xin Li
Name and title of main supervisor:	Prof. Károly Németh
In which chapter is the manuscript/published work?	Chapter 3

Describe the contribution that the student and members of the supervisory team have made to the manuscript/published work:[1]

Mrs Julie Palmer
Prof. Alan Palmer

Please select one of the following three options:

○	The manuscript/published work is published or in press Please provide the full reference of the research output:
○	The manuscript is currently under review for publication Please provide the name of the journal:
◉	It is intended that the manuscript will be published, but it has not yet been submitted to a journal

Student's signature:	Bo'xin Li	Main supervisor's signature:	Karoly Nemeth Digitally signed by Karoly Nemeth Date: 2024.02.27 03:49:04 +13'00'

This form should be placed at the beginning of each relevant thesis chapter.

[1] Refer to the Massey University Publishing and Authorship guidelines (OneMassey for staff, Stream for students) and/ or Contributor Roles Taxonomy (CRediT) guidelines for guidance.

MASSEY UNIVERSITY
TE KUNENGA KI PŪREHUROA
UNIVERSITY OF NEW ZEALAND

GRADUATE RESEARCH SCHOOL

STATEMENT OF CONTRIBUTION
DOCTORATE WITH PUBLICATIONS/MANUSCRIPTS

We, the student and the student's main supervisor, certify that all co-authors have consented to their work being included in the thesis and they have accepted the student's contribution as indicated below in the Statement of Originality.

Student name:	Bo'xin Li
Name and title of main supervisor:	Prof. Károly Németh
In which chapter is the manuscript/published work?	Chapter 4

Describe the contribution that the student and members of the supervisory team have made to the manuscript/published work:[1]

Prof. Károly Németh conceptualization, supervision, editing, funding
Mrs Julie Palmer supervision, editing
Prof. Alan Palmer supervision

Please select one of the following three options:

- (●) **The manuscript/published work is published or in press**

  Please provide the full reference of the research output:

  Li, B. x., Németh, K., Zakharovskyi, V., Palmer, J., Palmer, A., & Proctor, J. (2023b). Geodiversity estimate of the Arxan-Chaihe Volcanic Field extending across two geoparks in Inner Mongolia, NE China. Geological Society, London, Special Publications, 530(1), SP530-2022-2130. https://doi.org/doi:10.1144/SP530-2022-130

- ( ) **The manuscript is currently under review for publication**

  Please provide the name of the journal:

- ( ) **It is intended that the manuscript will be published, but it has not yet been submitted to a journal**

Student's signature:	Bo'xin Li	Main supervisor's signature:	Karoly Nemeth Digitally signed by Karoly Nemeth Date: 2024.02.27 03:50:40 +13'00'

This form should be placed at the beginning of each relevant thesis chapter.

[1] Refer to the Massey University Publishing and Authorship guidelines (OneMassey for staff, Stream for students) and/ or Contributor Roles Taxonomy (CRediT) guidelines for guidance.

MASSEY UNIVERSITY
TE KUNENGA KI PŪREHUROA
UNIVERSITY OF NEW ZEALAND

GRADUATE RESEARCH SCHOOL

STATEMENT OF CONTRIBUTION
DOCTORATE WITH PUBLICATIONS/MANUSCRIPTS

We, the student and the student's main supervisor, certify that all co-authors have consented to their work being included in the thesis and they have accepted the student's contribution as indicated below in the Statement of Originality.

Student name:	Bo'xin Li
Name and title of main supervisor:	Prof. Károly Németh
In which chapter is the manuscript/published work?	Chapter 5

Describe the contribution that the student and members of the supervisory team have made to the manuscript/published work:[1]

Prof. Károly Németh conceptualization supervision funding
Mrs Julie Palmer supervision, reviewing editing
Prof. Alan Palmer supervision editing

Please select one of the following three options:

- (●) **The manuscript/published work is published or in press**

  Please provide the full reference of the research output:

  Li, B. x., Németh, K., Palmer, J., Palmer, A., Zakharovskyi, V., & Gravis, I. (2023a). Eruption Scenario Builder Based on the most Recent Fissure-Feed Lava-Producing Eruptions of the Arxan-Chaihe Volcanic Field (ACVF), NE China. In N. Dr. Károly (Ed.), Updates in Volcanology - Linking Active Volcanism and the Geological Record

- ( ) **The manuscript is currently under review for publication**

  Please provide the name of the journal:

- ( ) **It is intended that the manuscript will be published, but it has not yet been submitted to a journal**

Student's signature:	Bo'xin Li	Main supervisor's signature:	Karoly Nemeth Digitally signed by Karoly Nemeth Date: 2024.02.27 03:51:50 +13'00'

This form should be placed at the beginning of each relevant thesis chapter.

[1] Refer to the Massey University Publishing and Authorship guidelines (OneMassey for staff, Stream for students) and/ or Contributor Roles Taxonomy (CRediT) guidelines for guidance.

MASSEY UNIVERSITY
TE KUNENGA KI PŪREHUROA
UNIVERSITY OF NEW ZEALAND

GRADUATE RESEARCH SCHOOL

STATEMENT OF CONTRIBUTION
DOCTORATE WITH PUBLICATIONS/MANUSCRIPTS

We, the student and the student's main supervisor, certify that all co-authors have consented to their work being included in the thesis and they have accepted the student's contribution as indicated below in the Statement of Originality.

Student name:	Bo'xin Li
Name and title of main supervisor:	Prof. Károly Németh
In which chapter is the manuscript/published work?	Chaper 6

Describe the contribution that the student and members of the supervisory team have made to the manuscript/published work:[1]

Prof. Károly Németh conceptualization scientific discussion editing funding

Please select one of the following three options:

- (●) **The manuscript/published work is published or in press**

  Please provide the full reference of the research output:

  Li, B. x., & Németh, K. (2023). Geodiversity Elements of a Young Fissure System as an Immediate Precursory Event of the Youngest Fissure-Fed Eruption within the Arxan UNESCO Global Geopark, Inner Mongolia, NE China. Proceedings, 87(1), 15. https://www.mdpi.com/2504-3900/87/1/15

- ( ) **The manuscript is currently under review for publication**

  Please provide the name of the journal:

- ( ) **It is intended that the manuscript will be published, but it has not yet been submitted to a journal**

Student's signature:	Bo'xin Li	Main supervisor's signature:	Karoly Nemeth Digitally signed by Karoly Nemeth Date: 2024.02.27 03:52:45 +13'00'

This form should be placed at the beginning of each relevant thesis chapter.

[1] Refer to the Massey University Publishing and Authorship guidelines (OneMassey for staff, Stream for students) and/ or Contributor Roles Taxonomy (CRediT) guidelines for guidance.